MAINTAINING REGENERATIVE COMPETENCE OF MUSCLE STEM CELLS: ROLE OF MITOCHONDRIAL DYNAMICS

Xiaotong Hong

TESI DOCTORAL UPF / 2022

THESIS DIRECTOR

Dra. Pura Muñoz-Cánoves

THESIS CO-SUPERVISOR

Dr. José Antonio Enríquez

DEPARTMENT OF MEDICINE AND LIFE SCIENCES

SCIENCES

Universitat Pompeu Fabra Barcelona

致我亲爱的母亲
她不仅给予了我生命
更给予了我无限的爱与希望

My most sincere thanks to:

First of all, to my thesis director and scientific mentor, who granted me this wonderful opportunity to learn, to explore and to grow; who has selflessly dedicated so much of her time and effort to support me and guide me through this journey of scientific adventures; who has taught me so much more by being a great example herself and without whom everything in this thesis would not exist. My deepest appreciations to you, ***Pura****. Also, to the co-director and co-supervisor of my project, who welcomed me into his group as a member of their own; who never failed to inspire me with his brilliant ideas and who encouraged me to challenge the known and the unknown. My most sincere thanks to you,* ***Toño****.*

To my beloved parents who have provided me with endless love, care and support; who are always and will always be there for me, no matter what.

To the great senior advisors, who are so knowledgeable yet so humble; who are generous with knowledge and help. To ***Joan****, who serves as the "scientific wikipedia" of the lab, who is full of ideas and always willing to share. To* ***Antonio****, who has been a great teacher. To* ***Eusebio****, who knows so much and is always there to help.*

To my dearest lab mates, who have been there with me through thick-and-thins; who have given me so much joy and laughter during these 5 years of life; who are not only colleagues but friends

*and family. To **Silvia, Nacho** and **Merche**, who have been wonderful teammates and friends; with whom I spent great time together, at work and out of work. To **José**, **Ángela**, **Jessica**, **Laura** and **Vera**, whose supports have made everything much better.*

*To all the members in the CNIC cellomics, microscopy, genomics, bioinformatics, viral vector and animal facility. To everyone who has helped me during my thesis in CNIC. To **Elena**, who stayed with me many nights in the cellomic facility, who has provided me so much help and company, even outside of her working schedule. To **Verónica**, who has provided me with substantial advice in imaging and image analysis. To all the members from GENOXPHOS lab, who are a second family in CNIC. To everybody from 1N, who have been great bench neighbours. To **Guilen**, **Nacho**, **Gillian**, **Laura**, **Cristina**, **Andrea**, **Mauro**, **Irene** and **Wen**, who are not only colleagues but also friends; who are very generous to share knowledge and reagents; who made my days in CNIC full of joy.*

*To my partner **Franck**, who is always there for me; who is my friend, my soulmate, my family.*

To all my friends and family, without whom life will not be the same.

Thank you!

ABSTRACT-RESUMEN

Abstract

Skeletal muscle regeneration depends on the correct expansion of resident quiescent stem cells (satellite cells), a process that becomes less efficient with aging, for largely unknown reasons. Here we show *in vivo* in mouse models that mitochondrial dynamics is essential for the successful regenerative capacity of satellite cells. Loss of mitochondrial fission in satellite cells—due to physiological aging or genetic impairment—deregulates the mitochondrial electron transport chain (ETC) subunits, resulting in inefficient oxidative phosphorylation (OXPHOS) metabolism, depressed mitophagy, and increased oxidative stress. Overall, this state results in muscle regenerative failure, caused by reduced proliferation and functional loss of satellite cells. Regenerative functions can be restored in fission-impaired or physiologically-aged satellite cells by re-establishment of mitochondrial dynamics (by directly activating fission or preventing fusion), OXPHOS metabolism, and/or mitophagy. Thus, mitochondrial shape and physical networking control stem cell regenerative functions by regulating metabolism and proteostasis. As mitochondrial fission occurs less frequently in satellite cells also from older humans, our findings have implications for therapies of muscle regeneration in sarcopenia.

Keywords: Muscle stem cells, muscle regeneration, mitochondria, mitochondrial dynamics, DRP1, mitophagy, metabolism, OXPHOS, aging

Resumen

La regeneración del músculo esquelético depende de la expansión correcta de las células madre inactivas residentes (células satélite), un proceso que se vuelve menos eficiente con el envejecimiento, por razones en gran parte desconocidas. Aquí mostramos que la dinámica mitocondrial es esencial para la capacidad regenerativa exitosa de las células satélite. La pérdida de la fisión mitocondrial en las células satélite, debido al envejecimiento fisiológico o al deterioro genético, desregula las subunidades de la cadena de transporte de electrones (ETC) mitocondrial, lo que da como resultado un metabolismo de fosforilación oxidativa ineficiente (OXPHOS), mitofagia deprimida y aumento del estrés oxidativo. En general, este estado da como resultado una falla en la regeneración muscular, causada por una menor proliferación y pérdida funcional de las células satélite. Las funciones regenerativas se pueden restaurar en células satélite dañadas por la fisión o envejecidas fisiológicamente mediante el restablecimiento de la dinámica mitocondrial (mediante la activación directa de la fisión o la prevención de la fusión), el metabolismo de OXPHOS o la mitofagia. Por lo tanto, la forma mitocondrial y la red física controlan las funciones regenerativas de las células madre al regular el metabolismo y la proteostasis. Como la fisión mitocondrial ocurre con menos frecuencia en las células satélite de los humanos mayores, nuestros hallazgos tienen implicaciones para las terapias de regeneración muscular en la sarcopenia.

Palabras clave: Células satélite, regeneración muscular, mitocondrias, dinámica mitocondrial, DRP1, mitofagia, metabolismo, OXPHOS, envejecimiento

PREFACE

The work presented in this Doctoral Thesis was supported by Severo Ochoa FPI fellowship (BES-2017-07910) and was done in Centro Nacional de Investigaciones Cardiovasculares (CNIC) in Madrid and in the Cell Biology Group at the Department of Experimental and Health Sciences of the Pompeu Fabra University (DCEXS-UPF) in Barcelona.

The content of this thesis provides new insight to our understanding on how mitochondria, metabolism and cellular proteostasis affect stem cell regenerative capacity in mammals and reveals how these machineries supporting stem cell functions are declined with aging as well as possible rejuvenation routes. Parts of this thesis have already been submitted for publication.

TABLE OF CONTENTS

TABLE OF CONTENTS

INTRODUCTION

1. Skeletal muscle stem cells and myogenesis

1.1 The skeletal muscle and its resident stem cells, the satellite cells

Skeletal muscle is one of the most abundant and plastic tissues of the human body, accounting for approximately 40% of the adult human body weight and containing 50-70% of the body's proteins[1–3]. Skeletal muscle contributes remarkably to a variety of bodily functions. From a mechanical perspective, skeletal muscle offers support and allows for mobility of the organism by converting chemical energy into mechanical energy to generate force and power, therefore contributes greatly to the individual's functional independence in their social and occupational settings. From a metabolic point of view, skeletal muscle plays essential roles in basal energy metabolism, storage of important substrates such as amino acids and carbohydrates, thermoregulation, and energy balance regulation via physical activities[2].

Skeletal muscle is composed of bundles of multinucleated muscle fibers (myofibers) together with blood vessels, nerve fibers, and connective tissue. The outer connective tissue, the epimysium, wraps the muscle and connect the muscle to the tendons. Inside each skeletal muscle, muscle fibers are organized into bundles called fascicles that are surrounded by a middle layer of connective tissue, the perimysium. Inside each fascicle, each muscle fiber is surrounded by a thin connective tissue layer, the endomysium (also called the basement membrane or basal lamina). Each myofiber is a functional unit of the skeletal muscle and consist of myofibrils containing the proteins actin, myosin, and troponin, which are primarily responsible for the contractile properties of skeletal muscle[2,4,5] (**Figure 1**).

As a post-mitotic tissue, adult skeletal muscle has a low turnover under normal conditions, with only sporadic fusion of satellite cells during daily wear-and-tear[6]. Nevertheless, skeletal muscle displays a remarkable regenerative capacity in response to injury thanks to its resident muscle stem cells, also called satellite cells (hereafter, "SCs"). Skeletal muscle regeneration was first properly described in the 1860s, but it was not until almost a century later until the cellular mechanisms of this process were illustrated[7]. In 1961, these small cells were initially identified by Alexander Mauro[8] using transmission electron microscope (TEM) and were given the name “satellite cells” based on their unique anatomical position at the periphery of the myofibers - “wedged” between the plasma membrane of the muscle fiber and the surrounding basement membrane[7,9–11] (**Figure 1**). Apart from their special location, TEM also revealed the morphology of SCs: large nuclear-to-cytoplasmic ratio, few organelles due to the striking paucity of the cytoplasm, and condensed interphase chromatin (**Figure 1**). In the past decades, it has been conclusively demonstrated that SCs function as the primary player during muscle regeneration and are capable of self-renewal; thus, they are generally recognized as the *bona fide* stem cells of skeletal muscle[11–14].

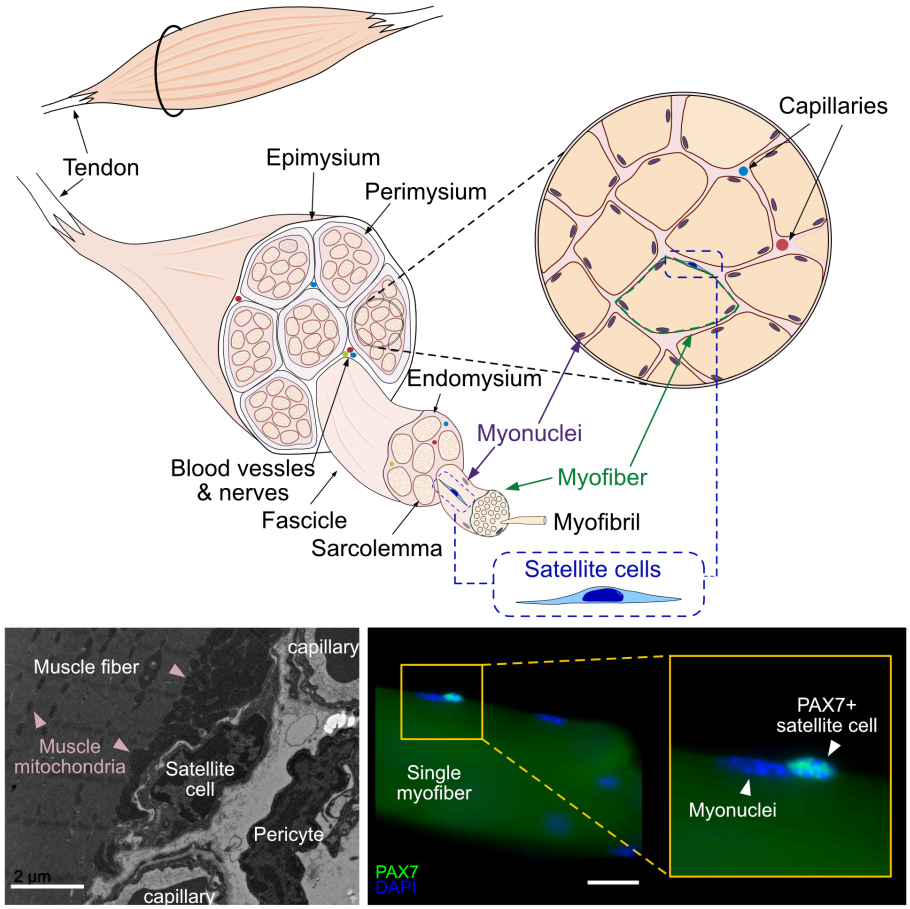

Figure 1 Schematic representation of the skeletal muscle structure (top). The muscle tissue is connected to the bones through its tendon and is surrounded by an outer layer of connective tissue celled epimysium. Inside each muscle tissue, myofibers are organized in bundles called fascicles and are wrapped by another layer of connective tissue called the perimysium. Each myofiber is considered as one multi-nucleated cell, composed by a large number of myofibrils and are surrounded by endomysium. SCs are located between the connective tissue sheet and the myofiber plasma membrane, called sarcolemma (Figure adapted from[15]). Transmission electron microscope (TEM) image of the soleus muscle showing the muscle fiber, mitochondria as well as one satellite cell, one pericyte and capillaries (lower left). Scale bar, 2 µm. Immunofluorescence (IF) staining of PAX7 and DAPI on an isolated single myofiber. One PAX7^{+} satellite cell was identified. Scale bar, 20 µm.

Skeletal muscle in vertebrates originates from cells found in the mesoderm[16,17]. During embryogenesis, parts of the mesoderm give rise to the somites, which are segmented clusters aligned along the posterior axis of the embryo[18]. Embryonic muscle progenitors derived from the somites, the paraxial head mesoderm and the prechordal mesoderm,

are responsible for the prenatal myogensis and are marked by the expression of two paired-box (Pax) transcription factors Pax3 and Pax7[19–25]. These progenitors undergo two rounds of prenatal myogenesis: the embryonic myogenesis (in mice between embryonic day E10.5 and E12.5[26]) that give rise to primary muscle fibers, followed by fetal myogenesis (in mice between E14.5 to birth[27]), giving rise to the majority of skeletal-muscle fibers present at birth[28–30]. In mice, SCs expressing the transcription factor Pax7 appear at approximately embryonic day 16.5 (E16.5) in the developing limb muscle[31]. It is notable that SCs in different anatomical regions are derived from various embryonic regions. The majority of SCs (from trunk, limb, diaphragm, and tongue) arise from the somite, whereas the remainder of the head muscles and SCs derive from cells of the paraxial head mesoderm and the prechordal mesoderm[23–25,31–35].

Moreover, SCs reside in a specialized local microenvironment, or niche, comprising of the resident myofiber, the extracellular matrix (ECM), and other non-SC populations, including fibro-adipogenic progenitors (FAPs), immune cells, endothelial cells, and others. The niche has a great impact on SCs, both in quiescence and during muscle regeneration, via secretions of growth factors and cytokines as well as by the modification of matrix stiffness[10,36].

1.2 Satellite cells during muscle regeneration

In adulthood under physiological conditions, SCs are maintained in a cell cycle–arrested state called quiescence[37] (G_0 state of the cell cycle), characterized by low transcriptional and metabolic activity[11,38–40]. Following environmental stimuli (such as muscle injury), SCs are capable of rapidly activating to exit the quiescence state and of

proliferating to expand the pool of myogenic progeny, which will then differentiate and fuse with damaged myofibers or form new myofibers to repair and maintain tissue homeostasis[9,14,41].

The states of SCs and myogenic progenitors are defined at the molecular level by the fine-tuned temporal expression of transcription factors (TFs). Over the past decades, various TFs have been identified as markers of the quiescent state as well as of activation and commitment to the myogenic lineage. Among these factors, the "paired box" transcription factors Pax7 and Pax3 as well as the myogenic regulatory factors (Mrfs: Myf5, MyoD, and myogenin) are of special importance due to their unique roles in muscle stem cell homeostasis, lineage progression, and fate specification[42–45]. SCs are characterized by the expression of Pax7, which is expressed in both the quiescent and activated states and is essential for SC development and survival[21,46,47]. Both Pax7 and the closely related Pax3 are expressed in quiescent satellite cells (hereafter, QSCs) and are essential in preventing early myogenic differentiation[32,48–50]. The Mrfs, on the other hand, play essential roles in myogenic specification, differentiation, and maintenance during muscle development and regeneration[51]. The expression of *Myf5* is detected in the majority of QSCs in adult skeletal muscle[52]. However, protein translation of Myf5 is suspended in QSCs due to the fact that *Myf5* mRNA and microRNA-31 (miR-31), which suppresses Myf5 translation, are sequestered in messenger ribonucleoprotein (mRNP) granules (mRNP granules) in this state[53]. In QSCs, neither *MyoD* mRNA nor MYOD protein are detected[54]. Upon muscle injury, SCs start to express *MyoD* and initiate the myogenic program. SC activation is accompanied by the accumulation of *Myf5* due to the dissociation of mRNP granules and reduced levels of miR-31, leading to the initiation of the myogenic program in satellite cells[53]. When

proliferating progenies progress into lineage commitment, they start to express myogenin and become terminally-differentiated myocytes.

Accordingly, during muscle regeneration, the stem cell state can be distinguished based on Pax7, MyoD, and myogenin protein expression: $Pax7^{+}MyoD^{-}myogenin^{-}$ cells are in a quiescent state, whereas $Pax7^{+}MyoD^{+}myogenin^{-}$ cells are in an activated or proliferating state that can be further distinguished using a cell cycle marker such as Ki67. $Pax7^{-}MyoD^{+/-}myogenin^{+}$ cells are undergoing myogenic differentiation and will eventually fuse into an existing myofiber or fuse with each other to form a new myofiber[55,56]. On the other hand, not all proliferating SCs will undergo differentiation: a minor fraction of activated or proliferating SCs can give rise to $Pax7^{+}MyoD^{-}$ cells that exit cell cycle and return to the quiescent state, thereby replenishing the stem cell pool[55]. The adult myogenesis process is illustrated schematically in **Figure 2**.

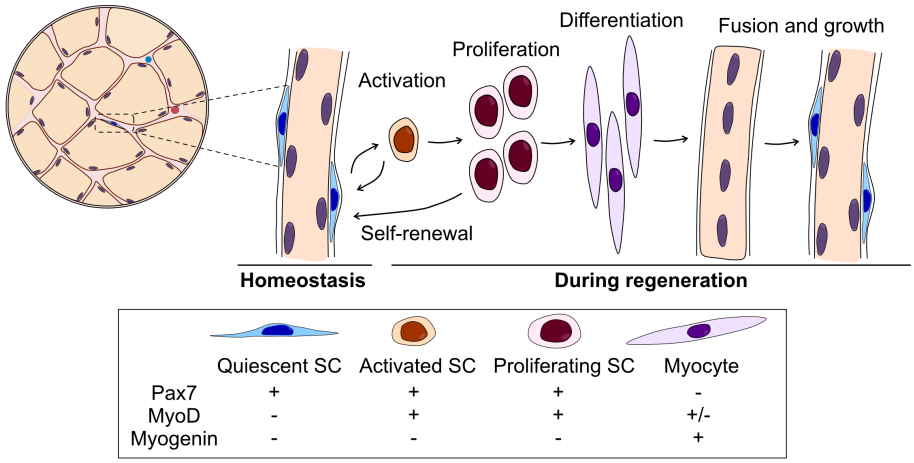

Figure 2 Schematic representation of the distinct steps of adult myogenesis after injury.

Recent discoveries of specific SC surface markers enabled the identification and isolation of SCs using fluorescence-activated cell sorting (FACS) procedures, contributing greatly to the advance of SC research. To date, the most recognized surface markers include VCam1,

α7-integrin, NCam1, cMet, m-Cadherin, Synd3/4, CXCR4, and CD34[57–64]. A recent study using a Pax7-zsGreen reporter line has further confirmed the efficiency of quiescent SC FACS isolation using the combination of surface marker α7-integrin and CD34, β1-integrin and CXCR4 or VCAM1 alone where high overlapping was observed using these 3 distinct sorting schemes[65].

Apart from the function of SCs, efficient muscle regeneration requires a precisely orchestrated regulation and coordination of all cell types in the niche[10,36]. Upon acute muscle injury, the myofiber undergo necrosis and increased permeability, leading to leakage of muscle proteins and microRNAs[9,66]. Following myofiber necrosis, resident leukocytes secrete burst of cytokines and chemokines, resulting in the attraction of circulating granulocytes (including mainly neutrophils)[67,68]. The infiltrated neutrophils secrete chemokines (such as MIP-1α and MCP-1) that further contribute to the recruitment of monocytes[69,70]. Once infiltrated, monocytes undergo differentiation into macrophages: an initial wave of proinflammatory (M1) macrophages, followed by a second wave of anti-inflammatory (M2) macrophages[71–73]. M1 and M2 macrophages are responsible for the stimulation of early and late phases of myogenesis, respectively. M1 macrophages secrete the proinflammatory factors IL-1β, IL-6, and TNF-α that are essential for inducing SC proliferation, whereas M2 macrophages secrete IL-4 and IGF-1, which promote progenitor differentiation[71,74,75]. In addition to immune cells, FAPs show supportive functions during muscle regeneration via the production of WNT1 Inducible Signaling Pathway Protein 1 (WISP1), a matricellular signaling protein that is required for efficient muscle regeneration via regulating SC expansion and asymmetric commitment[76]. FAPs are also major source of IL-33 production, which is essential for the recruitment of muscle regulatory T (Treg) cells that aid muscle repair[77].

1.3 The quiescent state and satellite cell heterogeneity

During embryonic and postnatal development, the formation and growth of skeletal muscle relies vastly on the fusion of myogenic progenitors generated by fast-dividing satellite cells[9,78–80]. During this process, some SCs escape the differentiation fate and anchor to myofibers, thereby maintaining a prolonged cell cycle–arrested state of low cellular activity called quiescence[81]. In adults, muscle growth is achieved primarily via muscle fiber hypertrophy whereas SCs contribute very little to the maintenance of muscle fiber size and type[82]. Recently, it has been demonstrated that local and minor lesions can be repaired by myofibers in an autonomous manner without the participation of satellite cells[83]. As a result, the majority of SCs are maintained in a quiescent state throughout life. Although it was believed that quiescence is a state of cellular inactivity, increasing evidence suggests that quiescence is dynamically regulated and contributes the long-term capacity of the stem cells to maintain their regenerative functions.

Molecular pathways inhibiting cell cycle progression are essential to govern the quiescence state in satellite cells. For instance, mitogenic activity in QSCs are repressed through cyclin-dependent kinase (CDK) inhibitors such as $p27^{Kip1}$ [84]and $p57^{Kip2}$ [85]. The repression of the p38α/β MAPK pathway has been shown to be a key player during SC commitment and self-renewal is also critical for the maintenance of SC quiescence[86–88]. Another example is the inhibition of fibroblast growth factor (Fgf) signaling by Sprouty1 (Spry1), which has been identified as a key quiescence gene[89]. Furthermore, post-transcriptional regulation by microRNAs also contributes to the regulation of SC quiescence, such as the previously mentioned suppression of Myf5 by miR-31[53]. Other

examples include miR-489 by repressing Dek[90] and miR-708 by inhibiting cell migration[91]. Examples of niche-associate SC quiescence include interaction with myofiber via Notch-delta-like 1 (Dll1) interaction and Notch intracellular signaling[92–95] and Wnt signaling[96,97], with ECM via Notch-collagen signaling[98], with endothelial cells and the vasculature via VEGF and Notch signaling[99].

SC quiescence is also achieved through cellular proteostasis and metabolic regulations. Our previous work illustrated that autophagy (see Introduction Chapter 4) is required for SC quiescence maintenance, and that the deletion of key autophagy gene *Atg7* in SCs leads to loss of QSCs and disruption of homeostasis[100]. We showed that autophagy is essential for maintaining SC stemness by preventing the cells from entering into senescence, which is one of the factors contributing to the loss of SC functions in old age[101]. In addition to the removal of damaged protein autophagy, QSCs show low protein synthesis, which is achieved by the phosphorylation of eIF2α. Specifically, eIF2α phosphorylation is required for SC quiescence and self-renewal, and its loss leads to SC activation and differentiation and reduced regenerative capacity[102]. Although studying SC metabolism in quiescence has been challenging due to the low metabolic activity of these cells, recent studies have revealed links between energy metabolism and SC quiescence regulation. For instance, high levels of NAD^+ in SCs triggers deacetylation of histone H4K16 via the cellular energy sensor sirtuin 1 (Sirt1), which leads to the inhibition of genes involved in cell cycle progression[103]. Moreover, by studying SCs from truly unperturbed muscle or the uninjured contralateral muscle from an injured mouse, a new concept of G_{Alert} state has been described, referred to a non-proliferating state, which has an increased metabolic activity that functions an ‘alerting’ mechanism and prepares cells for responding rapidly upon potential injury[104]. The study demonstrated that the

transition of G_0 to G_{Alert} is regulated by the mammalian target of rapamycin complex 1 (mTORC1), a key cellular metabolic regulator. On the other hand, the energy sensor AMP-activated protein kinase (AMPK) is reported to regulate the return to quiescence (self-renewal) via the inhibition of lactate dehydrogenase (LDH) activity[105], and the upstream AMPK activator liver kinase b1 (LKB1) plays a role in maintaining the quiescent state through AMPK-mediated inhibition of mTOR[106].

The heterogeneity of QSCs was first suggested in the late 1990s[107,108]. Since then, emerging studies from mouse transgenesis, *in vivo* labelling, and single-cell transcriptomic analyses support the fact that the QSC pool is a not a homogeneous population[13,40,64,109–114]. For instance, using *Myf5-Cre/ROSA-YFP* reporter alleles, researchers reported a subpopulation of QSCs that never express Myf5 throughout life ($Pax7^+/Myf5^-$)[13]. This 10% of $Pax7^+/Myf5^-$ cells are in a higher stem cell hierarchy in the quiescent pool and are able to give rise to the lower hierarchical subpopulation ($Pax7^+/Myf5^+$) via asymmetric division, thereby contributing to the stem cell reservoir. The hierarchy in QSC pool was also reported by another group using a transgenic *Pax7-nGFP* mouse line, who showed that SCs expressing high level of Pax7 ($Pax7^{Hi}$) are the more stem-like subpopulation as opposed to the $Pax7^{Low}$ subpopulation. These $Pax7^{Hi}$ cells are the label-retaining population in tandem pulse labeling experiments, indicating that "older" chromosomes are segregated into the stem-like subpopulation whereas newly synthesized chromosomes are inherited by the less "stem" $Pax7^{Low}$ cells. More recently, our group showed that a subset of QSCs expressing high levels of CD34 surface marker display higher stemness properties (i.e., the "genuine state"), while another subset of SCs with low levels of CD34 expression is more prone to differentiation (i.e., a "primed state")[64]. The genuine state population is preserved until advanced old age but

collapses in extreme old age due to the loss of FoxO transcription factors activity.

In recent years, deep cartography of resident cell populations within skeletal muscle combining single-cell RNA sequencing (scRNA-seq) and mass cytometry by time of flight (CyTOF) led to the discrimination of certain degree of heterogeneity within SCs and the discovery of new muscle resident non-myogenic populations[111]. scRNA-seq also helped to identify a small SC subpopulation that resembles a more quiescent state, due to the higher expression of Pax7 as well as other quiescent-core genes, whereas the larger SC subpopulation displays an early-activation profile due to the increased expression of myogenic commitment genes such as *Myod1*[110,115]. Additionally, a small quiescent SC subpopulation enriched in Dll1/Notch2 signaling was shown to promote self-renewal in regenerative conditions[92]. Finally, SC heterogeneity was also documented in human muscle[116,117].

1.4 Satellite cell expansion and self-renew: symmetric *vs* asymmetric division

Like other stem cell types, SCs are able to give rise to committed progenitors as well as to self-renew in order to replenish the stem cell pool. During muscle regeneration, SCs are activated and undergo proliferation. The majority of daughter myogenic precursors eventually differentiate into myocyte and fuse into myofibers whereas a small population of cells returns to QSCs as a self-renewal process. The first evidence of SC self-renewal came from a single myofiber transplantation experiment that showed that as few as seven SCs within one single myofiber, when transplanted into radiation-ablated muscle, were able to give rise to over 100 SCs and thousands of myonuclei[12].

These results highlight the capability of SCs to undergo self-renewal as well as differentiation and show that they are self-sufficient as a source of regeneration.

Over the last decades, numerous studies have elucidated which genes essentially regulate muscle SC self-renewal. Intrinsic regulation of SCs self-renewal can be attributed to Mrfs such as Myod1 and Myf5 and their upstream regulators Pax7, Pax3, and sineoculis homeobox homolog 1 (Six1) and 4 (Six4)[118]. For instance, downregulation of Myod1 is essential for the self-renewal process[50,54,55,119,120], and Myf5 has been suggested to be one of the key modulators of SC self-renewal[121]. Six1 can directly activate Myod1 and Myog expression, which in turn promote SC differentiation[122]. SC-specific Six1 deletion resulted in impaired myogenic cell differentiation and muscle regeneration but increased SC self-renewal. In addition to the intrinsic TFs, SC self-renewal is also under the regulation of extrinsic signaling pathways, including ERK signalling[89,122], p38 α/β MAPK pathway[86–88], Wnt7a[97], Notch[94,95,123–126] and calcitonin receptor singaling[85,127].

Studies of SC heterogeneity revealed a subpopulation of more “stem” satellite cells that are able to undergo asymmetric division, in contrast to the more “primed” subpopulation that are more subjected to symmetric division and differentiation[13,40]. Earlier studies using *ex vivo* cultured myofiber as a model for SC proliferation identified different patterns of SC expansion: basal division that generate two identical daughter cells (symmetric division) and apical division that generate one committed progenitor and one stem cell[13]. However, recent studies applying histone H3-SNAP[128] or 5-ethynyl-2′-deoxyuridine (EdU)[129] pulse tracing provided evidence that SCs undergo symmetric division *in vivo* during early regeneration in order to provide sufficient progenies whereas self-renewal starts at later regenerative stages. It was shown

that equivalent H3-SNAP signal was detected in daughter cells at 3 days post-injury (DPI), whereas asymmetric division was observed at 5-DPI[128]. Another group showed that following an induced muscle injury, myonuclei are generated within the first four days, which requires massive expansion of myogenic progenitors derived from satellite cells. The SC pool is replenished by self-renewal only later during regeneration, namely, from 5- to 14-DPI[129]. These new findings suggested after injury, SCs first undergo extensive symmetric division to generate sufficient progeny and then later undergo asymmetric division, to differentiate and repair the myofiber or self-renew to maintain the stem cell pool.

2. Mitochondria: its metabolism, function and dynamics

2.1 Mitochondrial metabolism and its cellular function

Cells obtain energy through metabolism, which comprises two categories of processes: anabolism, or the building up of cell components (e.g., proteins and nucleic acids), and catabolism, or the breaking down of intracellular components (thereby releasing energy for anabolism). Increasing evidence demonstrates that stem cell functions are largely controlled by metabolism[39,103,130], and that a balance of anabolic and catabolic processes is essential for the homeostasis of the cell.

Adenosine triphosphate (ATP), the key energy-transporting molecule, is generated mainly via oxidative-phosphorylation (OXPHOS) or glycolysis. As one of the most important energy sources, glucose can be processed to pyruvate via glycolysis and yields small amounts of ATP molecules. Pyruvate derived from glycolysis can either be converted into acetyl-CoA in the mitochondria, which then enters the tricarboxylic acid (TCA cycle, also called Krebs cycle and citric acid cycle), or it can be converted to lactate in the cytoplasm when oxygen is limited (a process termed anaerobic glycolysis). In fact, ATP generation by mitochondria via OXPHOS is much more efficient than that by glycolysis: Mitochondria can produce up to 36 ATP from one molecule of glucose, whereas glycolysis produces only 2 molecules of ATP[131]. Further, mitochondria can also use intermediates from the metabolism of other energy sources. For instance, the metabolism of fatty acids involves a series of oxidation steps (termed fatty acid oxidation, FAO) that generate acetyl-CoA, which enters the TCA cycle and glutaminolysis, a process

that converts glutamine into glutamate; this can also be coupled to TCA cycle upon conversion of glutamate to α-ketoglutarate (α-KG) (**Figure 3**).

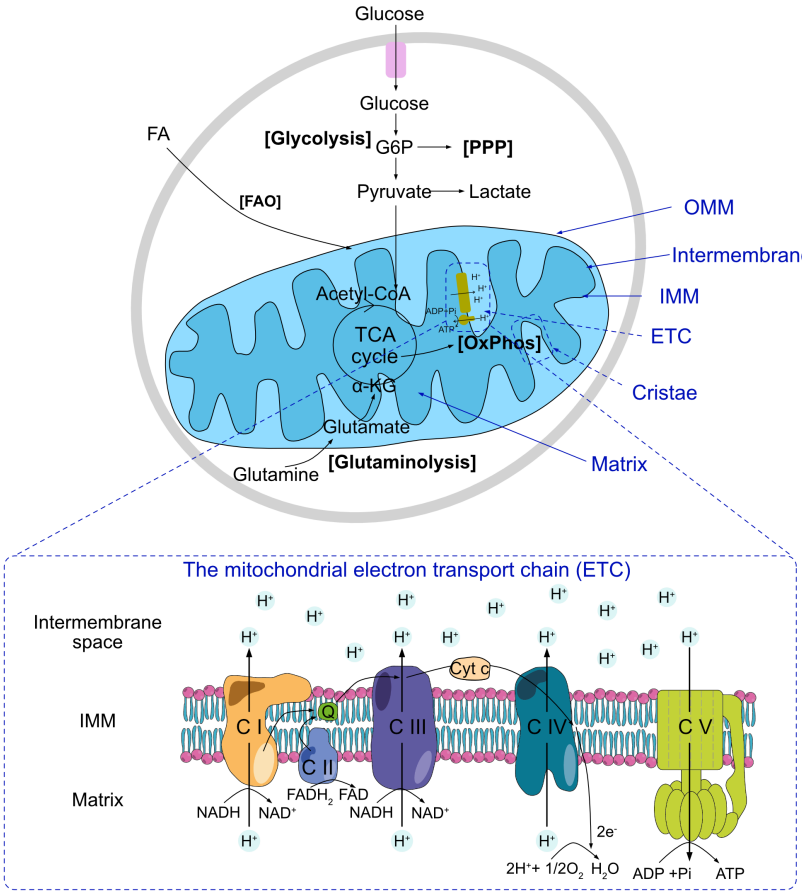

Figure 3 Schematic representation of the major cellular energy metabolism pathways (top) and the mitochondrial electron transport chain. G6P, glucose-6-phosphate; FA, fatty acid; FAO, fatty acid oxidation; PPP, pentose phosphate pathway; TCA cycle, tricarboxylic acid cycle/ Krebs cycle; α-KG, α-ketoglutarate; OMM, outer mitochondrial membrane; IMM, inner mitochondrial membrane; ETC, electron transport chain; OXPHOS, oxidative phosphorylation; CI-CV: electron transport chain complex I-V; Q, coenzyme Q; Cyt c, cytochrome c; NAD^+/NADH; Nicotinamide adenine dinucleotide; FAD/$FADH_2$, flavin adenine dinucleotide.

Mitochondria are present in most eukaryotic cells and have an inner mitochondrial membrane (IMM) and an outer mitochondrial membrane (OMM). The OMM is highly permeable, allowing the passage of small molecules < ~5,000 Da by diffusion. It contains porins and translocases

that facilitates the molecular exchange between the cytosol and the mitochondrion. For instance, the voltage-dependent anion channel (VDAC) locating on the IMM is the primary transporter responsible for the exchange of metabolites, ions and nucleotides[132–134]. Apart from its cargo function, the OMM forms interfaces with other subcellular structures such as the endoplasmic reticulum (ER), peroxisomes, lysosomes, endosomes, melanosomes, lipid droplets and the plasma membrane to establish membrane contact sites[135]. The space between the inner and outer membrane is referred to as the intermembrane space (IMS), also termed the perimitochondrial space, exhibits similar composition as the cytosol due to the high permeability of the OMM. The IMM encloses the mitochondrial lumen (termed the "matrix") where the TCA cycle, mitochondrial DNA (mtDNA) replication, protein biosynthesis take place. The IMM includes two main subcompartments: the inner boundary membrane (IBM) and mitochondrial cristae. The IBM is adjacent to the OMM and contains various channel transporters that shuttle ions and small metabolites between the cytoplasm and the mitochondrial matrix. Further, mitochondrial cristae are invaginations of inner membrane that protrude into the matrix space, this special structure expands the surface area and harbors the machinery required for mitochondrial respiration: ETC complexes and ATP synthase. In addition, according to the cristae junction (CJ) model[136,137], cristae are connected to the IBM via narrow clefts that close the cristae called CJs, which prevent the contents of the cristae from being released into the IMS.

The mitochondrial ETC locating on the IMM is composed of 5 complexes: NADH:ubiquinone oxidoreductase (complex I, CI), succinate dehydrogenase (complex II, CII), Coenzyme Q-cytochrome c reductase (complex III, CIII), cytochrome c oxidase (complex IV, CIV), and the F_1F_0 ATP synthase (complex V, CV)[138], as illustrated in **Figure 3**.

Electrons derived from NADH or $FADH_2$ are transported through complex I/III/IV or complex II/III/IV in an exergonic process that drives the proton pumping from the mitochondrial complex into the intermembrane space. The accumulated proton gradient then drives the synthesis of ATP via complex V, or can be consumed by uncoupling. Unlike the OMM, the IMM is highly impermeable, which, together with the proton gradient generated by the proton pumping activities of the ETC contribute to the building-up of mitochondrial membrane potential ($\Delta\Psi m$). Under physiological conditions, the level of $\Delta\Psi m$ is kept relatively stable with limited fluctuations, thereby a long-lasting drop or rise of $\Delta\Psi m$ could reflex unwanted loss of cell viability and have deleterious effects[139].

Besides their major function associated with cellular bioenergetics (ATP production), mitochondria also play important roles in various cellular processes such as programmed cell death[140–143], reactive oxygen species (ROS) signaling[144,145], autophagy[146–149], calcium homeostasis, and signaling[150–152]. In addition, emerging studies have demonstrated the participation of mitochondria in the regulation of stem cell fate decisions[153–160] and the immune response[161,162].

Mitochondria contain their own genome, the mtDNA, which is located in the mitochondrial matrix. First described in the 1960s, the mitochondrial genome is a small, double-stranded DNA molecule[163] encoding 37 genes in humans: 13 subunits of the OXPHOS system, 2 ribosomal subunits (12S and 16S), and 22 transfer RNAs (tRNAs)[164]. The majority of mitochondrial genes (~1,500), on the other hand, are nuclear-encoded[165]. The number of mtDNA copies per cell ranges from hundreds to thousands, and their replication, segregation, and distribution are essential for mtDNA maintenance and mitochondrial functions[166,167]. Mitochondrial genomes are packaged into discrete

mtDNA-protein complexes, termed nucleoids by the HMG box architectural transcription factor A (TFAM)[165]. Each mitochondrial nucleoid contains numerous copies of mtDNA and functions as a unit of mtDNA propagation for mtDNA replication, segregation, and gene expression[168].

2.2 Mitochondrial dynamics

Since the early electron microscopic observations in the 1950s, mitochondria have been viewed as static, bean-shaped organelles[169]. However, this canonical view was challenged by recent advances in live cell imaging and genetic screening, which demonstrated that mitochondria are in fact highly dynamic organelles that continuously undergo fusion and fission events and show frequent movements[169,170], generally referred to as "mitochondrial dynamics". Mitochondria also show dynamic subcellular distribution and internal structure arrangement[169]. The core machinery regulating mitochondrial dynamics is governed by a family of GTPases and their adaptor proteins (**Figure 4**). Extensive evidence in the past decade has suggested that mitochondria actively modify their morphology in adaptation to cellular needs and tissue demands[135]. In some cases, alterations in mitochondrial dynamics in one cell type could have impacts in the whole individual. For instance, genetic deletion of mitochondrial-dynamics regulators in pro-opiomelanocortin (POMC) neurons showed impacts on the energy-sensing functions of these cells, which, in turn, affect other tissues in the body due to altered response to nutrient intake[171–173]. Apart from the metabolic point of view, mitochondrial dynamics has been shown to be involved in mitochondrial quality control, cell cycle, cellular senescence and the interactions with other intracellular components such as lipid droplets, the ER and the peroxisome (Reviewed in[135]).

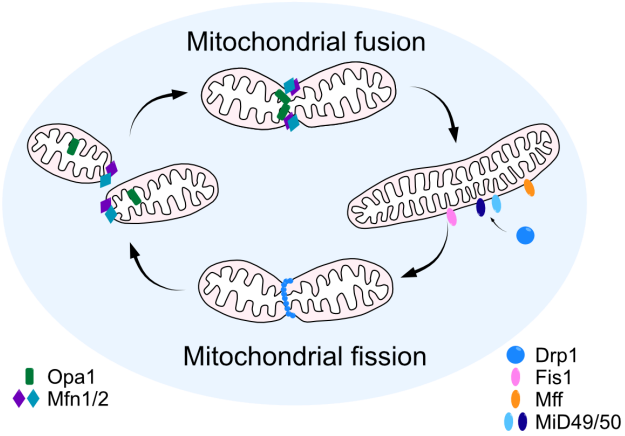

Figure 4 Schematic representation of mitochondrial dynamics and the regulatory proteins.

2.2.1 Mitochondrial fission

The fission of mitochondria is primarily regulated by the GTPase dynamin-related protein 1 (DRP1; Dnm1 in yeast)[174], a cytosolic protein that can translocate to the mitochondria at special sites pre-marked by the ER and actin[175,176]. When recruited to the mitochondria, DRP1 binds to its OMM receptors, including mitochondrial fission factor (Mff), mitochondrial fission 1 protein (Fis1), mitochondrial dynamics protein of 49 kDa (MID49) and MID51[177–180]. Following this binding, DRP1 protein oligomerizes, forming a ring-like structure that facilitate the scission of the mitochondria into two parts (illustrated in **Figure 4**). In addition, it has been shown that the complete separation step requires other DRPs such as dynamin 2[181], although the role of other DRPs besides DRP1 in mitochondrial fission remains understudied[182].

The activity of DRP1 can be modulated by multiple posttranslational modifications, such as phosphorylation, ubiquitylation, SUMOylation, and S-nitrosylation (reviewed in[135,169,183]), among which the phosphorylation occurs at two serine residues: Ser-616 (pS616) and

Ser-637 (pS637) (in humans; corresponding to pS600/pS579 in mouse Drp1 isoform 3, and to pS643/pS622 in mouse Drp1 isoform 1[184]) has gained the most attention[183]. The translocation of DRP1 to the mitochondrion depends on the phosphorylation of S637 mediated by cyclic AMP (cAMP)-dependent protein kinase A (PKA). Phosphorylation at S616 decreases the activity of DRP1, leading to reduced fission and mitochondrial elongation[185,186]. The same site can be dephosphorylated by the $Ca2^{+}$-dependent phosphatase calcineurin[187]. In contrast, phosphorylation at S637 increases the fission activity of DRP1. S637 phosphorylation is generally catalyzed by the cyclin dependent kinase 1 (Cdk1/cyclin B) and is associated with DRP1 translocation to the mitochondria during mitosis, which is believed to facilitate balanced mitochondrial segregation to the daughter cells[188]. S637 can also be phosphorylated by other kinases, such as the extracellular signal-regulated kinases (ERK1/2)[189,190], protein kinase C δ (PKCδ)[191], Cdk5[192]and phosphoglycerate mutase 5 (PGAM5)[193]. Further, the phosphorylation of the Drp1 receptor MFF by energy-sensing AMPK can result in the recruitment of DRP1 and final mitochondrial fragmentation[194] .

By regulating mitochondrial fission, DRP1 participates in essential cell functions. As mitochondria cannot be formed *de novo*, the biogenesis of mitochondria is thereby dependent on the fission of pre-existing organelles[195]. The fission activity also plays a role in cellular quality control. Mitophagy (the autophagy of mitochondria) requires the fission machinery to separate the damaged mitochondrion, which can then be engulfed by the autophagosome[196–200]. Apart from the mechanistic function of splitting the mitochondria, the fission machinery can regulate autophagy through energy sensing. For instance, nutrient excess and cellular damage induce mitochondrial fission and promote mitophagy[201]. In contrast, nutrient deprivation (starvation) downregulates the activity

of DRP1 through PKA-mediated S637 phosphorylation, resulting in elongated mitochondria that are less subjected to cell death[147]. Indeed, the metabolic state of the cell is closely associate the dynamics of the mitochondria. It was generally believed that cells with a more fragmented network tend to adapt to a glycolytic metabolism, whereas those with an interconnected network are more dependent on mitochondrial OXPHOS[170]. However, this view is being challenged by more recent studies in stem cells, where discrepancies can be found across cell types regarding the shape and metabolism, indicating that the relation of mitochondrial morphology and their metabolic state is more complicated that at simple correlation (See Introduction Chapter 4). Moreover, mitochondrial fission is also associated with several other functions including facilitating mitochondrial transport[202], calcium homeostasis[203], regulating cell fate and reprogramming[204,205]. Furthermore, DRP1 has been shown to regulate the fission of peroxisomes[206–208] (**Figure 5**).

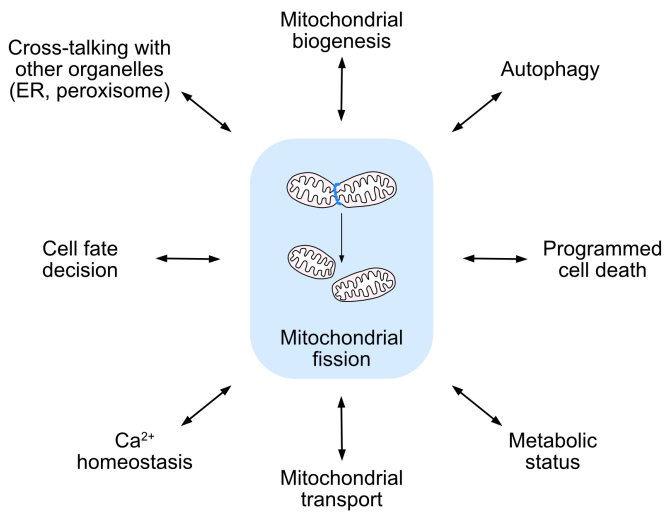

Figure 5 Interplay of mitochondrial fission with other cellular functions.

In line with the important roles of DRP1, mutations in DRP1 and its adaptors can lead to severe pathological consequences in humans

including neonatal lethality[207], encephalopathy[207–209], microcephaly[210] and autosomal dominant optic atrophy[211] (summarized in **Table 1**). In mice, full-body DRP1-knockout mice are embryonic lethal[212,213] and tissue-specific knockout of *Drp1* in the cerebellum[213] or muscle[149] also causes lethality. Other tissue-specific *Drp1* deletion also lead to impaired cellular functions. For instance, loss of *Drp1* in T cells impairs T cell maturation, proliferation, metabolic reprogramming, and antitumour responses[214].

2.2.1 Mitochondrial fusion

In contrast to the fission activity, the process of fusion joins two individual mitochondria the fusion of mitochondria via through two steps, whereby OMM fusion is followed by fusion of the IMM. In mammalian cells, OMM fusion is regulated by two mitofusins Mfn1 and Mfn2, both of which belong to the dynamin-related family of large GTPases[169,215,216], whereas the fusion of IMM is mainly regulated by optic atrophy 1 (Opa1)[215]. Although Mfn1 and Mfn2 exhibit high degree of homology and similar structural organization[217], their deletion differentially affects mitochondrial morphology. Depletion of *Mfn1* leads to highly fragmented mitochondria organized in small fragments distributed in the cytosol whereas depletion of *Mfn2* results in bigger mitochondrial fragments that cluster perinuclearly[216]. Mfn1 is the key component that participate in the fusion of OMM, whereas the exact role of Mfn2 in fusion remains elusive[218,219]. It has been suggested that mitofusin complexes act in trans between adjacent mitochondria, which facilitate the tethering and subsequent fusion of the OMM[220], but the exact mechanisms of how mitofusins participate in OMM fusion remain unclear. It is notable that mitofusins have been extensively associated with mitophagy[221,222]. Specially, Mfn2 has been demonstrated to play essential roles in PTEN-induced putative kinase protein 1 (PINK1)/Parkin-mediated mitophagy

as a direct Parkin receptor[223] (details of the PINK1/Parkin-mediated mitophagy is discussed in **Introduction Chapter 3**).

OPA1 mediates the fusion of IMM but is in parallel involved in cristae remodelling[224–226], making its role in mitochondrial dynamics regulation highly complex. OPA1 is present in the IMM and the IMS and is subjected to a number of poste-translational modifications by cleavage of proteases, including mitochondrial processing peptidase (MPP), ATP-dependent protease YME1L and ATP-independent metalloendopeptidase OMA1[227,228]. The post-translational cleavage of OPA1 protein generates several forms of OPA1, which can be categorized into the long forms (L-OPA1) and the short forms (S-OPA1). While the exact mechanism of how OPA1 mediates mitochondrial fusion is still unresolved, it is generally accepted that the fusion of IMM depends on the appropriate balance between L-OPA1 and S-OPA1[135]. For instance, it was demonstrated that deletion of OMA1 reduces the accumulation of S-OPA1 in the cells, which restores the tubular mitochondria, whereas re-expression of S-OPA1 in *Yme1l-/- Oma1-/-* double knock-out (KO) MEFs lead to mitochondrial fragmentation[229]. Furthermore, overexpression of S-OPA1 in wild-type cells was also accosiated with increased mitochondrial fission[230] . These data link uncleaved L-OPA1 to mitochondrial fusion and cleaved S-OPA1 to mitochondrial fission. Similar to loss of mitochondrial fission, deficient mitochondrial fusion by mutations of mitofusins and OPA1 also lead to severe diseases in humans (**Table 1**).

Table 1. Human diseases caused by mutated fission/fusion factors

Gene	Disease	Ref
Drp1	Encephalopathy, neonatal letality	207
	Autosomal dominant optic atrophy	211
	Microcephaly and pain insensitivity	210
Mff	Leigh-like encephalopathy, optic atrophy and peripheral neuropathy	231
	Encephalopathy due to defective mitochondrial and peroxisomal fission	209
MID49	Mitochondrial myopathy	232
OPA1	Optic atrophy	233,234
	Behr syndrome	235
	Mitochondrial DNA depletion syndrome	236
	Syndromic Parkinson disease and dementia	237
MFN2	Charcot–Marie–Tooth disease type 2A, hereditary motor and sensory neuropathy VIA	238

3. Mitochondrial autophagy (mitophagy)

Autophagy (originated from Greek for 'self-eating') is a cellular degradation and recycling process highly conserved in eukaryotes that removes unnecessary or dysfunctional cytosolic components such as organelles or macromolecules through lysosomes[239–241]. Autophagy is an adaptive process that helps to support energy balance and metabolic requirements during metabolic stress such as nutrient deprivation, growth factor depletion, infection and hypoxia[239]. In general, autophagy can be categorized into three types: macroautophagy, microautophagy and chaperone-mediated autophagy (CMA)[242].

Macroautophagy (hereafter referred to as autophagy) can be summarized into the following steps: initiation and nucleation, elongation, maturation, fusion and degradation (**Figure 6**). During autophagy initiation, cytosolic components are engulfed by a flat membrane sheet known as phagophore. This phagophore then elongates and seals itself leading to a double membrane vesicle called autophagosome. The autophagosome then fuses with the lysosome, giving rise to the autolysosome where the intracellular components subjected to autophagy are degraded by the lysosomal hydrolases[243,244]. Several autophagy-related gene (Atg) products including the ATG8/MAP1LC3 protein (microtubule-associated protein 1 light-chain 3, hereafter referred to as LC3) regulate autophagosome formation and maturation into autolysosomes. LC3 is a cytosolic protein that is cleaved and conjugated to phosphatidylethanolamine (PE) giving rise to the membrane-bound form of LC3, also referred to as LC3-II, the level of which is known to be correlated with the number of autophagosomes[245]. Moreover, LC3-II in the autophagosome interacts with autophagy adaptors, such as P62/SQSTM1, NDP52, OPTN, NBR1 or TAX1BP1, that act as a linkage between autophagosome and the substrate[246]. It

has been shown that bafilomycin A1 (Baf A1), a macrolide antibiotic, is an inhibitor of autophagy by inhibiting fusion between autophagosomes and lysosomes[247]. Previous work from our colleague showed that treatment of Baf A1 lead to significant accumulation of autophagosomes in satellite cells[100], marked by increased LC3 puncta accumulated in the cytoplasm. The difference in LC3 puncta level before and after Baf A1 treatment has been established as a readout for autophagy flux[100]. On the other hand, in microautophagy, the lysosome itself engulfs small components of the cytoplasm by inward invagination of the lysosomal membrane. Finally, chaperone-mediated autophagy (CMA) targets cellular proteins and does not involve membrane reorganization. Substrate proteins contain at least one amino acidic motif biochemically related to the penta-peptide KFERQ can be recognized by chaperones that help to translocate these proteins directly across the lysosomal membrane[242].

Mitophagy, referred to as the selective autophagy of mitochondria, contributes to mitochondrial quality control by enabling the degradation of dysfunctional and damaged mitochondria and is therefore essential for the maintenance of cellular fitness. In addition, mitophagy plays key role in the regulation of mitochondrial mass to adapt to the cellular energy requirements[248]. In mammals, the PINK1/Parkin- and receptor-mediated mitophagy pathways have been described and extensively studied (**Figure 6**).

In PINK1/Parkin-mediated mitophagy, the serine/threonine kinase PINK1 and the E3 ubiquitin ligase Parkin cooperatively sense cellular stress and mediate the autophagic elimination of damaged mitochondria. In healthy mitochondria with normal $\Delta\Psi m$, PINK1 is imported into the mitochondria where it is cleaved by the intramembrane protease presenilin associated rhomboid like (PARL) to produce the 52 kDa form

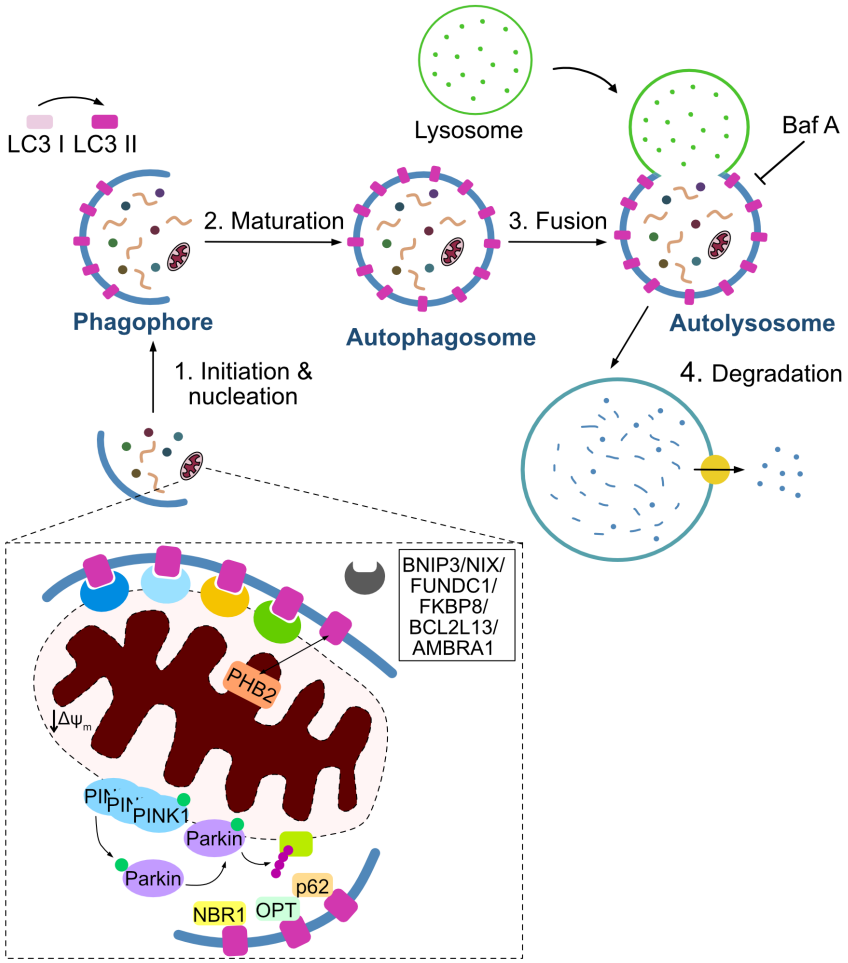

Figure 6 Schematic model of the macroautophagy (top) and mitophagy (dashed line box) processes (schematic adapted and modified from[249]).

of PINK1. The cleaved PINK1 is less stable, leading to its retro-translocation into the cytosol and rapid proteasomal degradation[250]. Mitochondrial depolarization caused by mitochondrial stress leads to reduced ΔΨm and subsequent stabilization and accumulation of PINK1 in the OMM. This allows for the recruitment and phosphorylation of Parkin to the OMM where it interacts with PINK1, leading to ubiquitination of OMM proteins such as VDAC and mitofusins[222,251–254]. Mitochondrial ubiquitination then serves as signal for autophagy mediators including P62, optineurin (OPTN) or utophagy

Cargo Receptor 1 (NBR1), promoting the engulfment of mitochondria by the autophagosome and subsequent autophagic degradation[246] (illustrated in **Figure 6**). Moreover, other E3 ubiquitin ligase such as SMURF 1 or GP78 can also act as mitophagy regulators in a PINK1-dependent or -independent manner[255,256].

On the other hand, receptor-mediated mitophagy depends on mitophagy receptors that contain at least one LC3 interacting region (LIR). These mitophagy receptor are located in the OMM and can interact with LC3 via the conserved LIR motif to mediate mitophagy when mitochondria become damaged. Such receptors include BCL2 interacting protein 3 (BNIP3), BCL2 interacting protein 3 like (BNIP3L, better known as NIX), BCL2-like 13 (BCL2L13), FUN14-domain containing protein 1 (FUNDC1), FKBP Prolyl Isomerase 8 (FKBP8) and Autophagy and Beclin 1 Regulator 1 (AMBRA1) (reviewed in[255]). Apart from OMM proteins, the mitochondria inner membrane protein prohibitin 2 (PHB2) has been identified as a mitophagy receptor[257]. Moreover certain types of lipids such as cardiolipin and ceramide have been reported to interact with LC3 and to mediate mitophagy[258,259].

As discussed in the previous chapter, mitochondria are highly dynamic organelles that constantly undergo fusion and fission to regulate their morphology. Emerging evidence has indicated a strong interplay between mitochondrial dynamic and mitophagy that together regulate the quality control of mitochondria[201]. For instance, Mfn2 functions as a mitochondrial receptor for the PINK1-dependent recruitment of Parkin and participate directly in the PINK1/Parkin-mediated mitophagy process[251]. Importantly, mitochondrial fission was suggested to be necessary for mitochondrial degradation due to two facts: first, mitochondrial fission leads to asymmetric division of mitochondria[260], with transient mitochondrial depolarization in one of the two daughter

mitochondria[261]. However, the depolarization is prolonged in around 5% of the events[262], rendering the mitochondria to be targeted by the mitophagy machinery. Second, fragmented mitochondria are more susceptible to undergo mitophagic degradation owing to their smaller size. Studies visualizing mitochondria within autophagosomes revealed small mitochondria in a variety of cell types[263–265]. Although reduction of mitochondrial size alone independently of their energetic status does not trigger mitophagy, fission inhibition and or fusion promotion was shown to significantly reduce the mitophagic rate[261]. Drp1 deficiency in cardiomyocyte[266] and skeletal muscle[149] has been shown to impair mitophagy. Further, Mfn1/2 deletion in cardiomyocyte also blocks mitophagy[267] while downregulation of Mfn2 in the skeletal muscle inhibits autophagy and triggers a ROS-dependent adaptive signaling pathway through induction of BNIP3[268]. On the other hand, autophagy and mitophagy can also modulate mitochondrial dynamics. Mitophagy receptors such as FUNDC1 and BNIP3 were shown to promote mitochondrial fission under stressful conditions[269–271]. *Fundc1* deletion or inhibition of FUNDC1-LC3 interaction prevented hypoxia-induced mitophagy and lead to mitochondrial fragmentation possibly due to accumulation of damaged mitochondria[271]. BNIP3 was shown to directly interact with OPA1 and inhibit mitochondrial fusion[269].

4. Mitochondrial dynamics, metabolism, autophagy, and stem cell fate

Over recent years, mitochondrial dynamics, metabolism, and protein homeostasis (proteostasis) have emerged as important regulators in stem cell identity and function. Stem cells and their progenitors show distinct energetic demands and the stem cell fate decision (i.e. to "decide" to undergo lineage commitment or maintain the stem cell property) is increasingly recognized as a metabolism-dependent process[39,153,158]. Mitochondria are highly plastic organelles that are able to undergo morphological and functional changes in response to cellular demands. Owing to this plasticity, mitochondria have been viewed as key mediators of metabolism and cell fate decision. As a key mechanism guarding cellular proteostasis, autophagy has been shown to play essential roles in maintaining stem cell homeostasis and function[100].

4.1 Metabolism in different stem cell states

In the absence of stress, most adult stem cells are quiescent and maintain low metabolic activity, which is considered as a conserved mechanism to ensure long-term stem cell potency[39]. On the other hand, embryonic stem cells (ESC) constantly replicate, suggesting distinct metabolic activities and regulatory mechanism among different stem cell types. Increasing body of evidence indicates that "metabolic shift" serves as an important process during stem cell fate conversion and occurs early during this transition[103,272].

It has been shown that most types of stem cells rely mainly on glycolysis whereas their committed progenitors tend to undergo a metabolic reprogramming towards increased mitochondrial OXPHOS[273–278]. For

instance, long-term hematopoietic stem cells (LT-HSCs) reside in a hypoxic niche in the bone marrow and are dependent on glycolysis to maintain a non-proliferative quiescent state[277,279]. Interestingly, LT-HSCs express high level of pyruvate dehydrogenase kinase (Pdk) 2 and 4, which inactivate pyruvate dehydrogenase suppress pyruvate influx into the mitochondria, compared to short-term HSCs (ST-HSCs). Ablation of *Pdk2* and *4* results in reduced glycolysis and HSC functional exhaustion whereas restoration of glycolysis in deficient HSCs through either *Pdk* overexpression or pharmacologic inhibition of mitochondrial pyruvate entry restored HSC quiescence and transplantation capacity[279]. On the other hand, mitochondrial OXPHOS activation has been associated with differentiation of pluripotent stem cell (PSC)[154] and neuronal stem cells (NSC)[280,281] as well as exit from quiescence of HSC[282,283]. Whiles these examples in adult stem cells indicated a unidirectional metabolic pattern of stem cell metabolism: glycolysis in the stem cell state *vs* increased OXPHOS in the progenitor state, studies in PSCs revealed more a more complicated scenario. Naïve ESCs were shown to rely both on glycolysis and OXPHOS and are therefore bioenergetically bivalent whereas slightly differentiated primed EpiSCs utilize exclusively glycolysis as their energy source[284]. In fact, maintenance and induction of naïve pluripotency was shown to be dependent on mitochondrial OXPHOS[285–287]. Interestingly, FAO is also shown to play a role in stem cell quiescence maintenance as both HSC and NSC show higher FAO activity in comparison to their committed progenitors[288,289]. Inhibition of FAO in HSC lead to symmetric commitment of HSC daughter cells and quiescence exit of NSCs. These studies show that the metabolic regulation of stem cell fate is not a non-linear process and that different stem cell types exhibit different metabolic requirements and regulations[153].

SCs are exposed to distinct micro-environment and energy demands in their different myogenic states, and therefore exhibit distinct metabolic profiles[38]. Adult QSCs possess very small mitochondrial content and low metabolic activity[40,64,104]. Unlike HSCs and NSCs that mainly rely on glycolysis, QSCs are shown to rely more on FAO[103]. Upon muscle injury, SCs exhibit a progressive increase of mitochondrial content and transcripts associated with TCA cycle and ETC complexes from quiescence to activation/proliferation states[38,103,104]. In comparison to adult satellite cells, proliferating fetal and perinatal SCs also show significantly higher mitochondrial content[38,110]. Interestingly, despite having higher mitochondrial content, activated SCs was shown to undergo a metabolic switch from FAO to glycolysis upon activation *in vitro* and rely mainly on glycolysis during proliferation[103]. Similarly, proliferating fetal myogenic cells have been shown to rely mainly on glycolysis[38]. However, compared to quiescent satellite cells, proliferating SCs in response to muscle injury experience a dramatic increase of OXPHOS, glycolysis activity and FAO, as indicated by the OCR, ECAR and the content of L-carnitine, respectively. On the other hand, fully differentiated myofibers exhibit increased mitochondrial content, ETC complex and TCA cycle enzymes[290–293], indicating increased OXPHOS during SC differentiation. Indeed, deletion of *Pdh* in SCs lead to defective proliferation and poor terminal differentiation with reduced skeletal muscle regeneration[294], suggesting the requirement of pyruvate for efficient OXPHOS during differentiation.

Apart from the cellular energetics point of view, mitochondrial metabolism can also regulate stem cell fate via oxidative stress induction and epigenetic modifications. As the harbor of the ETC and OXPHOS, mitochondria serve as major sources of ROS. ROS signaling has been shown to play essential roles in stem cell fate decision. While LT-HSC exhibits very low level of ROS, ROS induction is required for

successful HSC differentiation[277,295,296]. In SCs, QSCs display high level of antioxidants that protect them from ROS[297]. ROS generation is associated with SC activation and subsequent differentiation[298,299]. Mitochondria is also a source of metabolic intermediates involved in epigenetic regulation[300]. For example, the level of acetyl-CoA sourced from the mitochondria is crucial to maintain histone acetylation that is important for proper SC functions[301]. Further, SC fate and function is also regulated by histone methylation. QSCs show high levels of H3K4me3 associated with active transcription of Pax7 and undetectable level of H3K27me3[302,303] whereas activated SCs have the repressive mark H3K27me3 on the myogenin promoter [302,304] to prevent premature differentiation. Interestingly, TCA cycle intermediate α-KG is a cofactor of histone demethylases Jumonji C domain demethylases (JMJDs) and DNA demethylases ten eleven translocases (TETs). Moreover, glycine metabolism in the mitochondria interplays with one-carbon metabolism that generate S-adenosylmethionine (SAM), a universal substrate for protein methylation[305,306].

4.2 Mitochondrial dynamics in stem cells

Mitochondria constantly undergo fusion and fission in response to metabolic cues. Due to the distinct metabolic status during stem cell fate conversion, emerging studies have revealed roles of mitochondrial dynamics in stem cell fate regulation. The morphology of mitochondria has been associated with their metabolism judging by the efficiency of cristae organization. Researchers tend to agree that cells with the elongated mitochondria adapt better to OXPHOS metabolism whereas cells with rounded or fragmented mitochondria rely more on glycolysis[170]. This relation has been explored in the stem cell field.

As described, LT-HSC and NSC both rely mainly on glycolysis whereas their committed progenitors display metabolic shift towards OXPHOS. With respect to mitochondrial morphology, LT-HSCs show highly fragmented mitochondria, whereas slightly differentiated ST-HSC display increased in mitochondrial length[159]. On the contrary, elongated mitochondria was reported in uncommitted NSC whereas the committed progenitors exhibit fragmented mitochondrial shape[157,160]. In addition, naïve ESCs show bivalent metabolism of glycolysis and OXPHOS and display fragmented mitochondria. On the other hand, glycolysis-dependent primed EpiSCs show elongated mitochondrial network[284,307]. In accordance to this observation, *in vitro* differentiation of naïve ESC to cardiomyocytes (which show high OXPHOS activity) is accompanied with mitochondrial elongation[308] and up-regulation of mitochondrial fusion regulators Mfn1 and Opa1.

Studies have also established a causal link between mitochondrial dynamics and stem cell fate. It was shown that during the transition from LT-HSC to ST-HSC, MFN2 was up-regulated to promote mitochondrial fusion while deletion of *Mfn2* lead to loss of ST-HSC[159]. During neurogenesis, post-mitotic daughter cells that are destined to a self-renew fate undergo mitochondrial fusion whereas those display highly fragmented mitochondria undergo differentiation into neurons. Moreover, by modulating mitochondrial dynamics one can re-direct the fate of daughter cells[160]. Similarly, modulations of mitochondrial fission/fusion machinery also lead to distinct ESC fate decision[308]. These recent studies altogether showed an important role of mitochondrial dynamics in the regulation of stem cell fate decision. However, these studies also indicated that there is no simple shape-fate relation, implying deeper mechanisms underlying the modulation of stem cell fate by mitochondrial dynamics. The relation of stem cell potency, metabolism and mitochondrial morphology in PSC, HSC and NSC is summarized in

Figure 7. In satellite cells, little is known about the mitochondrial dynamics and cell fate decision.

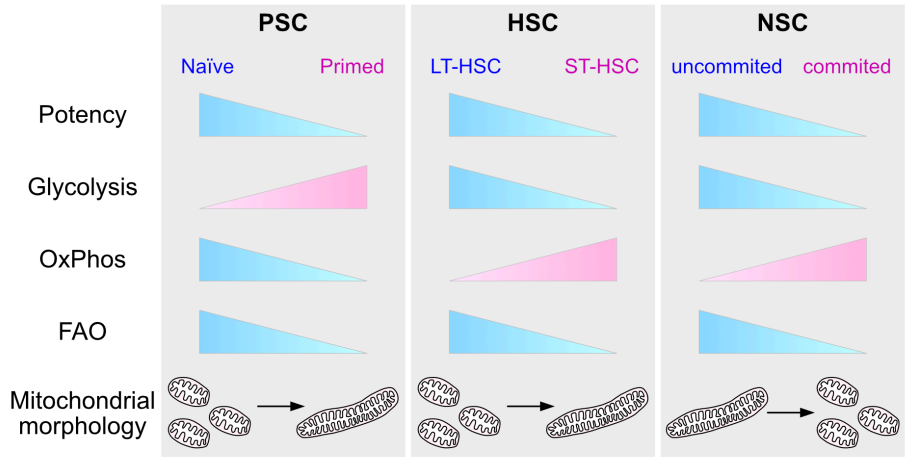

Figure 7 Schematic summary of the relation connecting stem cell potency, metabolism and mitochondrial dynamics in 3 types of stem cells. PSC, pluripotent stem cell; HSC, hematopoietic stem cell; NSC, neural stem cell (schematic adapted and modified from[153]).

4.3 Autophagy regulates stem cell function and fate

Autophagy has been shown to be essential for the maintenance of stem cell functions. In HSCs, autophagy is critical for proper HSC maintenance[309,310], mobilization[311] and for HSC survival under acute metabolic stress[312]. In satellite cells, autophagy is required both in quiescence maintenance and in activation induction. QSCs with deficient autophagy induced by *Atg7* deletion lead to accumulation of damaged mitochondria and increased ROS, which further contributed to DNA damage and cellular senescence[100]. Interestingly, pharmacological repression of ROS production in Atg7-deficient SCs prevents senescence entry and promotes SC self-renewal. Autophagy has also been shown to be important for SC activation by supporting cells bioenergetics demands[313,314] and for myoblast differentiation[315] as well as myotube formation[316]. Further, autophagy is required also for

iPSC reprogramming, as *Atg 3,5,7* deficiency resulted in reprogramming failure of mouse embryonic fibroblasts into iPSCs[317]. The study also indicated that transient down-regulation of mammalian target of rapamycin (mTOR) by Sox2 is essential for the induction of autophagy during early re-programming. Consistent with these findings, cells lacking TOR kinase inhibitor Tsc2 are shown to exhibit increased mTOR activity and reduced autophagy, resulting in reprogramming failure[318]. Mitophagy is also shown to play a key role during iPSC reprogramming, as *Pink1* deletion lead to impaired reprograming[319]. Notably, mitophagy deficiency was associated with alterations in metabolism and numerous glycolysis- and TCA-related metabolites such as α-KG, indicating interconnection between autophagy and metabolism. During aging, autophagy is down-regulated in satellite cells, accompanied by mitochondrial dysfunction and altered metabolism[100,320], we will therefore further discuss the this matter in the aging session (See Introduction Chapter 5.2).

5. Aging

Aging is characterized by the progressive loss of physiological functions across multiple tissues and organs, often linked to the functional decline of the resident stem cells[321]. In skeletal muscle, aging has been associated with a loss of muscle mass and function, generally referred to as "sarcopenia"[322]. Sarcopenia increases from 14% in those aged between 65 to 70 years, to 53% in those above 80 years of age[322]. Sarcopenia increases risk of falls and fractures, impairs daily activity, and increases risks of other diseases such as cardiac failure, respiratory diseases, and cognitive impairment; overall, these result in compromised quality of life for elderly people[323]. The number of aging population is increasing, accounting for 703 million older people aged 65 years or above in 2019, and is projected to reach 1.5 billion in by 2050; therefore, knowledge and therapeutic strategies targeting skeletal muscle aging is of extreme importance.

Globally, the hallmarks of aging across different species have been proposed, including genomic instability, telomere attrition, epigenetic alterations, loss of proteostasis, deregulated nutrient-sensing, mitochondrial dysfunction, cellular senescence, stem cell exhaustion, and altered intercellular communication[321]. In the case of skeletal muscle, its outstanding regenerative capacity is affected by the aging process due to a decline in size of the satellite-cell pool and reduction in the functionality.

5.1 Overview of satellite cell aging

Early discoveries using whole-muscle transplantation and heterochronic parabiosis revealed that the mechanisms contributing to the functional decline of SCs may be mainly caused by the aged environment[324,325].

However, more recent studies using transplantation of purified SCs into aged muscle or aged myofibers demonstrated cell-autonomous mechanisms underlying SC aging[101,326]. Reductions in SC numbers likely occur in the early stages of muscle aging and have been linked to both niche and cell-autonomous alterations that together impair the physiological balance between cell quiescence, proliferation, and apoptosis[84,326]. This decline in regenerative capacity is maximized in geriatric age, where SCs switch from a quiescent to a pre-senescent state that eventually leads to full senescence when exposed to a regenerative pressure[101]. Thus, old SCs show a reduced capacity for expansion after injury and produce insufficient progeny to sustain muscle regeneration. Furthermore, the surviving fraction of the SC pool within the skeletal muscle suffers from functional defects that weaken their regenerative capacity[327]. These defects in old SCs lead to higher levels of symmetric division, reducing the pool of progenitor cells. Moreover, old SCs progressively show a stronger tendency to commit to alternative lineages resulting in an enhanced fibrotic response to injury[328]. These cell-autonomous as well as extrinsic factors together perturb the proper balance of SC quiescence maintenance, proliferation, and apoptosis, resulting in depleted stem cell pools and impaired muscle regenerative capacity in advance ages (reviewed in [329]).

5.1.1 Satellite cell intrinsic alterations during aging

Numerous signaling pathways are altered in SCs during aging, which can be attributed to both cell-intrinsic changes and influences from the environment. Increased activity of JAK-STAT signaling with aging contributes to intensify the myogenic commitment of SCs, resulting in a decline in their regenerative capacity and exhaustion of the progenitor cell pool[330]. On the other hand, inhibition of the JAK-STAT pathway recovers progenitor cell numbers and enhances muscle repair. In

addition, aged SCs show abnormal activation of p38α/β MAPK signaling through enhanced phosphorylation of both p38α/β MAPK and its target mitogen-activated protein kinase-activated protein kinase-1 (MAPKAPK-1). Increased p38α/β MAPK signaling leads to impaired SC asymmetric division and self-renewal whereas pharmacological inhibition of p38 MAPK restores asymmetric division and regenerative potential of aged SCs by decreasing the expression of cell-cycle inhibitors (such as $p16^{INK4a}$)[326,331]. As described in the previous section, aged SCs exhibit insufficient Notch signaling, partially initiated from the niche. While the SC number and functional loss at the initial of the aging process can be restored by providing the cells with youthful surroundings[324,325], SCs undergo irreversible functional decline at an advanced age that can no longer be rescued by altering the host environment alone[101], indicating the important roles of cell-intrinsic factors in SC aging.

Aged SCs exhibit cell-autonomous hallmarks of aging. At the genetic level, aged SCs show increased DNA damage[332] and accumulation of somatic mutations[333], together contributing to the genome instability. In addition, global modifications in the epigenetic landscape have been detected in aging satellite cells, leading to altered histone modification (for instance H3K27me3)[302] and chromatin accessibility[334]. Aberrant chromatin activation in aged activated SCs results in functional decline via the activation of Homeobox protein Hox-a9 (Hoxa9)-targeted developmental pathways[335]. Alterations in the epigenetic stress response from SCs during aging results in the upregulation of Hoxa9 gene, which in turn activates several pathways known to mine SC function in aging (such as the WNT, TGF-β or JAK/STAT signaling pathways)[335]. At the single-gene level, epigenetics modifications play essential roles during SC quiescence-to-pre-senescence transition through the cell cycle regulator $p16^{INK4a}$ [101]. Age-related decrease of

transcriptional repressor Slug in SCs results in insufficient de-repression of $p16^{INK4a}$ and acceleration of SC pre-senescence transition whereas Slug overexpression improves aged SC self-renewal through active repression of $p16^{INK4a}$ transcription[336].

Moreover, aging SCs show perturbed proteostasis[39,100], resulting in increased cellular senescence[100,101] as well as altered metabolism, including mitochondrial dysfunction[320] (**Figure 8**) (see also Chapter 5.2 for an in-depth discussion).

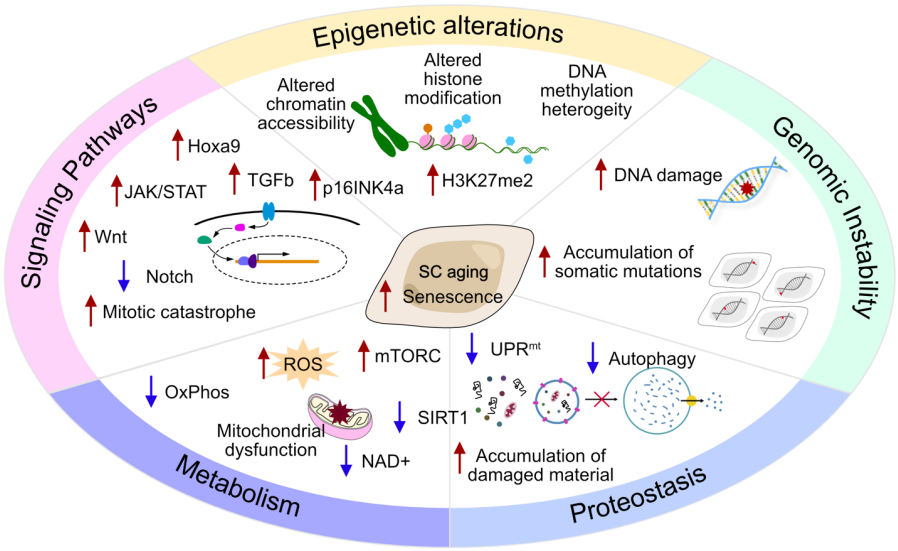

Figure 8 Satellite-cell intrinsic changes during aging (schematic adapted from [329]).

5.1.2 Extrinsic factors associated with satellite cell aging

SCs are profoundly affected by system-derived factors as well as the local microenvironment (niche)[10,36,337]. Early muscle transplant experiments indicated that the regenerative capacity of old and young muscles is mainly depending on the age of the host[324,338]. Heterochronic parabiosis experiments have demonstrated the important role of the aging systemic factors on SC functions. By surgically pairing the circulatory systems of two mice, it was demonstrated that aged system

promotes increased Wnt signaling which causes aberrant fibrogenic commitment of SCs and increased fibrosis in young mice whereas muscle regeneration in aged mice can be restored by being exposed to a youthful systemic environment, marked by increased SC expansion and differentiation as well as reduced fibrosis[325]. Interestingly, a recent study using blood exchange between young and old mice showed improvement of muscle regeneration and reduced fibrosis in old mice receiving young blood, coinciding with the results from parabiosis experiments[339]. Circulating factors, such as oxytocin, apelin, and growth differentiation factor 11 (GDF11), have been proposed as rejuvenating factors[340–342], although the role of GDF11 is still controversial[332,343–346].

As discussed in Chapter 1, proper communication and coordination of SCs and its niche is essential for maintaining SC homeostasis and for efficient muscle regeneration upon injury. In old mice, for instance, increased levels of FGF2 secreted by aged muscle fibers leads to spontaneous activation of SCs and gradual exhaustion of the SC pool[84]. FGF2 can also inhibit the expression of Spry1, an intracellular inhibitor of the MAPK/ERK signaling pathway, whose downregulation in activated SCs impairs their ability to return to quiescence and promotes apoptosis[89]. Alterations in ECM composition, such as age-related loss of fibronectin and β1-integrin activity, lead to the compromised regenerative capacity of SCs in old skeletal muscle[347,348]. β1-integrin cooperates with FGF2 to synergistically activate the ERK/MAPK axis, their common downstream pathway[348]. Furthermore, aged FAPs have reduced production of the matricellular signaling protein WISP1, further affecting the SC–ECM interactions and SC functionality by regulating SC expansion and asymmetric commitment[76]. Since the efficient muscle regeneration requires a finely orchestrated immune response post injury, immune cells play critical roles in the SC cell regenerative niche[36,349–352]. Bone marrow transplantation from old donor mice can cause impairment

of SC function in young mice, with reduced SC numbers and increased fibrogenic conversion[353], partially due to increased TNFα signaling in aged mice[354]. Aged mice have been shown to respond to muscle injury with delayed kinetics transition, showing altered macrophage pro-/anti-inflammatory profiles, which influence their communication with SCs [355]. In addition, aged muscle presents increased NFκB signaling, leading to disturbed niche and declined SC functions[356]. Further, aberrant production of chemokines and cytokines as well as activities of their receptors in the aged niche also lead to altered cell-cell communications. Such molecules include CXCL10[357], growth differentiation factor 3 (GDF3)[358], IL-33[77] and chemokine-receptor 2 (CCR2)[359] and CCR5[360].

5.2 Proteostatic and metabolic alterations in satellite cells during aging

Proteome homeostasis (proteostasis) is a key determinant for the correct cell and tissue function. When protein folding fails, mechanisms such as the unfolding protein response (UPR) are activated to restore proteome stability[361]. In contrast, damaged proteins or aggregates are degraded by the UPS (ubiquitin-proteasome system) or autophagy. During aging, altered organelles and proteins accumulate affecting stem cell function by driving to genome instability, senescence and apoptosis[39]. Therefore, clearance of damaged organelles and macromolecules is important for the maintenance of healthy adult stem cells, particularly in stem cells that are mainly in quiescence and only activate in response to stress or regenerative demands, such as SCs[100]. Although autophagy has been described as catabolic process induced by stress, it is indispensable for the maintenance of stemness in QSCs. Impairment of autophagy by *Atg7*-genetic deletion in young SCs causes the accumulation of damaged mitochondria that increases intracellular ROS levels, causing protein and DNA damage. Notably, aged SCs show

impaired autophagic activity and recapitulate the phenotype observed in autophagy-deficient young SCs[100]. This autophagy failure together with the consequent accumulation of harmful intracellular waste is linked to epigenetic downregulation of the $p16^{INK4a}$ locus, and their switch from reversible quiescence into senescence in extreme old SCs (also referred to as geriatric SCs)[100,101].

SCs in different myogenic states are exposed to distinct micro-environment and energy demand and therefore can exhibit distinct metabolic profile. Although the metabolism of SCs in different myogenic states and during aging remains to be better understood, a recent study has shown that freshly isolated QSCs display very low energy demands and low metabolic activity[38]. Proliferating fetal myoblasts, on the other hand, rely mainly on glycolysis as energy source. Interestingly, SCs show a simultaneous boost of OXPHOS and glycolysis at 3 days post injury (3-DPI), whereas the ratio skew towards OXPHOS at 5-DPI. In addition, a metabolic shift from FAO to glycolysis was described in SCs upon activation *in vitro*[103]. During aging, QSCs exhibit reduced OXPHOS capacity and rely rather on glycolysis[38] . A recent study has indicated that both age-related systemic decline of α-Klotho and genetic silencing of α-Klotho in young SCs lead to decreased mitochondrial bioenergetics activity, mitochondrial DNA damage, and increased senescence[362], indicating that mitochondrial function in SCs was indeed compromised during aging. Furthermore, proteomics-based analysis in human SCs revealed reduced glucose oxidation in senescent SCs due to impaired glycolysis and TCA cycle in senescent myoblasts[363], adding more evidence to the hypothesis that metabolism SCs is altered in during aging.

Emerging studies from the last decade have revealed how the interconnection of autophagy and metabolism affect SC function during

aging. Due to its role in nutrient sensing, mTORC1 constitutes a link between the metabolism and proteostasis regulation through both protein synthesis and autophagy modulation[39]. In addition to this notion, mTOR inhibition with rapamycin improved aged SC functionality *in vivo* partially through autophagy enhancement[100]. Autophagy is induced to facilitate SC activation and proliferation[313,314] to meet the metabolic demands during muscle regeneration and the inhibition of the autophagic machinery can perturb mitochondrial function and ATP production[100,313]. In addition, important nutrient sensors AMPK and SIRT1 play important roles in autophagy regulation in SCs. In times of energy stress, AMPK promotes autophagy either directly through phosphorylation of Unc-51 Like Autophagy Activating Kinase 1 (ULK1)[364] or indirectly through inhibition of mTOR1. Proper AMPK function in SCs is essential for efficient muscle regeneration[105]. The AMPK signaling pathway regulates both autophagy and apoptosis through phosphorylation of $p27^{Kip1}$ [365]. In contrast to their younger counterparts, activated aged SCs show reduced activation of AMPK/$p27^{Kip1}$ axis, which in turns impairs autophagy and increases their susceptibility to apoptosis *in vitro*[314]. Activation of AMPK/$p27^{Kip1}$ pathway enhances autophagy and reduces not only apoptosis but also markers of cell senescence in aged SCs, with improvement of their transplantation potential. Moreover, autophagy inhibition or SIRT1 deficiency in young SCs results in delayed SC activation, probably due to the lack of nutrients[313]. These results suggest that SIRT1 may modulate autophagy in SCs through the AMPK pathway, which has been previously shown to link SIRT1 activity to autophagy[366,367]. In addition to reporting the metabolic switch to glycolysis of SCs during activation, Ryall and colleagues illustrated that this switch leads to reduced NAD^+ levels in the cell, which then represses SIRT1 activity in the nucleus and causes increased acetylation of H4K16[103]. Furthermore, loss of SIRT1 in SCs also leads to increased H4K16 acetylation and

leads to premature differentiation of SCs[103]. Zhang et al. (2016) further revealed that mitochondrial function and quality control is fundamental for the maintenance of SC function in aging [320]. Decreased cellular NAD^+ and reduction of mitochondrial unfolded protein response (UPR^{mt}) was identified in aged SCs compared to the young level, leading to SC senescence. Treatment with nicotinamide riboside (NR), the precursor of NAD^+, was able to improve mitochondrial function in aged SCs and prevent them from undergoing senescence[320].

SCs have a rhythmic circadian machinery that is retained in aged SCs. However, the oscillatory transcriptome is reprogrammed during aging by switching from homeostasis-related genes to stress-related genes, probably to cope with the stress associated with the aged environment[368]. Moreover, while adult SCs show rhythmicity in autophagy genes, aged SCs are unable to sustain a rhythmic autophagy. On the other hand, short-term caloric restriction (CR) is sufficient to show beneficial effects in SC function through the modulation of mitochondrial biogenesis and induction of longevity genes including Sirt1 and FoxO3[369]. Consistent with these results, activated aged SCs from short-term CR-treated mice have shown increased activation of the AMPK/$p27^{Kip1}$ axis compared to the aged SCs from *ad-libitum* fed mice, which as previously mentioned, is involve in autophagy modulation SC function[314]. In addition, long-term CR can prevent the oscillatory transcriptome reprogramming observed in aged SCs by promoting a protective effect, which includes the maintenance of their ability to undergo rhythmic autophagy[368]. However, the beneficial effect of CR in aged SC function and regenerative capacity has not been studied in aged mice after injury.

Similar to murine SCs, human geriatric SCs show P62 and mitochondrial accumulation, indicative of defective protein and organelle clearance

This phenotype was associated with increased ROS levels and increased number of senescent SCs, as well as reduced proliferative capacity. As in aged SCs from mice, treatment with rapamycin restores autophagy and organelle homeostasis in human geriatric SCs, which is sufficient to rescue senescence[100].

OBJECTIVES

SCs exhibit low metabolic activity in quiescence; however, upon replicative stress induced by muscle injury, vast amounts of energy are required to fulfil the cells' need for rapid expansion. It is largely unknown how SCs adapt their metabolism to the quiescence exit and during proliferation, or whether (and if so, how) mitochondria and mitochondrial dynamics play a role in this process. Stem cell functions decline with aging. However, how mitochondria play a role in stem cell maintenance throughout life is understudied.

My major aim in my PhD Thesis was to investigate the molecular mechanisms that govern the regenerative competence of SCs during their lifetime, with the underlying hypothesis that mitochondrial dynamics, especially mitochondrial fission plays essential role in the upkeep of SCs functions. To this end, I proposed the following specific objectives:

1. Explore the nature of how SCs regulate their mitochondrial morphology and metabolism in homeostasis and during muscle regeneration.

2. Determine the role of mitochondrial dynamics in the maintenance of SC function and the mechanism(s) behind it.

3. Decipher whether mitochondrial dynamics are affected during aging, and explore potential routes for rejuvenation of aged satellite cells.

RESULTS

1. Dynamic regulation of mitochondrial morphology and metabolism in satellite cells

1.1 Mitochondrial morphology in satellite cells undergoes significant alterations during satellite cell quiescence-to-proliferation transition

Emerging studies in the past decade have shown that quiescent satellite cells (QSCs) maintain a hypo-metabolic state and undergo dramatic metabolic alterations upon quiescence exit[38,64,103,110]. However, challenges in the interpretation of SC metabolism arose due to discrepancies in the literature caused by different techniques applied. To study how SCs respond to muscle injury at the transcriptional level, we performed an RNA sequencing (RNA-seq)-coupled bioinformatic analysis of SCs isolated by fluorescence-activated cell sorting (FACS) using an inducible satellite cell-specific *Pax7*^{CreER}*-Rosa26-YFP* reporter mouse line (**Figure 9A**). SCs were taken from unperturbed muscle (e.g., QSCs) or from regenerating muscle at 1- or 3 days post-injury (DPI) (herein, 1DPI-SCs or 3DPI-SCs), which are in an activated or proliferating state, respectively (**Figure 9B**), as confirmed by immunofluorescence (IF) staining of myogenic markers PAX7, MYOD and proliferation marker KI67 (**Figure 9C**). As expected, pathways related to cell cycle and proliferation were enriched in 1DPI-SCs and 3DPI-SCs as compared to QSCs (**Figure 9D**). In addition, we observed a simultaneous boost of various energy-producing pathways (glycolysis, TCA and OXPHOS) (**Figure 9D**), comparable to previously published results[38]. Furthermore, fatty acid metabolism showed a switch from very-long-chain fatty acid utilization and fatty acid synthesis to mitochondrial β-oxidation (Figure 9D).

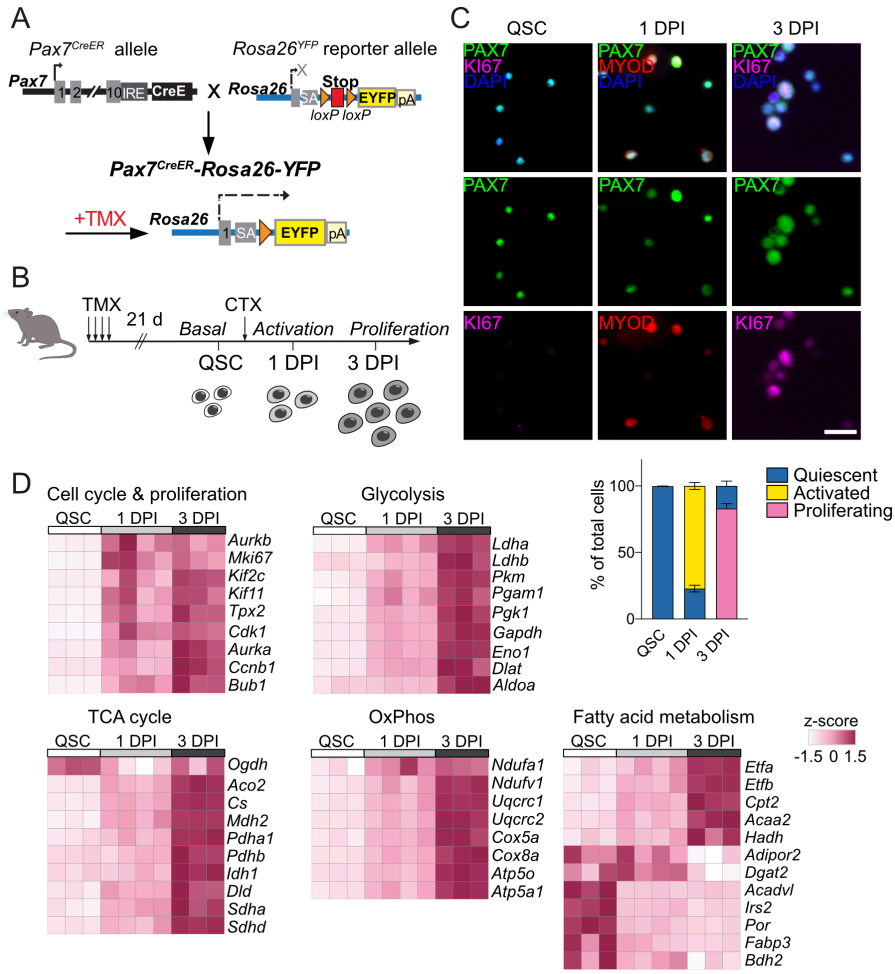

Figure 9 (**A**) Schematic representation of the tamoxifen (TMX) inducible Pax7-specific YFP reporter (*Pax7^{CreER}-Rosa26-YFP*). (**B**) Schematics of isolation of quiescent satellite cells (QSCs) in intact muscle (basal condition), or from muscles at 1- or 3-days post injury (DPI) with intramuscular injection of cardiotoxin (CTX): activated SCs (1DPI-SCs) or proliferating SCs (3DPI-SCs). Mice were injected with TMX 3 weeks prior to sample collection and YFP$^+$ cells were obtained by FACS. (**C**) Representative images of IF staining of PAX7, KI67, MYOD and DAPI (top) as well as quantification (bottom) of percentages of QSCs (PAX7$^+$KI67$^-$), activated SCs at 1 DPI (PAX7$^+$MYOD$^+$) and proliferating SCs at 3 DPI (PAX7$^+$KI67$^+$). (**D**) Expression of selected genes involved in cell cycle and proliferation, glycolysis, TCA cycle, OXPHOS and fatty acid metabolic pathways represented as a heatmap, normalized using z-score. White bar, QSCs; light grey bar: 1DPI-SCs; dark grey bar, 3DPI-SCs.

Interestingly, we found a previously unnoticed signature of upregulated genes related to mitochondrial dynamics in 1DPI-SCs, which was further augmented in 3DPI-SCs (**Figure 10A**), among which the expression of mitochondrial fission regulator (*Dnml1/Drp1*) and its receptors *Fis1* and

Mff were significantly enhanced during the quiescence-to-proliferation transition (**Figure 10B**). Consistent with the RNA-seq results, DRP1 protein levels were significantly upregulated in 3DPI-SCs as compared to QSCs (**Figure 10C**). Importantly, by normalizing the amount of DRP1 puncta to the cell volume, we confirmed that the increase in DRP1 expression exceeded the increase in cell growth (**Figure 10C**), suggesting a predominant involvement of mitochondrial fission during SC quiescence-to-proliferation transition.

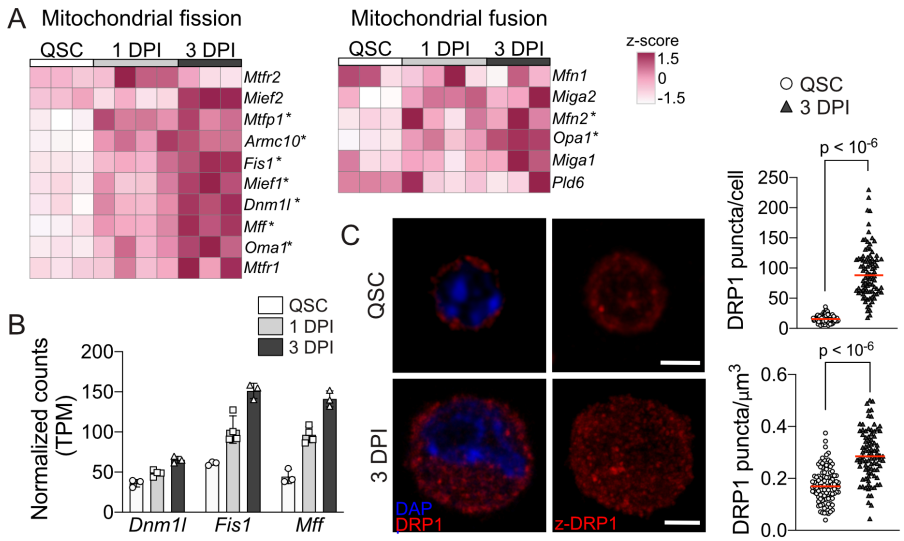

Figure 10 (**A**) Heatmap showing the expression of the signature of mitochondrial fission (left) and fusion (right) genes. Results are represented in z-score. *DE (differentially expressed) genes (adj. *P* value < 0.05). (**B**) Expression of the *Dnm1l* (*Drp1*), *Fis1 and Mff* genes is presented in transcript per million (TPM). (**C**) Representative images (left) and quantification (right) of DRP1 protein puncta in QSCs and 3DPI-SCs by immunofluorescence (IF). The results are presented in puncta per cell (upper right) or puncta per µm^3 (lower right). Scale bar, 3 µm. Data are mean ± s.d. P values were determined by two-tailed unpaired *t*-test.

Next, to examine mitochondria shape remodeling in SCs during this injury-induced transition, FACS-isolated SCs were stained with MitoTracker Red CMXRos[100], and labelled mitochondria were imaged and processed using Huygens deconvolution software, followed by 3D

mitochondrial network reconstruction using the Imaris software (**Figure 11A**).

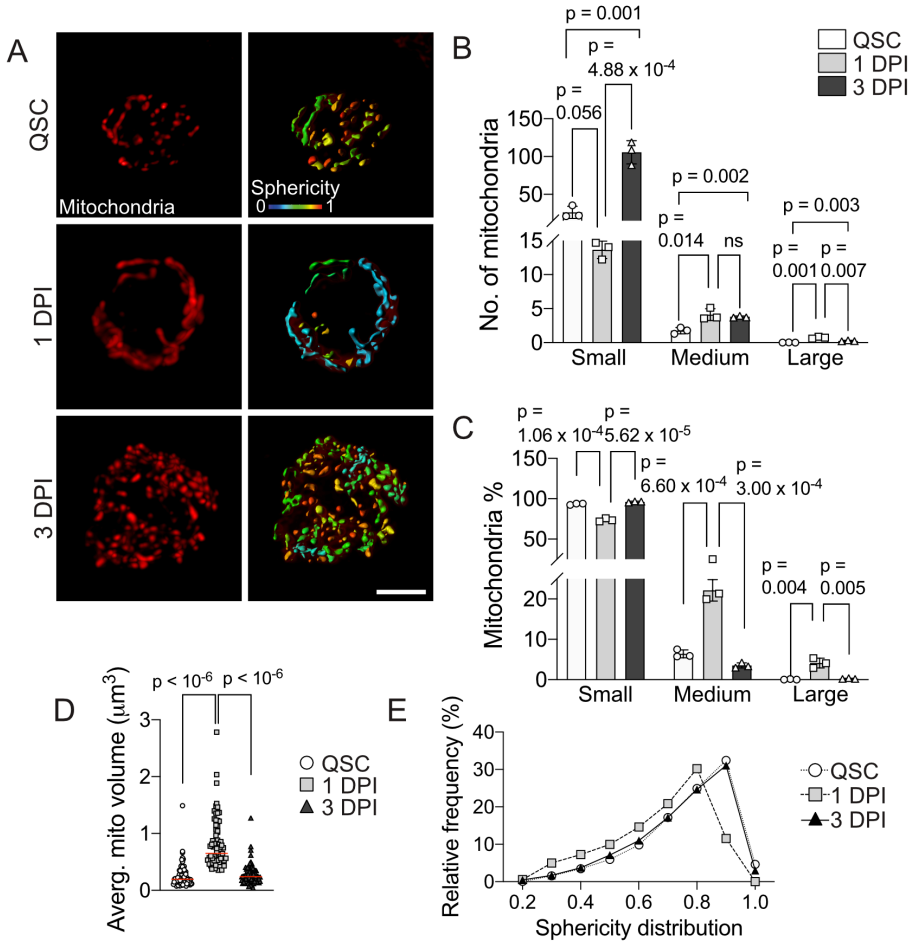

Figure 11 (**A**) Representative images of mitochondrial morphological analysis in QSCs, 1DPI-SCs and 3DPI-SCs using MitoTracker CMXRos Red (left) followed by deconvolution and 3D-reconstruction in Imaris software (right). The reconstructed mitochondria are colored by their sphericity (0–1). Scale bar, 3 µm. (**B,C**) Average number (**B**) and percentage (**C**) of mitochondria in each cell categorized as small (< 0.5 μm^3), medium (0.5–4 μm^3) or large (> 4 μm^3). (**D**) Average reconstructed mitochondrial volume in each cell in quiescence and at 1- or 3-DPI. (**E**) Frequency distribution curve showing mitochondrial sphericity of QSCs, 1DPI-SCs, or 3DPI-SCs. Data are mean ± s.d. P values were determined by two-tailed unpaired *t*-test.

Our results show low amount of mitochondria in QSCs, with the majority of them being small (~95% had a volume < 0.5 μm^3) and a small proportion being medium (~5% had a volume from 0.5 to 4 μm^3) whereas almost no large mitochondria was present in the quiescent

state (< 0.1% had a volume of > 4 μm^3) (**Figure 11B,C**). Accordingly, the mitochondria in QSCs present low average mitochondrial volume (**Figure 11D**) and high sphericity (**Figure 11E**). In contrast, 1DPI-SCs had more medium-large mitochondria, with a larger average size (**Figure 11C,D**), which formed a more complex network with reduced sphericity (**Figure 11E**), indicative of fusion during the early activation stage. Strikingly, 3DPI-SCs contained an increasing number of small mitochondria in comparison to 1DPI-SCs (**Figure 11B-D**) with increased sphericity (**Figure 11E**), indicating the mitochondria in proliferating SCs at 3DPI have low network complexity (more spherical). Altogether, these results suggested that mitochondria reorganize actively their shape when QSCs exit quiescence after injury and become smaller and less complex during the key proliferative stage.

1.2 Increased mitochondrial biogenesis and OXPHOS metabolism after SC quiescence exit

While analyzing the 3D mitochondrial network, we uncovered drastic increase of total mitochondrial volume upon injury at 1DPI and further at 3DPI (**Figure 12A**), suggesting induction of mitochondrial biogenesis. In consistence with the increase of mitochondrial volume, comparison of the RNA-seq data to an inventory of 1140 mitochondrial genes (MitoCarta3.0) showed a high upregulation of mitochondrial genes in 1DPI-SCs and 3DPI-SCs as compared to QSCs (**Figure 12B**). In addition, analysis of differentially expressed (DE) genes identified upregulation of mitochondrial biogenesis and metabolism pathways (**Figure 12C**). Of interest, almost all genes encoding ETC complex subunits were upregulated after quiescence exit, in 1DPI-SCs, with a peak in 3DPI-SCs (**Figure 12D**), supporting the hypothesis that SCs adapt their metabolism towards OXPHOS for proliferation.

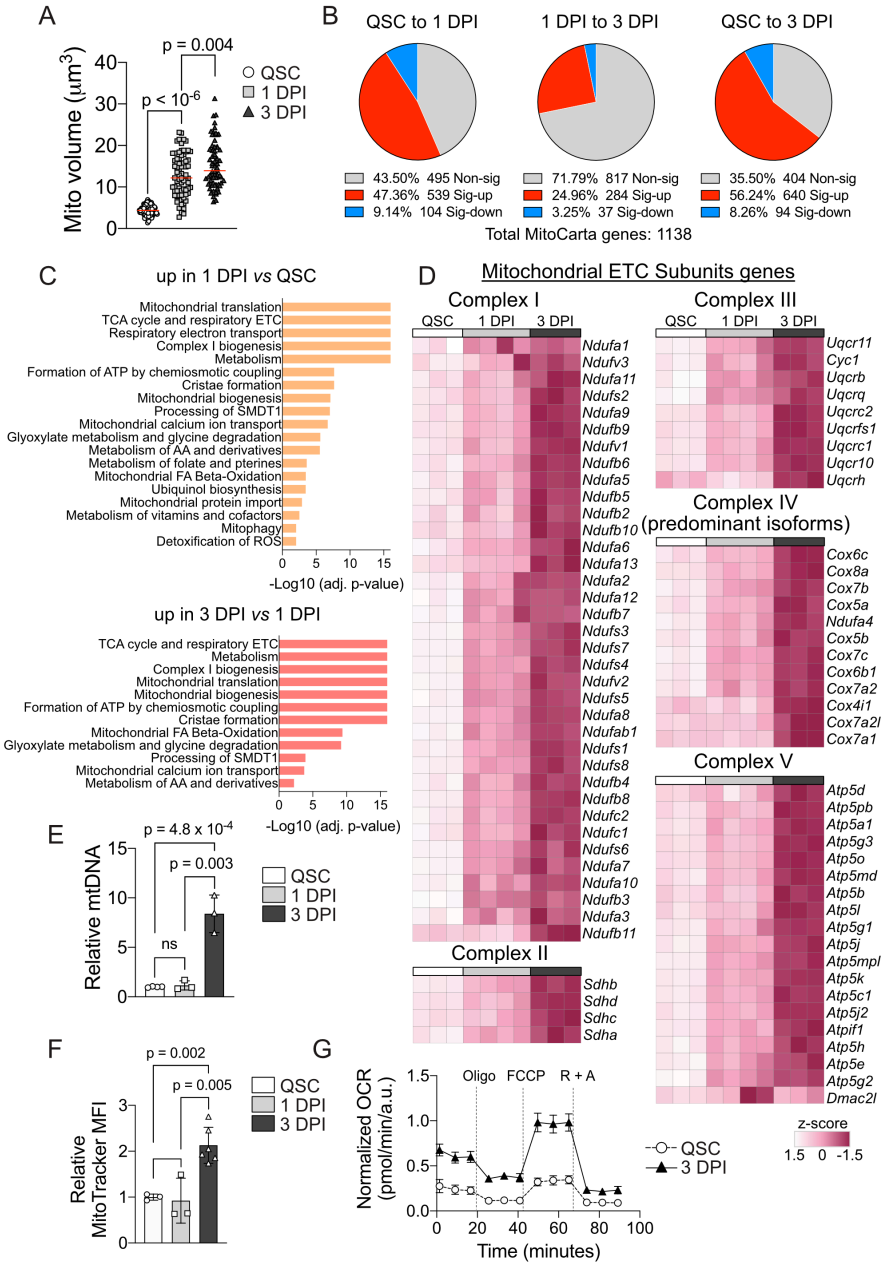

Figure 12 (**A**) Quantification of total mitochondrial volume per cell from **Figure 11A**. (**B**) Percentage and number of Mitocarta3.0 genes that were significantly upregulated (in red) or downregulated (in blue), or non-significantly altered (in grey), from one state to another (left, from QSCs to 1DPI-SCs; middle, from 1DPI-SCs to 3DPI-SCs; right, from QSCs to 3DPI-SCs). The Mitocarta gene list was obtained from Broad Institute mouse Mitocarta3.0. (**C**) Top mitochondria-related Reactome pathways upregulated in 1DPI-SCs compared to QSCs (top) and upregulated in 3DPI-SCs compared to 1DPI-SCs (bottom). Enriched pathways were obtained from a g:Profiler website-based analysis. (**D**) Mitochondrial ETC subunit gene expression represented in heatmap, normalized

using z-score. White bar, QSCs; light grey bar: 1DPI-SCs; dark grey bar, 3DPI-SCs. (**E**) Quantification of mtDNA copy number in indicated states relative to QSC levels. mtDNA copy numbers were normalized to genomic DNA copy numbers, as quantified by qPCR ($2^{-\Delta CT}$). (**F**) Quantification of MitoTracker CMXRos Red median fluorescence intensity (MFI) in indicated states, results are normalized to QSC levels. (**G**) Normalized oxygen consumption rate (OCR) of QSCs and 3DPI-SCs at baseline and in response to oligomycin A (oligo), FCCP or rotenone plus antimycin A (R + A). Data were obtained using Seahorse XF96 and normalized to protein level using Cyquant cell proliferation assay. Data are mean ± s.d. P values were determined by two-tailed unpaired *t*-test.

Analysis of mtDNA copy number revealed that 1DPI-SCs did not show significant increase of mtDNA. It is notable that the mtDNA copy number was normalized to genomic DNA (gDNA); thus, during activation (in which gDNA was increasing), it is possible that there was mtDNA synthesis that is proportional to the increase of gDNA. At 3DPI, however, SCs increased their mtDNA copy number dramatically, to almost 10 times that of the quiescent level (**Figure 12E**), confirming increased mitochondrial biogenesis during SC quiescence-to-proliferation transition. Accordingly, similar results were obtained using flow cytometry approaches, with MitoTracker MFI showing a significant increase at the proliferation state (3DPI) as compared to quiescence (**Figure 12F**). Importantly, mitochondrial respiration analysis by Seahorse showed a boost of mitochondrial oxygen consumption (OCR) in 3DPI-SCs as compared to QSCs, indicating increased OXPHOS activity during SC proliferation, in accordance to the results revealed by RNAseq (**Figure 12D**).

Our transcriptomic and functional studies together support increased mitochondrial biogenesis and OXPHOS metabolism after SC quiescence exit.

2. Mitochondrial fission maintains satellite cell regenerative competence

2.1 Mitochondrial fission in satellite cells is required for muscle regeneration

To investigate whether the disruption of mitochondria fission machinery could causally alter SC functions, we crossed a floxed mouse line for *Drp1* with the tamoxifen (TMX)-inducible satellite cell-specific *Pax7*^{CreER}-*Rosa26-YFP* reporter mouse line, giving *Drp1*$^{\Delta Pax7ER}$*;ROSA26*^{YFP} (herein, *Drp1*$^{\Delta Pax7ER}$) (**Figure 13A**). At 21 days after 4 consecutive daily TMX injections, we observed 65-85% of YFP$^+$ cells within the SC population (α7-integrin$^+$/CD34$^+$) in Cre$^+$ *Drp1*$^{\Delta Pax7ER}$*;ROSA26*^{YFP} mice (**Figure 13B**), indicating efficient Cre-Lox recombination. Moreover, the expression of YFP was shown exclusively in satellite cells, as almost all YFP$^+$ cells expressed α7-integrin$^+$ and CD34$^+$ (**Figure 13C**). Among the YFP$^+$ population, we observed significant reduction of *Drp1* RNA as compared to the wild-type (WT) control (**Figure 13D**). The deletion of DRP1 was even clearer at the protein level, as both QSCs and 3DPI-SCs almost completely lacked DRP1 protein (**Figure 13E**). Our results indicate efficient SC-specific deletion of *Drp1* gene using our genetic model and induction scheme.

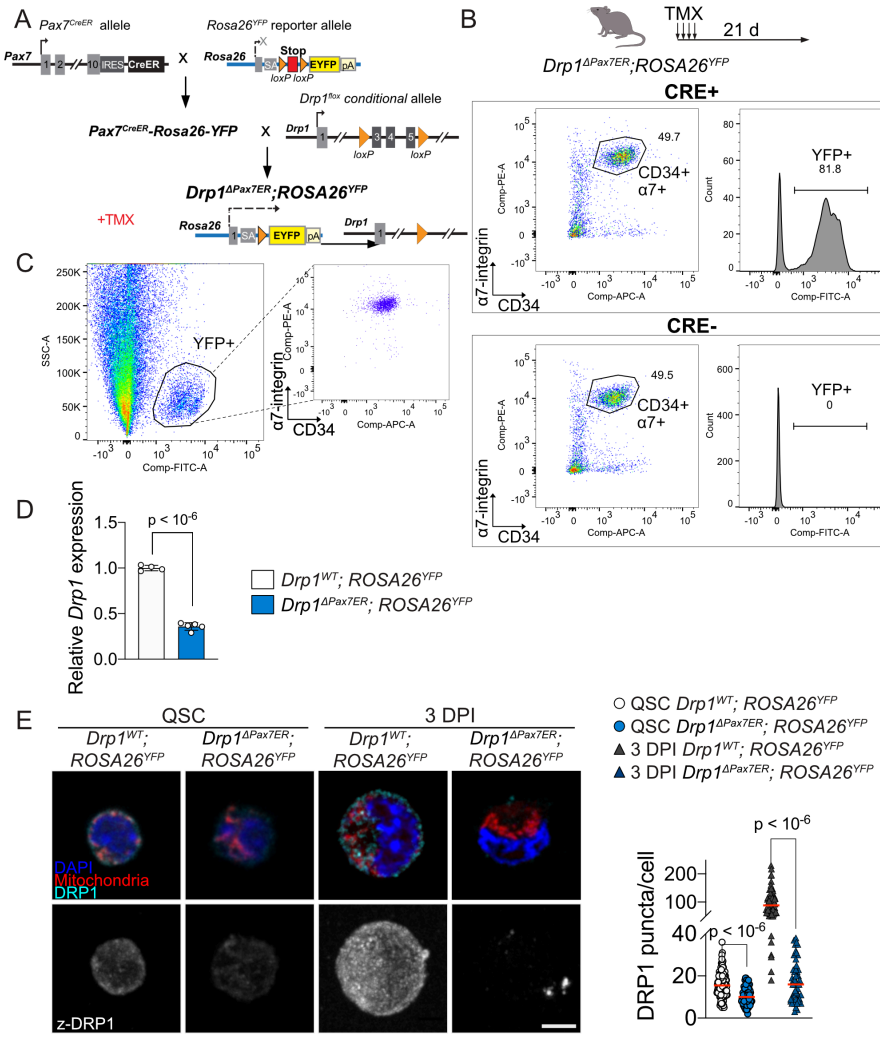

Figure 13 (**A**) Schematic of the genomic alterations introduced in the *Drp1*-floxed allele and the expected rearrangement after Cre-mediated recombination of the *loxP* sites flanking the targeted exons. (**B**) Schematic of tamoxifen (TMX) treatment (top) and the efficiency of Cre recombinase in *Drp1*$^{\Delta Pax7ER}$*:ROSA26*^{YFP} mice after 3 weeks of TMX treatment. The percentage of YFP^{+} SCs within the α7-integrin^{+}/CD34^{+} population was measured by flow cytometry. (**C**) Specificity of the YFP reporter. The expression of α7-integrin and CD34 in YFP^{+} population from *Drp1*$^{\Delta Pax7ER}$:ROSA26^{YFP} mice was measured by flow cytometry. (**D**) Relative expression of *Drp1* in YFP^{+} SCs isolated from *Drp1*^{WT} or *Drp1*$^{\Delta Pax7ER}$ mice, quantified by real time qPCR. (**E**) Representative images of DRP1 protein IF staining (left) and quantification of DRP1 protein puncta per cell (right) in *Drp1*^{WT} or *Drp1*$^{\Delta Pax7ER}$ QSCs and 3DPI-SCs. Scale bar, 3 µm. Data are mean ± s.d. P values were determined by two-tailed unpaired *t*-test.

3D analysis of the mitochondrial shape in YFP^{+}-sorted SCs from muscles in resting conditions (QSCs), or after injury (3DPI-SCs), revealed that the fission-impaired *Drp1*$^{\Delta Pax7ER}$ QSCs showed increased

average mitochondrial volume and decreased sphericity but did not show major changes in mitochondrial size by category compared to those of the WT mice (*Drp1*^{WT}*;ROSA26*^{YFP}*;* herein, *Drp1*^{WT}) (**Figure 14A-C**), whereas *Drp1*$^{\Delta Pax7ER}$ 3DPI-SCs had a higher number of medium- to large-sized mitochondria and a lower number of small-sized mitochondria, than the *Drp1*^{WT} 3DPI-SCs (**Figure 14D**). Further, the mitochondrial shape was more complex in *Drp1*$^{\Delta Pax7ER}$ than in *Drp1*^{WT} satellite cells, as evidenced by the lower mitochondrial sphericity (**Figure 14C,D**), thus confirming that decreased mitochondrial fission occurred in the absence of *Drp1*.

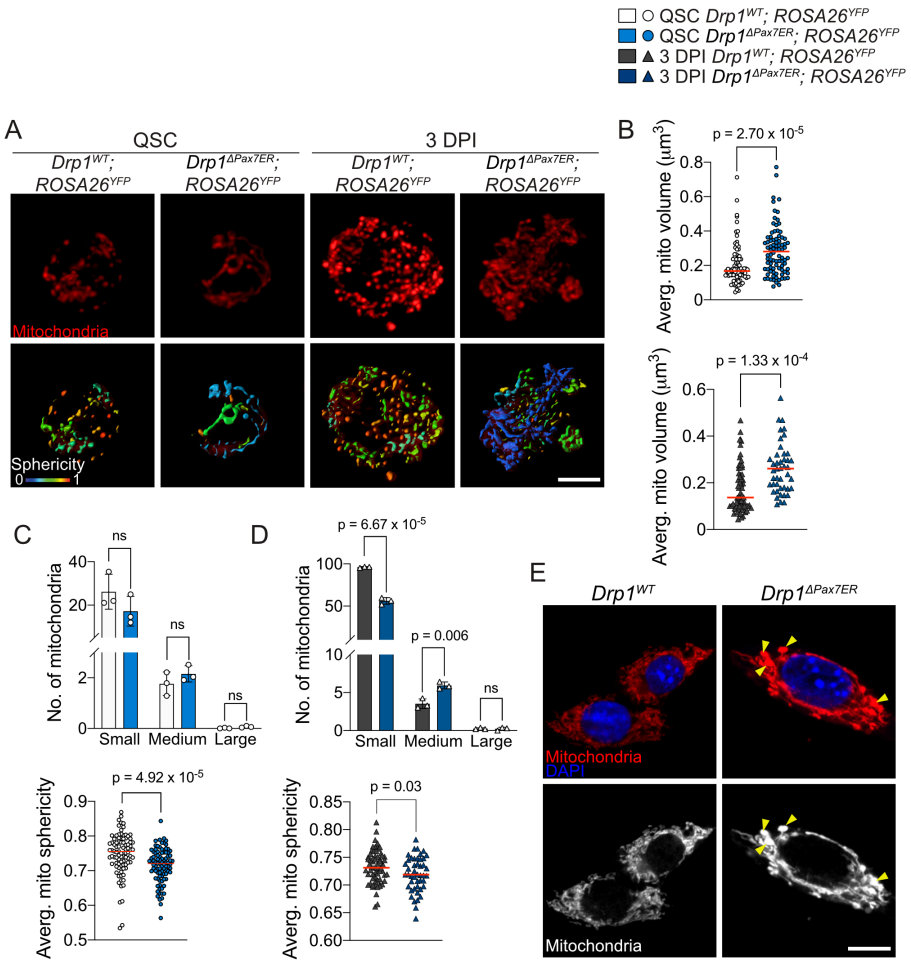

Figure 14 (**A**) Representative images of mitochondrial morphology of *Drp1*^{WT} or *Drp1*$^{\Delta Pax7ER}$ QSCs and 3DPI-SCs using MitoTracker CMXRos Red, followed by

deconvolution and 3D-reconstruction using Imaris software. The reconstructed mitochondria are colored by their sphericity (0–1). Scale bar, 3 µm. (**B**) Quantification of average mitochondrial volume of *Drp1*^{WT} or *Drp1*$^{\Delta Pax7ER}$ QSCs in quiescence (top) or 3DPI-SCs (bottom). (**C,D**) Quantification of average number of mitochondria from 3 categories (top) and average mitochondrial sphericity (bottom) in *Drp1*^{WT} or *Drp1*$^{\Delta Pax7ER}$ SCs in quiescence (**C**) and 3DPI-SCs (**D**).Mitochondria were categorized as small (< 0.5 µm^3), medium (0.5–4 µm^3) or large (> 4 µm^3). (**E**) Representative images of mitochondrial morphology in proliferating *Drp1*^{WT} and *Drp1*$^{\Delta Pax7ER}$ myoblasts derived from YFP$^+$ FACS-sorted satellite cells. Mitochondria were stained with MitoTracker CMXRos Red. Scale bar, 10 µm. Data are mean ± s.d. P values were determined by two-tailed unpaired *t*-test.

Moreover, IF imaging of proliferating *Drp1*$^{\Delta Pax7ER}$ myoblasts derived from YFP$^+$ SCs exhibited a clear hyper-fused mitochondria network with the presence of structure termed “mito-bulbs” (**Figure 14E**), a phenotype that is well-described in *Drp1*-null cells[180,370,371]. Interestingly, in addition to the expected hyper-fused/enlarged mitochondrial morphology (**Figure 15A**, green arrows), our transmission electron microscopic (TEM) analysis revealed abnormal mitochondrial ultrastructure in proliferating *Drp1*$^{\Delta Pax7ER}$ myoblasts (**Figure 15A,** asterisks). An “onion-like”, or concentric cristae structure (indicated with yellow asterisks) has been found exclusively in *Drp1*-null cells, indicating that loss of DRP1 could lead to defects in cristae maintenance. Further, TEM images also revealed enlarged cellular structures that are exclusively found in *Drp1*$^{\Delta Pax7ER}$ myoblasts (**Figure 15B**) which are identified to be peroxisomes, confirming DRP1´s role in regulating the fission of both mitochondria and peroxisome. Indeed, we show elongated peroxisomes in quiescent *Drp1*$^{\Delta Pax7ER}$ SCs but not in *Drp1*^{WT} QSCs (**Figure 15C**) as well as increased average peroxisomal volume in *Drp1*$^{\Delta Pax7ER}$ QSCs (**Figure 15C**). This phenotype is exacerbated at 3DPI, at which point *Drp1*^{WT} SCs displayed mainly puncta-like peroxisomes while *Drp1*$^{\Delta Pax7ER}$ SCs exclusively showed large network of elongated peroxisomes (**Figure 15C**). Interestingly, the total peroxisomal volume was increased in *Drp1*$^{\Delta Pax7ER}$ SCs at 3DPI (**Figure 15C**).

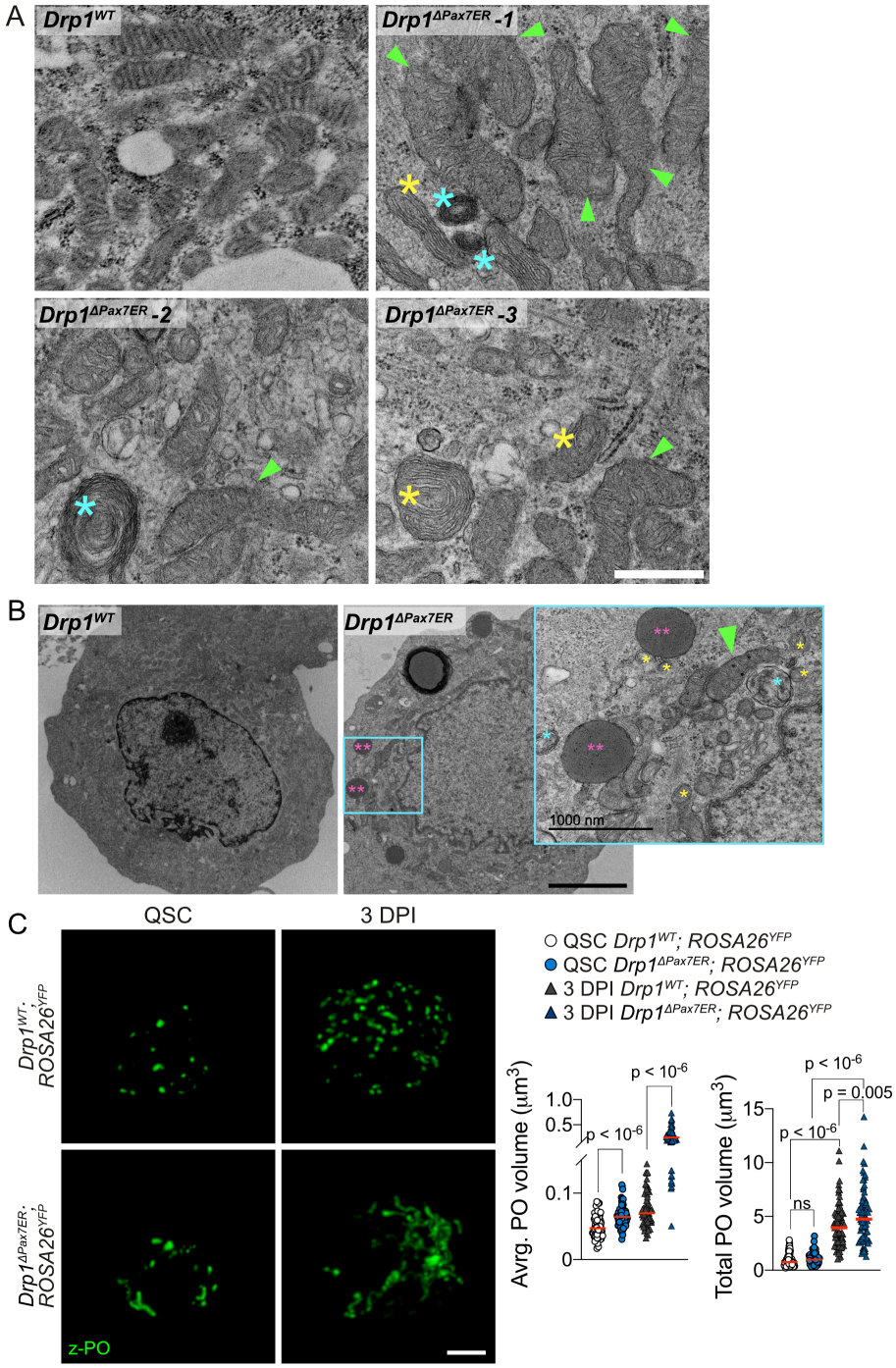

Figure 15 (**A**) Representative images of mitochondria with ultrastructure from *Drp1*^{WT} or *Drp1*$^{\Delta Pax7ER}$ SCs revealed by transmission electron microscopy (TEM). Yellow *, concentric cristae; blue *, disorganized cristae; green triangles, enlarged mitochondria. Images were acquired at 50 k. Scale bar, 500 nm. (**B**) Representative images of *Drp1*^{WT} or *Drp1*$^{\Delta Pax7ER}$ SCs revealed TEM. Images were acquired at 12 k or 50 k (amplified)

magnifications. Scale bar, 2 µm (15 k) and 1000 nm (50 k). ** peroxisome; yellow *, concentric cristae; blue *, disorganized cristae; green triangles, enlarged mitochondria. (**C**) Representative images of IF staining of peroxisomes (PO, PEX14) (left) and quantification of average (middle) and total (right) volume of peroxisomes in *Drp1*^{WT} or *Drp1*$^{\Delta Pax7ER}$ SCs in quiescence and at 3 DPI. Scale bar, 3 µm. Data are mean ± s.d. P values were determined by two-tailed unpaired *t*-test.

To study the effects of *Drp1* deletion in SC functions, we first examined the basal muscle of *Drp1*$^{\Delta Pax7ER}$ mice. We show that the number of SCs in resting muscles of *Drp1*$^{\Delta Pax7ER}$ mice were comparable to those in the corresponding WT control mice (**Figure 16**), and that no significant difference in muscle fiber size was present. A histological analysis along the injury time course (at basal/non-injury, 5-,7- and 14-DPI) (**Figure 17A**) was carried out to study the regenerative capacity of SCs in *Drp1*$^{\Delta Pax7ER}$ mice.

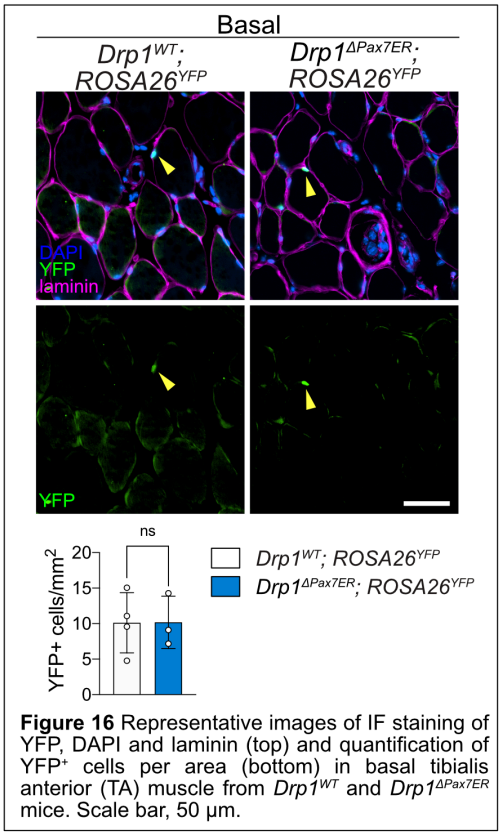

Figure 16 Representative images of IF staining of YFP, DAPI and laminin (top) and quantification of YFP^{+} cells per area (bottom) in basal tibialis anterior (TA) muscle from *Drp1*^{WT} and *Drp1*$^{\Delta Pax7ER}$ mice. Scale bar, 50 µm.

Despite the initial stem-cell numerical similarity, in response to injury, muscles of *Drp1*$^{\Delta Pax7ER}$ mice exhibited a dramatic regeneration defect, as shown by the smaller size of myofibers expressing embryonic myosin heavy chain (eMHC) (indicative of newly-formed, regenerating myofibers) at 5- and 7 DPI, as compared to the WT controls (**Figure 17B,C**). This defect persisted even at 14 DPI (**Figure 17A,17D**), indicating that mitochondrial fission is necessary for SC regenerative functions.

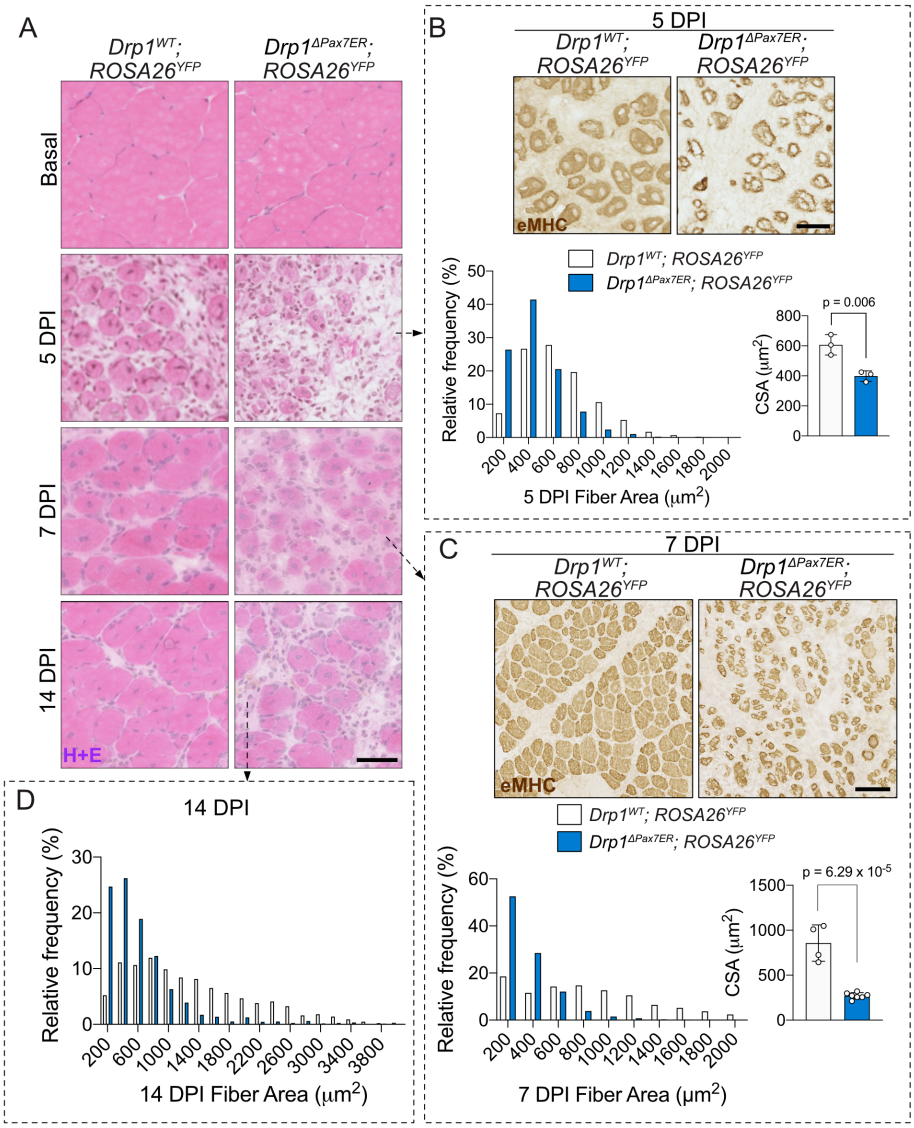

Figure 17 (**A**) Representative images of hematoxylin–eosin (HE) staining in TA muscles obtained from *Drp1*^{WT} or *Drp1*$^{\Delta Pax7ER}$ mice that were non-injured or at 5-, 7- or 14 DPI. Scale bar, 50 μm. (**B,C**) Representative images of embryonic myosin heavy chain (eMHC) staining by immunohistochemistry (IHC) in 5DPI (**B**) and 7DPI (**C**) muscle from *Drp1*^{WT} and *Drp1*$^{\Delta Pax7ER}$ mice (top), and quantification of eMHC^{+} fiber size represented in size distribution (lower left) and average cross-section area (CSA, lower right). Scale bar, 50 μm. (**D**) Size distribution of central-nucleated fibers of 14DPI TA muscles from *Drp1*^{WT} or *Drp1*$^{\Delta Pax7ER}$ mice. Data are mean ± s.d. *P* values were determined by two-tailed unpaired *t*-test.

Thus, we conclude that mitochondria change their shape as SCs progress from quiescence to proliferation, with fission of mitochondria being indispensable for efficient muscle regeneration.

2.2 Mitochondrial fission permits satellite cell expansion after tissue injury

To understand how mitochondria fission blockade impairs satellite cell-dependent muscle repair, we performed RNA-seq of YFP^{+}-sorted QSCs, 1DPI-SCs or 3DPI-SCs from muscles of young $Drp1^{\Delta Pax7ER}$ or $Drp1^{WT}$ mice, followed the same scheme as describe in **Figure 9B**. Transcriptome analysis of genes differentially expressed across different satellite states allowed us to build a DRP1-related interaction network where several important biological pathways such as cell cycle, proteostasis, metabolism and programed cell death were altered upon *Drp1* gene deletion (**Figure 18A**). Our results are comparable to the known interactions of DRP1 according to the mouse protein database (STRING) (**Figure 18B**)[135] except for metabolism- and cell-cell interaction-related clusters, which were unique in our dataset. Furthermore, the 11 DE genes that were shown to be consistently altered in $Drp1^{\Delta Pax7ER}$ SCs in all the three analyzed states are involved in proteostasis, cell cycle, cell-cell interactions, and programed cell death (**Figure 18A, 18C**).

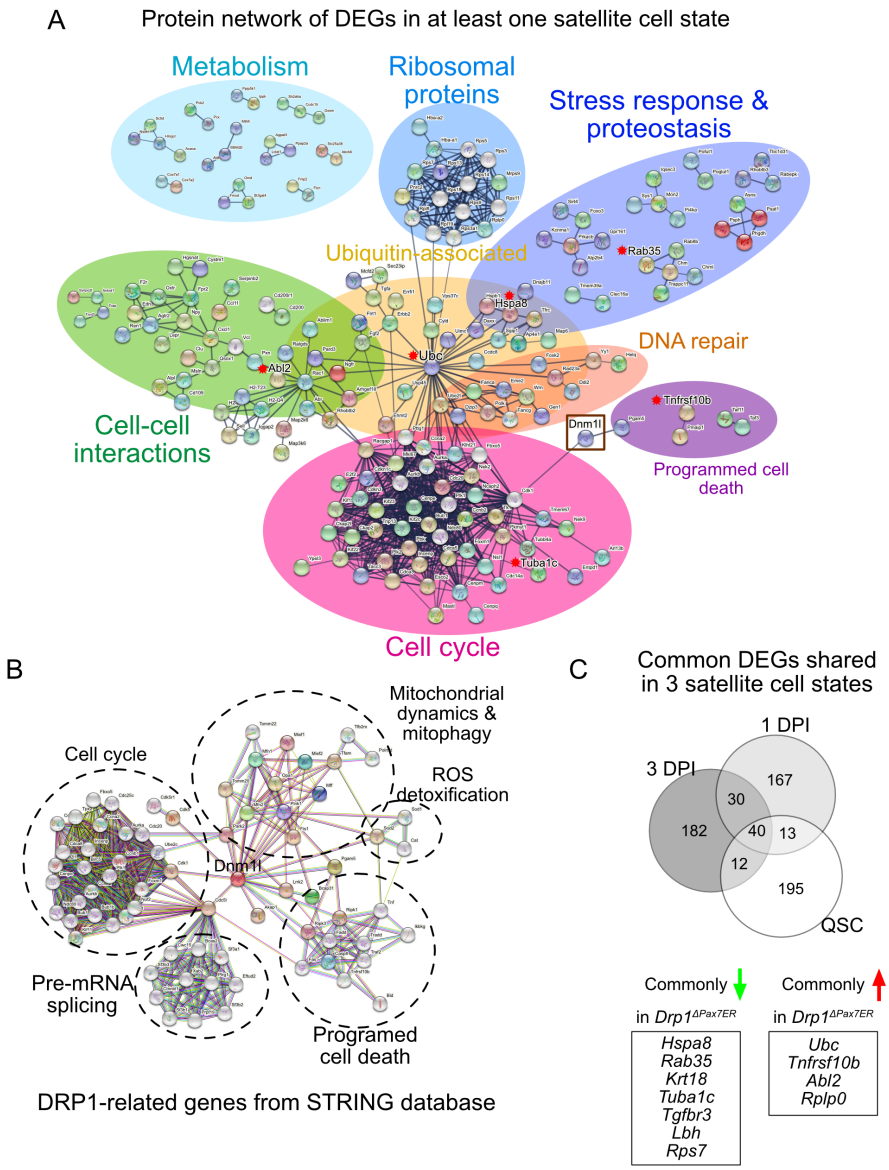

Figure 18 (**A**) Protein networks built in STRING using DE genes between *Drp1*^{WT} and *Drp1*$^{\Delta Pax7ER}$ SCs. The full network of proteins was filtered by a minimum interaction score of 0.7 (high confidence). Coloured nodes, DE genes; white nodes, interactors of DE genes (no more than 20 interactions); red stars, DE genes that were altered in all 3 analyzed states (QSCs, 1DPI-SCs and 3DPI-SCs). (**B**) DRP1-related proteins from STRING mouse database. The full network of proteins was filtered by a minimum interaction score of 0.7 (high confidence). Both 1st and 2nd shell contained no more than 50 interactions. Colorful nodes: query protein DNM1L (DRP1) and first shell of interactors. White nodes: second shell of interactors. Empty nodes: proteins of unknown 3D structure. Filled nodes: some 3D structure is known or predicted. Network edges were evidence based with the line color indicating the type of interaction evidence. Lines: known interactions from curated databases (skyblue) or experimentally determined (purple). Predicted interactions by gene neighborhood (green), gene fusion (red) and gene co-occurrence (blue). Other colors are from other sources. (**C**) Differentially

expressed (DE) genes commonly altered in quiescent (QSCs), 1DPI-SCs and 3DPI-SCs. Venn diagram was obtained from deepvenn[372].

We next analyzed the transcriptomic data by SC state (QSCs, 1DPI-SCs, or 3DPI-SCs) using gene set enrichment analysis (GSEA) followed by Cytoscape Enrichment Map analysis or DE gene pathway analysis.

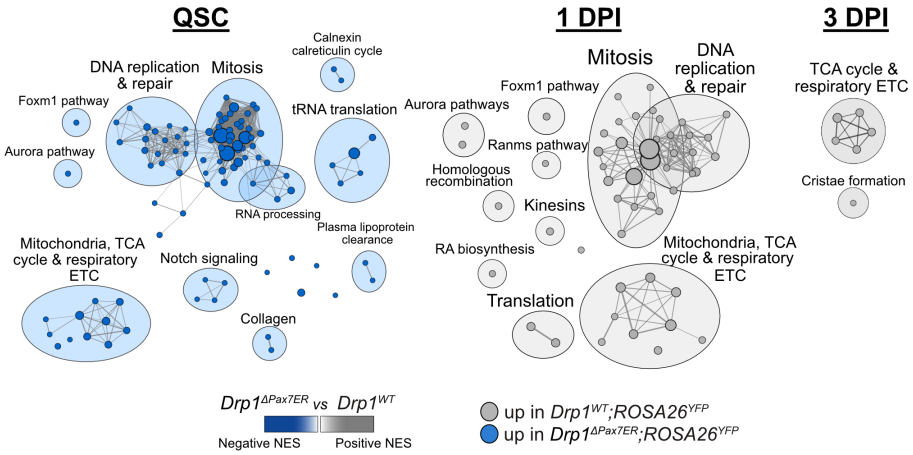

Figure 19 Enrichment map of gene sets enriched in *Drp1*$^{\Delta Pax7ER}$ SCs (blue) or *Drp1*^{WT} SCs (grey) obtained from resting muscle (QSCs), or injured (1-DPI or 3-DPI) limb muscles (GSEA GO_BP, FDR < 0.075). Grey node, positive NES; blue node, negative NES. Node size is proportional to the number of genes identified in each gene set (minimum 10 genes/gene set). Clusters were automatically annotated using Autoannotate app in Cytoscape.

In basal condition, compared to *Drp1*^{WT} QSCs, *Drp1*$^{\Delta Pax7ER}$ QSCs were enriched in genes related to cell division (including mitosis, DNA replication and repair, the Foxm1 and Aurora pathways, and RNA processing) and metabolism (including TCA cycle and the mitochondrial electron transport chain (ETC)) (**Figure 19**). Similarly, DE gene-based pathway analysis showed that cell division–related (RNA polymerase II transcription, cell cycle, M phase, G2/M transition and DNA repair) and metabolism (TCA cycle and respiratory electron transport chain) pathways are altered between the genotypes (lists of DE genes are presented in **Supplementary Table 1**). In addition, cellular stress

response as well as autophagy (and mitophagy) pathways were distinct between *Drp1*^{WT} and *Drp1*$^{\Delta Pax7ER}$ QSCs (**Figure 20**).

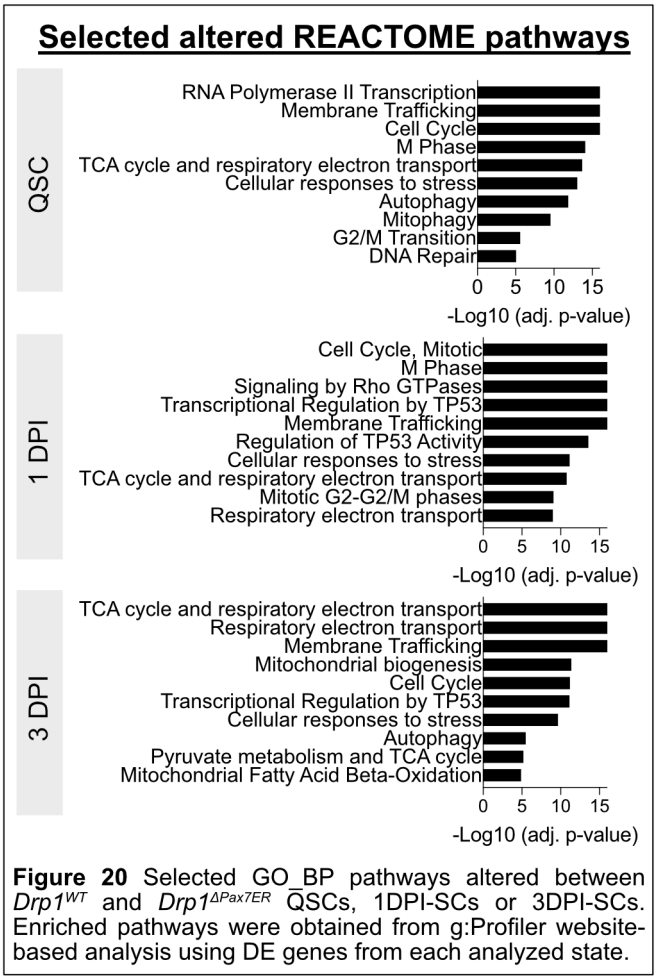

Figure 20 Selected GO_BP pathways altered between *Drp1*^{WT} and *Drp1*$^{\Delta Pax7ER}$ QSCs, 1DPI-SCs or 3DPI-SCs. Enriched pathways were obtained from g:Profiler website-based analysis using DE genes from each analyzed state.

Of note, the quiescent state is characterized with low metabolic activity and reversible cell cycle arrest[39,104]. We show that cell cycle pathways (such as G2/M checkpoint, mitotic cell cycle) and mitochondrial metabolic pathways (such as OXPHOS and TCA cycle) were only upregulated after injury in *Drp1*^{WT} cells (comparing 1DPI-SCs and QSCs) (**Figure 21A**). In addition, enrichment of cell division– and metabolism-related pathways is a hallmark of more primed QSCs, as compared to more genuine QSCs that had more stemness and were more dormant[40,64]. Interestingly, we found the transcriptome of *Drp1*$^{\Delta Pax7ER}$ QSCs, but not *Drp1*^{WT} QSCs, to be closer to the reported gene signature of primed QSCs than to the more dormant/genuine QSCs[40,64] (**Figure 21B**), indicating QSCs lacking *Drp1* might be in a "primed" state with low stemness. However, despite increased

expression of cell cycle genes in *Drp1*$^{\Delta Pax7ER}$ QSCs, no expression of the proliferation marker KI67 was observed in these cells (**Figure 21C**).

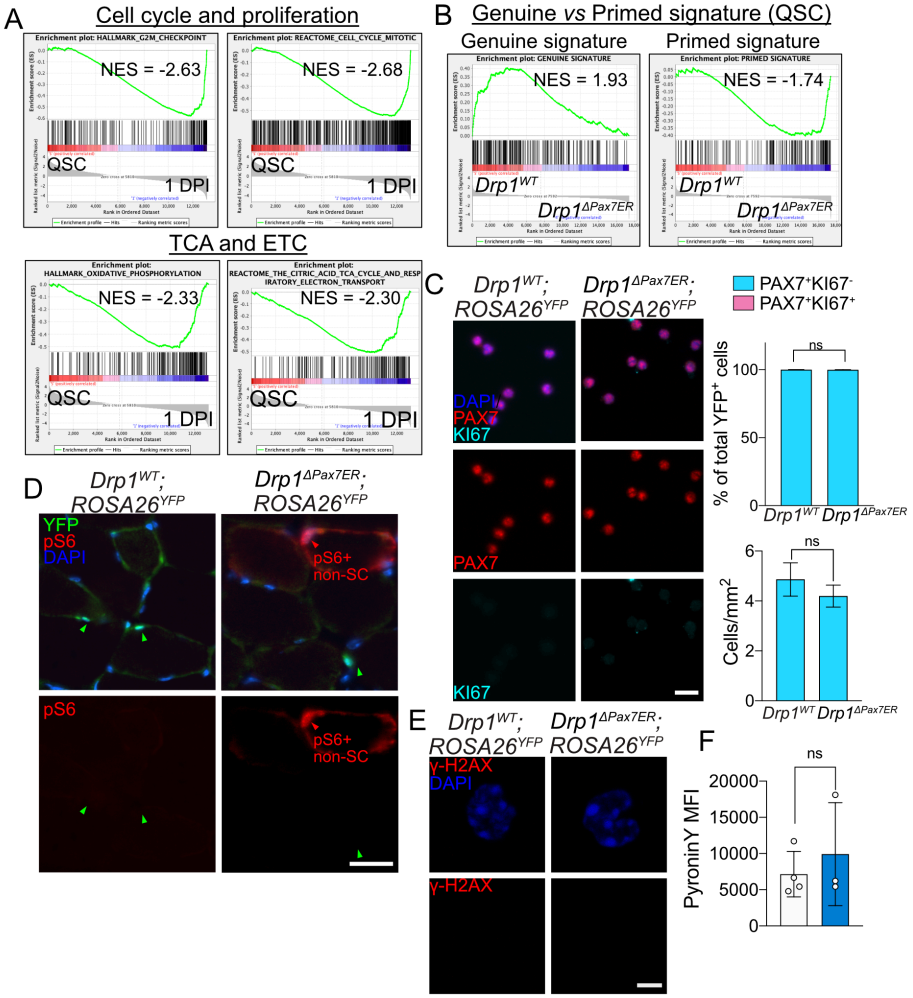

Figure 21 (**A**) GSEA analysis of cell cycle-related (Reactome M5336 and Hallmark M5901) and TCA-ETC–related (Reactome M516 and Hallmark M5936) pathways in *Drp1*^{WT} QSCs *vs* 1DPI-SCs. Red indicates positive NES (enriched in QSCs); blue, negative NES (enriched in 1DPI-SCs). (**B**) GSEA analysis of the "genuine" (referring to more dormant and stem QSCs) and "primed" (referring to QSCs more prone to myogenic differentiation QSCs) gene signatures[64] in *Drp1*$^{\Delta Pax7ER}$ or *Drp1*^{WT} QSCs. Red indicates positive NES (enriched in *Drp1*^{WT}), and blue, negative NES (enriched in *Drp1*$^{\Delta Pax7ER}$). (**C**) Representative images (left) and quantification (upper right) of PAX7 and KI67 in quiescent YFP^{+} SCs obtained from *Drp1*^{WT} or *Drp1*$^{\Delta Pax7ER}$ mice. Quantification of PAX7 and KI67^{+} cells in basal TA muscles from *Drp1*^{WT} or *Drp1*$^{\Delta Pax7ER}$ mice (lower right). Scale bar, 10 µm. (**D**) Representative images of phosphorylated S6 (pS6), YFP and DAPI IF staining in basal TA muscles from *Drp1*^{WT};*ROSA26*^{YFP} and *Drp1*$^{\Delta Pax7ER}$;*ROSA26*^{YFP} mice. No pS6 was detected in YFP^{+} SCs of either genotype. Scale bar, 25 µm. (**E**) Representative images of γ-H2AX and DAPI IF staining in sorted quiescent YFP^{+} cells from *Drp1*^{WT};*ROSA26*^{YFP} and *Drp1*$^{\Delta Pax7ER}$;*ROSA26*^{YFP} mice. No γ-H2AX signal was

detected in either genotype. Scale bar, 3 μm. (**F**) Quantification of PyroninY median fluorescence intensity (MFI) in sorted quiescent YFP$^+$ cells from *Drp1^{WT};ROSA26^{YFP}* and *Drp1$^{\Delta Pax7ER}$;ROSA26^{YFP}* mice. Data are mean ± s.d. *P* values were determined by a two-tailed unpaired *t*-test.

In addition, *Drp1$^{\Delta Pax7ER}$* QSCs were not in a "alerted" state[104], as shown by the negative immunostaining for phosphorylated S6 (**Figure 21D**) and they showed no DNA damage (as determined by γ-H2AX staining; **Figure 21E**) or increased RNA content (as determined by pyronin Y staining; **Figure 21F**). These results indicate that, in resting muscle, SCs with disrupted mitochondrial fission are "molecularly primed" (i.e. "transcriptionally primed") for activation but did not functionally leave the quiescence state.

Strikingly, in contrast to QSCs, the response to muscle injury of 1DPI-SCs from *Drp1$^{\Delta Pax7ER}$* mice showed lower expression of genes related to cell cycle and cell proliferation than those from *Drp1^{WT}* mice (**Figure 19, 22A**). In fact, whereas *Drp1$^{\Delta Pax7ER}$* SCs had higher expression levels of G2/M-related genes in quiescence (**Figure 22B**) (in agreement with the enriched GSEA pathways related to DNA replication, mitosis, Aurora and Foxm1 (**Figure 19**)), after muscle injury, the expression of G2/M-related genes increased dramatically in *Drp1^{WT}* 1DPI-SCs but showed a blunted slope in *Drp1$^{\Delta Pax7ER}$* 1DPI-SCs; these alterations were attenuated at 3DPI (**Figure 22B**).

Prompted by these cell cycle–related differences at the transcriptional level, we analyzed whether *Drp1* loss had functional consequences on the activation and proliferation stages of SCs *in vivo*. To our surprise, even though the main differences of cell cycle genes were detected at 1DPI (activation), we found that at this time point the activation of SCs was similar in *Drp1^{WT}* and *Drp1$^{\Delta Pax7ER}$* mice, as shown by the comparable expression of satellite-cell activation markers (which are absent in QSCs) in 1DPI-SCs from both genotypes (**Figure 22C**).

Moreover, the number of cells expressing MYOD protein (a marker of SC activation; determined by immunostaining) did not differ in SCs from either genotype (**Figure 22D**), supporting that *Drp1*$^{\Delta Pax7ER}$ SCs have no defect in activating from quiescence.

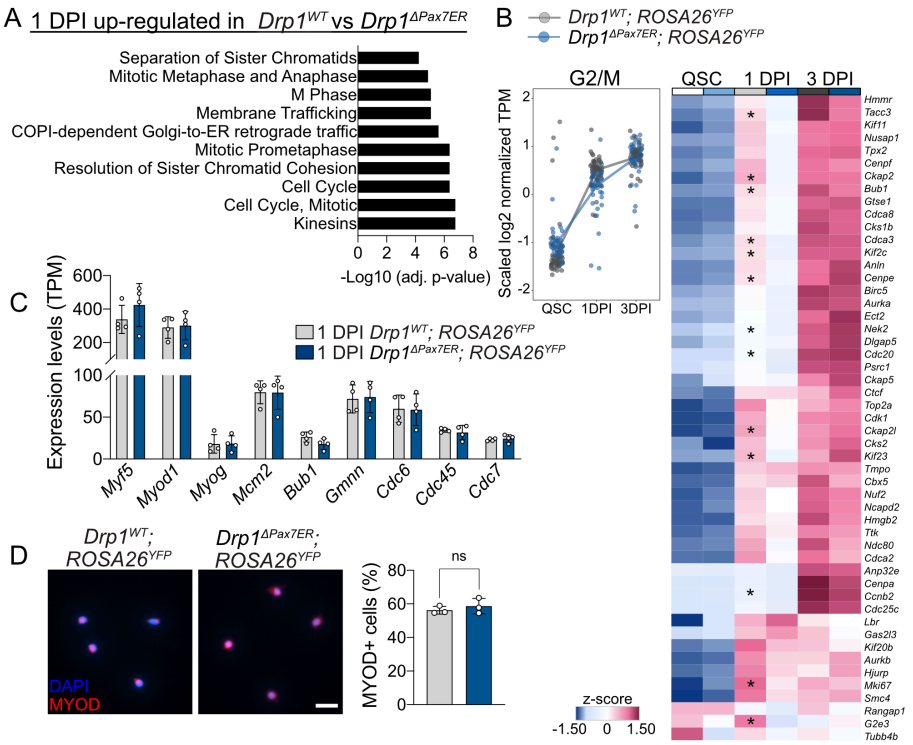

Figure 22 (**A**) Pathway analysis of DE genes upregulated in *Drp1*^{WT} *vs Drp1*$^{\Delta Pax7ER}$ 1DPI-SCs. Pathway analysis was carried out in g:Profiler; top Reactome pathways are presented. (B) Z-score analysis of G2/M cell-cycle genes during analyzed states in *Drp1*^{WT} and *Drp1*$^{\Delta Pax7ER}$ satellite cells, presented as dot graph (left) or heatmap (right). The heatmap was generated in https://software.broadinstitute.org/morpheus. Each thin line represents z-score trajectory of a single gene, and the thick lines, the average z-score trajectory of the pathway. *DE genes (adj. *P* value < 0.05). Detailed expression matrices are shown in the **Supplementary Table 2**. (**C**) Expression level of satellite-cell activation markers in 1DPI-SCs from *Drp1*^{WT}*;ROSA26*^{YFP} and *Drp1*$^{\Delta Pax7ER}$*;ROSA26*^{YFP} mice, represented in transcript per million (TPM). (E) Representative images (left) and quantification (right) of MYOD in 1DPI-SCs. Scale bar, 25 µm. Data are mean ± s.d. *P* values were determined by a two-tailed unpaired *t*-test.

To study whether the alteration of G2/M genes in *Drp1*$^{\Delta Pax7ER}$ SCs affect cell proliferation, we analyzed the total and proliferating SCs at 3DPI from muscle of *Drp1*^{WT} or *Drp1*$^{\Delta Pax7ER}$ mice.

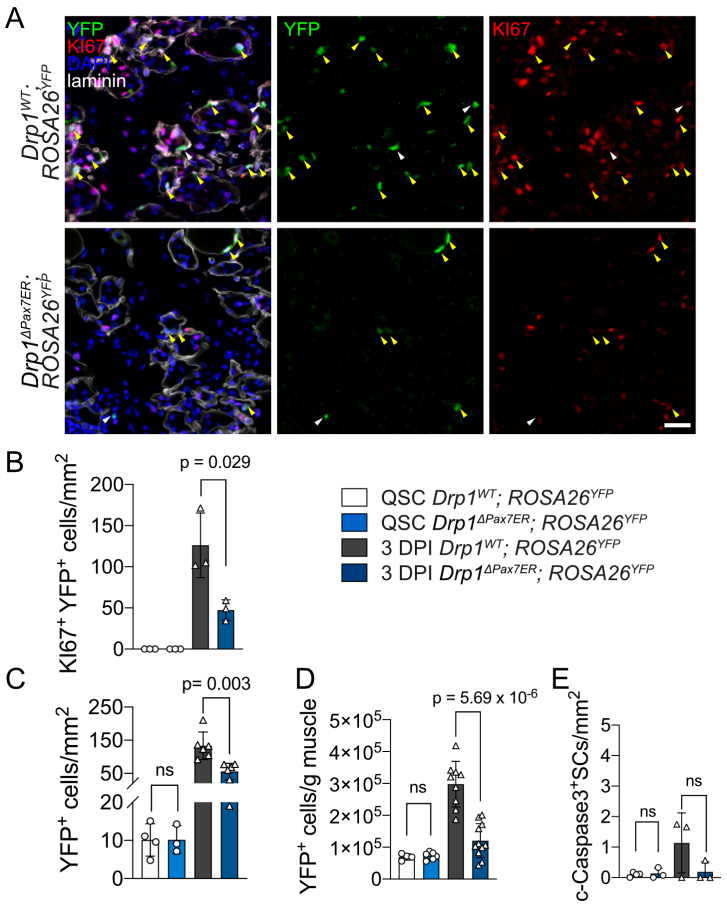

Figure 23 (**A**) Representative images of YFP, KI67, DAPI and laminin immunofluorescence (IF) staining of *Drp1*^{WT} and *Drp1*$^{\Delta Pax7ER}$ 3-DPI TA muscles. Scale bar, 50 µm. (**B-D**) Quantification of proliferating SCs (KI67^{+}YFP^{+}) (**B**) and total YFP^{+} SCs (**C**) from (**A**), as well as YFP^{+} SCs obtained by FACS (**D**) from muscles of *Drp1*$^{\Delta Pax7ER}$ or *Drp1*^{WT} mice in quiescence (QSCs) and at 3-DPI. Data are mean ± s.d. *P* values were determined by a two-tailed unpaired *t*-test.

As expected, *Drp1*^{WT} SCs expanded enormously. Strikingly, however, *Drp1*$^{\Delta Pax7ER}$ cells exhibited a dramatic proliferative impairment, as demonstrated by the reduction of proliferating (KI67^{+}) YFP^{+} 3DPI-SCs in muscles of *Drp1*$^{\Delta Pax7ER}$ compared to *Drp1*^{WT} mice (**Figure 23A,B**). Moreover, using both IF staining on muscle sections and by YFP^{+}-based sorting, we observed significant less amount of YFP^{+} cells in *Drp1*$^{\Delta Pax7ER}$ 3DPI muscle, despite the starting number of YFP^{+} SCs in quiescence was the same (**Figure 23C,D**), confirming at the functional level the cell-cycle molecular differences found in *Drp1*$^{\Delta Pax7ER}$ 3DPI-SCs. Furthermore,

we did not observe increased levels of cell death in *Drp1*$^{\Delta Pax7ER}$ 3DPI muscle (**Figure 23E**). These results indicate that the muscle regenerative defect in *Drp1*$^{\Delta Pax7ER}$ mice after injury cannot be attributed to a defect in early activation, but is rather caused by the subsequent incapacity of SCs to proliferate adequately and generate sufficient progeny to form new fibers when mitochondrial fission is blunted.

2.3 Mitochondrial fission allows satellite cells to induce OXPHOS metabolism during regeneration

Notably, apart from cell division–associated pathways, our transcriptomic data revealed alterations of mitochondria-related pathways in *Drp1*$^{\Delta Pax7ER}$ SCs such as TCA cycle and respiratory ETC, mitochondrial biogenesis, etc. (**Figure 19, 20**). To understand the causes of the proliferative defect of mitochondrial fission-deficient SCs after muscle injury given the special prominence of the TCA and ETC pathways, we analyzed the mitochondrial metabolism of these cells in more depth, at both transcriptional and functional levels. The GSEA results showed that OXPHOS pathways are significantly enriched in *Drp1*$^{\Delta Pax7ER}$ QSCs (**Figure 24A**), when the cells are supposed to be metabolically inactive, in agreement with their molecular primed state (as discussed previously; see Results 2.2). In response to injury during activation (1DPI), wild-type SCs increased their OXPHOS activity dramatically to adapt to their metabolic needs (see Results 1.2 and **Figure 12**); in contrast, *Drp1*$^{\Delta Pax7ER}$ 1DPI-SCs expressed lower level of OXPHOS genes as compared to *Drp1*^{WT} 1DPI-SCs, as OXPHOS pathway is significantly enriched in *Drp1*^{WT} (**Figure 22A**). In 3DPI-SCs, the TCA and ETC pathway genes remained downregulated in *Drp1*$^{\Delta Pax7ER}$ as compared to *Drp1*^{WT} SCs (**Figure 19**); accordingly, OXPHOS pathways are enriched in *Drp1*^{WT} SCs (**Figure 22A**). In

particular, genes encoding the mitochondrial TCA pathway and ETC complex IV proteins (such as *Pfkm*, *Cox7a1*, *Cox7a2* and *Cox10*) were downregulated in *Drp1*$^{\Delta Pax7ER}$ 3DPI-SCs, whereas *Pck2* (involved in gluconeogenesis) was upregulated (**Supplementary Table 1**). Furthermore, by adapting a curated OXPHOS gene list from MitoCarta3.0, similar results are obtained (**Figure 22B**). Consistent with this, all five ETC complex subunit genes showed an upregulated expression in *Drp1*$^{\Delta Pax7ER}$ as compared to *Drp1*^{WT} QSCs, and this trend changed at the 1- and 3-DPI time points (**Figure 22C**). These molecular analyses suggested an altered mitochondrial metabolism and a lower OXPHOS activity in mitochondrial fission–deficient satellite cells, which were particularly marked at the proliferative stage.

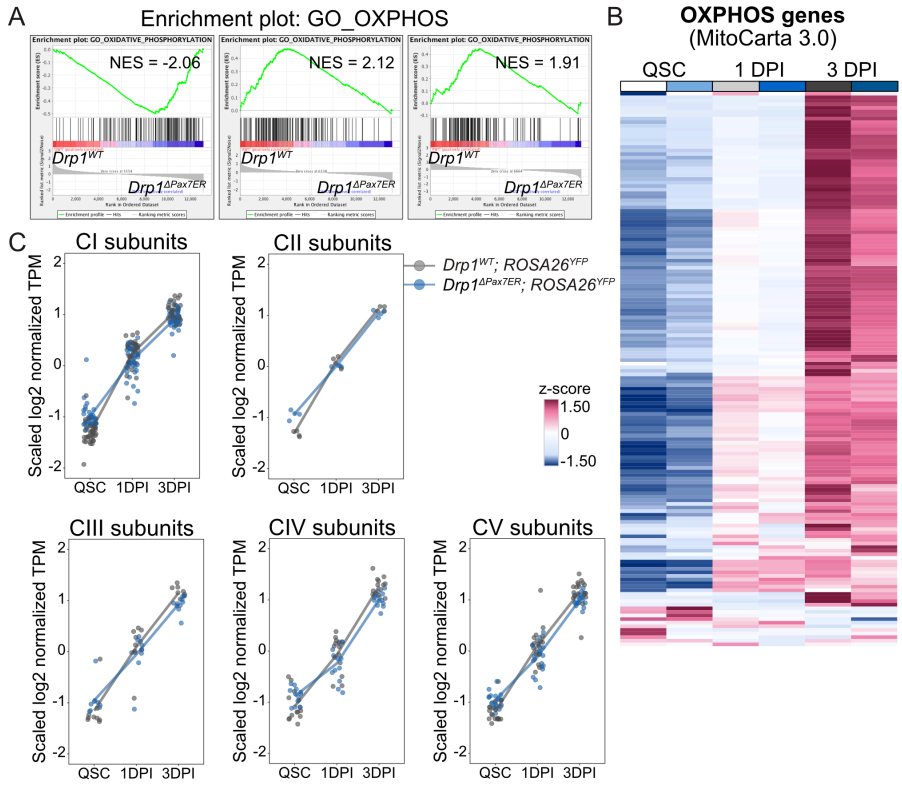

Figure 24 (**A**) GSEA analysis of OXPHOS (GO:0006119) pathways in *Drp1*$^{\Delta Pax7ER}$ *vs* *Drp1*^{WT} QSCs. Red indicates positive NES (enriched in *Drp1*^{WT}), and blue, negative NES (enriched in *Drp1*$^{\Delta Pax7ER}$). (**B**) Z-score analysis of total OXPHOS genes in the analyzed states in *Drp1*^{WT} and *Drp1*$^{\Delta Pax7ER}$ SCs presented as a heatmap. The OXPHOS gene set was obtained from the mouse MitoCarta3.0 database. Detailed gene names and

expression matrices are shown in **Supplementary Table 2**. The heatmap was generated on the Morpheus platform. (**C**) Z-score analysis of electron transport chain (ETC) complex I to V subunit genes during the analyzed states in *Drp1*^{WT} and *Drp1*$^{\Delta Pax7ER}$ satellite cells, presented as dot graphs. ETC complex gene sets were obtained from the mouse MitoCarta3.0 database. Each dot represents z-score of a single gene, and the thick lines show the average z-score trajectory of the pathway.

Interestingly, functional cellular respiratory analysis by Seahorse revealed that *Drp1*$^{\Delta Pax7ER}$ QSCs had similar basal and maximal oxygen consumption rates (OCRs) as *Drp1*^{WT} QSCs, but tended to have a higher proton leak (less ATP production by OXPHOS) (**Figure 25A**).

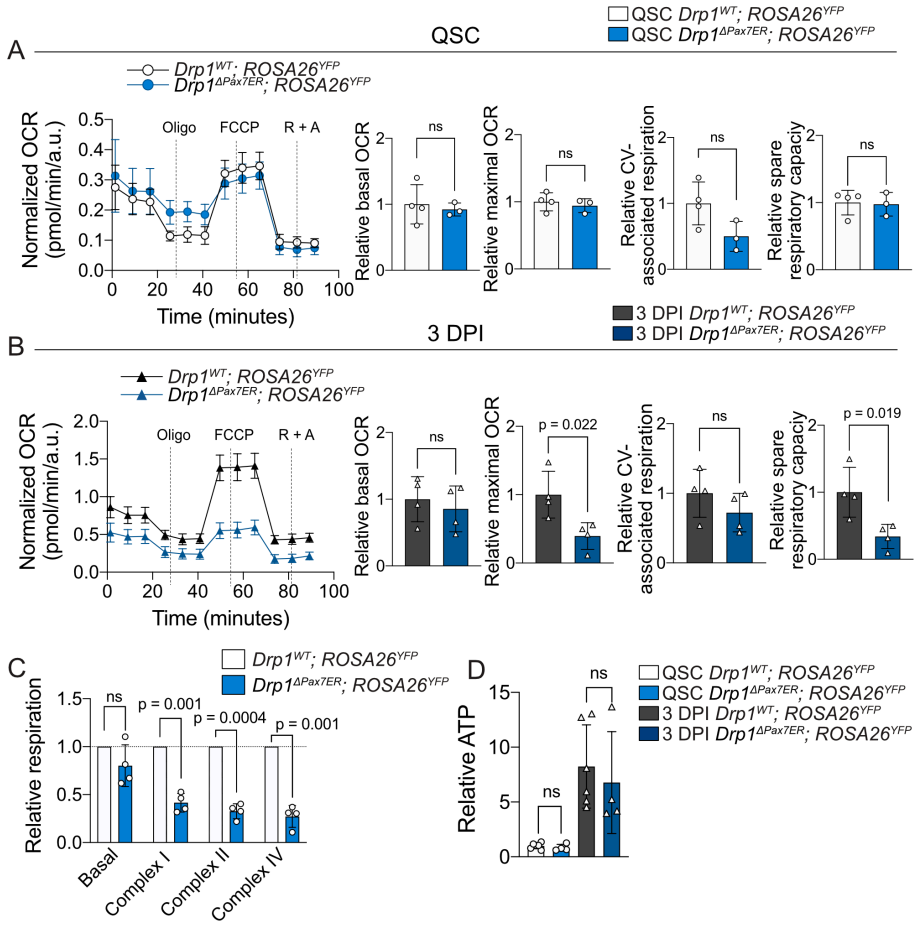

Figure 25 (**A,B**) Seahorse analysis of cellular respiration of QSCs (**A**) and 3DPI-SCs (**B**) represented in normalized oxygen consumption rate (OCR) at baseline and in response to oligomycin A (oligo), FCCP or rotenone plus antimycin A (R + A) as well as calculated basal OCR, maximal OCR, complex V activity and spare respiratory capacity. Data were obtained using Seahorse XF96 and normalized to protein level using Cyquant cell proliferation assay. (**C**) Relative respiration of each mitochondrial ETC complex measured by oxygraph (Oroboros). Values were normalized to cell number and to the

level of *Drp1*^{WT}. (**D**) Relative total cellular ATP level, normalized to the QSC *Drp1*^{WT} level. Data are mean ± s.d. *P* values were determined by a two-tailed unpaired *t*-test.

At 3-DPI, on the other hand, we observed a dramatic reduction of cellular maximal respiration and spare respiratory capacity in *Drp1*$^{\Delta Pax7ER}$ SCs (**Figure 25B**). This is consistent with our RNA-seq results, in which *Drp1*$^{\Delta Pax7ER}$ 3DPI-SCs showed significant lower expression of OXPHOS genes compared to *Drp1*^{WT} 3DPI-SCs (**Figure 24**). Non-mitochondrial respiration was also lower in *Drp1*$^{\Delta Pax7E}$ than *Drp1*^{WT} SCs, but no significant differences in basal OCR and complex V activity (ATP-associated OCR) were detected between either genotype (**Figure 25B**).

To examine the respiratory capacity of each mitochondrial ETC complex, we performed oxygen consumption analysis with Oroboros oxygraph using proliferating myo-progenitors derived from YFP^{+} *Drp1*^{WT}or *Drp1*$^{\Delta Pax7ER}$ SCs. Cells are placed in oxygen chamber to measure their basal and each mitochondrial ETC complex-associated respiration. More specifically, cells were permeabilized with digitonin to allow for the equal distribution of substrates and inhibitors into the mitochondria, followed by complex-specific substrates and inhibitors treatment: pyruvate + malate + ADP, succinate, rotenone, antimycin A, TMPD + ascorbate and sodium azide. Using this robust method, our results revealed a global impairment of the mitochondrial respiration in *Drp1*$^{\Delta Pax7ER}$ cells, marked by significantly reduced mitochondrial ETC complex I, II and IV (**Figure 25C**) activities, confirming that mitochondrial OXPHOS is impaired upon DRP1 loss. On the other hand, the total cellular ATP level was similar in cells of both genotypes (**Figure 25D**), indicating that *Drp1*$^{\Delta Pax7ER}$ SCs used other energy sources for ATP production. Together, these results suggested that mitochondrial fission–impaired SCs cannot efficiently reprogram their metabolism after

muscle injury, with an evident quantitative and qualitative alteration in the global mitochondrial ETC expression program.

The mammalian mtDNA encodes for 13 proteins of the mitochondrial ETC and is an important component of the mitochondria[164]. Although basically unstudied in stem cells, the synthesis and assembly of the ETC are known to depend on the proportion and distribution of the mtDNA along with the mitochondrial network[212,373]. As mitochondrial activity was altered in *Drp1*$^{\Delta Pax7ER}$ SCs, we next analyzed whether the copy number of mtDNA was affected in *Drp1*$^{\Delta Pax7ER}$ SCs. We found *Drp1*$^{\Delta Pax7ER}$ QSCs had a lower mtDNA copy number than *Drp1*^{WT} QSCs (**Figure 26A**), despite similar mitochondrial volumes (**Figure 26B**). Further, at 3 DPI, the mtDNA content increased in both genotypes, but the copy number remained lower in *Drp1*$^{\Delta Pax7ER}$ than in *Drp1*^{WT} cells (**Figure 20A**), indicating inefficient mtDNA replication in proliferating SCs when mitochondrial fission was impaired. In mammalian cells, mtDNA genome are packaged as a DNA-protein complex, termed mitochondrial nucleoids[165]. Surprisingly, both the size and distribution of mitochondrial nucleoids were aberrant in *Drp1*$^{\Delta Pax7ER}$ QSCs, with fewer and larger-sized nucleoids (**Figure 26C**). This nucleoid imbalance was further exacerbated in 3DPI-SCs, as shown by the abnormally enlarged nucleoids (**Figure 26C**), and this could impact ETC assembly[212,373]. In sum, following injury, mitochondrial fission blockade in SCs impeded normal mitochondrial metabolic reprogramming and induced the presence of abnormal nucleoids, which together could underpin the low efficiency of the ETC and OXPHOS during the regenerative demand.

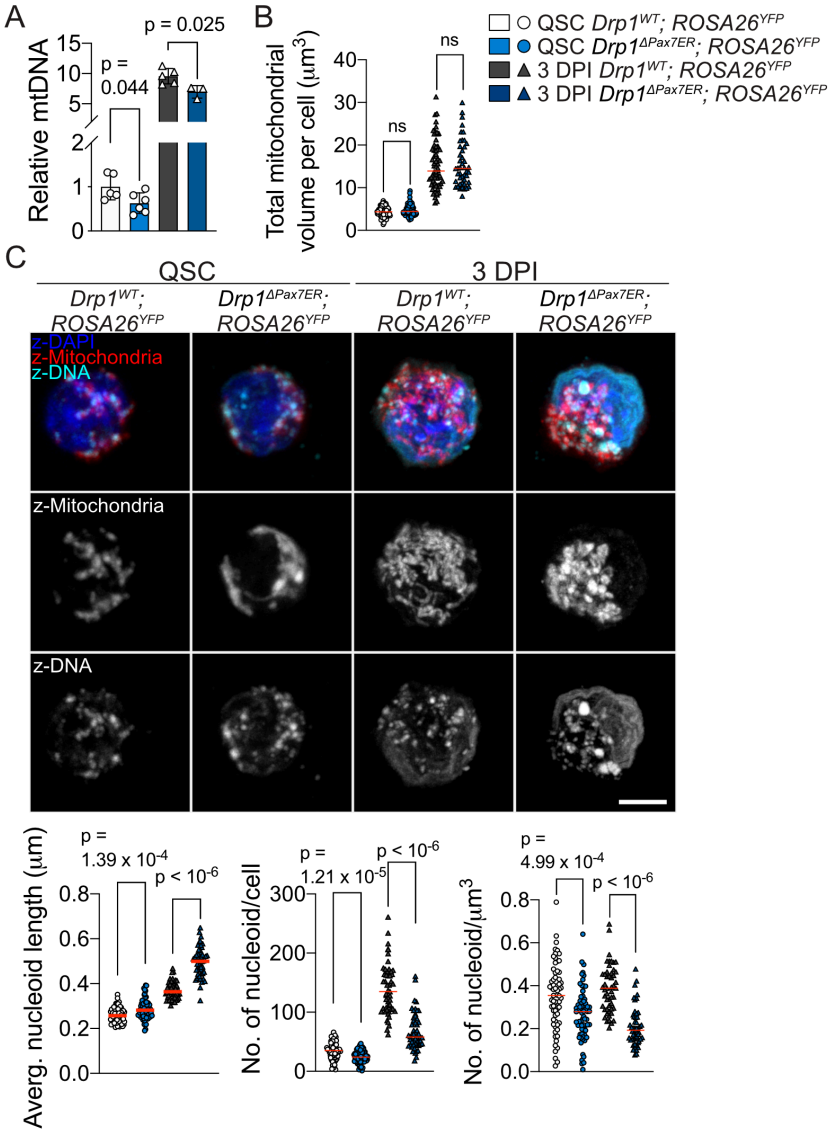

Figure 26 (**A**) Copy number of mtDNA in QSCs or 3DPI-SCs from *Drp1*^{WT} or *Drp1*$^{\Delta Pax7ER}$ muscles (normalized to *Drp1*^{WT} QSC levels). mtDNA copy number were normalized to genomic DNA copy number, quantified by qPCR ($2^{-\Delta CT}$). (**B**) Reconstructed total mitochondrial volume in *Drp1*^{WT} or *Drp1*$^{\Delta Pax7ER}$ QSCs or 3DPI-SCs. The analysis was carried out based on images acquired in **Figure 14A**. (**C**) Representative IF images (upper panel) and quantification of mitochondrial nucleoid parameters (lower panel): average nucleoid length (left), number of nucleoid per cell (middle) and per µm^3 (right). Mitochondria were detected with citrate synthase antibodies. Scale bar, 3 µm. Data are mean ± s.d. *P* values were determined by a two-tailed unpaired *t*-test.

2.4 Mitochondrial fission deficiency impairs satellite cell mitophagy

In addition to alterations in pathways related to cell proliferation and mitochondrial metabolism, we also identified numerous stress response and proteostasis-related genes, such as cellular responses to stress, autophagy and mitophagy (**Figure 20A**). At the single gene level, for instance, the increased expression of asparagine synthetase (*Asns*) could reflect a need to dispose of the aspartate accumulated due to mitochondrial dysfunction and a reduced TCA cycle flux [374] (**Supplementary Table 1**). Accordingly, we observed evident accumulations of ROS puncta in the mitochondrial matrix (**Figure 27A**). In addition, our quantification showed significantly increased cellular and mitochondrial ROS level in the $Drp1^{\Delta Pax7ER}$ SCs (**Figure 27B**), suggesting increased levels of malfunctioning or damaged mitochondria upon *Drp1* loss. This could be due to: i) the compromised clearance of damaged mitochondria by mitophagy (i.e., the elimination of mitochondria by autophagy), caused by the increased mitochondrial size in $Drp1^{\Delta Pax7ER}$ satellite cells; and/or ii) the saturated autophagic capacity, caused by the abnormal generation rates of damaged mitochondria in the mutant cells.

To analyze these possibilities, we treated freshly-sorted SCs from $Drp1^{\Delta Pax7ER}$ and $Drp1^{WT}$ mice with the autophagy-flux inhibitor bafilomycin A1 (Baf), which blocks the elimination of autophagosomes by fusion with lysosomes[100]. This treatment increased the $LC3^{+}$ puncta (i.e., autophagosomes) in $Drp1^{WT}$ but not $Drp1^{\Delta Pax7ER}$ SCs, indicating that autophagy is blunted in the absence of *Drp1* (**Figure 27C-E**). Notably, mitophagy was also defective in $Drp1^{\Delta Pax7ER}$ SCs, as indicated by the accumulation of mitochondria inside autophagosomes (e.g., LC3-mitochondria co-localization in Baf-treated sorted cells) (**Figure 27E**).

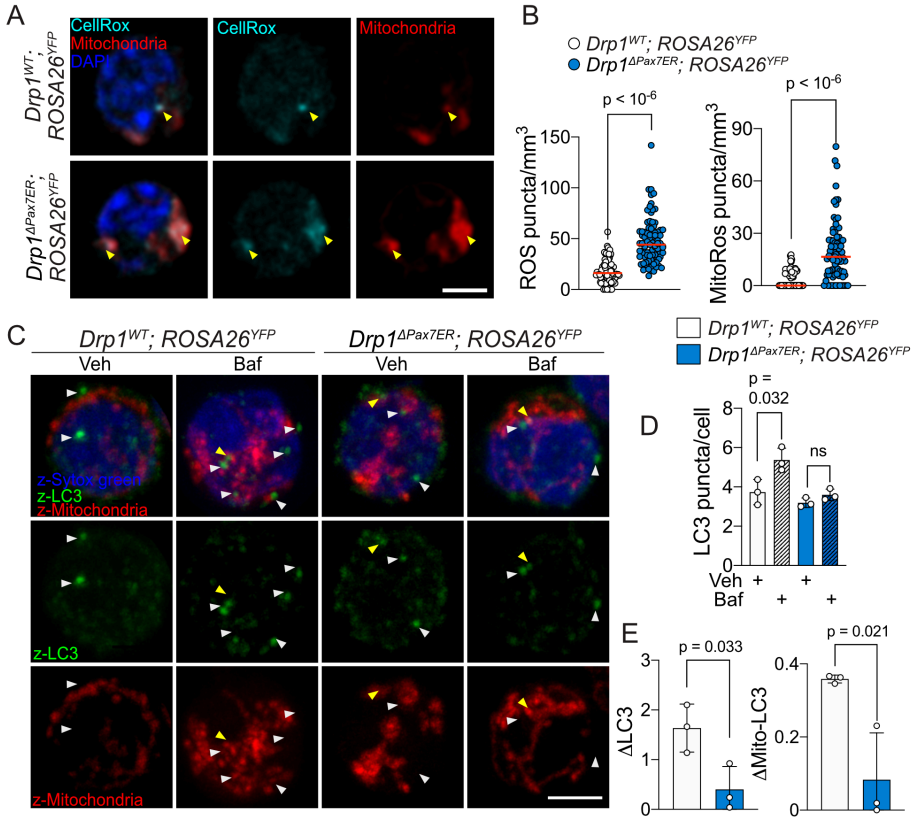

Figure 27 (**A**) Representative images of ROS (CellRox) and mitochondria (MitoTracker CMX ROS) in SCs from *Drp1*^{WT} vs *Drp1*$^{\Delta Pax7ER}$. (**B**) Quantification of total (left) and mitochondria-specific (right) ROS puncta from (**A**), values are normalized to cell volume (μm^3). Scale bar, 3 μm. (**C**) Representative IF images of LC3 and mitochondria in *Drp1*^{WT} or *Drp1*$^{\Delta Pax7ER}$ SCs after 4 h of treatment with vehicle (Veh; DMSO) or bafilomycin A1 (Baf). Scale bar, 3 μm. (**D**) Quantification of total LC3 puncta per cell from (**C**). (**E**) Quantification of total flux of LC3 (ΔLC3) (left) and mitochondria-related flux of LC3 (mito-ΔLC3) (right) in *Drp1*^{WT} or *Drp1*$^{\Delta Pax7ER}$ SCs from (**C**). Data are mean ± s.d. *P* values were determined by a two-tailed unpaired *t*-test.

Next, *Drp1*^{WT} and *Drp1*$^{\Delta Pax7ER}$ SCs were treated with a natural mitophagy inducer urolithin A (UA[375]). As expected, UA treatment significantly increased LC level in *Drp1*^{WT} SCs (**Figure 28A-C**). This UA-induced flux, however, is blunted in *Drp1*$^{\Delta Pax7ER}$ SCs as using bafilomycin A1 treatment (**Figure 28A-C**), consistent with the published data[375] that show that the function of UA on mitophagy induction relies on functional mitochondria. Further, UA-induced *Drp1*$^{\Delta Pax7ER}$ SCs tended to show larger size of LC3 protein but not in numbers (**Figure 28A**). However,

further investigations need to be conducted in order to explain this interesting phenomenon.

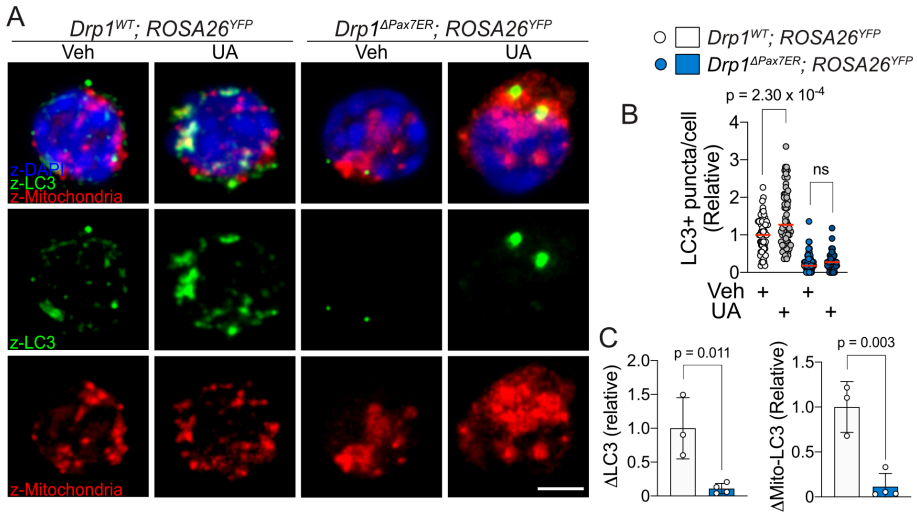

Figure 28 (**A**) Representative IF images of LC3 and mitochondria in *Drp1*^{WT} or *Drp1*$^{\Delta Pax7ER}$ SCs after 4 h of treatment with vehicle (Veh; DMSO) or urolithin A (UA). Scale bar, 3 µm. (**B**) Quantification of total LC3 puncta per cell from (**A**). (**C**) Quantification of total flux of LC3 (ΔLC3) (left) and mitochondria-related flux of LC3 (mito-ΔLC3) (right) in *Drp1*^{WT} or *Drp1*$^{\Delta Pax7ER}$ SCs from (**A**). Data are mean ± s.d. P values were determined by a two-tailed unpaired *t*-test.

Consistent with this outcome, we observed increased levels of p62 in *Drp1*$^{\Delta Pax7ER}$ SCs, both at the cellular level and in mitochondria (**Figure 29A**), indicating increased accumulation of damaged mitochondria and other cellular components upon DRP1 loss that are not removed by the autophagy machinery. To further investigate the mitophagy machinery, we examined the level of Parkin, a key regulator of the PINK1/Parkin-mediated mitophagy[263], in *Drp1*$^{\Delta Pax7ER}$ *vs Drp1*^{WT} SCs. We observed a significant increase of Parkin signal in *Drp1*$^{\Delta Pax7ER}$ SCs but reduced Parkin-mitochondria colocalization compared to *Drp1*^{WT} SCs (**Figure 29B**), suggesting that the impaired mitophagy in *Drp1*$^{\Delta Pax7ER}$ SCs could be partially due to deficient Parkin recruitment to the mitochondria upon mitochondrial damage. Interestingly, Parkin recruitment to the damaged mitochondria is known to be induced by low mitochondrial membrane potential $\Delta\Psi m$[263,376–378] which is significantly increased in *Drp1*$^{\Delta Pax7ER}$

SCs despite the accumulation of ROS (**Figure 29C, 27A**), which could explain the cytoplasmic Parkin accumulation in these cells. This reflected the inability of SCs to remove damaged mitochondria when mitochondrial fission was impaired, which would also account for the excessive ROS accumulation. We thus conclude that impaired mitochondrial fission impedes both mitochondrial metabolic reprogramming and mitophagy in SCs upon injury, which blunts their regenerative functions.

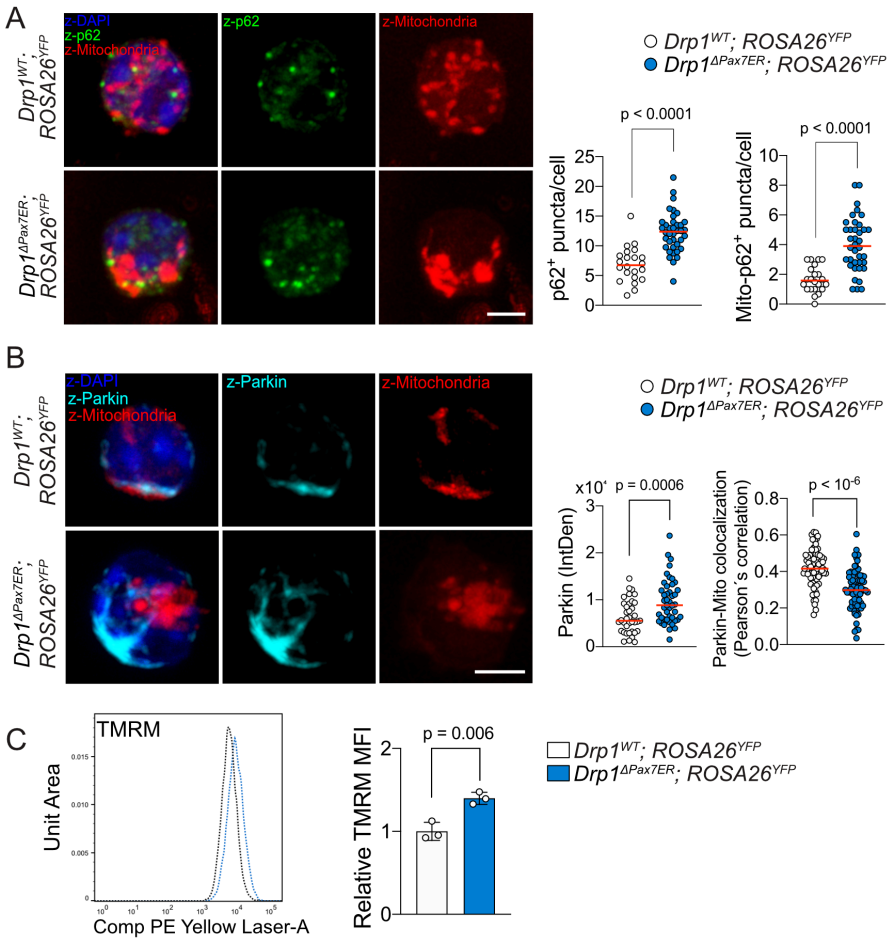

Figure 29 (**A**) Representative images of p62 and mitochondria (left) and quantification of total p62 puncta (middle) and colocalization of p62 to mitochondria (Mito-p62; right) in *Drp1*^{WT} or *Drp1*$^{\Delta Pax7ER}$ SCs. Mitochondria were detected with MitoTracker CMX ROS labeling. Scale bar, 3 µm. (**B**) Representative images of Parkin and mitochondria (left) and quantification of Parkin signal (IntDen; middle) and colocalization of Parkin to mitochondria (Pearson´s correlation; right) in *Drp1*^{WT} or *Drp1*$^{\Delta Pax7ER}$ SCs. Mitochondria were detected with MitoTracker CMX ROS labeling. Scale bar, 3 µm. (**C**) Representative

histogram (left) and relative MFI (right) of TMRM signals analyzed by flow cytometry. Values were normalized to the *Drp1*^{WT} level. Data are mean ± s.d. *P* values were determined by a two-tailed unpaired *t*-test.

2.5 Transient adynamism restores the proliferative capacity of *Drp1*-null SCs

In cardiomyocytes, forced mitochondrial adynamism by genetically ablating *Drp1* and mitofusins (*Mfn1/Mfn2*) simultaneously can relieve the undesirable effects introduced by imbalanced mitochondrial dynamics, at least in the short term[267]. As a known receptor for Parkin, *Mfn2* plays an essential role in the Pink1/Parkin-mediated mitophagy[223]. To avoid the influence of *Mfn2* on mitophagy, we investigated the effects of mitochondrial adynamism by silencing the *Mfn1* gene with siRNA (si-Mfn1) in *Drp1*-null SCs. To verify the efficiency of siRNA sequencing, we treated WT SCs with 25 nM of si-Mfn1 and si-Sramble *in vitro* for 48 h; treatment of si-Mfn1 then led to significant reduced expression of *Mfn1* gene (**Figure 30A,B**), confirming the efficiency of gene silencing. Further, we observed fragmented mitochondria in WT SCs treated with si-Mfn1, and 3D reconstruction of mitochondrial network showed significantly reduced average mitochondrial volume in si-Mfn1-treated cells as compared to the scramble-RNA–treated group (**Figure 30C**), indicating deficient mitochondrial fusion, as expected from *Mfn1* silencing.

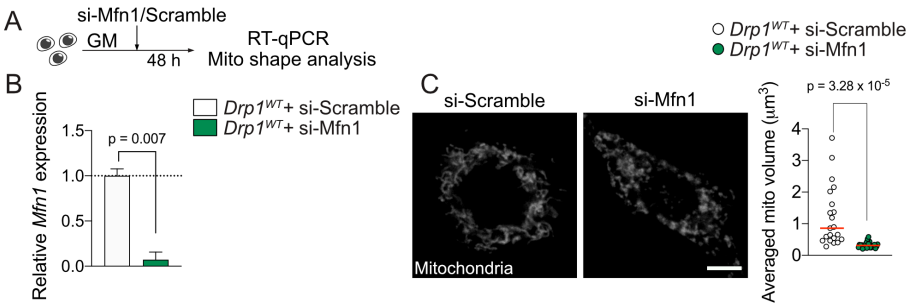

Figure 30 (**A**) Schematics of siRNA treatment *in vitro* in wild type cells (**B,C**) Verification of siRNA efficiency by analyzing *Mfn1* gene expression (RT-qPCR; **B**) and mitochondrial

morphological analysis (**C**). Mitochondria were labeled with MitoTracker CMX ROS and average mitochondrial volume was quantified using 3D reconstructed images in Imaris software. Scale bar, 3 µm. Data are mean ± s.d. *P* values were determined by a two-tailed unpaired *t*-test.

Similarly, after *Drp1*$^{\Delta Pax7ER}$ SCs were treated with si-Mfn1, they exhibited a decreased average mitochondrial volume (**Figure 31**), suggesting the enlarged mitochondrial network in *Drp1*-null SCs can be dissociated by repressing mitochondrial fusion.

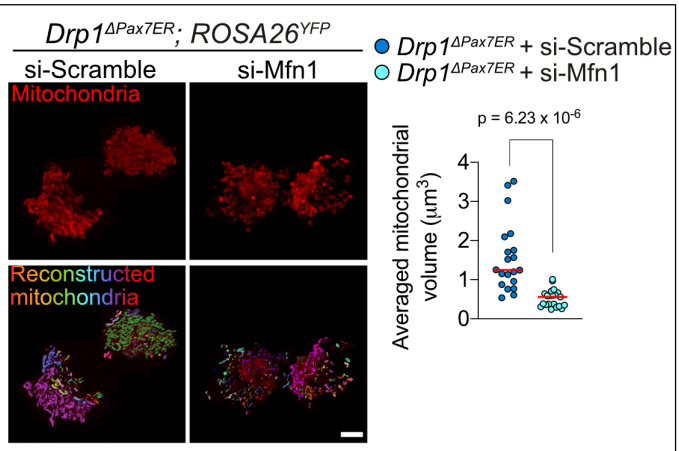

Figure 31 Representative images of mitochondrial morphological analysis in *Drp1*$^{\Delta Pax7ER}$ SCs after *in vitro* si-Scramble or si-Mfn1 treatment (left) and quantification of average mitochondrial volume in these cells (right). Mitochondria were labeled with MitoTracker CMX ROS and volume reconstruction was performed using Imaris software. Scale bar, 3 µm. Data are mean ± s.d. P values were determined by a two-tailed unpaired t-test.

To study the effects of inefficient fusion alone as well as adynamic mitochondria in SCs *in vivo* during muscle regeneration, we adapted a previously established transplantation model[64,100], whereby freshly-isolated WT or YFP^{+} *Drp1*$^{\Delta Pax7ER}$ SCs were treated *ex vivo* with si-Mfn1/si-Scramble for 3 hours, followed by transplantation into immunodeficient hosts that were previously subjected to cryo-injury (**Figure 32, 33A**). For WT, cells were labelled *ex vivo* with DiI stain prior to the transplantation procedure (**Figure 32**). *Mfn1* silencing in WT cells reduced the transplantation efficiency in WT cells (**Figure 32**), as shown by fewer DiI^{+} cells per area at 4 days post-transplantation.

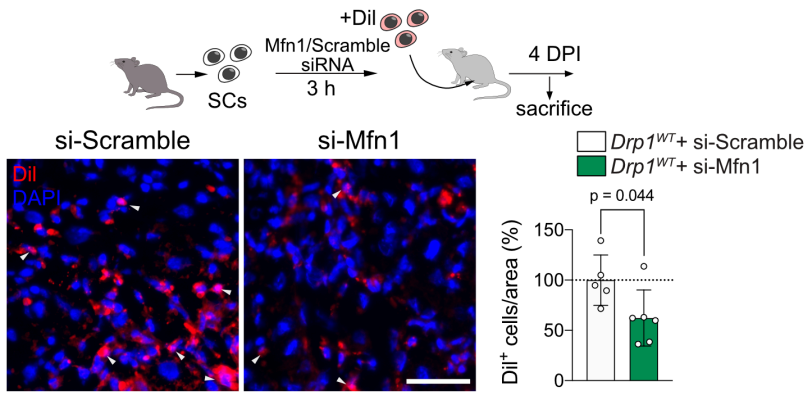

Figure 32 Schematics of transplantation of SCs from young WT mice (after *Mfn1* siRNA (or scramble) treatment (top)) into pre-injured muscles of immunodeficient mice. Representative images are shown of DiI and DAPI (lower left) and quantification (lower right) of DiI$^+$ cells per area. Data were analyzed at 4-days post-transplantation. The values presented are relative to the level of control (si-Scramble-treated group). Data are mean ± s.d. *P* values were determined by a two-tailed unpaired *t*-test. Scale bar, 25 µm.

Interestingly, si-Mfn1 treatment in YFP$^+$ *Drp1*$^{\Delta Pax7ER}$ SCs (**Figure 33A**) significantly increased the transplantation outcome of these cells, marked by increased YFP$^+$ cells per area at 4 days post transplantation (**Figure 33B**). Moreover, using a cytoplasmic YFP reporter, we compared the newly generated myofibers derived from YFP$^+$ transplanted SCs. Although the median CSA of YFP$^+$ YFP did not increase significantly upon si-Mfn1 treatment, we showed fewer fibers smaller than 100 µm^2 and increased number of larger fibers presented in the si-Mfn1-treated group (**Figure 33C**).

Based on the altered mitochondrial metabolism and mitophagy in *Drp1*$^{\Delta Pax7ER}$ SCs, we hypothesized that several possible mechanisms could underlie the rescue effect of mitochondrial adynamism in *Drp1*-deficient satellite cells: i) by reducing the large network of mitochondria, thereby decreasing the abnormal aggregation of mitochondrial nucleoids (“mito-bulbs”) (**Figure 26C**); ii) by improving mitophagy efficiency thanks to the reduced size of mitochondria; iii) by enhancing OXPHOS metabolism.

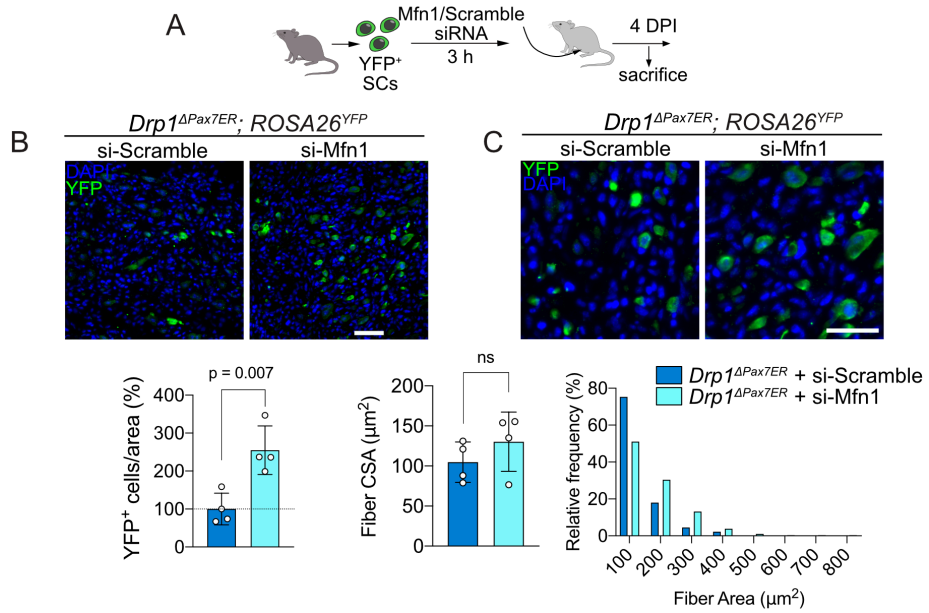

Figure 33 (**A**) Schematics of transplantation of SCs from *Drp1*$^{\Delta Pax7ER}$ mice (after Mfn1 siRNA or scramble treatment (top)) into pre-injured muscles of immunodeficient mice. (**B**) Representative images are shown of YFP and DAPI (top) and quantification (bottom) of YFP^{+} cells per area. Scale bar, 25 µm. (**C**) Representative images are shown of YFP and DAPI (top) and quantification of YFP^{+} fiber median CSA (lower left) and fiber size distribution (lower right). Data were analyzed at 4-days post-transplantation. Scale bar, 25 µm. Data are mean ± s.d. *P* values were determined by a two-tailed unpaired *t*-test.

Our results show that the aggregation of mitochondrial nucleoids observed in *Drp1*$^{\Delta Pax7ER}$ SCs was partially rescued by *Mfn1* silencing as shown by the reduced average nucleoid length and reduced number of extremely large nucleoids (length > 0.8 µm) (**Figure 34A**). Furthermore, the mitophagic flux was increased (**Figure 34B**) and the maximal respiration of *Drp1*$^{\Delta Pax7ER}$ SCs was improved upon *Mfn1* silencing (**Figure 34C**). Our results indicated that short-term forced mitochondrial adynamism improved the proliferative capacity of *Drp1*$^{\Delta Pax7ER}$ SCs, which could be due to the joint effects of reduced mitochondrial nucleoid aggregation, improved mitochondrial respiratory capacity, and enhanced mitophagy.

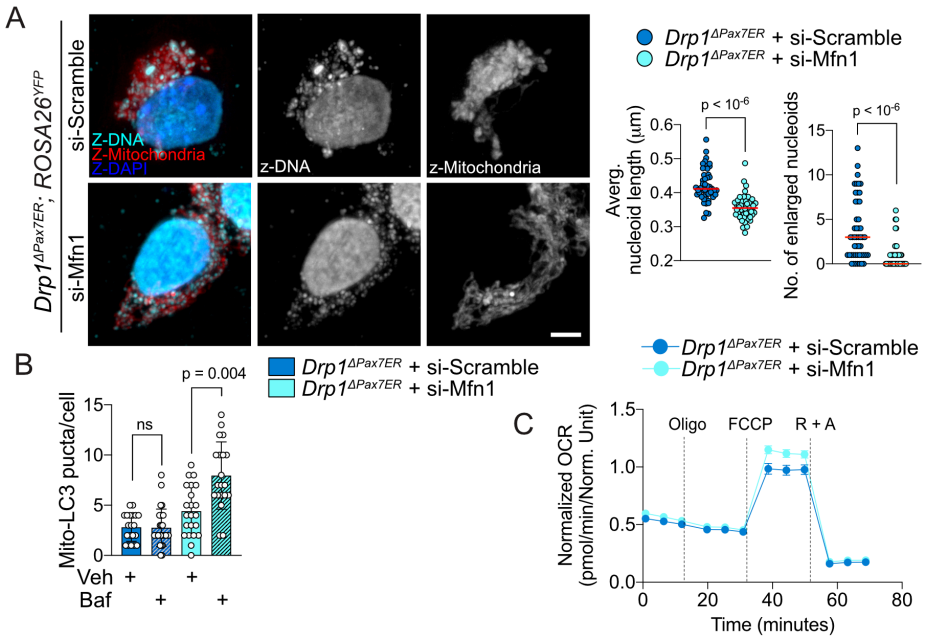

Figure 34 (**A**) Representative IF images of mitochondrial nucleoid size and mitochondria (left) as well as quantification of nucleoid size by average mitochondrial nucleoid length (middle) and number of extreme-large nucleoids (length > 0.8 µm; right) in *Drp1*$^{\Delta Pax7ER}$ proliferating myoblasts after *in vitro* si-Scramble or si-Mfn1 treatment. Mitochondria were detected with MitoTracker CMX ROS. Scale bar, 3 µm. (**B**) Quantification of LC3-mitochondria colocalization in *Drp1*$^{\Delta Pax7ER}$ SCs after *ex-vivo* si-Scramble or si-Mfn1 treatment, followed by 4 h of treatment with vehicle (Veh, DMSO) or bafilomycin A1 (Baf). (**C**) Normalized oxygen consumption rate (OCR) of *Drp1*$^{\Delta Pax7ER}$ SCs after *ex-vivo* si-Scramble or si-Mfn1 treatment at baseline and in response to oligomycin A (oligo), FCCP or rotenone plus antimycin A (R + A). Data were obtained using Seahorse XF96 and normalized to protein level using Cyquant cell proliferation assay. Data are mean ± s.d. *P* values were determined by a two-tailed unpaired *t*-test.

2.6 Restoring OXPHOS and mitophagy rescues the regenerative failure of the fission-impaired satellite cells

Based on the defective OXPHOS and mitophagy observed in *Drp1*$^{\Delta Pax7ER}$ SCs, and the mechanism underlying the rescue effects of mitochondrial adynamism, we hypothesized that the dysregulated mitochondrial oxidation and impaired mitophagy were underlying the loss of regenerative potential in *Drp1*$^{\Delta Pax7ER}$ satellite cells. To this end, we tried to boost both OXPHOS and autophagy activities in these cells and then assessed for potential functional improvement.

Dichloroacetate (DCA) is a pan-inhibitor of pyruvate dehydrogenase kinase (PDK), which phosphorylates the active form of pyruvate dehydrogenase (PDH) and converts it into the inactive form (p-PDH) (**Figure 35A**[379]) Thus, by stimulating the activity of pyruvate dehydrogenase, DCA diverts glucose metabolism from lactic fermentation to TCA cycle and mitochondrial OXPHOS by stimulating the activity of PDH via inhibiting PDKs. We confirmed that DCA treatment significantly increased OCR and mitochondrial ATP production rates in SCs (**Figure 35B**).

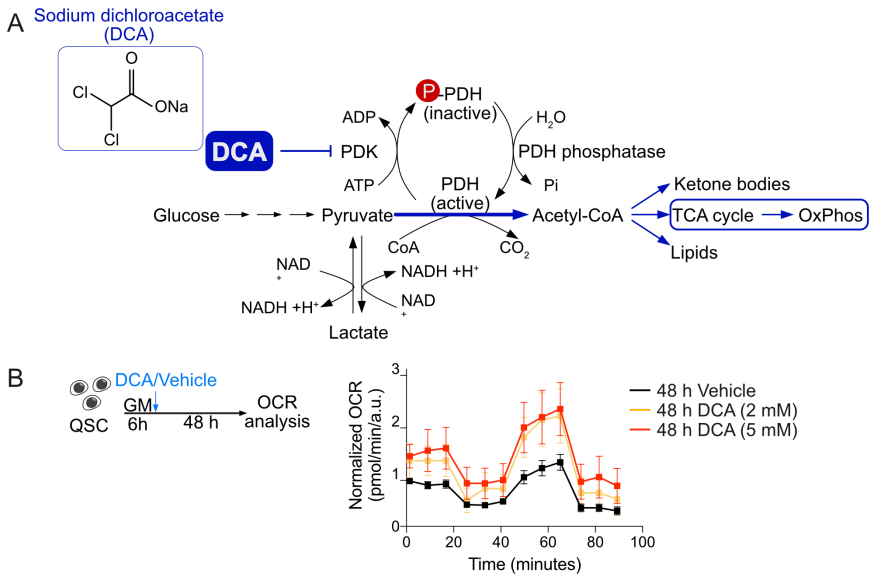

Figure 35 (**A**) Schematics showing the structure of sodium dichloroacetate (DCA) and its site of action. (**B**) Schematics of DCA *in vitro* treatment followed by Seahorse OCR analysis (left) and normalized OCR of 48-h treatment with DCA or vehicle of SCs at baseline and in response to oligomycin A (Oligo), FCCP or rotenone plus antimycin A (R + A) (right). Data were obtained using Seahorse XF96 and normalized to protein level using Cyquant cell proliferation assay.

To examine the regenerative capacity of SCs of *Drp1*$^{\Delta Pax7ER}$ mice after OXPHOS stimulation, *Drp1*$^{\Delta Pax7ER}$ mice were treated daily subcutaneously over the injured area with DCA or vehicle for four days (**Figure 36A**) followed by the analysis. DCA treatment triggered an increase in the proliferation of SCs in the injured muscles of *Drp1*$^{\Delta Pax7ER}$ mice, as revealed by the increase of proliferating SCs (KI67^{+}YFP^{+}) in

tissue cryosections (**Figure 36B**). Moreover, DCA treatment also rescued the defective muscle regeneration in *Drp1*$^{\Delta Pax7ER}$ mice, as shown by the increased number and size of newly-formed YFP^{+} (or eMHC^{+}) myofibers in muscle after injury (**Figure 36B,C**).

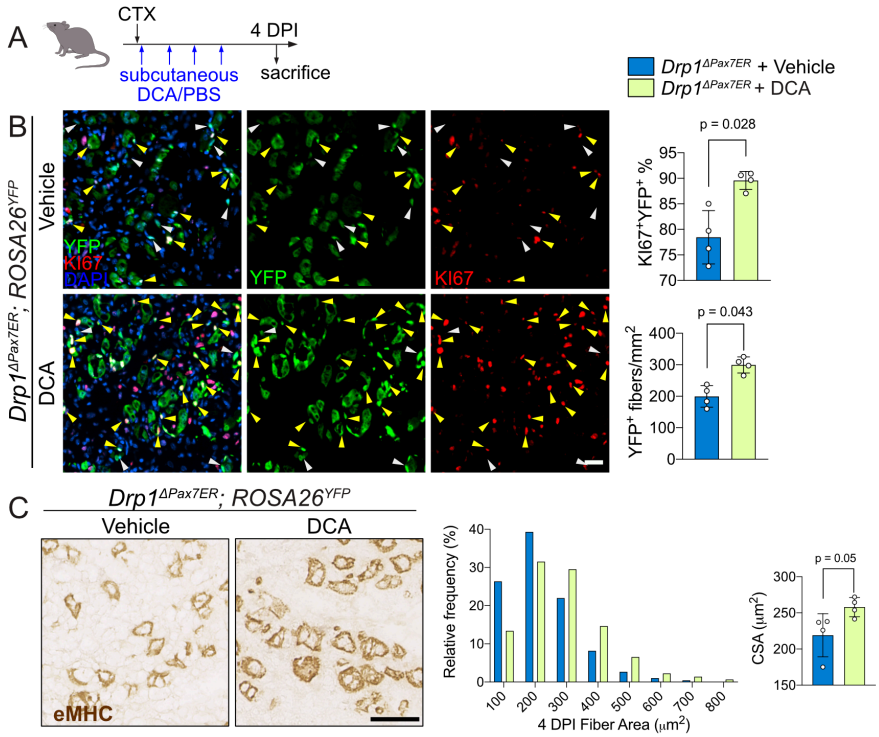

Figure 36 (**A**) Schematics of DCA and vehicle (PBS) application after CTX injury. (**B**) Representative immunofluorescent images of YFP, KI67 and DAPI staining in muscles of *Drp1*$^{\Delta Pax7ER}$ mice (+/– DCA treatment) at 4-DPI (left) and quantification of the percentage of KI67^{+} cells to total YFP^{+} cells (upper right) and the number of YFP^{+} fibers per mm^2 damaged muscle area (lower right) in *Drp1*$^{\Delta Pax7ER}$ mice (+/– DCA treatment) at 4-DPI. Scale bar, 25 μm. (**C**) Representative images of eMHC immunohistochemistry (left) and eMHC^{+} fiber size distribution (middle) and median muscle fiber CSA (right) in muscles of *Drp1*$^{\Delta Pax7ER}$ mice (+/– DCA treatment) at 4-DPI (bottom). Scale bar, 50 μm. Data are mean ± s.d. *P* values were determined by a two-tailed unpaired *t*-test.

Although treatment with DCA has provided promising results on rescuing the regenerative defects in *Drp1*$^{\Delta Pax7ER}$ mice, questions may arise due to the fact that the subcutaneous application of DCA can affect lactate metabolism in other cell types in the niche. For instance, it has been reported recently that lactate shuttling by endothelial cells in the niche facilitates the M2-like macrophage polarization, which enables

macrophages to promote proliferation of SCs and muscle regeneration[380]. To exclude possible effects of DCA on other cell types of the injured tissue, we looked into specific inhibition of *Pdk* genes in SCs using genetic approaches. Our transcriptomic data showed that *Pdk4* is the predominant isoform of *Pdk* gene expressed in satellite cells, with more than 10-times above the expression level of all the other three isoforms (**Figure 37A**) in quiescence. Interestingly, the expression of *Pdk4* dropped dramatically upon injury to merely a quarter of the quiescent level, coinciding with the observed increase in OXPHOS metabolism after quiescence exit. On the other hand, the expression of other isoforms remained low in comparison to *Pdk4* at all the analyzed time points; nevertheless, the expression of *Pdk2* and *Pdk3* showed a trend to increase upon injury, suggesting possible compensatory effects of other isoforms when *Pdk4* is downregulated. To test whether *Pdk* inhibition can improve the proliferation and regenerative capacity of *Drp1*$^{\Delta Pax7ER}$ SCs, we designed two possible schemes: i) silencing *Pdk4* gene alone with si-Pdk4 or ii) repressing the expression of all isoforms of *Pdk* genes using a pool of 4 *Pdk* siRNAs. We confirmed the efficiency of siRNA in both scenarios (**Figure 37B,C**).

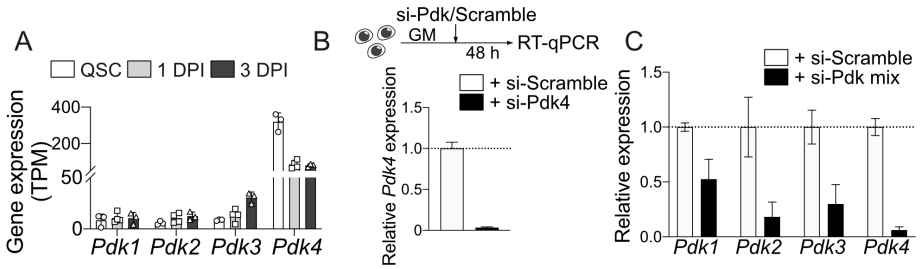

Figure 37 (**A**) Expression of the 4 *Pdk* genes in wild type QSCs 1- and 3DPI-SCs presented in transcript per million (TPM). (**B**) Schematics of siRNA treatment *in vitro* in WT cells (top) and verification of siRNA efficiency by analyzing expression of *Pdk4* gene (RT-qPCR) upon *Pdk4* siRNA (or scramble) treatment (bottom). (**C**) Verification of siRNA efficiency by analyzing expression of *Pdk1,2,3,4* genes (RT-qPCR) upon mixed *Pdk* siRNA (or scramble) treatment. Values are normalized to the control level (si-Scramble-treated group). Data are mean ± s.d. *P* values were determined by a two-tailed unpaired *t*-test.

Next, we applied similar transplantation methodology as described previously (See **Figure 32,33**). Our results show that silencing *Pdk4* gene alone was able to increase the expansion of *Drp1*$^{\Delta Pax7ER}$ SCs following transplantation (**Figure 38A,B**) but had no effect on improving YFP^{+} fiber size (**Figure 38C**) whereas silencing all isoforms of *Pdk* genes improved significantly the YFP^{+} expansion as well as the YFP^{+} fiber size (**Figure 39A-C**).

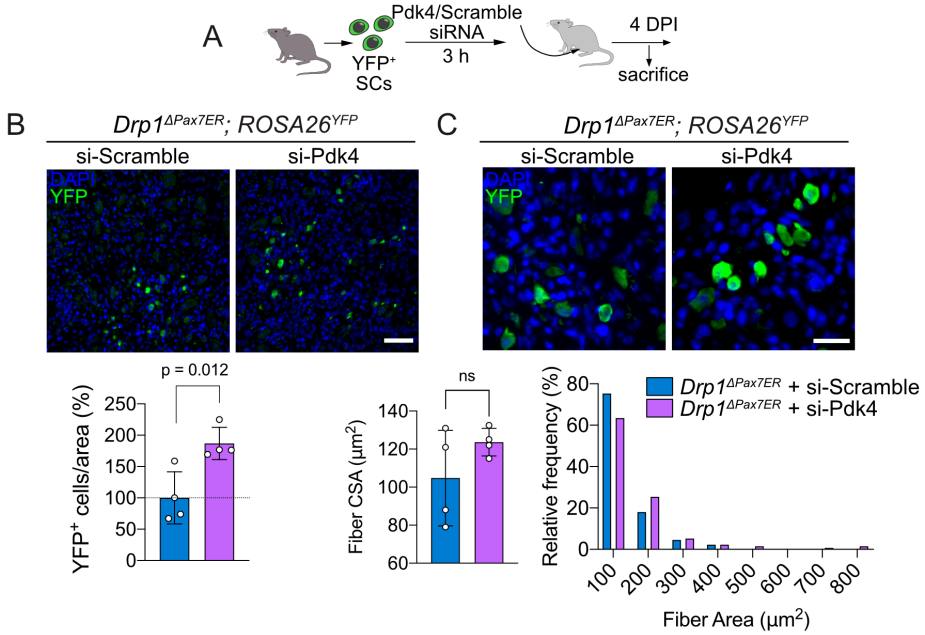

Figure 38 (**A**) Schematics of transplantation of SCs from *Drp1*$^{\Delta Pax7ER}$ mice (after Pdk4 siRNA or scramble treatment) into pre-injured muscles of immunodeficient mice. (**B**) Representative images are shown of YFP and DAPI (top) and quantification (bottom) of YFP^{+} cells per area after *Pdk4* siRNA or scramble treatment. Scale bar, 50 μm. (**C**) Representative images are shown of YFP and DAPI (top) and quantification of YFP^{+} fiber median CSA (lower left) and fiber size distribution (lower right). Scale bar, 25 μm. Data were analyzed at 4-days post-transplantation. Data are mean ± s.d. *P* values were determined by a two-tailed unpaired *t*-test.

We therefore conclude that OXPHOS enhancement by either a pharmacological (DCA treatment) or a genetic (silencing *Pdk* genes) approach restored the proliferation and regenerative capacity of *Drp1*-null satellite cells.

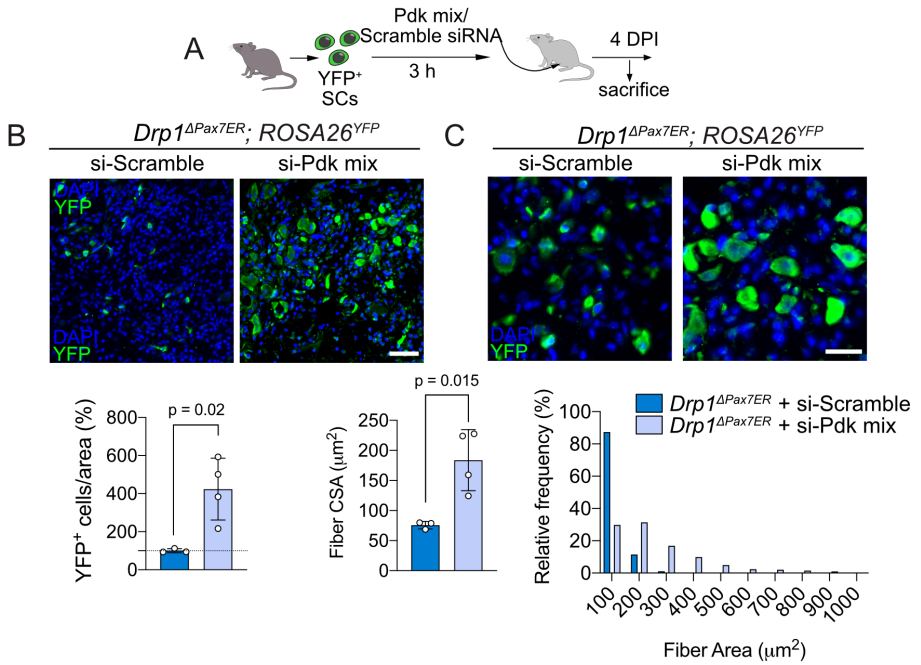

Figure 39 (**A**) Schematics of transplantation of SCs from *Drp1*$^{\Delta Pax7ER}$ mice (after mixed Pdk siRNA or scramble treatment) into pre-injured muscles of immunodeficient mice. (**B**) Representative images are shown of YFP and DAPI (top) and quantification (bottom) of YFP^{+} cells per area after Pdk siRNA or scramble treatment. Scale bar, 50 μm. (**C**) Representative images are shown of YFP and DAPI (top) and quantification of YFP^{+} fiber median CSA (lower left) and fiber size distribution (lower right). Scale bar, 25 μm. Data were analyzed at 4-days post-transplantation. Data are mean ± s.d. *P* values were determined by a two-tailed unpaired *t*-test.

Based on the defective mitophagy in *Drp1*$^{\Delta Pax7ER}$ satellite cells, we next assessed whether restoring autophagy could rescue the regenerative block of these cells. For this, we performed transplantation experiments of SCs previously subjected to rapamycin (a well-known autophagy-inducing regime[381] treatment to reactivate autophagy, as we described previously[100]. Freshly-sorted SCs from *Drp1*$^{\Delta Pax7ER}$ mice were pre-treated with rapamycin or a control vehicle, labelled with DiI, and then transplanted into pre-injured muscles of immuno-deficient recipient mice (**Figure 40**). We showed that rapamycin pre-treatment significantly restored the expansion and engraftment of these mitochondrial fission

deficient SCs after transplantation, as shown by the higher number of Dil^{+} SCs in the regenerating muscles of the recipient mice (**Figure 40**).

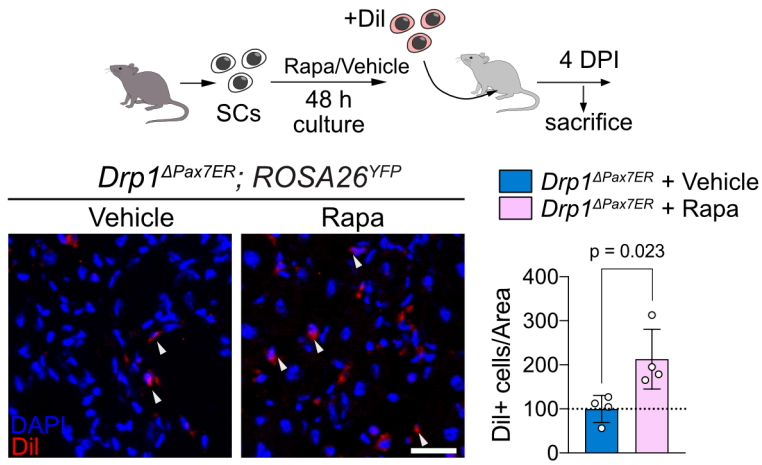

Figure 40 Schematics of transplantation of SCs from *Drp1*$^{\Delta Pax7ER}$ mice (after *ex-vivo* rapamycin (or vehicle) treatment (top)) into pre-injured muscles of immunodeficient mice. Representative images are shown of Dil and DAPI (lower left) and quantification (lower right) of Dil^{+} cells per area in muscles transplanted with *Drp1*$^{\Delta Pax7ER}$ vehicle- or rapamycin-treated satellite cells. Data were analyzed at 4-DPI post-transplantation. The values presented are relative to the level of control (si-Scramble-treated group). Scale bar, 25 µm. Data are mean ± s.d. *P* values were determined by a two-tailed unpaired *t*-test.

3. Assessing mitochondrial dynamics in aging satellite cells

3.1 Age-related loss of satellite cell function is associated with deficient mitochondrial fission at old age

Interestingly, we noticed that the functional defects of young *Drp1*-null SCs resemble those of SCs from old mice. Consistent with published data reporting reduced SC proliferation in aging[100,101], we showed reduced total SC number at 3- and 4-DPI (**Figure 41A,B**) in aging (24- to 28-month-old) mice compared to young (3- to 5-month-old) mice with less proliferation (**Figure 41B**). Previous work from our colleagues revealed that autophagy was down-regulated in aging satellite, leading to increased cellular ROS and entry into senescence cells[100]. By measuring mitochondria-ROS colocalization, we showed an upregulation of total as well as mitochondria-specific ROS in aged SCs compared to young SCs (**Figure 41C**). Consistently, aged SCs show blunted LC3 flux upon Baf treatment (**Figure 41D**) and increased accumulation of lysosomal-associated membrane protein 1 (LAMP1) proteins in the mitochondria (**Figure 41E**), indicating reduced autophagy and mitophagy. These observations correlated with defective muscle regeneration in old mice after injury (**Figure 41F**), as expected (see revision[382–384]). Our results show that both young *Drp1*$^{\Delta Pax7ER}$ young SCs and WT aged SCs have reduced mitophagy and impaired proliferation, suggesting that SCs with genetic mitochondrial-fission impairment undergo a form of premature aging.

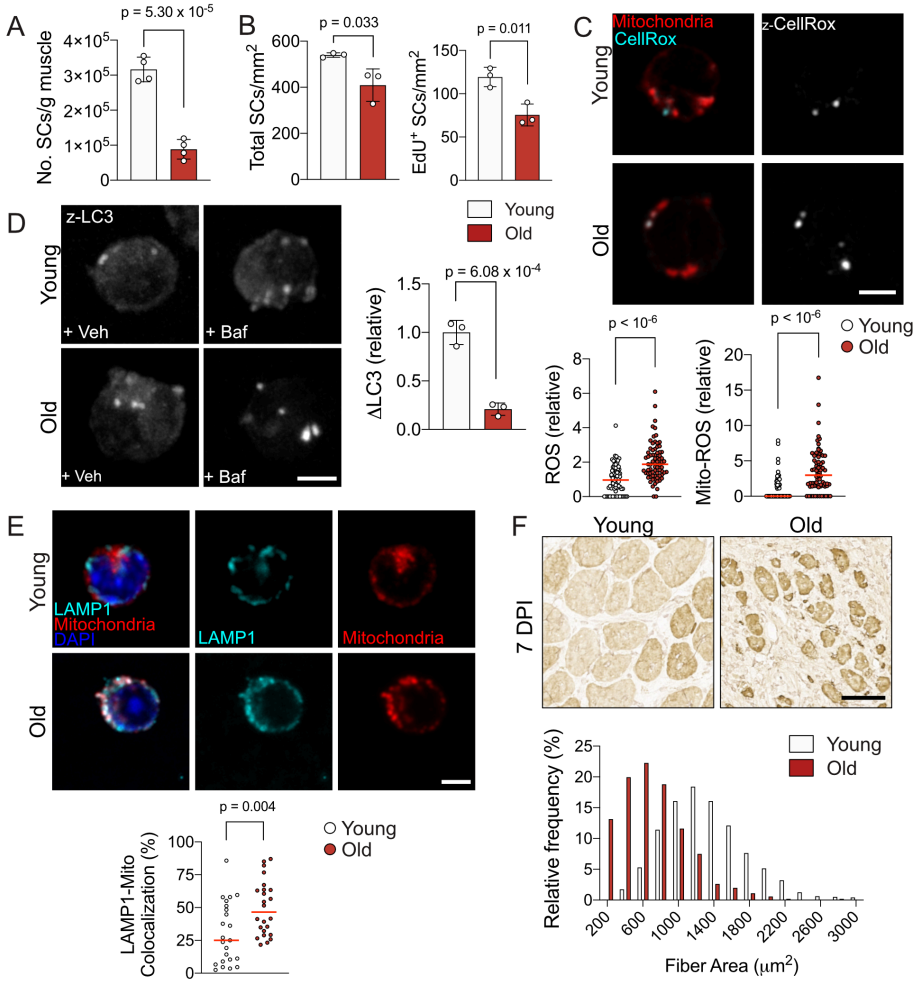

Figure 41 (**A**) Quantification of the number of 3DPI-SCs by FACS from muscles of young (2.5-3 months old) or old (24-28 months old) mice. (**B**) Quantification of the amount of total (left, PAX7$^+$ or Myogenin$^+$) or proliferating (right, PAX7$^+$EdU$^+$) 4DPI-SCs per mm^2 injured area of TA muscle from young or old mice. (**C**) Representative IF images of mitochondria (MitoTracker CMXRos Red) and ROS (CellRox Deep Red) (top) and quantification of total (lower left) and mitochondrial (lower right) ROS in young or old 3DPI-SCs. Scale bar, 3 μm. (**D**) Representative IF images of LC3 (left), and quantification of LC3 flux (ΔLC3) (right), in young or old SCs after 4 h of treatment with vehicle (veh, DMSO) or bafilomycin A (Baf). Scale bar, 3 μm. (**E**) Representative IF images of LAMP1 and mitochondria (top) and quantification of LAMP1-mitochondria colocalization (bottom). Scale bar, 3 μm. (**F**) Representative images of eMHC IHC in young and old TA muscle at 7-DPI (top), and quantification of fiber size distribution (bottom). Scale bar, 50 μm. Data are mean ± s.d. *P* values were determined by a two-tailed unpaired *t*-test..

To further investigate potential aging molecular signatures in *Drp1*$^{\Delta Pax7ER}$ SCs, we performed a comparative bioinformatic analysis of RNA-seq

data of genes and pathways altered in aging SCs (compared to young SCs) and in *Drp1*$^{\Delta Pax7ER}$ SCs (compared to *Drp1*^{WT} SCs). First, our RNA-seq data comparing young *vs* old WT SCs in quiescence or at 1-DPI or 3-DPI showed drastic alterations of pathways associated with mitochondria, cell cycle, RNA metabolism, immune response, and ECM/tissue organization (**Figure 42**).

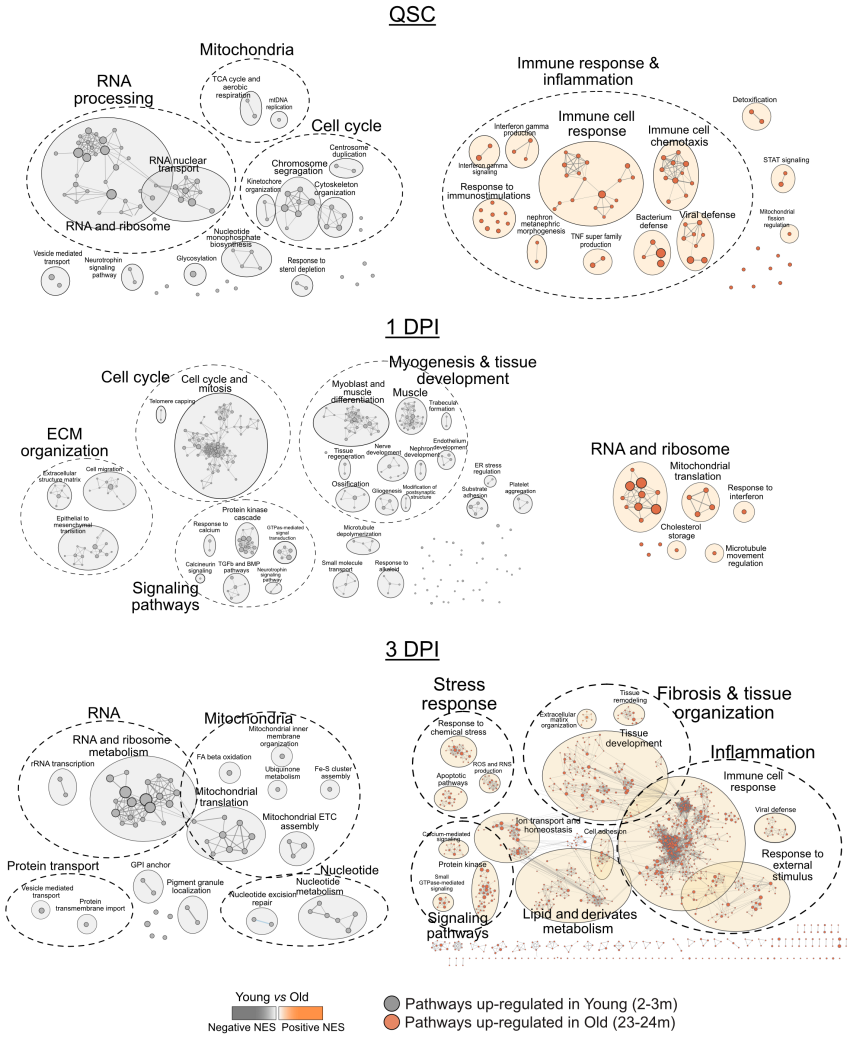

Figure 42 Enrichment map of gene sets enriched in young (grey) or old (orange) SCs obtained from resting muscle (QSCs), or injured (1-DPI or 3-DPI) limb muscles (GSEA GO_BP, FDR < 0.075). Grey node, negative NES, enriched in young; orange node, positive NES, enriched in old. Node size is proportional to the number of genes identified

in each gene set (minimum 10 genes/gene set). Clusters were automatically annotated using Autoannotate app in Cytoscape.

Comparing DE genes commonly altered in aging and *Drp1*$^{\Delta Pax7ER}$ SCs, we show that aged and *Drp1*-null SCs do not share great similarities in the quiescent stage except for 6 commonly down-regulated genes (**Figure 43**). The finding that few genes contribute significantly to the autophagy pathway coincides with our previous results that autophagy is downregulated in both aging and *Drp1*$^{\Delta Pax7ER}$ SCs (**Figure 27-29**; **Figure 41C-E**). At 1-DPI, however, striking similarities of genes and pathways were identified in aging and *Drp1*$^{\Delta Pax7ER}$ SCs related to mitosis and cell cycle (**Figure 43**), in accordance to the fact that both old and *Drp1*-null SCs showed defective proliferation post-injury (**Figure 23**; **Figure 41A,B**). Based on GSEA-Cytoscape analysis, we further detected pathways related to mitochondrial ETC and ATP synthesis that are commonly down-regulated in old and *Drp1*$^{\Delta Pax7ER}$ SCs (**Figure 44**), indicating potential common defects in mitochondrial functions. At 3-DPI, increasing number of common DE genes were detected between aging and *Drp1*-null SCs, most of which are associated with cellular metabolism. Notably, genes related to electron transport chain and mitochondrial organization pathways are commonly down-regulated in aging and *Drp1*$^{\Delta Pax7ER}$ SCs, again suggesting potential common defects in mitochondrial metabolism.

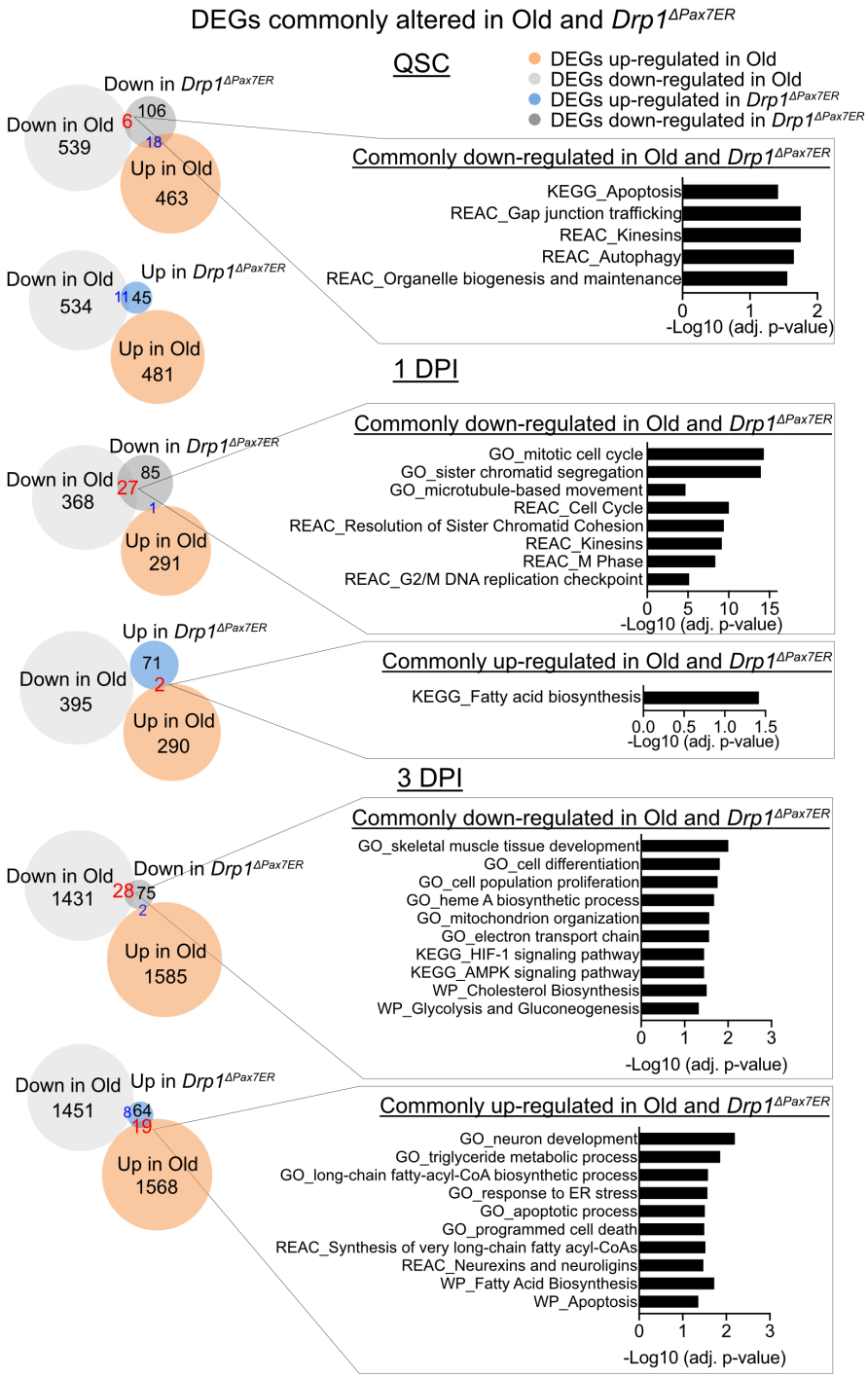

Figure 43 Commonly altered pathways detected in QSC, 1DPI- and 3DPI-SCs from young *vs* old, and $Drp1^{WT}$ *vs* $Drp1^{\Delta Pax7ER}$ dataset. Commonly altered DE genes were analyzed in g:Profiler. The top GO, REACTOME and KEGG pathways are shown. DE genes of the 2 datasets are listed in **Supplementary Table 1** and **3**.

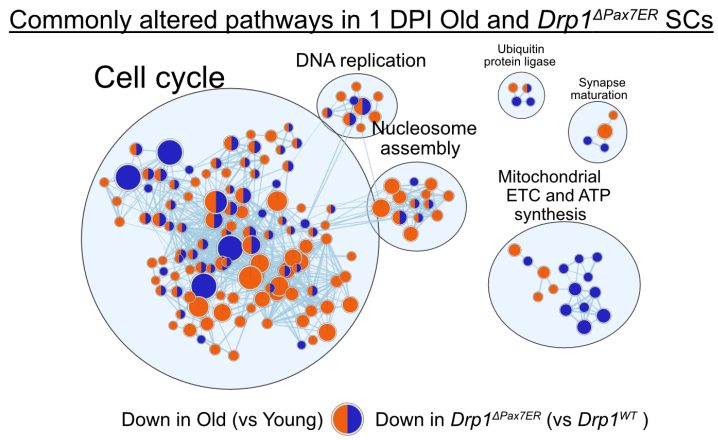

Figure 44 Enrichment map of common pathway clusters enriched in old or *Drp1*$^{\Delta Pax7ER}$ 1DPI-SCs. Orange nodes represent pathways downregulated in old *vs* young 1DPI-SCs (GSEA GO_BP, FDR < 0.25); blue nodes, pathways downregulated in *Drp1*$^{\Delta Pax7ER}$ *vs* *Drp1*^{WT} 1DPI-SCs; and nodes with 2 colors, commonly altered gene sets in old and *Drp1*$^{\Delta Pax7ER}$ 1DPI-SCs. Node size is proportional to the number of genes identified in each gene set (minimum 10 genes/gene set). Clusters were automatically annotated using Autoannotate app in Cytoscape.

Given the similarities between young *Drp1*$^{\Delta Pax7ER}$ and old WT SCs, we hypothesized that mitochondrial dynamics might also be altered with normal aging and impede stem-cell metabolic and regenerative functions. Our transcriptomic data indicated continuous increase of *Drp1* (*Dnm1l*) gene expression post injury in young WT SCs. On the other hand, while old SCs showed an initial up-regulation of *Drp1* gene at 1-DPI, the trend is blunted at 3-DPI (**Figure 45A**). Consistent with the RNA-seq results, at the peak of proliferation (3-DPI), the level of DRP1 was significantly reduced in Pax7^{+} SCs in the injured aged muscle as compared to young controls (**Figure 45B**). Moreover, both the total and the activated form of DRP1 (i.e., phosphorylated protein at serine residue 579 in mice, equivalent to residue 616 in humans (pDRP1)) were reduced in SCs from old mice as compared to those from young mice (**Figure 45C**), suggesting reduced mitochondrial fission activity with aging. Consistent with this, old SCs showed a higher number of large mitochondria with a higher average volume as compared to young

SCs (**Figure 45D**), indicating that with aging, SCs remodel their mitochondria after muscle injury, with an abnormal shift towards fusion due to the reduced DRP1 activity.

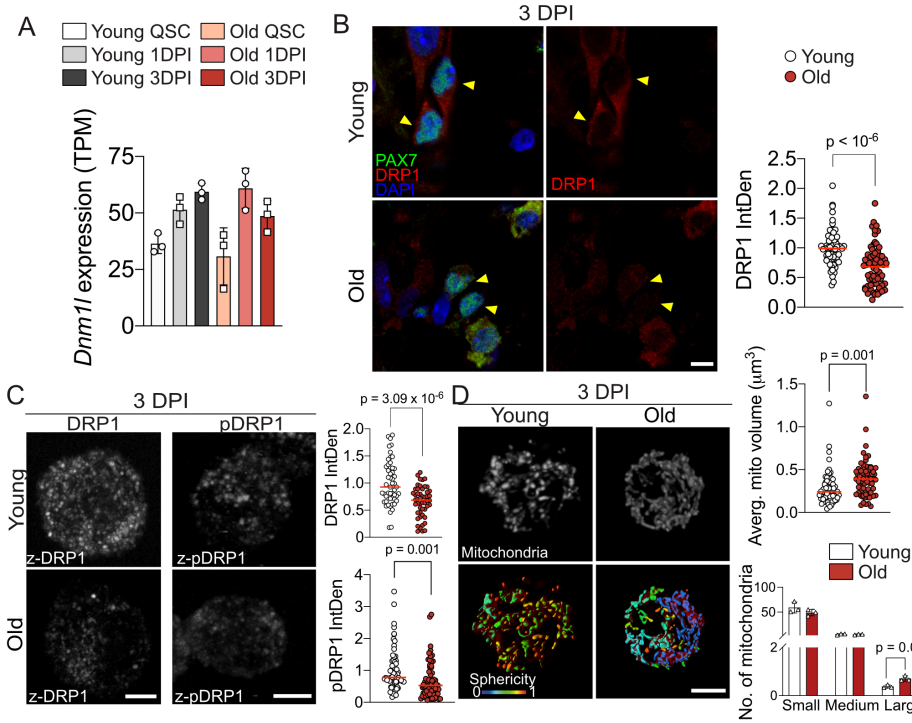

Figure 45 (**A**) Expression levels of *Dnm1l* (*Drp1*) gene in young and old QSC, 1DPI- or 3DPI-SCs. Gene expression is represented in transcript per million (TPM). (**B**) Representative IF images of PAX7, DRP1 and DAPI staining (left) and quantification of DRP1 signal (right) of young and old 3DPI TA muscles. Scale bar, 5 µm. (**C**) Representative IF images of total and active DRP1 (phosphorylated DRP1, pDRP) staining (left) and quantification of DRP1 (upper right) and pDRP (lower right) signal in 3DPI-SCs from young or old mice. Scale bar, 3 µm. (**D**) Representative images of mitochondrial morphology in 3DPI-SCs from young or old mice using MitoTracker CMXRos Red (left, upper panel) followed by deconvolution and 3D-reconstruction using Imaris software (left, lower panel) and the quantification of average mitochondrial volume in each cell (upper right) and average number of mitochondria in each cell is categorized as small (< 0.5 µm^3), medium (0.5–4 µm^3) or large (> 4 µm^3) (lower right). Data are representative of young and old SCs mitochondrial size distribution at 3-DPI. The reconstructed mitochondria were colored based on their sphericity. Scale bar, 3 µm. Data are mean ± s.d. *P* values were determined by a two-tailed unpaired *t*-test.

Of note, human SCs with high levels of active DRP1 were found in damaged areas of human muscle biopsies but not in intact muscle areas (**Figure 46A**), confirming an increased mitochondrial fission activity also in SCs of human muscle after damage/regeneration. Further, as in mice,

human myoblasts from old individuals showed reduced DRP1 activity compared to young human myoblasts (**Figure 46B,C**), consistent with their reduced proliferative potential (**Figure 46D**). Thus, fission activity is specifically induced in SCs after muscle damage, but this activity is reduced with aging in both humans and mice.

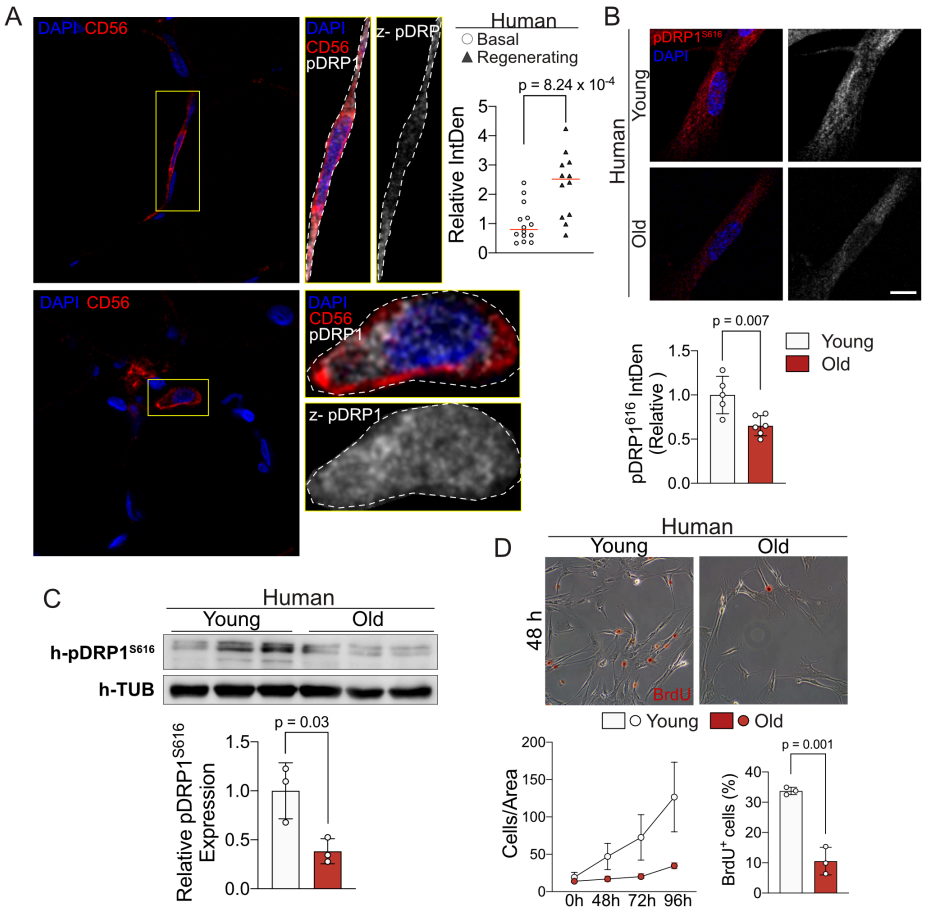

Figure 46 (**A**) Representative images (left) and quantification (right) of pDRP1^{S616} in human SCs in basal (upper panel) or regenerating (lower panel) muscle areas. Scale bar, 25 µm. (**B**) Representative images (top) and quantification (bottom) of pDRP1^{S616} intensity in human SCs isolated from young or old individuals. Scale bar, 10 µm. (**C**) Western blotting of pDRP1^{S616} in protein lysates extracted from young *vs* old human satellite cells. (**D**) Representative images of BrdU incorporation in young *vs* old human SCs after 48 h in culture (top). Cell proliferation curve is shown from 0–96 h (lower left), and BrdU incorporation is shown at 48 h after plating (lower right). Data are mean ± s.d. *P* values were determined by a two-tailed unpaired *t*-test.

Bases on these observations, we intended to study whether restoring proper mitochondrial fission in aging SCs could rescue their proliferative

phenotype. To directly increase DRP1 expression in aged satellite cells, we designed a lentiviral vector expressing DRP1 under a PGK promotor (LV-DRP1). As an experimental control for transduction efficiency, we first showed that LV-DRP1 transduction in *Drp1*$^{\Delta Pax7ER}$ SCs induced DRP1 protein expression (**Figure 47A**) and successfully restored their proliferative capacity upon transplantation (**Figure 47B**).

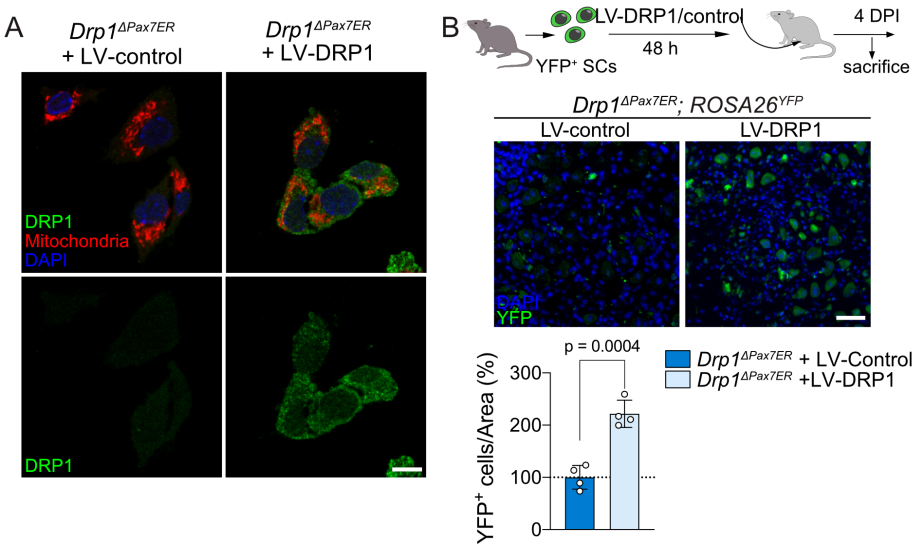

Figure 47 (**A**) Representative IF images of DRP1 staining in *Drp1*$^{\Delta Pax7ER}$ SCs with control (LV-control) or DRP1 (LV-DRP1) lentiviral vector treatment. Scale bar, 10 µm. (**B**) Schematics of transplantation of SCs from *Drp1*$^{\Delta Pax7ER}$ mice (after *ex-vivo* DRP1 or control lentiviral vector infection) (top) into pre-injured muscles of immunodeficient mice. Representative images are shown of YFP and DAPI (middle) and quantification (bottom) of YFP^{+} cells per area. Data were analyzed at 4-DPI post-transplantation. The values presented are relative to the level of control (LV-control-treated group). Scale bar, 50 µm. Data are mean ± s.d. *P* values were determined by a two-tailed unpaired *t*-test.

Importantly, we showed that re-introduction of DRP1 expression through LV-DRP1 transduction in aged SCs restored their engraftment capacity upon transplantation in regenerating muscle, as compared to LV-control-transduced aged SCs (**Figure 48**).

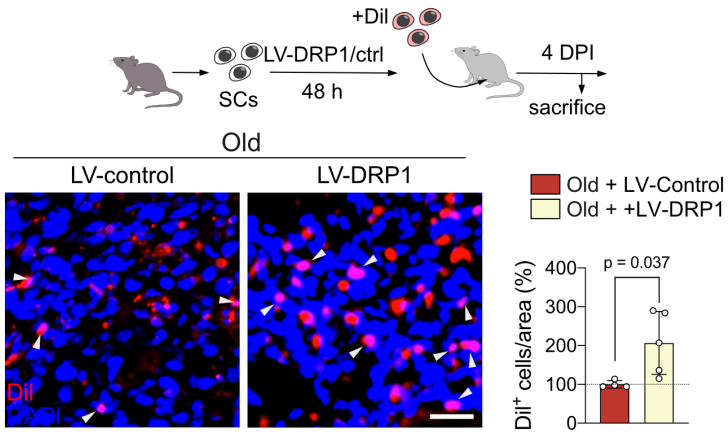

Figure 48 Schematics of transplantation of SCs from old mice (after DRP1 or control lentiviral vector infection) (top) into pre-injured muscles of immunodeficient mice. Representative images are shown of DiI and DAPI (lower left) and quantification (lower right) of DiI^+ cells per area. Data were analyzed at 4-DPI post-transplantation. The values presented are relative to the level of control (LV-control-treated group). Scale bar, 25 µm. Data are mean ± s.d. *P* values were determined by a two-tailed unpaired *t*-test.

3.2 Restoring OXPHOS and mitophagy rescues the regenerative failure of physiologically-aged satellite cells

In agreement with the downregulation of OXPHOS pathways with aging, old SCs showed reduced expression of genes involved in all ETC complexes compared to young (**Figure 49A**) and had lower mitochondrial respiration (**Figure 49B**) (see also[38]). This difference reached a maximal level in 3DPI-SCs, which also showed a significant increase in total and mitochondria-specific ROS levels at old age (**Figure 49C**). As in young *Drp1*-null SCs, mitophagy was impaired in old SCs (**Figure 41C-E**) (see also[100]). Thus, despite having less mitochondrial OXPHOS activity, old SCs accumulated more oxidative damage than young ones after injury, which could be ascribed to the impaired mitophagy and accumulation of defective mitochondria. Furthermore, after muscle damage, old SCs showed an abnormal mtDNA replication, as evidenced by the 10-fold increase in mtDNA copy number in young 3DPI-SCs but only 2- to 3-fold in aged 3DPI-SCs

(**Figure 49D**). These findings further show that the molecular, cellular and functional alterations of physiologically-aged WT SCs are comparable to those of young *Drp1*-null SCs, and reinforce the notion that i) *Drp1*-null young SCs show premature aging, and ii) the decline in mitochondrial fission activity in aging SCs may trigger their regenerative deficits.

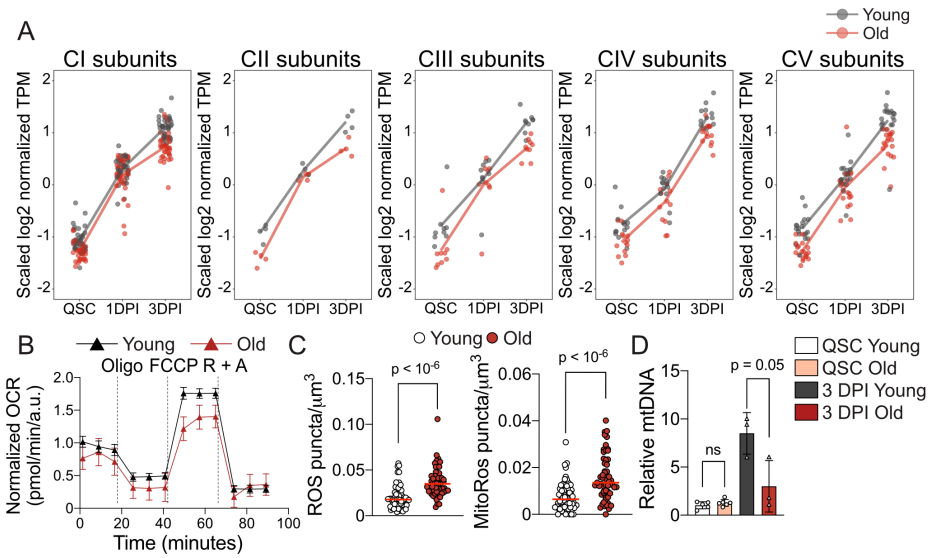

Figure 49 (**A**) Z-score analysis of ETC complex I-V genes throughout analyzed states in young or old SCs (QSCs, 1DPI-SCs or 3DPI-SCs), presented in dot graph. Detailed gene names are shown in **Supplementary Table 4**. (**B**) Normalized OCR of 48-h cultured young or old SCs at baseline and in response to oligomycin A (oligo), FCCP or rotenone plus antimycin A (R + A). Data were obtained using Seahorse XF96 and normalized to protein level using Cyquant cell proliferation assay. (**C**) Quantification of total (left) and mitochondrial (right) ROS (CellRox) in young or old 3DPI-SCs. (**D**) Quantification of mtDNA copy number relative to young QSC levels. mtDNA copy numbers were normalized to genomic DNA copy numbers, as quantified by qPCR ($2^{-\Delta CT}$). Data are mean ± s.d. *P* values were determined by a two-tailed unpaired *t*-test.

Prompted by these shared features, we searched for more hallmarks of aging in *Drp1*-null SCs and old SCs that could further explain their dysfunction, by comparing their transcriptomes with those of old tissues from various species (including humans)[385–387]. We found common downregulation of OXPHOS and cell cycle-related pathways, such as G2/M cell-cycle checkpoint and E2F and MYC signaling (**Figure 50**), consistent with multiple previously published transcriptional datasets of

aging human, rodent and killifish[385–387]. Notably, unlike old WT satellite cells, *Drp1*$^{\Delta Pax7ER}$ SCs did not reveal signs of exacerbated inflammation, another hallmark of aging (**Figure 50**). Thus, young *Drp1*-null SCs exhibited some (but not all) specific hallmarks of aging, in particular the downregulation of metabolic/mitochondrial and proliferative pathways. Old SCs did exhibit most hallmarks of aging, including age-associated inflammation (inflammaging)[388], particularly at the 3-DPI proliferative stage, which could in turn add to their reduced regenerative potential.

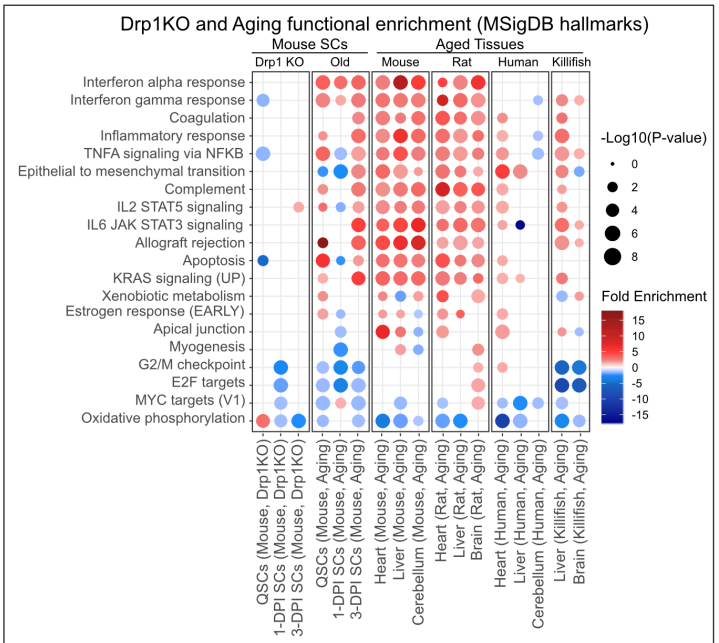

Figure 50 Dot plot comparing functional enrichments of MSigDB 5.1 hallmarks in *Drp1*$^{\Delta Pax7ER}$ and old satellite cells. MSigDB 5.1 hallmarks were tested using the minimum hypergeometric test in different tissues from aged mice, rats, humans and killifish.

Similar to young *Drp1*$^{\Delta Pax7ER}$ SCs, we hypothesized that the dysregulated mitochondrial OXPHOS and impaired mitophagy underlie the loss of regenerative potential in physiologically-aged WT satellite cells. We confirmed that the regenerative capacity of SCs in injured muscles of old WT mice was enhanced upon DCA treatment, as revealed by the higher number of SCs that incorporated EdU ($PAX7^+/EdU^+$) in tissue cryosections of aging mice (**Figure 51A**), suggesting that enhancing OXPHOS through pharmacological approach restores the proliferative capacity of aged SCs. In addition,

DCA treatment also rescued the defective muscle regeneration in aged WT mice, as shown by the increased number and size of newly-formed eMHC$^+$ myofibers after injury (**Figure 51B**).

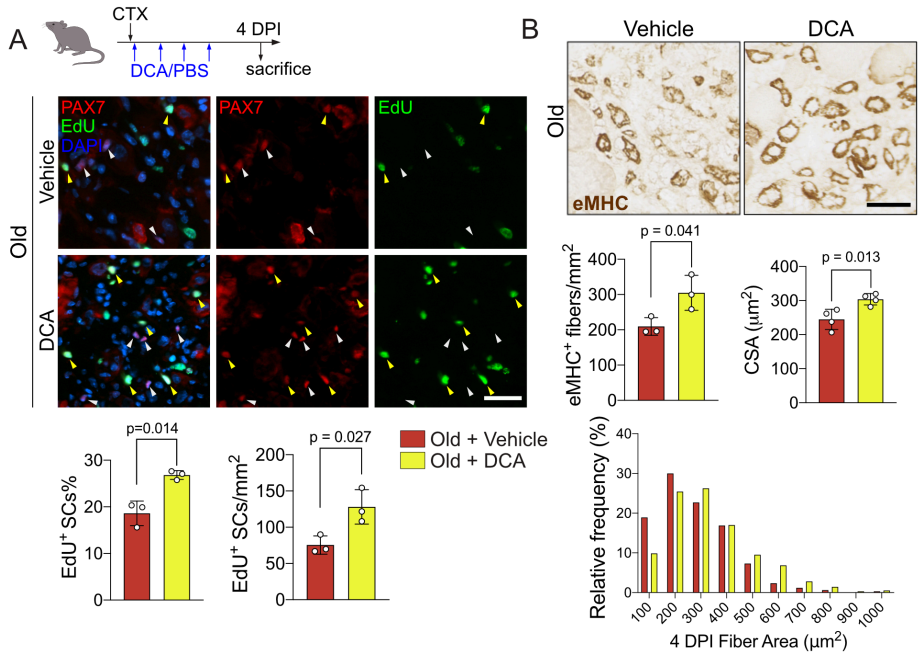

Figure 51 (**A**) Schematics of DCA/vehicle (PBS) treatment scheme in old mice (top), and representative images of PAX7, EdU, DAPI IF staining in old muscle (+/– DCA treatment) at 4-DPI (middle). Quantification of percentage of EdU$^+$ SCs (lower left) and number of EdU$^+$ SCs per mm^2 injured area and (lower right) in old muscle (+/– DCA treatment) at 4-DPI. Scale bar, 25 µm. (**B**) Representative images of eMHC IHC (top) and quantification of: number of eMHC$^+$ fibers normalized to mm^2 injured area (middle left); eMHC$^+$ fiber median CSA (middle right); fiber size distribution (bottom) in old mice +/– DCA treatment. Scale bar, 50 µm. Data are mean ± s.d. *P* values were determined by a two-tailed unpaired *t*-test.

Moreover, we show that *Pdk* gene silencing in aged SCs (by targeting all *Pdk* genes) significantly increased the engraftment of these cells upon transplantation in regenerating muscle, as evidenced by the higher number of DiI$^+$ cells in the damaged muscle area (**Figure 52**), suggesting an improved stem cell proliferation potential of old SCs when *Pdk* genes are down-regulated. Thus, OXPHOS enhancement by DCA treatment and *Pdk* silencing restores the proliferative and functional capacity of physiologically-aged SCs with impaired mitochondrial fission activity, as well as of young cells with genetic loss of mitochondrial

fission (that showed “aged-like” features) (**Figure 36-39**), thus bringing back muscle regeneration. These results demonstrate that defective mitochondrial fission causes proliferative failure in satellite cells, at least in part, by reducing functional mitochondrial metabolism; critically, enhancement of mitochondrial OXPHOS function rescues these defects.

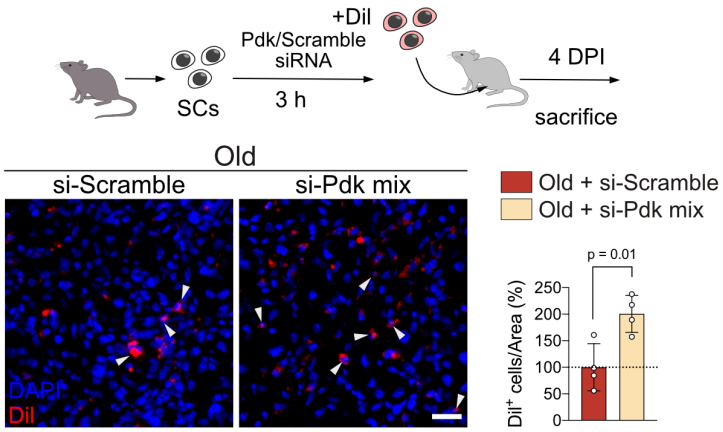

Figure 52 Schematics of transplantation of SCs from old mice (after mixed *Pdk* siRNA or scramble treatment (top)) into pre-injured muscles of immunodeficient mice. Representative IF images are shown of DiI and DAPI (lower left) and quantification (lower right) of DiI^{+} cells per area. Data were analyzed at 4-DPI post-transplantation. The values presented are relative to the level of control (si-Scramble-treated group). Scale bar, 25 μm. Data are mean ± s.d. *P* values were determined by a two-tailed unpaired *t*-test.

On the other hand, based on the defective mitophagy in old WT SCs, we investigated whether enhancing autophagy and mitophagy could rescue the regenerative defects of these cells. We found that rapamycin pre-treatment significantly restored the expansion and engraftment of old SCs after transplantation, as shown by the higher number of DiI^{+} SCs in the regenerating muscles of the recipient mice (**Figure 53A,B**). Additionally, treatment of a recently described natural mitophagy inducer urolithin A[375,389,390] also enhanced the engraftment results (**Figure 53C**) although to a lesser extent compared to rapamycin treatment. Furthermore, LV-DRP1 transduction also enhanced the mitophagic flux in aged satellite cells, as shown by the reduced LC3 accumulation in basal state (without BafA1 treatment) (**Figure 53D**),

thus suggesting that enhanced functionality of aged SCs upon DRP1 re-expression may be partially ascribed to mitophagy re-induction.

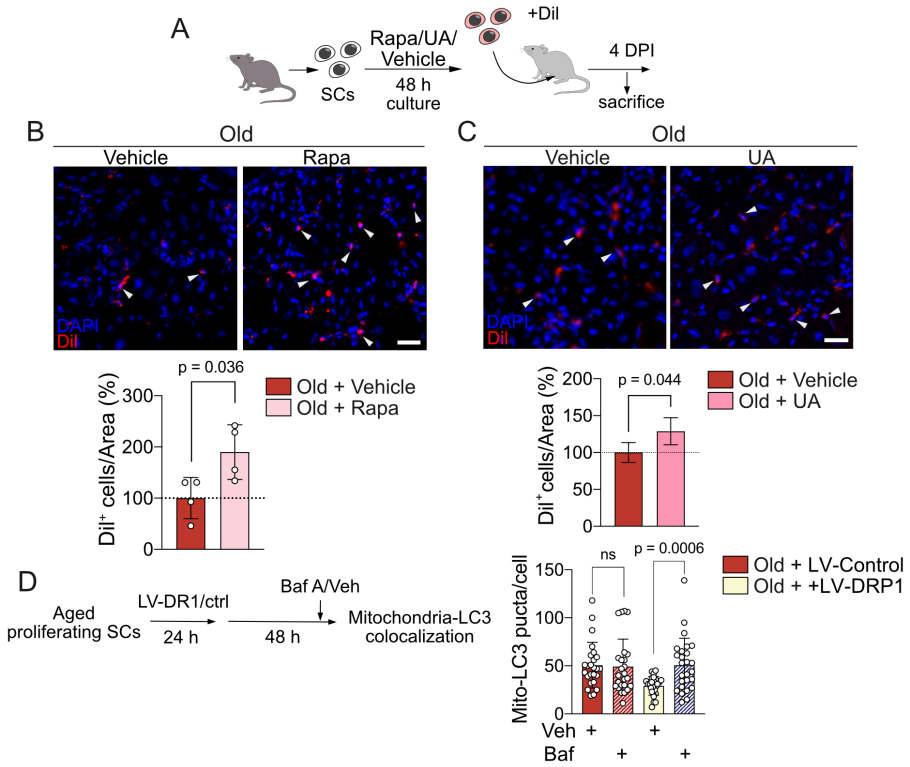

Figure 53 (**A**) Schematics of transplantation of SCs from old mice (after rapamycin, urolithin A or vehicle treatment) into pre-injured muscles of immunodeficient mice. Rapa, rapamycin; UA, urolithin A. (**B**) Representative IF images are shown of Dil and DAPI (top) and quantification (low) of Dil$^+$ cells per area in muscles transplanted with old vehicle- or rapamycin-treated satellite cells. The values presented are relative to the level of control (vehicle-treated group). Scale bar, 25 µm. (**C**) Representative IF images are shown of Dil and DAPI (top) and quantification (low) of Dil$^+$ cells per area in muscles transplanted with old vehicle- or urolithinA-treated satellite cells. The values presented are relative to the level of control (vehicle-treated group). Scale bar, 25 µm. (**D**) Schematics of *ex vivo* DPR1 or control lentiviral vector infection followed by 4 h of treatment with vehicle (veh, DMSO) or bafilomycin A1 (Baf) (left). Quantification of LC3-mitochondria colocalization in old SCs after *ex vivo* DPR1 or control lentiviral vector treatment (right). Data are mean ± s.d. *P* values were determined by a two-tailed unpaired *t*-test.

Thus, the detrimental functional consequences of impaired mitochondrial fission in satellite cells, as during aging, and even after complete ablation of the *Drp1* gene, can be positively overcome by re-inducing mitochondrial metabolism and mitophagy, as well as by direct DRP1 expression.

DISCUSSION

The results obtained in the present work can be summarized in the following concepts:

1. Satellite cells dynamically regulate their mitochondrial morphology and metabolism during their quiescence-to-proliferation transition induced by muscular injury.
2. Disturbance of mitochondrial dynamics by genetic deletion of DRP1 in satellite cells leads to impaired OXPHOS metabolism and mitophagy, thereby causing defective proliferation and muscle regeneration.
3. Altered mitochondrial dynamics during physiological aging contributes to the loss of function in satellite cells and muscle regenerative defects.
4. The proliferative defects in young *Drp1*-null or old WT satellite cells can be rescued by restoring the mitochondrial dynamics balance or by boosting OXPHOS and mitophagy in these cells.

In the first part of the project, we revealed the nature of mitochondrial morphology in three satellite states and demonstrated the metabolic changes during SC quiescence-to-proliferation transition. We showed that the mitochondrial network in SCs first undergoes increased fusion during activation, followed by increased fission during proliferation. This process is accompanied by substantial mitochondrial biogenesis and drastic increase of OXPHOS metabolism.

In the past decade, emerging studies have attempted to uncover the role of mitochondrial dynamics in stem cell fate modulation in numerous cell types[153,157,159,160]. However, due to the cell type–specific metabolic requirements and the high plasticity of the mitochondrial dynamics, conclusions drawn from one cell type are hardly applicable to another[153]. A few studies have tried to decipher the metabolism of muscle satellite cells (SCs) in quiescence and during activation/proliferation[38,103], but no conclusion has been reached due to the low number of studies and

certain discrepancies in the results. Moreover, no study to date has documented the mitochondrial morphology in SCs or how mitochondrial dynamics affect SC function.

Glycolysis is a relatively inefficient way to generate ATP compared to OXPHOS. However, glycolysis is advantageous for fast proliferating cells (such as cancer cells) due to its ability to rapidly generate ATP as well as to generate glycolytic intermediates for the biosynthesis of essential biomolecules[391,392]. It was long believed that quiescent SCs (QSCs) rely mainly on FAO, undergoing a metabolic switch from FAO to glycolysis upon activation and relying mainly on glycolysis during proliferation[103]. However, another recent study showed that injury-induced SC activation and proliferation is accompanied by simultaneous increase of glycolysis, TCA cycle and OXPHOS metabolism[38]. In addition, transcriptomic data from different labs (including ours) suggested increased expression of genes involved in glycolysis, TCA cycle. and OXPHOS[38,60,101]. In this thesis, we show increased mitochondrial biogenesis as well as mitochondrial OXPHOS during SC quiescence-to-proliferation transition. We believe that the apparent discrepancies to previous studies is due to the approaches used to induce activation. For instance, the revolutionary study by Ryall et al.[103], illustrated for the first time the metabolism of SCs in quiescence and activation. However, the activation of SCs was induced by 24-h *in vitro* culture in growth medium, which is rich in glucose and growth factors. It is therefore possible that the availability of glucose in the medium contributes to the glycolytic phenotype of the activated SCs. On the other hand, during toxin-induced injury, the myofibers undergo necrosis, accompanied by large infiltration of immune cells[36]; therefore, the environment is vastly different from the *in vitro* scenario. Indeed, it was shown by Pala et al.[38] that proliferating fetal myogenic cells rely mainly on glycolysis, suggesting different environment affect the metabolic

requirement of proliferating SCs. For this reason, our work through this thesis is mainly based on *in vivo* injury-induced muscle injury.

We show that SCs adjust their mitochondrial morphology and mitochondrial content according to the stem cell state they are (quiescence, activation or proliferation). Interestingly, unlike some cell types in which the mitochondria display a clear preference towards fused or fragmented morphology[157,159,160], we observed a balanced mitochondrial morphology in QSCs with a few medium-sized elongated mitochondria and a bunch of small fragmented mitochondria. In addition, we believe the mitochondrial morphology in QSCs is in a dynamic balance instead of a static balance based on the fact that the alteration of mitochondrial shape was observed in the inducible *Drp1* deletion model within 3 weeks after TMX induction. This equilibrium of mitochondrial fusion and fission is then transiently disturbed in the activation state (1-DPI) with enlarged mitochondrial network accompanied by increased mitochondrial volume. Since mitochondria cannot be generated *de novo*[393], it is reasonable that mitochondrial morphology displays a transient shift towards fusion during activation in which the biogenesis of mitochondria is initiating (indicated by increased mitochondrial volume and ETC gene expression). During proliferation, the enlarged mitochondria should be fragmented for the efficient distribution of mitochondrial in the daughter cells[394]. Indeed, we observed significant increase of fragmented mitochondria in 3DPI-SCs with significantly increased mitochondrial content (summarized in **Figure 54**).

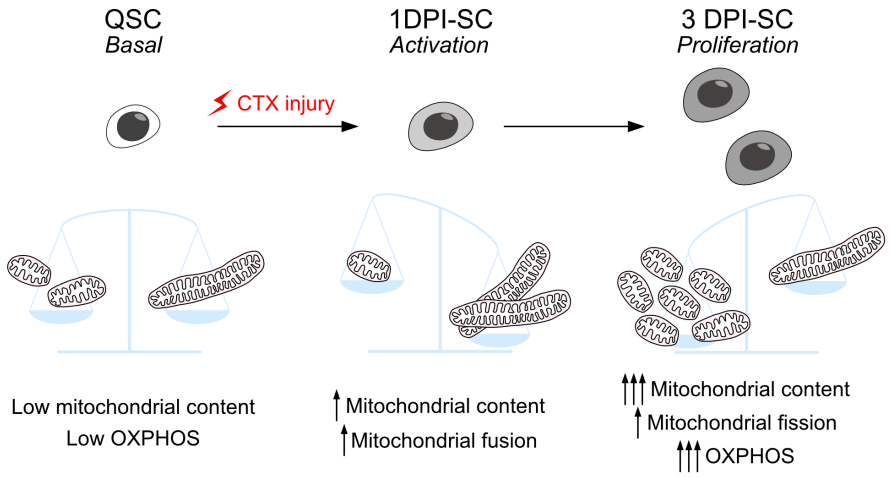

Figure 54 Schematics illustrating the mitochondrial morphology, content and OXPHOS metabolism in SCs in quiescence and upon activation and proliferation.

In addition, loss of DRP1 resulted in a "primed"-like molecular signature in quiescent *Drp1*$^{\Delta Pax7ER}$ with increased ROS, suggesting mitochondrial dynamics might also play in a role in the maintenance of SC quiescence. The morphology of mitochondria has been associated with mitochondrial metabolism and function, however, how exactly does Drp1 loss affect mitochondrial OXPHOS activity remains unclear. While numerous studies showed that *Drp1* silencing by genetic or pharmacological approaches increases mitochondrial respiration[157,205,395], others claim that *Drp1* loss or inhibition lead to impaired OXPHOS[212,373,396,397]. Our study for the first time analyzed the effect of *Drp1* deletion on the progression of stem cell *in vivo* regeneration, whereby the replicative stress, metabolic requirements, and extra cellular environment of the SCs are extremely distinct from the homeostasis (quiescence). Our RNA-seq and metabolic analysis results revealed a distinct molecular and metabolic signature of mitochondria- and cell cycle-related genes in *Drp1*$^{\Delta Pax7ER}$ SC across different states, implying that *Drp1*$^{\Delta Pax7ER}$ SCs might have uncoupled mitochondrial activity to the cellular demands.

In adult animals, SCs are maintained in quiescence with low metabolic activity and the disruption of the quiescent state is detrimental to their homeostatic and regenerative capacity[64,84,100,101]. *Drp1*$^{\Delta Pax7ER}$ QSCs showed QSC^{primed}-like molecular signature with increased OXPHOS and cell cycle gene expression as well as altered metabolic features such as increased ΔΨm and ROS compared to control SCs. It has been shown that haematopoietic stem cells (HSC) with low ΔΨm (ΔΨm^{low}) have higher capacity for multi-lineage reconstitution compared to ΔΨm^{high} HSCs, indicating that ΔΨm^{low} HSCs represent a population with more "stemness"[398]. Of note, the low ΔΨm referred to is still within a physiological range, as opposed to the extreme low ΔΨm presented in damaged mitochondria. Similarly, *Drp1*$^{\Delta Pax7ER}$ QSCs show significantly increased ΔΨm and less quiescent molecular signature compared to *Drp1*^{WT} QSCs, indicating that loss of Drp1 leads to impaired quiescence maintenance and decreased stemness in QSCs. Further, the mitophagy machinery was shown to be down-regulated in *Drp1*$^{\Delta Pax7ER}$ QSCs, possibly due to defective recruitment of Parkin. Since low ΔΨm in damaged mitochondria is responsible for Parkin recruitment[263,376–378], the high ΔΨm exhibited in *Drp1*$^{\Delta Pax7ER}$ QSCs could explain the defects in Parkin recruitment and thereby deficient mitophagy and increased ROS in these cells. Interestingly, although the role of DRP1 in ROS regulation remains poorly understood, increasing number of recent studies have revealed association of *Drp1* with antioxidative genes[399,400]. Further, mutations in mitochondrial dynamics machinery can often lead to mtDNA loss[401,402]; however, there has been conflicts in published literature about the exact impact of *Drp1* silencing on mtDNA content and mitochondrial function[212,371,373]. Our results confirmed that loss of *Drp1* gene can lead to mtDNA loss in freshly-isolated stem cells.

In the activation and proliferation states (in which mitochondrial biogenesis and cell cycle activities are expected to be increased), *Drp1*$^{\Delta Pax7ER}$ SCs showed delayed increase of mitochondria- and cell cycle-related pathway gene expression. Since the regenerative process is normally accompanied by rapid rearrangement of mitochondrial morphology and mitochondrial biogenesis, it is highly possible that loss of *Drp1* results in decreased efficiency in mitochondrial biogenesis and metabolic re-programing, which compromises the cells ability to meet the metabolic demand for entering cell cycle. Indeed, mtDNA replication was shown to be delayed in *Drp1*$^{\Delta Pax7ER}$ SCs. Furthermore, during mitosis, DRP1 is specifically phosphorylated by cyclin-dependent kinases 1 (Cdk1)/cyclin B on Ser585 and Ser616, which triggers mitochondrial fission during early cell cycle progression[188]. It is therefore possible that loss of *Drp1* could retrogradely affect cell cycle progression through interactions with key cell cycle regulators.

In mammalian cells, mtDNA genomes are packaged as a DNA-protein complex, termed a nucleoid[403]. In cultured cell lines, *Drp1* deletion generally induces enlarged mitochondrial nucleoids, which comprise of high number of mtDNA in areas of mitochondria called “Mitobulbs”[371] although the exact effects of mtDNA clustering in *Drp1*-KO cells remain to be determined. Apart from the reduced mtDNA copy number, we observed aberrant sizes and distribution of mitochondrial nucleoids in the *Drp1*$^{\Delta Pax7ER}$ SCs, which were present already in quiescence and exacerbated at 3-DPI. Previous studies have suggested that the uneven distribution of mtDNA can lead to a mosaic pattern of respiratory subunit distribution across the mitochondrial inner network and therefore cause reduced efficiency of the ETC[212,373]. A study by Ban-Ishihara et al.[371], on the other hand, showed that the mtDNA clustering did not affect respiration and had protective effects by inhibiting cytochrome c release and apoptosis. Our results indicate that *Drp1* knockout in SCs causes

mtDNA clustering, especially at 3 DPI, accompanied by impaired mitochondrial functions. Importantly, introducing mitochondrial adynamism by silencing *Mfn1* in *Drp1*-null SCs partially disassociated the aggregation of mitochondrial nucleoids and reduced the number of large “mitobulbs”. In addition, this rescue model also improved the maximal respiration and the proliferation of *Drp1*-null SCs, which supports the hypothesis that the uneven distribution of mtDNA could be responsible for the reduced ETC efficiency in *Drp1*-null SCs.

Further, it is by far unclear whether loss of DRP1 affect the organization of mitochondrial ultrastructure. It has been demonstrated that *Drp1*-dependent mitochondrial fission was essential for apoptotic cristae remodeling but *Drp1*-KO cells in homeostasis presented intact cristae structure[180]. In addition, *Drp1* deletion in the skeletal muscle did not alter the general cristae structure, however, 20% of *Drp1*-KO fibers contained mitochondria with vacuoles in the ultrastructure which could be due to degeneration of large swollen mitochondria[149]. In our study, we showed the majority of mitochondria in myo-progenitors derived from *Drp1*$^{\Delta Pax7ER}$ SCs were enlarged but did not present disorganized cristae. However, these *Drp1*-null cells displayed some mitochondria with “onion-like”, or concentric cristae, a phenotype that is generally observed in cells with mutations in mitochondrial contact site and cristae organizing system (MICOS)[404–406]. Although the role of DRP1 in cristae organization is not yet fully understood, recent studies have reported similar concentric cristae structure in cells with genetically induced elongated mitochondria[407,408], suggesting that proteins regulating mitochondrial dynamics could participate in mitochondrial ultrastructure maintenance. Further, in agreement to the phenotype in *Drp1*-null muscles, we observed disorganized cristae in a few but not all mitochondria in *Drp1*$^{\Delta Pax7ER}$ cultured myo-progenitors. Importantly, a very recent unpublished study[409] has reported very similar results using human-

derived fibroblasts from patients with mutations in DRP1. In this study, patient cells display elongated mitochondria and a lower coupling efficiency of the ETC, increased proton leak, and upregulation of glycolysis. In addition to these metabolic abnormalities, DRP1 mutant cells showed aberrant cristae structure and hyperpolarized mitochondrial membrane potential ΔΨm.

In sum, in homeostasis (quiescence state), loss of DRP1 caused elevated oxidative stress, reduced mtDNA, and increased ΔΨm with impaired autophagy, resulting in a QSC^{primed}-like molecular signature of *Drp1*-null QSCs. These changes indicated loss of stemness in $Drp1^{\Delta Pax7ER}$ SCs in homeostasis. On the other hand, upon replicative stress post-CTX injury, $Drp1^{\Delta Pax7ER}$ SCs failed to remodel their mitochondrial morphology and metabolism and thereby could not meet the cellular metabolic demand during proliferation, as indicated by insufficient increase of cell-cycle and OXPHOS genes during activation. At the time of proliferation peak in WT (e.g., at 3-DPI), $Drp1^{\Delta Pax7ER}$ SCs failed to increase their OXPHOS activity, possibly due to the joint effect of insufficient mitochondrial biogenesis and uneven mitochondrial nucleoid distribution as well as disturbed cristae organization (summarized in **Figure 55**).

Further, in addition to the modulation of mitochondrial fission, DRP1 is the main protein that regulates the fission of the peroxisome[206–208]. Indeed, *Drp1* KO SCs exhibit elongated peroxisome, forming a large network. In this work, our study was mainly focused on understanding the role of mitochondrial fission on SC function and muscle regeneration, however, future investigations of peroxisomal morphology and functions in SCs will be of our great interest.

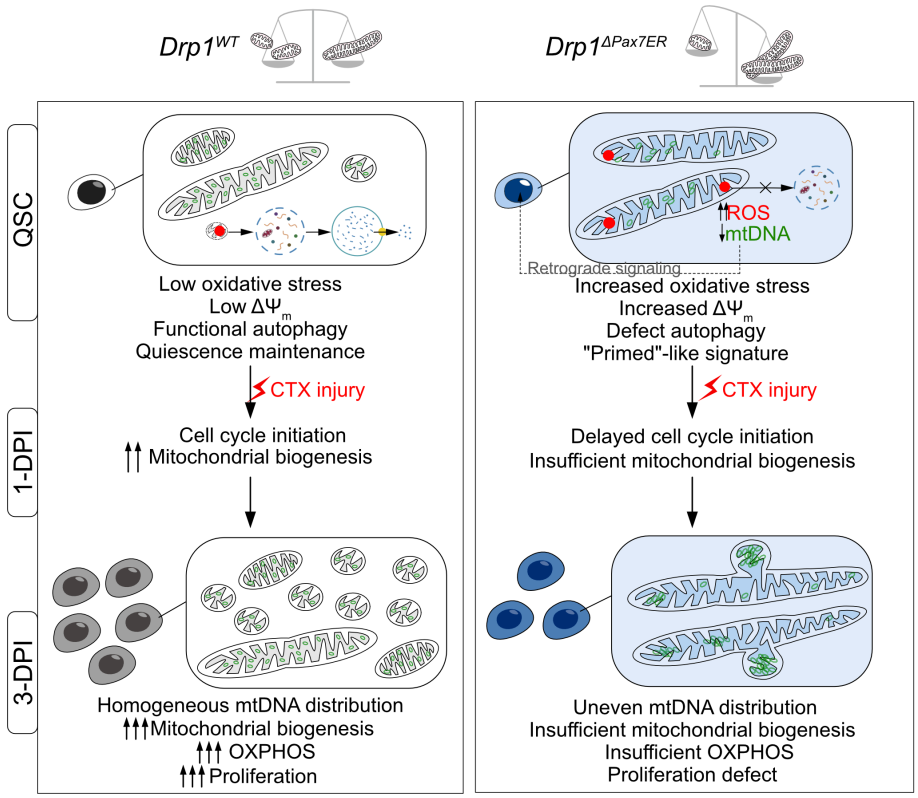

Figure 55 Schematics illustrating the alterations of mitochondrial morphology, mtDNA and metabolism in QSC, 1DPI- and 3-DPI SCs from *Drp1*$^{\Delta Pax7ER}$ *vs* *Drp1*^{WT} mice. CTX, cardiotoxin; ΔΨm, mitochondrial membrane potential; OXPHOS, oxidative phosphorylation.

The regenerative capacity of stem cells declines with aging. **In the third part**, we demonstrated the age-related SC functional decline was associated with lack of DRP1 activity, especially during the proliferation phase. We showed that young *Drp1*$^{\Delta Pax7ER}$ SCs resembled old WT SCs in several aspects: both old WT SCs and young *Drp1*$^{\Delta Pax7ER}$ SCs showed proliferative defects, reduced OXPHOS and impaired autophagy, resulting in defective muscle regeneration post injury (summarized in **Figure 56**).

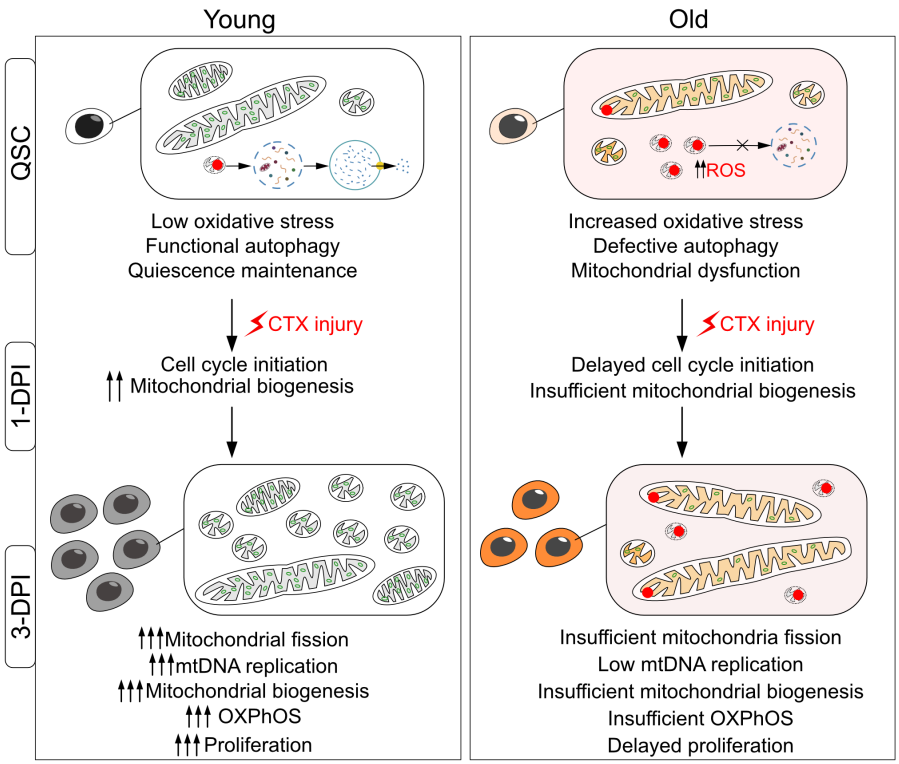

Figure 56 Schematics illustrating the alterations of mitochondrial morphology, mtDNA and metabolism in QSCs, 1DPI-SCs, and 3DPI-SCs from aged (24- to 26-month-old) *vs* young (2.5- to 3-month-old) mice.

Importantly, aged SCs showed decreased DRP1 expression and activity during the key proliferative stages, suggesting that a lack of DRP1 could contribute to the proliferative defects observed in old SCs. We showed that DRP1 re-expression in aging SCs by LV-DRP1 infection rescues the proliferative defect and improved mitophagy, indicating mitochondrial dynamics could be a potential target to achieve rejuvenation of aged stem cells. Interestingly, in elderly individuals, mitochondria have been shown to be abnormally enlarged, to be more rounded in shape, and to display matrix vacuolization and shorter cristae[410]. In accordance, another study has reported reduction of fusion and fission proteins in atrophic muscles of old sedentary people[411], confirming the loss of mitochondrial dynamics in aging. We show that

myoblast obtained from aged human donors showed reduced DRP1 activity, suggesting our findings have implications for therapies of muscle regeneration in sarcopenia.

It is also notable that aged SCs show large similarities with *Drp1*$^{\Delta Pax7ER}$ SCs during activation and proliferation, but less in quiescence. In quiescence, our transcriptomic data revealed low OXPHOS and mitochondria-related genes in aging QSCs, in accordance to previously published data[38], whereas *Drp1*$^{\Delta Pax7ER}$ QSCs showed the opposite molecular signature with regard to mitochondria-related pathways. Nevertheless, both cell types show increased ROS and reduced autophagy. One can notice that the ROS puncta in *Drp1*$^{\Delta Pax7ER}$ QSCs are located in the large mitochondrial matrix (**Figure 27A**) while in aging QSCs the ROS puncta are generally found in tiny fragmented mitochondria (**Figure 41C**), indicating that while mitophagy is impaired in both old and *Drp1*-null SCs, the detailed mechanisms might be distinct. The accumulation of ROS puncta in *Drp1*$^{\Delta Pax7ER}$ QSCs suggests that the mitophagy is impaired mainly due to inability of the cells to separate the damaged part of mitochondria from the healthy part, which is expected considering the mitochondrial fission is inhibited. On the other hand, the accumulation of ROS in fragmented mitochondria in old QSCs indicates inefficient removal of the damaged mitochondria by the autophagy machinery, consistent to our published data[100].

Finally, in both Part 2 and Part 3 of the thesis, we showed the proliferative defects observed in young *Drp1*-KO or aged WT SCs could be rescued by restoring the mitochondrial dynamics balance (either by re-expressing DRP1 or silencing *Mfn1*) or by boosting OXPHOS and mitophagy in these cells.

The regenerative capacity of the skeletal muscle replies on the proper function of its resident stem cell in homeostasis and in response to stress. Our results indicate that SCs of adult skeletal muscle require complex mitochondria physical remodeling after tissue injury to meet the regenerative demands—namely, they must rapidly expand and generate sufficient stem cell progeny to form new myofibers to replace damaged tissue.

Our data illustrate that inadequate mitochondria remodeling, either due to genetic ablation of *Drp1* or during physiological aging, compromises regeneration. We propose that mitochondrial morphology and mitochondrial function are tightly interconnected in stem cells, and that this connection is critical in the switch between quiescence and the proliferative fate of these cells during tissue repair. Our findings point to a model in which mitochondrial fission is indispensable for providing sufficient stem cell progeny during the regeneration process, by governing two major activities—mitochondrial OXPHOS and mitophagy (**Figure 57**). This fission mechanism fails with aging.

Mitochondria dynamics determine mtDNA distribution and transmission, as well the structure of the cristae and mitochondrial segregation and elimination. Therefore, its alteration directly impacts OXPHOS function at multiple levels: 1) by affecting the balanced synthesis and assembly of the mtDNA encoded proteins (reviewed in[412]; 2) by disturbing proper quality control of mitochondria by mitophagy[261]; and 3) by impacting the structural organization of the ETC[226,413]. Here we show that, unlike young/fit SCs, aged SCs (as well as those genetically impaired for mitochondrial fission) have: *i)* quantitative deregulation of most mitochondrial ETC subunits; *ii)* impaired mtDNA replication; and *iii)* an aberrant presence of nucleoids. Together, these mitochondrial

abnormalities underpin the low efficiency of the ETC and OXPHOS, which are critical functions for the stem cell proliferative phase after tissue injury. SCs were also incapable of removing damaged mitochondria when fission was impaired, due to depressed mitophagy, thus provoking excessive ROS (**Figure 57**). Thus, we propose that mitochondrial fission is a decisive factor in the switch between quiescence and the proliferative fate of muscle stem cells during regeneration, by governing metabolism and proteostasis. Restoration of mitochondrial fission (by directly increasing DRP1 levels) or provoking mitochondrial adynamism through mitochondrial fusion blockade (by silencing the fusion regulator *Mfn1*) enhanced the proliferative capacity of *Drp1*$^{\Delta Pax7ER}$ satellite cells, and aged satellite cells, correlating with enhanced mitochondrial respiratory capacity and mitophagy.

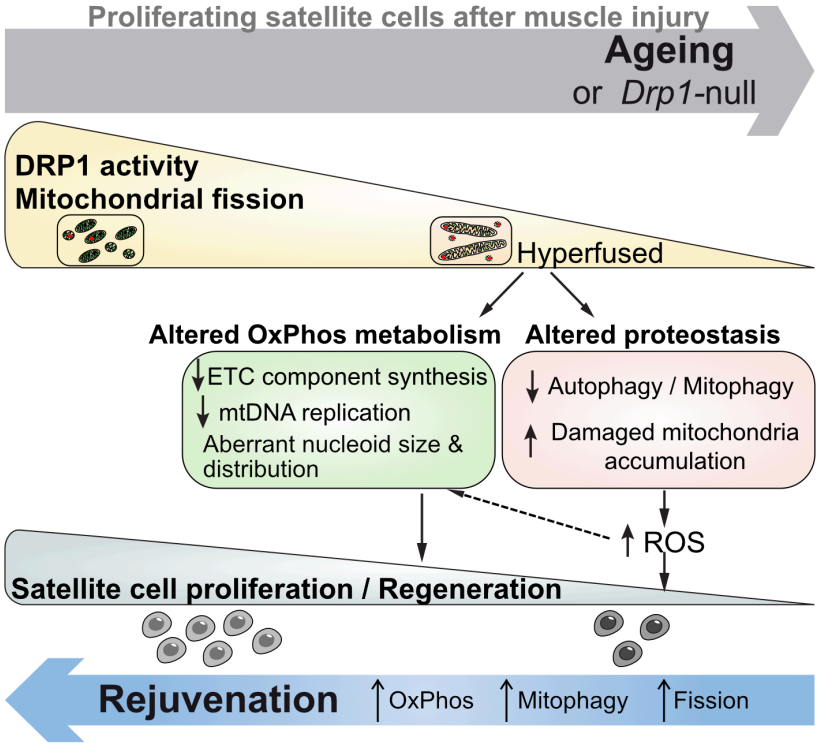

Figure 57 Summary schematic of the essential role of mitochondrial fission in regulating SC proliferation, and its decline during aging. DRP1 activity and mitochondrial fission are reduced during aging (and are lost in *Drp1*-null cells), leading to hyper-fused mitochondria in SCs during their proliferation (as after

injury or trauma). The hyperfused mitochondrial network causes i. inefficient oxidative phosphorylation (OXPHOS) metabolism (as a consequence of inadequate ETC component synthesis, reduced mtDNA replication and abnormal size and distribution of mitochondrial nucleoids) and ii. inefficient proteostasis (as a consequence of impaired autophagy and mitophagy, which in turn precipitates the accumulation of damaged mitochondria and enhances ROS levels). The combination of inefficient reprogramming towards OXPHOS metabolism and impaired proteostasis provokes faulty proliferation after injury in SCs from physiologically-aged mice (or from *Drp1*-null mice), eventually leading to defective muscle regeneration. Stimulation of OXPHOS, enhancing autophagy or increasing mitochondrial fission (by re-expressing DRP1, or by introducing mitochondrial adynamism) restore SC proliferation and muscle regeneration.

We also observed signs of reduced mitochondrial fission that correlated with deficient cell functions in human SCs from aged humans; notably, these cells also showed impaired autophagy[100]. Thus, this fission regulatory mechanism is also likely to deteriorate in human SCs during aging. Although aging-induced stem cell regenerative decline is often viewed as an irreversible process, we provide evidence that *in vivo* enhancement of either OXPHOS or autophagy rejuvenated SCs and surmounted their mitochondrial fission and functional failure. Conceptually, these findings suggest that the intrinsic hallmarks of aging in stem cells (such as the ones we identified here) can be pharmacologically manipulated to achieve better regeneration in human sarcopenia.

MATERIAL AND METHODS

Experimental Model and Subject Details

Mice

Male mice C57BL/6J (wild type, WT), C57BL/6N (WT), and the offspring of crossing *Drp1*$^{fl/fl}$ (Ishihara et al., 2009) (generously provided by L. Scorrano, University of Padova) with *Pax7*$^{CRE\text{-}ER}$*;ROSA26*^{YFP} line[414] (kindly provided by Dr. C. Keller) (*Drp1*$^{\Delta Pax7ER}$*;ROSA26*^{YFP}) were used at indicated ages. In *Drp1*$^{\Delta Pax7ER}$*;ROSA26*^{YFP} and, the deletion of the *Drp1* gene is inducible in satellite cells. The *Pax7*^{CreER} mouse line[414] was kindly provided by Dr. C. Keller). *Pax7*$^{CRE\text{-}ER}$*;ROSA26*^{YFP} or the CRE negative littermates were used as controls. In aging studies, female mice with different ages from the exact same WT lines were used. No statistical methods were used to predetermine sample size. CRE activity was induced by intraperitoneal injection (one injection per day for 4 continuous days) with 2 mg/30 g body weight tamoxifen (TMX) (Sigma; 20 mg/ml in corn oil) and experiments were carried out at 21 days post TMX induction. All animal experiments and procedures were approved by the CNIC Institutional and Regional animal research committees of the Madrid and Catalan Governments using sex-, age- and weight-matched littermate animals.

Human samples

Muscle biopsies from human adult subjects were obtained via the Tissue Banks for Research from Vall d'Hebron and Sant Joan de Deu Hospitals (Barcelona) and especially via the EU/FP7 MyoAge Consortium, and Incliva (Valencia) after electrical stimulation of muscles. Muscle biopsies were taken from the vastus lateralis muscle under local anesthesia (2% lidocaine). A portion of the muscle tissue was directly frozen in melting isopentane and stored at −80 °C. Human satellite cell-derived primary myoblasts from 3 young/adult (25 ± 4 years old) and 4 aged (75 ± 4

years old) subjects were obtained from the EU/FP7 Myoage Consortium or purchased from Cook Myosite and cultured following the provided instructions. Human cells were cultured in MyoTonic basal medium (MB-2222) with Myotonic growth supplement (MB-3333).

Method details

Muscle regeneration experiments

Mice were anesthetized with isoflurane inhalation. Regeneration of skeletal muscle was induced by intramuscular injection of cardiotoxin (CTX, Latoxan) in the tibialis anterior (TA), gastrocnemius and quadriceps muscle of the mice as previously described[415]. At the indicated times after injury, mice were euthanized and muscles were dissected, incubated in OCT and snap-frozen in isopentane/liquid nitrogen double bath, and stored at –80 °C until analysis. For GFP and YFP immunostaining samples and specially indicated samples, muscle samples were prefixed 2 h in 2% PFA at 4 ºC, washed and embedded in 30% sucrose at 4 °C and then frozen in isopentane/liquid nitrogen double bath.

SC isolation by FACS

Collected muscles were minced manually and dissociated in DMEM media containing Liberase (0.1 mg/g muscle weight) (Roche, 5401020001; 5 mg/ml) and Dispase (Sigma-Aldrich, D4693-1G) 0.3% at 37 °C for 1 h using the gentleMACS™ Octo Dissociator (Miltenyi Biotec, 130-095-937) or 1.5 h using the conventional water bath. The muscle homogenate was then filtered and pelleted. Cells were incubated in lysis buffer (eBioscience, 00-4333-57) for 5 min on ice, re-suspended in PBS with 1% goat serum (FACS buffer) and counted. PE-Cy7-conjugated anti-CD45 (Biolegend, 103114) and anti-Sca-1

(Biolegend, 108114), PE-Cy7-conjugated anti-CD31 (Biolegend 102418) antibodies were used for lineage-negative selection and Alexa Fluor 647-conjugated anti-CD34 (BD Pharmigen, 560230) and PE-conjugated anti-α7-integrin (AbLab, AB10STMW215) were used for double-positive staining of QSCs. Cells were sorted using a FACS Aria II (BD) sorter. Isolated SCs were collected in lysis buffer for RNA extraction and in FACS buffer for ATP and mtDNA quantification. For cell culture, proliferation assay and immunofluorescence (IF) staining, cells were collected in growth medium (GM) (Hams F10 (Biowest, L0140-500): DMEM 1:1 supplemented with 20% fetal bovine serum (FBS, Sigma-Aldrich F7524), 1% Penicillin/Streptomycin (P/S, Sigma-Aldrich, 15140-122) and 1% L-glutamine (Lonza, 17-605E) and bFGF (PEPROTECH, 100-18B; 0025 µg mL^{-1})).

RNA sequencing and transcriptomic analysis

RNA-seq sample and library preparation

RNA-seq of FACS sorted QSCs, 1-DPI SCs, or 3-DPI SCs from *Drp1*$^{\Delta Pax7ER}$ and *Drp1*^{WT} as well as from young and aged animals was performed as follows: 500 pg of total RNA were used for preparing RNA-seq libraries using the NEBNext Single Cell/Low Input RNA Library Prep Kit for Illumina (New England Biolabs) according to the manufacturer's instructions. Libraries were sequenced on a HiSeq 2500 (Illumina) to generate 60 bases single end reads. FastQ files for each sample were obtained using bcl2fastq 2.20 software (Illumina). NGS experiments were performed in the Genomics Unit of the CNIC.

Bulk RNA-seq Data Pre-processing

Reads were pre-processed by means of a pipeline that used FastQC (Babraham Institute), to asses read quality, and Cutadapt[416] to trim sequencing reads, eliminating Illumina adaptor remains, and to discard

reads that were shorter than 30 bp. Resulting reads were mapped against reference transcriptome GRCm38 and gene expression levels were calculated with RSEM[417], whose output includes raw count estimates, as well as Transcript per million (TPM) values. Raw count estimates (expected expression counts) were used to calculate trimmed mean of M-values (TMM)-normalized counts per million (CPM) values using Bioconductor package edgeR[418].

Differential gene expression and pathway enrichment analysis

For the differential analysis of gene expression, we considered only the genes with more than 4 CPM in all but one samples in at least one experimental group. Differentially expressed genes were found using Bioconductor package limma[419] with voom transformation, robust regression method for linear modeling and empirical Bayes statistics. Genes with adjusted p-value < 0.05 were considered for further analysis. Pathway enrichment was performed using the following protocol [420]. DE genes (adjusted p-value < 0.05) were analysed on g:Profiler platform (https://biit.cs.ut.ee/gprofiler/gost). Total annotated genes from the full reference genome were used as the reference set and a Benjamini-Hochberg FDR method was applied.

Gene Set Enrichment analysis (GSEA) and Cytoscape

Transcript per million (TPM) matrix of genes expressed with at least 1 TPM in at least three samples served as an input for GSEA software[421]. We used signal-to-noise metric to rank the genes, 1000 permutations with the gene set permutation type, and weighted enrichment statistics. Gene set sizes were chosen as 15-500 for MSigDB 7.1 Gene Ontology and Canonical Pathways[422]. Gene sets passing FDR < 0.075 threshold were subjected for further analysis. Network representation and clustering of GSEA results were performed using EnrichmentMap

(version 3.2.1) and AutoAnnotate (version 1.3.2) for Cytoscape (3.8.0) with the Jaccard coefficient set to 0.375.

Comparative enrichment analysis of senescent cells and previously published aging dataset

We used the minimum hypergeometric test implemented in R package mHG for the comparative enrichment analysis of senescent cells and previously published aging datasets: mouse, rat, African turquoise killifish, and human[385–387]. Data processing and analysis were performed as described before [385] with the following modifications: (1) differential expression analysis of SCs was performed using Bioconductor package limma, (2) to assess the differential expression for rat, killifish, and human datasets the Bioconductor DESeq2[423] 1.28.1 package version was used (instead of DESeq2 version 1.6.3), (3) both genders were analyzed for human dataset, (4) conversion to human orthologs was performed before the enrichment with MSigDB 5.1 hallmarks for all datasets except the Benayoun's mouse tissues, for which we took previously published enrichment results.

***In vivo* experiments**

SC transplantation

Cell transplants were performed as described in[424], following an adapted protocol[101].

For treatments with lentiviral particles:

Recombinant lentiviruses (LV) for expressing the human DRP1 wt form (LV-DRP1) or a fluorescent reporter gene instead as control (LV-control), were custom-designed and assembled using the Vectorbuilder platform (Vectorbuilder). Briefly, the LVs consists in a third-generation lentiviral vector backbone containing the human dynamin-like 1 (*DNML1*) ORF expression cassette driven by the human

phosphoglycerate kinase 1 (hPGK) promoter, and packed in a VSV-G envelope in our in-house viral vector facility.

For lentiviral ex-vivo transductions:

Freshly FACS-isolated SCs were collected in growth medium (GM) and plated in six-well plates coated with collagen (3 mg/ml, 40-50 k cells/well) overnight as described previously[101,424,425]. The cells were then transferred to a six-well plate coated with RetroNectin (Takara) and treated with lentiviral particles, followed by 5 min centrifuge at 50g and overnight incubation. The cells were collected the following day, centrifuged at 900g for 15 min and resuspended in PBS (1000 cells/µl). 10,000 cells were injected with a Hamilton syringe into pre-injured muscles of immunodeficient (recipient) mice. 4 days after cell injections, engrafted muscles were collected and processed for muscle histology.

For rapamycin and Urolinthin A treatment:

FACS-isolated SCs were collected in growth medium (GM), plated on collagen-treated plates and treated for 48 h with Rapamycin (100 ng/ml, LC Laboratories), Urolinthin A (Tocris, 100 µM) or vehicle (DMSO), to reactivate autophagy as described in[100]. The rapamycin/vehicle or Urolithin A/vehicle treated cells were labeled with Vybrant Dil Cell Labelling solution (Invitrogen, #V22889) according to manufacturer instructions before engraftment into as previously described [425].

For siRNA treatment:

FACS-isolated SCs were transfected with siRNA for 3h on ice and transplanted, as previously described [425]. For the transfection, Lipofectamine® 3000 reagent (Invitrogen) was applied according to the manufacturer's instructions with 20 nM of ON-TARGETplus non/targeting siRNA control pool or ON-TARGETplus siRNAs targeting the following genes:

Table 2. List of ON-TARGETplus siRNAs used in this study

Gene	Target Sequence	Gene	Target Sequence
Mfn1	CGAAAGAGAGAGAGUUUAA	*Pdk1*	CAAUACAAGUGGUUUAUGU

	CAGCAAGAAAUCAUCGAAA		CCUGUUAGAUUGGCAAAUA
	AGGGAAGACCAAAUCGAUA		UCAAUUAGAAUGCUACUCA
	GGAGAAUCCUAACGGCAGA		GGUUACGGAUUGCCCAUAU
Pdk2	CGACGUAUCGGGUCAGCUA	*Pdk3*	UAAUGUAGCUGAUGUGGUU
	GAGGACCACCGGACUCUAA		GACAAGAUCAAGAGUAAUA
	GAUCCCAACUGCAGCGUGU		AGACUUGUCCAUUAAGAUA
	GAGAAGACGUCAUUCACUU		CGAAACAUAUAGGGAGUAU
Pdk4	AGUCAGCCUUCAAACAUUA		
	GUACGUUCCUUCACACCUU		
	CGACCAGUAUUAUCUAACA		
	GAUCUGAAUCUCUACUCUA		

***In vivo* DCA treatment**

TA muscle of each mouse (old WT mice and young DRP1 mice) was injured with CTX as described in “Muscle regeneration experiments”. The same day of the injury, sodium dichloroacetate (DCA, Sigma 347795) or vehicle (saline) was administered daily subcutaneously for four days, over the lesioned area (5 mg/100 µl). For samples containing YFP+ cells (*Drp1*^{WT}*;ROSA26*^{YFP} *vs Drp1*$^{\Delta Pax7ER}$*;ROSA26*^{YFP}), at 4-days post injury, the muscles were collected and cut in two parts at the cross-section in the middle of the muscle. One part the muscle was incubated in OCT and snap-frozen in isopentane/liquid nitrogen double bath whereas the other half was cryo-preserved (fixed in 2% PFA at 4 ºC for 2 h, washed and embedded in 30% sucrose at 4 °C) and then frozen in isopentane/liquid nitrogen double bath. For samples without YFP (WT young *vs* old), the TA muscle was incubated in OCT and snap-frozen in isopentane/liquid nitrogen double bath. Samples were stored at -80 °C until analysis. All experiments requiring YFP IF were carried out using the cryo-preserved samples whereas other experiments (eMHC IHC, other IF stainings) were carried out using snap-frozen samples.

Ex vivo experiments

Cell culture

For mouse studies, SCs or proliferating progenitors were maintained in collagen-coated plates and in growth medium (GM) (Hams F10 (Biowest L0140-500): DMEM 1:1 supplemented with 20% fetal bovine serum (FBS, Sigma-Aldrich F7524), 1% Penicillin/Streptomycin (P/S, Sigma-Aldrich 15140-122) and 1% L-glutamine (Lonza 17-605E) and bFGF (PEPROTECH 100-18B; 0025 µg mL^{-1})). For coating, collagen (3 mg/ml) was added into the cell culture plate to cover the full surface, incubated at 37 °C for 30 min and removed and washed once with sterile PBS. For human cell studies, human primary myoblasts were maintained in Myotonic Basal Medium (MB-2222) supplied with MyoTonic Growth Supplement (MS-3333) and 1% P/S. Medium was changed every other day. The medium was changed every other day and the cell confluency was maintained below 50%. For *ex vivo* DCA treatment, DCA was dissolved in PBS and stored as 1M stock. For treatment, a final concentration of 2 mM and 5mM DCA was used and PBS was used as vehicle.

Transfection and infection

For the siRNA transfection, Lipofectamine® 3000 reagent (Invitrogen) was applied according to the manufacturer's instructions with 20 nM of ON-TARGETplus non/targeting siRNA control pool or ON-TARGETplus siRNAs. Lipofectamine and siRNA was first diluted in Opti-MEM™ medium separately. The siRNA prep was mixed the lipofectamine prep at 1:1 and the mixture was incubated at RT for 15 min before being added into the cell culture medium drop by drop. The total mixture volume added is 10% of the final total medium volume. For lentiviral infection, cells were maintained in six-well plates coated with collagen. The culture medium was moved and fresh medium supplied with

polybrene (1/500, provided by VectorBuilder) was added. The cells were incubated with LV-DRP1 or LV-control for 24 h, and the medium was replaced. Transduced cells were maintained in fresh medium for 3 days after lentivirus removal before further experiments were carried out to ensure expression of DRP1 protein.

Bafilomycin A and Urolithin A *in vitro* treatment for analysis of autophagy/mitophagy flux

FACS-isolated SCs were seeded into wells of 15-well chamber slide (Ibidi µ-Slide Angiogenesis 81506) coated with 0.01% poly-L-lysine (Sigma-Aldrich, P8920) at a density of 2000-3000 cells/well. Bafilomycin A (10 nM Sigma B1793) or Urolithin A (100 µ, Tocris 6762) was added to the cells for 4 h at 37 °C. At 3.5h after the treatment, 100 nM MitoTracker Red CMXRos was added to the cells and incubated for another 30 min at 37 °C in dark. After that, the cells were fixed with 4% PFA, washed with PBS and either proceed directly for immunofluorescence staining or sealed and stored in 4 °C.

Assays

Histology and immunohistochemistry (IHC) in muscle cryosections

TA muscles were snap-frozen or pre-fixed (4% PFA 2 h at 4 °C and washed in PBS), cryo-preserved and frozen in isopentane/liquid nitrogen double bath and stored at –80 °C until analysis. Hematoxylin/eosin (HE), immunochemistry and IF staining were performed in 10 µm sections. Labeling of cryosections with embryonic myosin heavy chain was performed using the peroxidase M.O.M kit staining (Vector Laboratories) according to the manufacturer's instructions. Double immunostaining was performed by sequential addition of each primary and secondary antibody using appropriate

positive and negative controls. For snap-frozen samples, sections were air dried, fixed on PFA 4%, washed on PBS and permeabilized with ice-cold methanol before antigen retrieval. For antigen retrieval, the sections were incubated in boiling citric acid (0.01 M, pH 6) for 10 min, cooled and washed with PBS. For pre-fixed TA muscles, 0.5% Triton-100 was used for permeabilization and no antigen retrieval was performed. The samples were then incubated with primary antibodies according to manufacturer's instructions after blocking for 1 h at room temperature with 5% BSA and M.O.M blocking diluted in PBS (30 min). Subsequently, the slides were washed on PBS and incubated with appropriate secondary antibodies and labeling dyes. For immunofluorescence, secondary antibodies were coupled (see below) and nuclei were stained with DAPI (Invitrogen) or SYTOX™ Green Nucleic Acid Stain (Invitrogen™, S7020). After washing, tissue sections were mounted with Fluoromount G (SouthernBiotech). Selected primary and secondary antibodies were applied.

Immunofluorescence (IF) in isolated satellite cells

SCs isolated from FACS were seeded into wells of 15-well chamber slide (Ibidi µ-Slide Angiogenesis 81506) coated with 0.01% poly-L-lysine (Sigma-Aldrich, P8920) at a density of 2000-3000 cells/well. The cells were fixed with 4% PFA, washed with PBS, permeabilized with 0.5% Triton-100 and blocked with 3% BSA for 1h at RT. Selected primary and secondary antibodies were applied.

Table 3. List of antibodies used for IF or IHC staining

Anibody	Ref	Company	Ig Type	Dilution
Citrate synthetase	ab 96600	abcam	Rabbit IgG	1:200
TOM20	ab56783	abcam	Mouse IgG1	1:100

eMHC	F1.652	DHSB	Mouse IgG1	1:1
GFP	GFP-1020	AVES Labs	Chicken IgG	1:400
KI67	ab15580	Abcam	Rabbit IgG	1:100
Laminin (AlexaFluor647)	NB300-144AF647	Novus Biological	Rabbit IgG	1:300
MYOD, M-318	sc-760	Santa Cruz	Rabbit IgG	1:20
Myogenin (M-225)	sc-576	Santa Cruz	Rabbit IgG	1:50
PAX7	sc-81648	Santa Cruz	Mouse IgG1	1:50
DRP1	#8570	Cell Signaling Technology (CST)	Rabbit IgG	1:200
pDRP1	#3455	CST	Rabbit IgG	1:200
CD56 (NCAM)	MON 9006	Monosan	Mouse IgG	1:50
dsDNA	ab27156	Abcam	Mouse IgG2a	1:500
LC3	0231-100 (clone5F10)	Nanotools	Mouse IgG1	1:50
P62	P0067	Merck	Rabbit IgG	1:150
Parkin	ab15494	Abcam	Rabbit IgG	1:100
LAMP1	sc-19992	Santa Cruz	Rat IgG2a	1:100
γ-H2AX	2577S	CST	Rabbit IgG	1:200
Cleaved Caspase-3 (Asp175)	9661T	CST	Rabbit IgG	1:200
PEX14	10594-1-AP	Proteintech	Rabbit IgG	1:200
Alexa Fluor 488 goat anti mouse	A11017	Invitrogen	Mouse IgG (H+L)	1:400
Alexa Fluor 488	A21121	Invitrogen	Mouse	1:400

goat anti mouse			IgG γ1	
Alexa Fluor 488 goat anti rabbit	A11008	Invitrogen	Rabbit IgG (H+L)	1:400
Alexa Fluor 568 goat anti mouse	A21124	Invitrogen	Mouse IgG γ1	1:400
Alexa Fluor 568 goat anti rabbit	A11036	Invitrogen	Rabbit IgG (H+L)	1:400
Alexa Fluor 568 goat anti rat	A11077	Invitrogen	Rat IgG (H+L)	1:400
Alexa Fluor 647 goat anti mouse	A21240	Invitrogen	Mouse IgG γ1	1:400
Alexa Fluor 647 goat anti rabbit	A21245	Invitrogen	Rabbit IgG (H+L)	1:400
Alexa Fluor 647 goat anti rat	A21247	Invitrogen	Rat IgG (H+L)	1:400
FITC goat anti chicken	F-1005	Aves Lab	Chicken IgY (H+L)	1:400
Alexa Fluor 568 goat anti chicken	A11041	Invitrogen	Chicken IgY (H+L)	1:400

Proliferation assays. To assess SC proliferation *in vivo*, muscles were injured by local CTX injection, and mice were administered with ethynyl-labeled deoxyuridine (EdU, Invitrogen, #A10044; 25.5 mg/kg; i.p.) 4 hours before the sacrifice at 3-4-DPI. Muscles were collected and processed for immunofluorescence staining in tissue slides or cell isolation by FACS. EdU-labeled cells were detected using the Click-iT EdU Imaging Kit (Invitrogen, #C10086). EdU-positive cells were quantified as the percentage of the total number of cells analyzed. Proliferation assays of human satellite cell-derived primary myoblasts from young and aged human individuals (see above) were cultured in MyoTonic basal medium (MB-2222) with Myotonic growth supplement (MB-3333), and cells were pulse-labeled with bromodeoxyuridine (BrdU,

Sigma-Aldrich, #B9285-1G; 1.5 µg/ml) for 1 h. BrdU-labeled cells were detected by immunostaining (Abcam, #AB6326; 1:500). Antibody binding was visualized using Vectastain Elite ABC reagent (Vector Laboratories, #PK-6100) and 3,3'-diaminobenzidine (DAB). BrdU-positive cells were quantified as the percentage of the total number of cells analyzed.

ATP content analysis

10,000 sorted SCs were pelleted and boiled in 100 mM Tris, 4 mM EDTA, pH 7.74 for 2 min. After boiling, the samples were centrifuged and the supernatant was used for analysis. ATP levels were measured using the ATP Bioluminescence Assay Kit CLS II (Roche) according to the manufacturer's instructions. Samples and ATP standard mixtures were mixed with one equal volume of luciferase and measured immediately in a luminometer (Berthold Detection Systems).

mtDNA quantification

10,000 sorted SCs were pelleted and lysed overnight in 150 µl Bradley lysis buffer (10 mM TRIS-HCL pH 7.5; 10 mM EDTA; 0.5% SDS; 10 mM NaCl in ddH_2O) with proteinase K (0.5 mg/ml) at 56 °C. Once cooled down to RT, samples were precipitated with 300 µl ice-cold EtOH/NaCl (75 mM NaCl in 100% EtOH) mix for 30 min at RT. The samples were centrifuged at 13,000 × g for 15 min and the supernatant was discarded. The pellet was washed twice with ice-cold 70% EtOH and the liquid was discarded and evaporated at RT. The dried pellet was resuspended in 20 µL TE buffer and incubated at 56 °C for 10 min. mtDNA was quantified by RT-qPCR using primers amplifying the Cytochrome b region on mtDNA (forward primer: 5´-CATTTATTATCGCGGCCCTA-3´, reverse primer: 5´-TGTTGGGTTGTTTGATCCTG-3´), relative to the β-actin region on gDNA (forward primer: 5´-CGGCTTGCGGGTGTTAAAAG-3´, reverse primer: 5´-

CGTGATCGTAGCGTCTGGTT-3´). 10 µl reaction volume for each well was loaded (1.5 µl DNA (2.5 ng/µl), 0.25 µl 10 mM forward and reverse primer, 5 µl SYBR green reagent and 3 µl H2O). $2^{*}(2^{\Delta Ct})$ was presented as the read-out (ΔCt= genomic Ct-mitochondrial Ct).

Cellular metabolic analysis

Cell oxygen consumption was measured using either the Seahorse XF96 Extracellular Flux Analyzer or the Oxygraph-2k (Oroboros).

For Seahorse analysis, SCs were sorted into GM. The cells were then placed into XF96-well plate precoated with CellTak (Corning®, 354240 following manufacturer's instructions) at a density of 80 k/well (quiescence) or 30 k/well (3-DPI). For experiments that require 48h *in vitro* treatments before Seahorse analysis (siRNA, DCA), 20 k QSCs/well or 8k proliferating myoblasts/well were seeded. After a gentle centrifuge (5 min, 50 g), the medium in each well was carefully removed without drying out the well and re-supplied carefully with 200 µl GM. For quiescence studies, the cells were maintained in hypoxia (3% O_2, 5%CO_2) for 6 h before the Seahorse analysis. XF-calibrant (Agilent, 100840) and cartridge submerged in ddH_2O were maintained in CO_2-free Seahorse incubator overnight. At the day of the Seahorse assay, GM was replaced with XF medium (phenol red-free DMEM pH = 7.4 supplied with 25 mM glucose, 1 mM sodium pyruvate and 2 mM glutamine) and incubated in CO_2-free Seahorse incubator for at least 45 min before the assay to deplete CO_2. Selected drugs were dissolved in phenol red-free DMEM (pH = 7.4 supplied with 2 mM glutamine) at desired concentrations (final working concentration 1 µM for oligomycin, FCCP, rotenone + antimycin A). The cartridge was then submerged in calibration medium and drugs were loaded into the loading ports of the cartridge (25 µl/port). After calibration, calibration plate was replaced by cell plate as indicated by the Seahorse program. At the end of the assay,

a normalization step was applied using CyQUANT™ NF Cell Proliferation Assay Kit (Invitrogen™ C35006). Briefly, assay medium was replaced with CyQUANT normalization medium applied (50 µl/well) and the plate was incubated at 37 °C for 30 min and protected from light until the end of the procedure. The emission was analyzed in a fluorometer (filters: excitation 485 nm, emission 538 nm) as an indicator for protein content.

For oxygraph analysis, proliferating primary myo-progenitors were trypsinized, counted, and resuspended in mitochondrial respiration medium (Mir05 Respiration Buffer, Oroboros Instruments). 300 k cells were loaded into the 0.5 ml chamber of the Oroboros instrument. For analyzing the respiration of each mitochondrial complex, the cells were permeabilized with 3 µg digitonin and the following substrates and inhibitors were sequentially injected: 5 mM pyruvate, 10 mM malate, 2.5 mM ADP (complex I respiration), 10 mM succinate (complex I +II respiration), 0.5 µM rotenone (complex II respiration), 2.5 µM antimycin A (non-mitochondrial respiration), 2 mM TMPD, 0.5 mM ascorbate (complex IV respiration) and 100 mM sodium azide (correction of complex IV respiration). The oxygen consumption was expressed as pmol O_2 consumed per second per ml per million of cells and the data was normalized to the level of WT cells in each experiment.

Flowcytometry assays

For mitochondrial membrane potential assay, SCs were sorted into GM and incubated with TMRM (50 nM) at 37 °C for 30 min, CCCP 5 µM was applied in parallel as quality control. TMRM signal was obtained using BD LSRFortessa™ flow cytometer. For mitochondrial content assay, SCs were resuspended in staining buffer (FACS buffer supplied with 50 µM Verapamil hydrochloride (Sigma, V4629)) and incubated with MitoTracker Red CMXRos (Invitrogen™, M7512, 100 nM) or

MitoTracker Deep Red (Invitrogen™, M22426, 100 nM) at 37 °C for 30 min. For pyronin Y assay, cells were resuspended in staining buffer and incubated in 1 µg/ml pyronin Y (abcam, ab146350) at 37 °C for 45 min and vortexed every 15 min. At the end of the staining, the cells were washed with ice-cold staining buffer and resuspended in an appropriate volume of ice-cold staining buffer. Median fluorescence intensity (M.F.I.) was calculated using FlowJo software.

CellRox assay

Freshly-sorted SCs were mixed with staining medium (5 µM CellROX Deep Red, 100 nM MitoTracker Red CMXRos) and loaded onto 15-well chamber slide (Ibidi µ-Slide Angiogenesis 81506) coated with 0.01% poly-L-lysine at a density of 2,000-3,000 cells/well. The chamber was then incubated at 37 °C for 30 min after a gentle centrifuge step (5 min, 50 xg). The staining medium was carefully removed and the cells were fixed with 3.7% formaldehyde for 15 min, washed with PBS and imaged within 24 hours. Total CellRox^{+} puncta and mitochondria-located CellRox puncta were quantified.

RT-qPCR: RNA extraction, cDNA synthesis and PCR

Total RNA was isolated from FACS-isolated SCs using PicoPure™ RNA Isolation Kit (ARN ARCTURUS®, KIT0204) and analyzed by RT-qPCR and next-generation sequencing (NGS) as described above. For experiments using proliferating myoblasts, RNA extraction was performed using RNeasy® Micro Kit (QIAGEN, 74004) according to manufacturer´s instructions. For qPCR experiments, DNase digestion was performed following manufacturer's instructions (QIAGEN). Complementary DNA (cDNA) was synthesized from 50 ng of total RNA using the First-Strand cDNA Synthesis kit (Roche). Real-time PCR reactions were performed on an AB7900-FAST-384 System using Light Cycler 480 SYBR Green I Master reaction mix (Roche Diagnostic

Corporation) and specific primers. Thermocycling conditions were as follows: initial step of 10 min at 95 °C, then 50 cycles of 15 s denaturation at 94 °C, 10 s annealing at 60 °C and 15 s extension at 72 °C. Reactions were run in triplicate and analyzed using SDS v2.3 Software. The detected threshold cycle (Ct) values were compared between samples. Transcripts of Tbp were used as the housekeeping gene.

Table 3. List of Taqman® primers used in this study

Gene	Forward primer sequence	Reverse primer sequence
Drp1	5′-GCGCTGATCCCGCGTCAT-3′	5′-CCGCACCCACTGTGTTGA-3′
Mfn1	5′-TTACTCAGTGGAACACCGCC-3′	5′-TTGGAGAGCCGCTCATTCACCT-3′
Pdk1	5′-TTACTCAGTGGAACACCGCC-3′	5′- GTTTATCCCCCGATTCAGGT -3′
Pdk2	5′-GAAGAATGCGTCCCTGGCAG-3′	5′-GGTTCCGGATGGTGACCAGG-3′
Pdk3	5′-TCCTGGACTTCGGAAGGGATA-3′	5′- GAAGGGCGGTTCAACAAGTTA-3′
Pdk4	5′-CCCGCTGTCCATGAAGCAGC-3′	5′-CCAATGTGGCTTGGGTTTCC-3′
Tbp	5′-ATCCCAAGCGATTTGCTG-3′	5′-CCTGTGCACACCATTTTTCC-3′

Western blotting

Preparation of mouse and human SC lysates and Western blotting were performed as described previously [426]. Antibodies used were anti-pDRP1^{S616} antibody produced in rabbit (CST #3455) and tubulin (Sigma T-6199).

Microscopy and image analysis

Digital image acquisition

Digital images were acquired using: (1) confocal images of isolated SCs and muscle sections were taken using an inverted Leica gated STED-3X- WLL SP8 confocal system with a HC PL Apo CS2 100×/1.4 NA or

63x/1.4 NA oil objective. (2) Low magnification IF images of muscle tissues were obtained using an inverted Nikon ECLIPSE Ti-TimeLapse microscope with a Plan Apo λ 20x/0,75 NA objective. The different fluorophores (3 to 4) were excited using the 405, 488, 568 and 633 nm excitation lines. Acquisition was performed using the LAS X 3.5.6. 21594 software. (3) Muscle tissue histology sections were digitalized using the NanoZoomer-2.0RS® from Hamamatsu and processed with the NDP.view2 software. To assess myofibre size, individual fibers were manually outlined and their cross-sectional area (CSA) was determined using Fiji software. Fluorescence intensity of selected proteins for each cell was quantified as integrated intensity (IntDen) using Fiji software. Images were composed and edited in Fiji, in which background was reduced using brightness and contrast adjustments applied to the whole image. Gaussian blur (1.0) was applied to representative confocal images using Fiji.

Mitochondrial morphology analysis

A minimum of 5,000 SCs were mixed with MitoTracker Red CMXRos (Invitrogen™, M7512, 100 nM) and plated in 15-well angiogenesis Ibidi chambers pre-coated with 0.01% poly-L-lysine. The ibidi chambers were centrifuged lightly for 2 min at 50 ×g and incubated in an incubator (37 °C, 21% O2, 5% CO2) for 45 min. After incubation, half volume of the medium was carefully removed and replaced with the same volume of 8% electron microscope standard PFA. The cells were incubated in PFA for 10 min, washed 3x by PBS and stored in PBS before IF staining. Before imaging, other IF staining could be performed and the wells were mounted with Fluoromount G. Z-stack images were acquired by Leica SP8 microscope with pinhole = 0.5A, Z = 250 nm. Acquired images were processed with Huygens professional deconvolution software. Specifically, automatic estimation of background (lowest mode, area radius = 0.7 µm) and a CMLE algorithm (maximum iterations = 30; signal

to noise ratio = 15; quality threshold = 0.05 with optimized iteration mode and automatic brick layout) was applied for the deconvolution. All images were batch-processed with the same algorithm. The processed images were then loaded to the Imaris 3 software for 3D reconstruction and surface analysis using the surface creating function.

Transmission electron microscopy

Cultured proliferating myoblasts derived from YFP^{+} *Drp1*^{WT} or *Drp1*$^{\Delta Pax7ER}$ SCs were prefixed with 1:1 volume of culture medium and fixation buffer (a mixture of 2.5% glutaraldehyde–2% paraformaldehyde in 0.1 M sodium cacodylate buffer pH 7.2 for 24 h) for 10 min at room temperature and the cells were harvested and pelleted. The pellet was then incubated at 4 °C in pure fixation buffer over night and post fixed in 1% osmium tetroxide for 1 h at 4 °C in the same buffer. The pelletets were dehydrated in an ascending series of ethanol (50%, 70%, 90% and 100%) in steps of 20 min each and transferred to propylene oxide (2 x 20 min). Afterwards, the specimens were sequentially infiltrated in EMbed 812 resin (EMS, USA). We used the sequence propylene oxide–resin 2:1, 1:1, and 1:2 throughout 24 h (8 h each). Then, samples were transferred to pure resin for 24 h. Resin blocks were then formed in silicon molds with fresh resin for 48 h at 65 °C. We placed the samples into the molds to obtain longitudinal sections of the tissues. After trimming, blocks were sectioned in an Ultracut Reicher ultramicrotome. Thin sections (50-70 nm thick) were mounted on nickel grids. After staining in aqueous 4% uranyl acetate and lead citrate, the sections were examined and photographed in a Jeol JEM 1400 electron microscope at the Servicio Centralizado de Apoyo a la Investigación (SCAI; University of Córdoba; Spain).

Genotyping of mice

For mice genotyping, the following PCR primers were used:

Drp1 flox (Fw): 5′-CAGCTGCACTGGCTTCATGACTC-3′

Drp1 flox (Rv): 5′-GTCAACTTGCCATAAACCAGAG-3′

ROSA: (R316)5′-GGAGCGGGAGAAATGGATATG-3′

(R883) 5′-AAAGTCGCTCTGAGTTGTTAT-3′

(R4982) 5′-AAGACCGCGAAGAGTTTGTC-3′

CRE pblast (Fw): 5′-CCCGCAGAACCTGAAGATGT-3′

CRE pblast (Rv): 5′-CAGCGTTTTCGTTCTGCCAA-3′

ACTIN-S: 5′-TCATCAGGTAGTCAGTGAGGTCGC-3′

ACTIN-AS: 5′-CACCACACCTTCTACAATGAGCTG-3′

Statistical analysis

The sample size of each experimental group is described in the corresponding figure caption, and all of the experiments were conducted with at least three biological replicates unless otherwise indicated. GraphPad Prism software was used for all statistical analyses except for sequencing-data analysis. Quantitative data displayed as histograms are expressed as mean ± standard deviation (represented as error bars). Results from each group were average and used to calculate descriptive statistics. Statistical significance was set at a P-value <0.05.

REFERENCES

1. Karagounis, L. G. & Hawley, J. A. Skeletal muscle: Increasing the size of the locomotor cell. *The International Journal of Biochemistry & Cell Biology* **42**, 1376–1379 (2010).
2. Frontera, W. R. & Ochala, J. Skeletal Muscle: A Brief Review of Structure and Function. *Calcified Tissue International* **96**, 183–195 (2015).
3. Janssen, I., Heymsfield, S. B., Wang, Z. & Ross, R. Skeletal muscle mass and distribution in 468 men and women aged 18–88 yr. *Journal of Applied Physiology* **89**, 81–88 (2000).
4. Zot, A. S. & Potter, J. D. Structural Aspects of Troponin-Tropomyosin Regulation of Skeletal Muscle Contraction. *Annual Review of Biophysics and Biophysical Chemistry* **16**, 535–559 (1987).
5. Laurie, G. W., Leblond, C. P. & Martin, G. R. Localization of type IV collagen, laminin, heparan sulfate proteoglycan, and fibronectin to the basal lamina of basement membranes. *Journal of Cell Biology* **95**, 340–344 (1982).
6. Schmalbruch, H. & Lewis, D. M. Dynamics of nuclei of muscle fibers and connective tissue cells in normal and denervated rat muscles. *Muscle & Nerve* **23**, 617–626 (2000).
7. Scharner, J. & Zammit, P. S. The muscle satellite cell at 50: the formative years. *Skeletal Muscle* **1**, 28 (2011).
8. Mauro, A. SATELLITE CELL OF SKELETAL MUSCLE FIBERS. *The Journal of Biophysical and Biochemical Cytology* **9**, 493–495 (1961).
9. Yin, H., Price, F. & Rudnicki, M. A. Satellite Cells and the Muscle Stem Cell Niche. *Physiological Reviews* **93**, 23–67 (2013).
10. Fuchs, E. & Blau, H. M. Tissue Stem Cells: Architects of Their Niches. *Cell Stem Cell* **27**, 532–556 (2020).
11. Brack, A. S. & Rando, T. A. Tissue-Specific Stem Cells: Lessons from the Skeletal Muscle Satellite Cell. *Cell Stem Cell* **10**, 504–514 (2012).
12. Collins, C. A. *et al.* Stem Cell Function, Self-Renewal, and Behavioral Heterogeneity of Cells from the Adult Muscle Satellite Cell Niche. *Cell* **122**, 289–301 (2005).
13. Kuang, S., Kuroda, K., le Grand, F. & Rudnicki, M. A. Asymmetric Self-Renewal and Commitment of Satellite Stem Cells in Muscle. *Cell* **129**, 999–1010 (2007).
14. Relaix, F. & Zammit, P. S. Satellite cells are essential for skeletal muscle regeneration: the cell on the edge returns centre stage. *Development* **139**, 2845–2856 (2012).
15. Sciorati, C., Rigamonti, E., Manfredi, A. A. & Rovere-Querini, P. Cell death, clearance and immunity in the skeletal muscle. *Cell Death & Differentiation* **23**, 927–937 (2016).
16. Gossler, A. & de Angelis, M. H. 6 Somitogenesis. in 225–287 (1997). doi:10.1016/S0070-2153(08)60248-3.
17. Kalcheim, C. & Ben-Yair, R. Cell rearrangements during development of the somite and its derivatives. *Current Opinion in Genetics & Development* **15**, 371–380 (2005).
18. Bentzinger, Cf., von Maltzahn, J. & Rudnicki, M. A. Extrinsic regulation of satellite cell specification. *Stem Cell Research & Therapy* **1**, 27 (2010).

19. Sambasivan, R. *et al.* Distinct Regulatory Cascades Govern Extraocular and Pharyngeal Arch Muscle Progenitor Cell Fates. *Developmental Cell* **16**, 810–821 (2009).
20. Daston, G., Lamar, E., Olivier, M. & Goulding, M. Pax-3 is necessary for migration but not differentiation of limb muscle precursors in the mouse. *Development* **122**, 1017–1027 (1996).
21. Seale, P. *et al.* Pax7 Is Required for the Specification of Myogenic Satellite Cells. *Cell* **102**, 777–786 (2000).
22. Rudnicki, M. A. *et al.* MyoD or Myf-5 is required for the formation of skeletal muscle. *Cell* **75**, 1351–1359 (1993).
23. Gros, J., Manceau, M., Thomé, V. & Marcelle, C. A common somitic origin for embryonic muscle progenitors and satellite cells. *Nature* **435**, 954–958 (2005).
24. Collins, B. C. & Kardon, G. It takes all kinds: heterogeneity among satellite cells and fibro-adipogenic progenitors during skeletal muscle regeneration. *Development* **148**, (2021).
25. Relaix, F., Rocancourt, D., Mansouri, A. & Buckingham, M. A Pax3/Pax7-dependent population of skeletal muscle progenitor cells. *Nature* **435**, 948–953 (2005).
26. Murphy, M. M., Lawson, J. A., Mathew, S. J., Hutcheson, D. A. & Kardon, G. Satellite cells, connective tissue fibroblasts and their interactions are crucial for muscle regeneration. *Development* **138**, 3625–3637 (2011).
27. Biressi, S. *et al.* Intrinsic phenotypic diversity of embryonic and fetal myoblasts is revealed by genome-wide gene expression analysis on purified cells. *Developmental Biology* **304**, 633–651 (2007).
28. Biressi, S., Molinaro, M. & Cossu, G. Cellular heterogeneity during vertebrate skeletal muscle development. *Developmental Biology* **308**, 281–293 (2007).
29. Tajbakhsh, S. Skeletal muscle stem cells in developmental versus regenerative myogenesis. *Journal of Internal Medicine* **266**, 372–389 (2009).
30. Deries, M. & Thorsteinsdóttir, S. Axial and limb muscle development: dialogue with the neighbourhood. *Cellular and Molecular Life Sciences* **73**, 4415–4431 (2016).
31. Kassar-Duchossoy, L. *et al.* Pax3/Pax7 mark a novel population of primitive myogenic cells during development. *Genes & Development* **19**, 1426–1431 (2005).
32. Buckingham, M. *et al.* The formation of skeletal muscle: from somite to limb. *Journal of Anatomy* **202**, 59–68 (2003).
33. Schienda, J. *et al.* Somitic origin of limb muscle satellite and side population cells. *Proceedings of the National Academy of Sciences* **103**, 945–950 (2006).
34. Sambasivan, R. & Tajbakhsh, S. Skeletal muscle stem cell birth and properties. *Seminars in Cell & Developmental Biology* **18**, 870–882 (2007).
35. Randolph, M. E. & Pavlath, G. K. A muscle stem cell for every muscle: variability of satellite cell biology among different muscle groups. *Frontiers in Aging Neuroscience* **7**, (2015).

36. Bentzinger, C. F., Wang, Y. X., Dumont, N. A. & Rudnicki, M. A. Cellular dynamics in the muscle satellite cell niche. *EMBO Rep* **14**, 1062–1072 (2013).
37. Schultz, E., Gibson, M. C. & Champion, T. Satellite cells are mitotically quiescent in mature mouse muscle: An EM and radioautographic study. *Journal of Experimental Zoology* **206**, 451–456 (1978).
38. Pala, F. *et al.* Distinct metabolic states govern skeletal muscle stem cell fates during prenatal and postnatal myogenesis. *Journal of Cell Science* **131**, (2018).
39. García-Prat, L., Sousa-Victor, P. & Muñoz-Cánoves, P. Proteostatic and Metabolic Control of Stemness. *Cell Stem Cell* **20**, 593–608 (2017).
40. Rocheteau, P., Gayraud-Morel, B., Siegl-Cachedenier, I., Blasco, M. A. & Tajbakhsh, S. A Subpopulation of Adult Skeletal Muscle Stem Cells Retains All Template DNA Strands after Cell Division. *Cell* **148**, 112–125 (2012).
41. Dumont, N. A., Bentzinger, C. F., Sincennes, M.-C. & Rudnicki, M. A. Satellite Cells and Skeletal Muscle Regeneration. in *Comprehensive Physiology* 1027–1059 (John Wiley & Sons, Inc., 2015). doi:10.1002/cphy.c140068.
42. Davis, R. L., Weintraub, H. & Lassar, A. B. Expression of a single transfected cDNA converts fibroblasts to myoblasts. *Cell* **51**, 987–1000 (1987).
43. Fong, A. P. & Tapscott, S. J. Skeletal muscle programming and re-programming. *Current Opinion in Genetics & Development* **23**, 568–573 (2013).
44. Tapscott, S. J. *et al.* MyoD1: A Nuclear Phosphoprotein Requiring a Myc Homology Region to Convert Fibroblasts to Myoblasts. *Science (1979)* **242**, 405–411 (1988).
45. Buckingham, M. & Relaix, F. PAX3 and PAX7 as upstream regulators of myogenesis. *Seminars in Cell & Developmental Biology* **44**, 115–125 (2015).
46. Oustanina, S., Hause, G. & Braun, T. Pax7 directs postnatal renewal and propagation of myogenic satellite cells but not their specification. *The EMBO Journal* **23**, 3430–3439 (2004).
47. Lepper, C., Conway, S. J. & Fan, C.-M. Adult satellite cells and embryonic muscle progenitors have distinct genetic requirements. *Nature* **460**, 627–631 (2009).
48. Montarras, D. *et al.* Direct Isolation of Satellite Cells for Skeletal Muscle Regeneration. *Science (1979)* **309**, 2064–2067 (2005).
49. Relaix, F. *et al.* Pax3 and Pax7 have distinct and overlapping functions in adult muscle progenitor cells. *Journal of Cell Biology* **172**, 91–102 (2006).
50. Hirai, H. *et al.* MyoD regulates apoptosis of myoblasts through microRNA-mediated down-regulation of Pax3. *Journal of Cell Biology* **191**, 347–365 (2010).
51. Tapscott, S. J. The circuitry of a master switch: Myod and the regulation of skeletal muscle gene transcription. *Development* **132**, 2685–2695 (2005).

52. Cornelison, D. D. W. & Wold, B. J. Single-Cell Analysis of Regulatory Gene Expression in Quiescent and Activated Mouse Skeletal Muscle Satellite Cells. *Developmental Biology* **191**, 270–283 (1997).
53. Crist, C. G., Montarras, D. & Buckingham, M. Muscle Satellite Cells Are Primed for Myogenesis but Maintain Quiescence with Sequestration of Myf5 mRNA Targeted by microRNA-31 in mRNP Granules. *Cell Stem Cell* **11**, 118–126 (2012).
54. Cornelison, D. D. W., Olwin, B. B., Rudnicki, M. A. & Wold, B. J. MyoD−/− Satellite Cells in Single-Fiber Culture Are Differentiation Defective and MRF4 Deficient. *Developmental Biology* **224**, 122–137 (2000).
55. Zammit, P. S. *et al.* Muscle satellite cells adopt divergent fates. *Journal of Cell Biology* **166**, 347–357 (2004).
56. Olguin, H. C. & Olwin, B. B. Pax-7 up-regulation inhibits myogenesis and cell cycle progression in satellite cells: a potential mechanism for self-renewal. *Developmental Biology* **275**, 375–388 (2004).
57. Gromova, A., Tierney, M. & Sacco, A. FACS-based Satellite Cell Isolation From Mouse Hind Limb Muscles. *BIO-PROTOCOL* **5**, (2015).
58. Conboy, M. J., Cerletti, M., Wagers, A. J. & Conboy, I. M. Immuno-Analysis and FACS Sorting of Adult Muscle Fiber-Associated Stem/Precursor Cells. in 165–173 (2010). doi:10.1007/978-1-60761-063-2_11.
59. Chapman, M. R. *et al.* Sorting single satellite cells from individual myofibers reveals heterogeneity in cell-surface markers and myogenic capacity. *Integrative Biology* **5**, 692–702 (2013).
60. Liu, L., Cheung, T. H., Charville, G. W. & Rando, T. A. Isolation of skeletal muscle stem cells by fluorescence-activated cell sorting. *Nature Protocols* **10**, 1612–1624 (2015).
61. Ieronimakis, N. *et al.* Absence of CD34 on Murine Skeletal Muscle Satellite Cells Marks a Reversible State of Activation during Acute Injury. *PLoS ONE* **5**, e10920 (2010).
62. Cornelison, D. D. W., Filla, M. S., Stanley, H. M., Rapraeger, A. C. & Olwin, B. B. Syndecan-3 and Syndecan-4 Specifically Mark Skeletal Muscle Satellite Cells and Are Implicated in Satellite Cell Maintenance and Muscle Regeneration. *Developmental Biology* **239**, 79–94 (2001).
63. Fukada, S. *et al.* Purification and cell-surface marker characterization of quiescent satellite cells from murine skeletal muscle by a novel monoclonal antibody. *Experimental Cell Research* **296**, 245–255 (2004).
64. García-Prat, L. *et al.* FoxO maintains a genuine muscle stem-cell quiescent state until geriatric age. *Nature Cell Biology* **22**, 1307–1318 (2020).
65. Maesner, C. C., Almada, A. E. & Wagers, A. J. Established cell surface markers efficiently isolate highly overlapping populations of skeletal muscle satellite cells by fluorescence-activated cell sorting. *Skeletal Muscle* **6**, 35 (2016).
66. Laterza, O. F. *et al.* Plasma MicroRNAs as Sensitive and Specific Biomarkers of Tissue Injury. *Clinical Chemistry* **55**, 1977–1983 (2009).
67. Brigitte, M. *et al.* Muscle resident macrophages control the immune cell reaction in a mouse model of notexin-induced myoinjury. *Arthritis & Rheumatism* **62**, 268–279 (2010).

68. Wang, Y. & Thorlacius, H. Mast cell-derived tumour necrosis factor- *α* mediates macrophage inflammatory protein-2-induced recruitment of neutrophils in mice. *British Journal of Pharmacology* **145**, 1062–1068 (2005).
69. Scapini, P. *et al.* The neutrophil as a cellular source of chemokines. *Immunological Reviews* **177**, 195–203 (2000).
70. Kasama, T., Strieter, R. M., Standiford, T. J., Burdick, M. D. & Kunkel, S. L. Expression and regulation of human neutrophil-derived macrophage inflammatory protein 1 alpha. *Journal of Experimental Medicine* **178**, 63–72 (1993).
71. Saclier, M. *et al.* Differentially Activated Macrophages Orchestrate Myogenic Precursor Cell Fate During Human Skeletal Muscle Regeneration. *Stem Cells* **31**, 384–396 (2013).
72. Dort, J., Fabre, P., Molina, T. & Dumont, N. A. Macrophages Are Key Regulators of Stem Cells during Skeletal Muscle Regeneration and Diseases. *Stem Cells International* **2019**, 1–20 (2019).
73. Walton, R. G. *et al.* Human skeletal muscle macrophages increase following cycle training and are associated with adaptations that may facilitate growth. *Scientific Reports* **9**, 969 (2019).
74. Dumont, N. & Frenette, J. Macrophages Protect against Muscle Atrophy and Promote Muscle Recovery in Vivo and in Vitro. *The American Journal of Pathology* **176**, 2228–2235 (2010).
75. Horsley, V., Jansen, K. M., Mills, S. T. & Pavlath, G. K. IL-4 Acts as a Myoblast Recruitment Factor during Mammalian Muscle Growth. *Cell* **113**, 483–494 (2003).
76. Lukjanenko, L. *et al.* Aging Disrupts Muscle Stem Cell Function by Impairing Matricellular WISP1 Secretion from Fibro-Adipogenic Progenitors. *Cell Stem Cell* **24**, 433-446.e7 (2019).
77. Kuswanto, W. *et al.* Poor Repair of Skeletal Muscle in Aging Mice Reflects a Defect in Local, Interleukin-33-Dependent Accumulation of Regulatory T Cells. *Immunity* **44**, 355–367 (2016).
78. Hutcheson, D. A., Zhao, J., Merrell, A., Haldar, M. & Kardon, G. Embryonic and fetal limb myogenic cells are derived from developmentally distinct progenitors and have different requirements for β-catenin. *Genes & Development* **23**, 997–1013 (2009).
79. Bachman, J. F. *et al.* Radiation-Induced Damage to Prepubertal Pax7+ Skeletal Muscle Stem Cells Drives Lifelong Deficits in Myofiber Size and Nuclear Number. *iScience* **23**, 101760 (2020).
80. Bachman, J. F. *et al.* Prepubertal skeletal muscle growth requires Pax7-expressing satellite cell-derived myonuclear contribution. *Development* (2018) doi:10.1242/dev.167197.
81. Cheung, T. H. & Rando, T. A. Molecular regulation of stem cell quiescence. *Nature Reviews Molecular Cell Biology* **14**, 329–340 (2013).
82. Fry, C. S. *et al.* Inducible depletion of satellite cells in adult, sedentary mice impairs muscle regenerative capacity without affecting sarcopenia. *Nature Medicine* **21**, 76–80 (2015).
83. Roman, W. *et al.* Muscle repair after physiological damage relies on nuclear migration for cellular reconstruction. *Science (1979)* **374**, 355–359 (2021).

84. Chakkalakal, J. v. *et al.* Early forming label-retaining muscle stem cells require p27kip1 for maintenance of the primitive state. *Development* **141**, 1649–1659 (2014).
85. Fukada, S. *et al.* Molecular Signature of Quiescent Satellite Cells in Adult Skeletal Muscle. *Stem Cells* **25**, 2448–2459 (2007).
86. Jones, N. C. *et al.* The p38α/β MAPK functions as a molecular switch to activate the quiescent satellite cell. *Journal of Cell Biology* **169**, 105–116 (2005).
87. Troy, A. *et al.* Coordination of Satellite Cell Activation and Self-Renewal by Par-Complex-Dependent Asymmetric Activation of p38α/β MAPK. *Cell Stem Cell* **11**, 541–553 (2012).
88. Perdiguero, E., Ruiz-Bonilla, V., Serrano, A. L. & Muñoz-Cánoves, P. Genetic Deficiency of p38α Reveals its Critical Role in Myoblast Cell Cycle Exit:The p38α-JNK Connection. *Cell Cycle* **6**, 1298–1303 (2007).
89. Shea, K. L. *et al.* Sprouty1 Regulates Reversible Quiescence of a Self-Renewing Adult Muscle Stem Cell Pool during Regeneration. *Cell Stem Cell* **6**, 117–129 (2010).
90. Cheung, T. H. *et al.* Maintenance of muscle stem-cell quiescence by microRNA-489. *Nature* **482**, 524–528 (2012).
91. Baghdadi, M. B. *et al.* Notch-Induced miR-708 Antagonizes Satellite Cell Migration and Maintains Quiescence. *Cell Stem Cell* **23**, 859-868.e5 (2018).
92. Yartseva, V. *et al.* Heterogeneity of Satellite Cells Implicates DELTA1/NOTCH2 Signaling in Self-Renewal. *Cell Reports* **30**, 1491-1503.e6 (2020).
93. Fujimaki, S. *et al.* Notch1 and Notch2 Coordinately Regulate Stem Cell Function in the Quiescent and Activated States of Muscle Satellite Cells. *Stem Cells* **36**, 278–285 (2018).
94. Bjornson, C. R. R. *et al.* Notch Signaling Is Necessary to Maintain Quiescence in Adult Muscle Stem Cells. *STEM CELLS* **30**, 232–242 (2012).
95. Mourikis, P. *et al.* A Critical Requirement for Notch Signaling in Maintenance of the Quiescent Skeletal Muscle Stem Cell State. *STEM CELLS* **30**, 243–252 (2012).
96. Eliazer, S. *et al.* Wnt4 from the Niche Controls the Mechano-Properties and Quiescent State of Muscle Stem Cells. *Cell Stem Cell* **25**, 654-665.e4 (2019).
97. Bentzinger, C. F. *et al.* Fibronectin Regulates Wnt7a Signaling and Satellite Cell Expansion. *Cell Stem Cell* **12**, 75–87 (2013).
98. Baghdadi, M. B. *et al.* Reciprocal signalling by Notch–Collagen V–CALCR retains muscle stem cells in their niche. *Nature* **557**, 714–718 (2018).
99. Verma, M. *et al.* Muscle Satellite Cell Cross-Talk with a Vascular Niche Maintains Quiescence via VEGF and Notch Signaling. *Cell Stem Cell* **23**, 530-543.e9 (2018).
100. García-Prat, L. *et al.* Autophagy maintains stemness by preventing senescence. *Nature* **529**, 37–42 (2016).
101. Sousa-Victor, P. *et al.* Geriatric muscle stem cells switch reversible quiescence into senescence. *Nature* **506**, 316–321 (2014).

102. Zismanov, V. *et al.* Phosphorylation of eIF2α Is a Translational Control Mechanism Regulating Muscle Stem Cell Quiescence and Self-Renewal. *Cell Stem Cell* **18**, 79–90 (2016).
103. Ryall, J. G. *et al.* The NAD+-Dependent SIRT1 Deacetylase Translates a Metabolic Switch into Regulatory Epigenetics in Skeletal Muscle Stem Cells. *Cell Stem Cell* **16**, 171–183 (2015).
104. Rodgers, J. T. *et al.* mTORC1 controls the adaptive transition of quiescent stem cells from G0 to GAlert. *Nature* **510**, 393–396 (2014).
105. Theret, M. *et al.* <scp>AMPK</scp> α1- <scp>LDH</scp> pathway regulates muscle stem cell self-renewal by controlling metabolic homeostasis. *The EMBO Journal* **36**, 1946–1962 (2017).
106. Shan, T. *et al.* Lkb1 Is Indispensable for Skeletal Muscle Development, Regeneration, and Satellite Cell Homeostasis. *Stem Cells* **32**, 2893–2907 (2014).
107. Schultz, E. Satellite Cell Proliferative Compartments in Growing Skeletal Muscles. *Developmental Biology* **175**, 84–94 (1996).
108. Beauchamp, J. R. *et al.* Expression of Cd34 and Myf5 Defines the Majority of Quiescent Adult Skeletal Muscle Satellite Cells. *Journal of Cell Biology* **151**, 1221–1234 (2000).
109. Chakkalakal, J. v., Jones, K. M., Basson, M. A. & Brack, A. S. The aged niche disrupts muscle stem cell quiescence. *Nature* **490**, 355–360 (2012).
110. Dell'Orso, S. *et al.* Single-cell analysis of adult skeletal muscle stem cells in homeostatic and regenerative conditions. *Development* (2019) doi:10.1242/dev.174177.
111. Giordani, L. *et al.* High-Dimensional Single-Cell Cartography Reveals Novel Skeletal Muscle-Resident Cell Populations. *Molecular Cell* **74**, 609-621.e6 (2019).
112. Scaramozza, A. *et al.* Lineage Tracing Reveals a Subset of Reserve Muscle Stem Cells Capable of Clonal Expansion under Stress. *Cell Stem Cell* **24**, 944-957.e5 (2019).
113. der Vartanian, A. *et al.* PAX3 Confers Functional Heterogeneity in Skeletal Muscle Stem Cell Responses to Environmental Stress. *Cell Stem Cell* **24**, 958-973.e9 (2019).
114. de Micheli, A. J. *et al.* Single-Cell Analysis of the Muscle Stem Cell Hierarchy Identifies Heterotypic Communication Signals Involved in Skeletal Muscle Regeneration. *Cell Reports* **30**, 3583-3595.e5 (2020).
115. Kimmel, J. C., Hwang, A. B., Scaramozza, A., Marshall, W. F. & Brack, A. S. Aging induces aberrant state transition kinetics in murine muscle stem cells. *Development* (2020) doi:10.1242/dev.183855.
116. de Micheli, A. J., Spector, J. A., Elemento, O. & Cosgrove, B. D. A reference single-cell transcriptomic atlas of human skeletal muscle tissue reveals bifurcated muscle stem cell populations. *Skeletal Muscle* **10**, 19 (2020).
117. Barruet, E. *et al.* Functionally heterogeneous human satellite cells identified by single cell RNA sequencing. *Elife* **9**, (2020).
118. Giordani, J. *et al.* Six proteins regulate the activation of *Myf5* expression in embryonic mouse limbs. *Proceedings of the National Academy of Sciences* **104**, 11310–11315 (2007).

119. Yoshida, N., Yoshida, S., Koishi, K., Masuda, K. & Nabeshima, Y. Cell heterogeneity upon myogenic differentiation: down-regulation of MyoD and Myf-5 generates 'reserve cells.' *Journal of Cell Science* **111**, 769–779 (1998).
120. Asakura, A. *et al.* Increased survival of muscle stem cells lacking the *MyoD* gene after transplantation into regenerating skeletal muscle. *Proceedings of the National Academy of Sciences* **104**, 16552–16557 (2007).
121. Gayraud-Morel, B. *et al.* Myf5 haploinsufficiency reveals distinct cell fate potentials for adult skeletal muscle stem cells. *Journal of Cell Science* (2012) doi:10.1242/jcs.097006.
122. le Grand, F. *et al.* Six1 regulates stem cell repair potential and self-renewal during skeletal muscle regeneration. *Journal of Cell Biology* **198**, 815–832 (2012).
123. Fukada, S. *et al.* Hesr1 and Hesr3 are essential to generate undifferentiated quiescent satellite cells and to maintain satellite cell numbers. *Development* **138**, 4609–4619 (2011).
124. Wen, Y. *et al.* Constitutive Notch Activation Upregulates Pax7 and Promotes the Self-Renewal of Skeletal Muscle Satellite Cells. *Molecular and Cellular Biology* **32**, 2300–2311 (2012).
125. Bi, P. *et al.* Stage-specific effects of Notch activation during skeletal myogenesis. *Elife* **5**, (2016).
126. Kim, J.-H. *et al.* Sex hormones establish a reserve pool of adult muscle stem cells. *Nature Cell Biology* **18**, 930–940 (2016).
127. Yamaguchi, M. *et al.* Calcitonin Receptor Signaling Inhibits Muscle Stem Cells from Escaping the Quiescent State and the Niche. *Cell Reports* **13**, 302–314 (2015).
128. Evano, B., Khalilian, S., le Carrou, G., Almouzni, G. & Tajbakhsh, S. Dynamics of Asymmetric and Symmetric Divisions of Muscle Stem Cells In Vivo and on Artificial Niches. *Cell Reports* **30**, 3195-3206.e7 (2020).
129. Cutler, A. A. *et al.* The regenerating skeletal muscle niche guides muscle stem cell self-renewal. *bioRxiv* 635805 (2021) doi:10.1101/635805.
130. Chandel, N. S., Jasper, H., Ho, T. T. & Passegué, E. Metabolic regulation of stem cell function in tissue homeostasis and organismal ageing. *Nature Cell Biology* **18**, 823–832 (2016).
131. Mookerjee, S. A. & Brand, M. D. Measurement and Analysis of Extracellular Acid Production to Determine Glycolytic Rate. *Journal of Visualized Experiments* (2015) doi:10.3791/53464.
132. Rostovtseva, T. & Colombini, M. ATP Flux Is Controlled by a Voltage-gated Channel from the Mitochondrial Outer Membrane. *Journal of Biological Chemistry* **271**, 28006–28008 (1996).
133. Rostovtseva, T. & Colombini, M. VDAC channels mediate and gate the flow of ATP: implications for the regulation of mitochondrial function. *Biophysical Journal* **72**, 1954–1962 (1997).
134. Hodge, T. & Colombini, M. Regulation of Metabolite Flux through Voltage-Gating of VDAC Channels. *Journal of Membrane Biology* **157**, 271–279 (1997).

135. Giacomello, M., Pyakurel, A., Glytsou, C. & Scorrano, L. The cell biology of mitochondrial membrane dynamics. *Nature Reviews Molecular Cell Biology* **21**, 204–224 (2020).
136. Zick, M., Rabl, R. & Reichert, A. S. Cristae formation—linking ultrastructure and function of mitochondria. *Biochimica et Biophysica Acta (BBA) - Molecular Cell Research* **1793**, 5–19 (2009).
137. Renken, C. *et al.* A thermodynamic model describing the nature of the crista junction: a structural motif in the mitochondrion. *Journal of Structural Biology* **138**, 137–144 (2002).
138. MITCHELL, P. Coupling of Phosphorylation to Electron and Hydrogen Transfer by a Chemi-Osmotic type of Mechanism. *Nature* **191**, 144–148 (1961).
139. Zorova, L. D. *et al.* Mitochondrial membrane potential. *Analytical Biochemistry* **552**, 50–59 (2018).
140. Hockenbery, D., Nuñez, G., Milliman, C., Schreiber, R. D. & Korsmeyer, S. J. Bcl-2 is an inner mitochondrial membrane protein that blocks programmed cell death. *Nature* **348**, 334–336 (1990).
141. Liu, X., Kim, C. N., Yang, J., Jemmerson, R. & Wang, X. Induction of Apoptotic Program in Cell-Free Extracts: Requirement for dATP and Cytochrome c. *Cell* **86**, 147–157 (1996).
142. Frank, S. *et al.* The Role of Dynamin-Related Protein 1, a Mediator of Mitochondrial Fission, in Apoptosis. *Developmental Cell* **1**, 515–525 (2001).
143. Scorrano, L. *et al.* A Distinct Pathway Remodels Mitochondrial Cristae and Mobilizes Cytochrome c during Apoptosis. *Developmental Cell* **2**, 55–67 (2002).
144. Shadel, G. S. & Horvath, T. L. Mitochondrial ROS Signaling in Organismal Homeostasis. *Cell* **163**, 560–569 (2015).
145. Hamanaka, R. B. & Chandel, N. S. Mitochondrial reactive oxygen species regulate cellular signaling and dictate biological outcomes. *Trends in Biochemical Sciences* **35**, 505–513 (2010).
146. Gomes, L. C., Benedetto, G. di & Scorrano, L. During autophagy mitochondria elongate, are spared from degradation and sustain cell viability. *Nature Cell Biology* **13**, 589–598 (2011).
147. Rambold, A. S., Kostelecky, B., Elia, N. & Lippincott-Schwartz, J. Tubular network formation protects mitochondria from autophagosomal degradation during nutrient starvation. *Proceedings of the National Academy of Sciences* **108**, 10190–10195 (2011).
148. Rambold, A. S. & Lippincott-Schwartz, J. Mechanisms of mitochondria and autophagy crosstalk. *Cell Cycle* **10**, 4032–4038 (2011).
149. Favaro, G. *et al.* DRP1-mediated mitochondrial shape controls calcium homeostasis and muscle mass. *Nature Communications* **10**, 2576 (2019).
150. Duchen, M. R. Mitochondria and calcium: from cell signalling to cell death. *The Journal of Physiology* **529**, 57–68 (2000).
151. Giorgi, C., Marchi, S. & Pinton, P. The machineries, regulation and cellular functions of mitochondrial calcium. *Nature Reviews Molecular Cell Biology* **19**, 713–730 (2018).
152. Rizzuto, R., de Stefani, D., Raffaello, A. & Mammucari, C. Mitochondria as sensors and regulators of calcium signalling. *Nature Reviews Molecular Cell Biology* **13**, 566–578 (2012).

153. Bahat, A. & Gross, A. Mitochondrial plasticity in cell fate regulation. *Journal of Biological Chemistry* **294**, 13852–13863 (2019).
154. Zhang, J. *et al.* UCP2 regulates energy metabolism and differentiation potential of human pluripotent stem cells. *The EMBO Journal* **30**, 4860–4873 (2011).
155. Kowno, M. *et al.* Prohibitin 2 Regulates the Proliferation and Lineage-Specific Differentiation of Mouse Embryonic Stem Cells in Mitochondria. *PLoS ONE* **9**, e81552 (2014).
156. Margineantu, D. H. & Hockenbery, D. M. Mitochondrial functions in stem cells. *Current Opinion in Genetics & Development* **38**, 110–117 (2016).
157. Khacho, M. *et al.* Mitochondrial Dynamics Impacts Stem Cell Identity and Fate Decisions by Regulating a Nuclear Transcriptional Program. *Cell Stem Cell* **19**, 232–247 (2016).
158. Folmes, C. D. L. & Terzic, A. Energy metabolism in the acquisition and maintenance of stemness. *Seminars in Cell & Developmental Biology* **52**, 68–75 (2016).
159. Luchsinger, L. L., de Almeida, M. J., Corrigan, D. J., Mumau, M. & Snoeck, H.-W. Mitofusin 2 maintains haematopoietic stem cells with extensive lymphoid potential. *Nature* **529**, 528–531 (2016).
160. Iwata, R., Casimir, P. & Vanderhaeghen, P. Mitochondrial dynamics in postmitotic cells regulate neurogenesis. *Science (1979)* **369**, 858–862 (2020).
161. Zhang, Q. *et al.* Circulating mitochondrial DAMPs cause inflammatory responses to injury. *Nature* **464**, 104–107 (2010).
162. Cloonan, S. M. & Choi, A. M. Mitochondria: sensors and mediators of innate immune receptor signaling. *Current Opinion in Microbiology* **16**, 327–338 (2013).
163. Nass, M. M. The circularity of mitochondrial DNA. *Proceedings of the National Academy of Sciences* **56**, 1215–1222 (1966).
164. Taanman, J.-W. The mitochondrial genome: structure, transcription, translation and replication. *Biochimica et Biophysica Acta (BBA) - Bioenergetics* **1410**, 103–123 (1999).
165. Bogenhagen, D. F. Mitochondrial DNA nucleoid structure. *Biochimica et Biophysica Acta (BBA) - Gene Regulatory Mechanisms* **1819**, 914–920 (2012).
166. Garrido, N. *et al.* Composition and Dynamics of Human Mitochondrial Nucleoids. *Molecular Biology of the Cell* **14**, 1583–1596 (2003).
167. Nunnari, J. & Suomalainen, A. Mitochondria: In Sickness and in Health. *Cell* **148**, 1145–1159 (2012).
168. Lee, S. R. & Han, J. Mitochondrial Nucleoid: Shield and Switch of the Mitochondrial Genome. *Oxidative Medicine and Cellular Longevity* **2017**, 1–15 (2017).
169. Detmer, S. A. & Chan, D. C. Functions and dysfunctions of mitochondrial dynamics. *Nature Reviews Molecular Cell Biology* **8**, 870–879 (2007).
170. Rambold, A. S. & Pearce, E. L. Mitochondrial Dynamics at the Interface of Immune Cell Metabolism and Function. *Trends in Immunology* **39**, 6–18 (2018).

171. Schneeberger, M. *et al.* Mitofusin 2 in POMC Neurons Connects ER Stress with Leptin Resistance and Energy Imbalance. *Cell* **155**, 172–187 (2013).
172. Ramírez, S. *et al.* Mitochondrial Dynamics Mediated by Mitofusin 1 Is Required for POMC Neuron Glucose-Sensing and Insulin Release Control. *Cell Metabolism* **25**, 1390-1399.e6 (2017).
173. Gómez-Valadés, A. G. *et al.* Mitochondrial cristae-remodeling protein OPA1 in POMC neurons couples Ca2+ homeostasis with adipose tissue lipolysis. *Cell Metabolism* **33**, 1820-1835.e9 (2021).
174. Smirnova, E., Griparic, L., Shurland, D.-L. & van der Bliek, A. M. Dynamin-related Protein Drp1 Is Required for Mitochondrial Division in Mammalian Cells. *Molecular Biology of the Cell* **12**, 2245–2256 (2001).
175. Friedman, J. R. *et al.* ER Tubules Mark Sites of Mitochondrial Division. *Science (1979)* **334**, 358–362 (2011).
176. Korobova, F., Ramabhadran, V. & Higgs, H. N. An Actin-Dependent Step in Mitochondrial Fission Mediated by the ER-Associated Formin INF2. *Science (1979)* **339**, 464–467 (2013).
177. Losón, O. C., Song, Z., Chen, H. & Chan, D. C. Fis1, Mff, MiD49, and MiD51 mediate Drp1 recruitment in mitochondrial fission. *Molecular Biology of the Cell* **24**, 659–667 (2013).
178. Palmer, C. S. *et al.* MiD49 and MiD51, new components of the mitochondrial fission machinery. *EMBO Rep* **12**, 565–573 (2011).
179. James, D. I., Parone, P. A., Mattenberger, Y. & Martinou, J.-C. hFis1, a Novel Component of the Mammalian Mitochondrial Fission Machinery. *Journal of Biological Chemistry* **278**, 36373–36379 (2003).
180. Otera, H. *et al.* Mff is an essential factor for mitochondrial recruitment of Drp1 during mitochondrial fission in mammalian cells. *Journal of Cell Biology* **191**, 1141–1158 (2010).
181. Lee, J. E., Westrate, L. M., Wu, H., Page, C. & Voeltz, G. K. Multiple dynamin family members collaborate to drive mitochondrial division. *Nature* **540**, 139–143 (2016).
182. Fonseca, T. B., Sánchez-Guerrero, Á., Milosevic, I. & Raimundo, N. Mitochondrial fission requires DRP1 but not dynamins. *Nature* **570**, E34–E42 (2019).
183. Mishra, P. & Chan, D. C. Metabolic regulation of mitochondrial dynamics. *Journal of Cell Biology* **212**, 379–387 (2016).
184. Valera-Alberni, M. *et al.* Crosstalk between Drp1 phosphorylation sites during mitochondrial remodeling and their impact on metabolic adaptation. *Cell Reports* **36**, 109565 (2021).
185. Chang, C.-R. & Blackstone, C. Cyclic AMP-dependent Protein Kinase Phosphorylation of Drp1 Regulates Its GTPase Activity and Mitochondrial Morphology. *Journal of Biological Chemistry* **282**, 21583–21587 (2007).
186. Cribbs, J. T. & Strack, S. Reversible phosphorylation of Drp1 by cyclic AMP-dependent protein kinase and calcineurin regulates mitochondrial fission and cell death. *EMBO Rep* **8**, 939–944 (2007).
187. Cereghetti, G. M. *et al.* Dephosphorylation by calcineurin regulates translocation of Drp1 to mitochondria. *Proceedings of the National Academy of Sciences* **105**, 15803–15808 (2008).
188. Taguchi, N., Ishihara, N., Jofuku, A., Oka, T. & Mihara, K. Mitotic Phosphorylation of Dynamin-related GTPase Drp1 Participates in

Mitochondrial Fission. *Journal of Biological Chemistry* **282**, 11521–11529 (2007).
189. Serasinghe, M. N. *et al.* Mitochondrial Division Is Requisite to RAS-Induced Transformation and Targeted by Oncogenic MAPK Pathway Inhibitors. *Molecular Cell* **57**, 521–536 (2015).
190. Kashatus, J. A. *et al.* Erk2 Phosphorylation of Drp1 Promotes Mitochondrial Fission and MAPK-Driven Tumor Growth. *Molecular Cell* **57**, 537–551 (2015).
191. Qi, X., Disatnik, M.-H., Shen, N., Sobel, R. A. & Mochly-Rosen, D. Aberrant mitochondrial fission in neurons induced by protein kinase Cδ under oxidative stress conditions in vivo. *Molecular Biology of the Cell* **22**, 256–265 (2011).
192. Strack, S., Wilson, T. J. & Cribbs, J. T. Cyclin-dependent kinases regulate splice-specific targeting of dynamin-related protein 1 to microtubules. *Journal of Cell Biology* **201**, 1037–1051 (2013).
193. Yu, B. *et al.* Mitochondrial phosphatase PGAM5 modulates cellular senescence by regulating mitochondrial dynamics. *Nature Communications* **11**, 2549 (2020).
194. Toyama, E. Q. *et al.* AMP-activated protein kinase mediates mitochondrial fission in response to energy stress. *Science (1979)* **351**, 275–281 (2016).
195. Jornayvaz, F. R. & Shulman, G. I. Regulation of mitochondrial biogenesis. *Essays in Biochemistry* **47**, 69–84 (2010).
196. Shen, Q. *et al.* Mutations in Fis1 disrupt orderly disposal of defective mitochondria. *Molecular Biology of the Cell* **25**, 145–159 (2014).
197. Xian, H., Yang, Q., Xiao, L., Shen, H.-M. & Liou, Y.-C. STX17 dynamically regulated by Fis1 induces mitophagy via hierarchical macroautophagic mechanism. *Nature Communications* **10**, 2059 (2019).
198. Kageyama, Y. *et al.* Parkin-independent mitophagy requires <scp>D</scp> rp1 and maintains the integrity of mammalian heart and brain. *The EMBO Journal* **33**, 2798–2813 (2014).
199. Burman, J. L. *et al.* Mitochondrial fission facilitates the selective mitophagy of protein aggregates. *Journal of Cell Biology* **216**, 3231–3247 (2017).
200. Oshima, Y. *et al.* Parkin-independent mitophagy via Drp1-mediated outer membrane severing and inner membrane ubiquitination. *Journal of Cell Biology* **220**, (2021).
201. Youle, R. J. & van der Bliek, A. M. Mitochondrial Fission, Fusion, and Stress. *Science (1979)* **337**, 1062–1065 (2012).
202. Fukumitsu, K. *et al.* Mitochondrial fission protein Drp1 regulates mitochondrial transport and dendritic arborization in cerebellar Purkinje cells. *Molecular and Cellular Neuroscience* **71**, 56–65 (2016).
203. Ponte, S. *et al.* Drp1-mediated mitochondrial fission regulates calcium and F-actin dynamics during wound healing. *Biology Open* (2020) doi:10.1242/bio.048629.
204. Prieto, J. *et al.* Early ERK1/2 activation promotes DRP1-dependent mitochondrial fission necessary for cell reprogramming. *Nature Communications* **7**, 11124 (2016).

205. Simula, L. *et al.* Drp1 Controls Effective T Cell Immune-Surveillance by Regulating T Cell Migration, Proliferation, and cMyc-Dependent Metabolic Reprogramming. *Cell Reports* **25**, 3059-3073.e10 (2018).
206. Kamerkar, S. C., Kraus, F., Sharpe, A. J., Pucadyil, T. J. & Ryan, M. T. Dynamin-related protein 1 has membrane constricting and severing abilities sufficient for mitochondrial and peroxisomal fission. *Nature Communications* **9**, 5239 (2018).
207. Waterham, H. R. *et al.* A Lethal Defect of Mitochondrial and Peroxisomal Fission. *New England Journal of Medicine* **356**, 1736–1741 (2007).
208. Koch, A. *et al.* Dynamin-like Protein 1 Is Involved in Peroxisomal Fission. *Journal of Biological Chemistry* **278**, 8597–8605 (2003).
209. Shamseldin, H. E. *et al.* Genomic analysis of mitochondrial diseases in a consanguineous population reveals novel candidate disease genes. *Journal of Medical Genetics* **49**, 234–241 (2012).
210. Sheffer, R. *et al.* Postnatal microcephaly and pain insensitivity due to a de novo heterozygous *DNM1L* mutation causing impaired mitochondrial fission and function. *American Journal of Medical Genetics Part A* **170**, 1603–1607 (2016).
211. Gerber, S. *et al.* Mutations in DNM1L, as in OPA1, result in dominant optic atrophy despite opposite effects on mitochondrial fusion and fission. *Brain* **140**, 2586–2596 (2017).
212. Ishihara, T. *et al.* Dynamics of Mitochondrial DNA Nucleoids Regulated by Mitochondrial Fission Is Essential for Maintenance of Homogeneously Active Mitochondria during Neonatal Heart Development. *Molecular and Cellular Biology* **35**, 211–223 (2015).
213. Wakabayashi, J. *et al.* The dynamin-related GTPase Drp1 is required for embryonic and brain development in mice. *Journal of Cell Biology* **186**, 805–816 (2009).
214. Hennings, T. G. *et al.* In Vivo Deletion of β-Cell Drp1 Impairs Insulin Secretion Without Affecting Islet Oxygen Consumption. *Endocrinology* **159**, 3245–3256 (2018).
215. Chen, H., Chomyn, A. & Chan, D. C. Disruption of Fusion Results in Mitochondrial Heterogeneity and Dysfunction. *Journal of Biological Chemistry* **280**, 26185–26192 (2005).
216. Chen, H. *et al.* Mitofusins Mfn1 and Mfn2 coordinately regulate mitochondrial fusion and are essential for embryonic development. *Journal of Cell Biology* **160**, 189–200 (2003).
217. Rojo, M., Legros, F., Chateau, D. & Lombès, A. Membrane topology and mitochondrial targeting of mitofusins, ubiquitous mammalian homologs of the transmembrane GTPase Fzo. *Journal of Cell Science* **115**, 1663–1674 (2002).
218. Ishihara, N., Eura, Y. & Mihara, K. Mitofusin 1 and 2 play distinct roles in mitochondrial fusion reactions via GTPase activity. *Journal of Cell Science* **117**, 6535–6546 (2004).
219. de Brito, O. M. & Scorrano, L. Mitofusin 2 tethers endoplasmic reticulum to mitochondria. *Nature* **456**, 605–610 (2008).
220. Koshiba, T. *et al.* Structural Basis of Mitochondrial Tethering by Mitofusin Complexes. *Science (1979)* **305**, 858–862 (2004).
221. Dorn, G. W. Mitofusins as mitochondrial anchors and tethers. *Journal of Molecular and Cellular Cardiology* **142**, 146–153 (2020).

222. McLelland, G.-L. *et al.* Mfn2 ubiquitination by PINK1/parkin gates the p97-dependent release of ER from mitochondria to drive mitophagy. *Elife* **7**, (2018).
223. Chen, Y. & Dorn, G. W. PINK1-Phosphorylated Mitofusin 2 Is a Parkin Receptor for Culling Damaged Mitochondria. *Science (1979)* **340**, 471–475 (2013).
224. Cipolat, S., de Brito, O. M., Dal Zilio, B. & Scorrano, L. OPA1 requires mitofusin 1 to promote mitochondrial fusion. *Proceedings of the National Academy of Sciences* **101**, 15927–15932 (2004).
225. Frezza, C. *et al.* OPA1 Controls Apoptotic Cristae Remodeling Independently from Mitochondrial Fusion. *Cell* **126**, 177–189 (2006).
226. Cogliati, S. *et al.* Mitochondrial Cristae Shape Determines Respiratory Chain Supercomplexes Assembly and Respiratory Efficiency. *Cell* **155**, 160–171 (2013).
227. Käser, M., Kambacheld, M., Kisters-Woike, B. & Langer, T. Oma1, a Novel Membrane-bound Metallopeptidase in Mitochondria with Activities Overlapping with the m-AAA Protease. *Journal of Biological Chemistry* **278**, 46414–46423 (2003).
228. MacVicar, T. & Langer, T. OPA1 processing in cell death and disease – the long and short of it. *Journal of Cell Science* (2016) doi:10.1242/jcs.159186.
229. Anand, R. *et al.* The i-AAA protease YME1L and OMA1 cleave OPA1 to balance mitochondrial fusion and fission. *Journal of Cell Biology* **204**, 919–929 (2014).
230. Ishihara, N., Fujita, Y., Oka, T. & Mihara, K. Regulation of mitochondrial morphology through proteolytic cleavage of OPA1. *The EMBO Journal* **25**, 2966–2977 (2006).
231. Koch, J. *et al.* Disturbed mitochondrial and peroxisomal dynamics due to loss of MFF causes Leigh-like encephalopathy, optic atrophy and peripheral neuropathy. *Journal of Medical Genetics* **53**, 270–278 (2016).
232. Bartsakoulia, M. *et al.* A novel mechanism causing imbalance of mitochondrial fusion and fission in human myopathies. *Human Molecular Genetics* **27**, 1186–1195 (2018).
233. Alexander, C. *et al.* OPA1, encoding a dynamin-related GTPase, is mutated in autosomal dominant optic atrophy linked to chromosome 3q28. *Nature Genetics* **26**, 211–215 (2000).
234. Delettre, C. *et al.* Nuclear gene OPA1, encoding a mitochondrial dynamin-related protein, is mutated in dominant optic atrophy. *Nature Genetics* **26**, 207–210 (2000).
235. Schaaf, C. P. *et al.* Early-onset severe neuromuscular phenotype associated with compound heterozygosity for OPA1 mutations. *Molecular Genetics and Metabolism* **103**, 383–387 (2011).
236. Spiegel, R. *et al.* Fatal infantile mitochondrial encephalomyopathy, hypertrophic cardiomyopathy and optic atrophy associated with a homozygous *OPA1* mutation. *Journal of Medical Genetics* **53**, 127–131 (2016).
237. Carelli, V. *et al.* Syndromic parkinsonism and dementia associated with <scp> *OPA* </scp> *1* missense mutations. *Annals of Neurology* **78**, 21–38 (2015).

238. Züchner, S. *et al.* Mutations in the mitochondrial GTPase mitofusin 2 cause Charcot-Marie-Tooth neuropathy type 2A. *Nature Genetics* **36**, 449–451 (2004).
239. Dikic, I. & Elazar, Z. Mechanism and medical implications of mammalian autophagy. *Nature Reviews Molecular Cell Biology* **19**, 349–364 (2018).
240. Klionsky, D. J. *et al.* A comprehensive glossary of autophagy-related molecules and processes (2 nd edition). *Autophagy* **7**, 1273–1294 (2011).
241. Parzych, K. R. & Klionsky, D. J. An Overview of Autophagy: Morphology, Mechanism, and Regulation. *Antioxidants & Redox Signaling* **20**, 460–473 (2014).
242. Kaushik, S. & Cuervo, A. M. The coming of age of chaperone-mediated autophagy. *Nature Reviews Molecular Cell Biology* **19**, 365–381 (2018).
243. Kroemer, G., Mariño, G. & Levine, B. Autophagy and the Integrated Stress Response. *Molecular Cell* **40**, 280–293 (2010).
244. Pyo, J. O., Nah, J. & Jung, Y. K. Molecules and their functions in autophagy. *Experimental and Molecular Medicine* **44**, 73–80 (2012).
245. Lee, Y.-K. & Lee, J.-A. Role of the mammalian ATG8/LC3 family in autophagy: differential and compensatory roles in the spatiotemporal regulation of autophagy. *BMB Reports* **49**, 424–430 (2016).
246. Kirkin, V. & Rogov, V. v. A Diversity of Selective Autophagy Receptors Determines the Specificity of the Autophagy Pathway. *Molecular Cell* **76**, 268–285 (2019).
247. Boya, P. *et al.* Inhibition of Macroautophagy Triggers Apoptosis. *Molecular and Cellular Biology* **25**, 1025–1040 (2005).
248. Ding, W.-X. & Yin, X.-M. Mitophagy: mechanisms, pathophysiological roles, and analysis. *bchm* **393**, 547–564 (2012).
249. Campanario, S., Ramírez-Pardo, I., Hong, X., Isern, J. & Muñoz-Cánoves, P. Assessing Autophagy in Muscle Stem Cells. *Frontiers in Cell and Developmental Biology* **8**, (2021).
250. Sekine, S. & Youle, R. J. PINK1 import regulation; a fine system to convey mitochondrial stress to the cytosol. *BMC Biology* **16**, 2 (2018).
251. Chen, Y. & Dorn, G. W. PINK1-Phosphorylated Mitofusin 2 Is a Parkin Receptor for Culling Damaged Mitochondria. *Science (1979)* **340**, 471–475 (2013).
252. Gegg, M. E. *et al.* Mitofusin 1 and mitofusin 2 are ubiquitinated in a PINK1/parkin-dependent manner upon induction of mitophagy. *Human Molecular Genetics* **19**, 4861–4870 (2010).
253. Geisler, S. *et al.* PINK1/Parkin-mediated mitophagy is dependent on VDAC1 and p62/SQSTM1. *Nature Cell Biology* **12**, 119–131 (2010).
254. Lazarou, M., Jin, S. M., Kane, L. A. & Youle, R. J. Role of PINK1 Binding to the TOM Complex and Alternate Intracellular Membranes in Recruitment and Activation of the E3 Ligase Parkin. *Developmental Cell* **22**, 320–333 (2012).
255. Fu, M. *et al.* Regulation of mitophagy by the Gp78 E3 ubiquitin ligase. *Molecular Biology of the Cell* **24**, 1153–1162 (2013).
256. Orvedahl, A. *et al.* Image-based genome-wide siRNA screen identifies selective autophagy factors. *Nature* **480**, 113–117 (2011).

257. Wei, Y., Chiang, W.-C., Sumpter, R., Mishra, P. & Levine, B. Prohibitin 2 Is an Inner Mitochondrial Membrane Mitophagy Receptor. *Cell* **168**, 224-238.e10 (2017).
258. Chu, C. T. *et al.* Cardiolipin externalization to the outer mitochondrial membrane acts as an elimination signal for mitophagy in neuronal cells. *Nature Cell Biology* **15**, 1197–1205 (2013).
259. Sentelle, R. D. *et al.* Ceramide targets autophagosomes to mitochondria and induces lethal mitophagy. *Nature Chemical Biology* **8**, 831–838 (2012).
260. Barsoum, M. J. *et al.* Nitric oxide-induced mitochondrial fission is regulated by dynamin-related GTPases in neurons. *The EMBO Journal* **25**, 3900–3911 (2006).
261. Twig, G. *et al.* Fission and selective fusion govern mitochondrial segregation and elimination by autophagy. *The EMBO Journal* **27**, 433–446 (2008).
262. Twig, G. & Shirihai, O. S. The Interplay Between Mitochondrial Dynamics and Mitophagy. *Antioxidants & Redox Signaling* **14**, 1939–1951 (2011).
263. Narendra, D., Tanaka, A., Suen, D.-F. & Youle, R. J. Parkin is recruited selectively to impaired mitochondria and promotes their autophagy. *Journal of Cell Biology* **183**, 795–803 (2008).
264. Navratil, M., Terman, A. & Arriaga, E. A. Giant mitochondria do not fuse and exchange their contents with normal mitochondria. *Experimental Cell Research* **314**, 164–172 (2008).
265. Elmore, S. P., Qian, T., Grissom, S. F. & Lemasters, J. J. The mitochondrial permeability transition initiates autophagy in rat hepatocytes. *The FASEB Journal* **15**, 1–17 (2001).
266. Ikeda, Y. *et al.* Endogenous Drp1 Mediates Mitochondrial Autophagy and Protects the Heart Against Energy Stress. *Circulation Research* **116**, 264–278 (2015).
267. Song, M., Franco, A., Fleischer, J. A., Zhang, L. & Dorn, G. W. Abrogating Mitochondrial Dynamics in Mouse Hearts Accelerates Mitochondrial Senescence. *Cell Metabolism* **26**, 872-883.e5 (2017).
268. Sebastián, D. *et al.* Mfn2 deficiency links age-related sarcopenia and impaired autophagy to activation of an adaptive mitophagy pathway. *The EMBO Journal* **35**, 1677–1693 (2016).
269. Landes, T. *et al.* The BH3-only Bnip3 binds to the dynamin Opa1 to promote mitochondrial fragmentation and apoptosis by distinct mechanisms. *EMBO Rep* **11**, 459–465 (2010).
270. Chen, M. *et al.* Mitophagy receptor FUNDC1 regulates mitochondrial dynamics and mitophagy. *Autophagy* **12**, 689–702 (2016).
271. Liu, L. *et al.* Mitochondrial outer-membrane protein FUNDC1 mediates hypoxia-induced mitophagy in mammalian cells. *Nature Cell Biology* **14**, 177–185 (2012).
272. Folmes, C. D. L., Dzeja, P. P., Nelson, T. J. & Terzic, A. Metabolic Plasticity in Stem Cell Homeostasis and Differentiation. *Cell Stem Cell* **11**, 596–606 (2012).
273. Folmes, C. D. L. *et al.* Somatic Oxidative Bioenergetics Transitions into Pluripotency-Dependent Glycolysis to Facilitate Nuclear Reprogramming. *Cell Metabolism* **14**, 264–271 (2011).

274. Cho, Y. M. *et al.* Dynamic changes in mitochondrial biogenesis and antioxidant enzymes during the spontaneous differentiation of human embryonic stem cells. *Biochemical and Biophysical Research Communications* **348**, 1472–1478 (2006).
275. Chung, S. *et al.* Mitochondrial oxidative metabolism is required for the cardiac differentiation of stem cells. *Nature Clinical Practice Cardiovascular Medicine* **4**, S60–S67 (2007).
276. Kondoh, H. *et al.* A High Glycolytic Flux Supports the Proliferative Potential of Murine Embryonic Stem Cells. *Antioxidants & Redox Signaling* **9**, 293–299 (2007).
277. Simsek, T. *et al.* The Distinct Metabolic Profile of Hematopoietic Stem Cells Reflects Their Location in a Hypoxic Niche. *Cell Stem Cell* **7**, 380–390 (2010).
278. Chen, C.-T., Shih, Y.-R. v., Kuo, T. K., Lee, O. K. & Wei, Y.-H. Coordinated Changes of Mitochondrial Biogenesis and Antioxidant Enzymes During Osteogenic Differentiation of Human Mesenchymal Stem Cells. *Stem Cells* **26**, 960–968 (2008).
279. Takubo, K. *et al.* Regulation of Glycolysis by Pdk Functions as a Metabolic Checkpoint for Cell Cycle Quiescence in Hematopoietic Stem Cells. *Cell Stem Cell* **12**, 49–61 (2013).
280. Agostini, M. *et al.* Metabolic reprogramming during neuronal differentiation. *Cell Death & Differentiation* **23**, 1502–1514 (2016).
281. Zheng, X. *et al.* Metabolic reprogramming during neuronal differentiation from aerobic glycolysis to neuronal oxidative phosphorylation. *Elife* **5**, (2016).
282. Maryanovich, M. *et al.* An MTCH2 pathway repressing mitochondria metabolism regulates haematopoietic stem cell fate. *Nature Communications* **6**, 7901 (2015).
283. Yu, W.-M. *et al.* Metabolic Regulation by the Mitochondrial Phosphatase PTPMT1 Is Required for Hematopoietic Stem Cell Differentiation. *Cell Stem Cell* **12**, 62–74 (2013).
284. Zhou, W. *et al.* HIF1α induced switch from bivalent to exclusively glycolytic metabolism during ESC-to-EpiSC/hESC transition. *The EMBO Journal* **31**, 2103–2116 (2012).
285. Carbognin, E., Betto, R. M., Soriano, M. E., Smith, A. G. & Martello, G. Stat3 promotes mitochondrial transcription and oxidative respiration during maintenance and induction of naive pluripotency. *The EMBO Journal* **35**, 618–634 (2016).
286. Zhang, J. *et al.* LIN28 Regulates Stem Cell Metabolism and Conversion to Primed Pluripotency. *Cell Stem Cell* **19**, 66–80 (2016).
287. Sperber, H. *et al.* The metabolome regulates the epigenetic landscape during naive-to-primed human embryonic stem cell transition. *Nature Cell Biology* **17**, 1523–1535 (2015).
288. Ito, K. *et al.* A PML–PPAR-δ pathway for fatty acid oxidation regulates hematopoietic stem cell maintenance. *Nature Medicine* **18**, 1350–1358 (2012).
289. Knobloch, M. *et al.* A Fatty Acid Oxidation-Dependent Metabolic Shift Regulates Adult Neural Stem Cell Activity. *Cell Reports* **20**, 2144–2155 (2017).
290. Lyons, C. N., Leary, S. C. & Moyes, C. D. Bioenergetic remodeling during cellular differentiation: changes in cytochrome *c* oxidase

regulation do not affect the metabolic phenotype. *Biochemistry and Cell Biology* **82**, 391–399 (2004).
291. Kraft, C. S. *et al.* Control of mitochondrial biogenesis during myogenesis. *American Journal of Physiology-Cell Physiology* **290**, C1119–C1127 (2006).
292. Remels, A. H. V. *et al.* Regulation of mitochondrial biogenesis during myogenesis. *Molecular and Cellular Endocrinology* **315**, 113–120 (2010).
293. Hoffmann, C. *et al.* The effect of differentiation and TGFβ on mitochondrial respiration and mitochondrial enzyme abundance in cultured primary human skeletal muscle cells. *Scientific Reports* **8**, 737 (2018).
294. Hori, S., Hiramuki, Y., Nishimura, D., Sato, F. & Sehara-Fujisawa, A. PDH-mediated metabolic flow is critical for skeletal muscle stem cell differentiation and myotube formation during regeneration in mice. *The FASEB Journal* **33**, 8094–8109 (2019).
295. Owusu-Ansah, E. & Banerjee, U. Reactive oxygen species prime Drosophila haematopoietic progenitors for differentiation. *Nature* **461**, 537–541 (2009).
296. Tothova, Z. *et al.* FoxOs Are Critical Mediators of Hematopoietic Stem Cell Resistance to Physiologic Oxidative Stress. *Cell* **128**, 325–339 (2007).
297. Pallafacchina, G. *et al.* An adult tissue-specific stem cell in its niche: A gene profiling analysis of in vivo quiescent and activated muscle satellite cells. *Stem Cell Research* **4**, 77–91 (2010).
298. Kozakowska, M., Pietraszek-Gremplewicz, K., Jozkowicz, A. & Dulak, J. The role of oxidative stress in skeletal muscle injury and regeneration: focus on antioxidant enzymes. *Journal of Muscle Research and Cell Motility* **36**, 377–393 (2015).
299. le Moal, E. *et al.* Redox Control of Skeletal Muscle Regeneration. *Antioxidants & Redox Signaling* **27**, 276–310 (2017).
300. Matilainen, O., Quirós, P. M. & Auwerx, J. Mitochondria and Epigenetics – Crosstalk in Homeostasis and Stress. *Trends in Cell Biology* **27**, 453–463 (2017).
301. Yucel, N. *et al.* Glucose Metabolism Drives Histone Acetylation Landscape Transitions that Dictate Muscle Stem Cell Function. *Cell Reports* **27**, 3939-3955.e6 (2019).
302. Liu, L. *et al.* Chromatin Modifications as Determinants of Muscle Stem Cell Quiescence and Chronological Aging. *Cell Reports* **4**, 189–204 (2013).
303. Machado, L. *et al.* In Situ Fixation Redefines Quiescence and Early Activation of Skeletal Muscle Stem Cells. *Cell Reports* **21**, 1982–1993 (2017).
304. Juan, A. H. *et al.* Polycomb EZH2 controls self-renewal and safeguards the transcriptional identity of skeletal muscle stem cells. *Genes & Development* **25**, 789–794 (2011).
305. Teperino, R., Schoonjans, K. & Auwerx, J. Histone Methyl Transferases and Demethylases; Can They Link Metabolism and Transcription? *Cell Metabolism* **12**, 321–327 (2010).

306. Shyh-Chang, N. *et al.* Influence of Threonine Metabolism on *S* -Adenosylmethionine and Histone Methylation. *Science (1979)* **339**, 222–226 (2013).
307. Takashima, Y. *et al.* Resetting Transcription Factor Control Circuitry toward Ground-State Pluripotency in Human. *Cell* **158**, 1254–1269 (2014).
308. Kasahara, A., Cipolat, S., Chen, Y., Dorn, G. W. & Scorrano, L. Mitochondrial Fusion Directs Cardiomyocyte Differentiation via Calcineurin and Notch Signaling. *Science (1979)* **342**, 734–737 (2013).
309. Mortensen, M. *et al.* The autophagy protein Atg7 is essential for hematopoietic stem cell maintenance. *Journal of Experimental Medicine* **208**, 455–467 (2011).
310. Liu, F. *et al.* FIP200 is required for the cell-autonomous maintenance of fetal hematopoietic stem cells. *Blood* **116**, 4806–4814 (2010).
311. Leveque-El Mouttie, L. *et al.* Autophagy is required for stem cell mobilization by G-CSF. *Blood* **125**, 2933–2936 (2015).
312. Warr, M. R. *et al.* FOXO3A directs a protective autophagy program in haematopoietic stem cells. *Nature* **494**, 323–327 (2013).
313. Tang, A. H. & Rando, T. A. Induction of autophagy supports the bioenergetic demands of quiescent muscle stem cell activation. *The EMBO Journal* **33**, 2782–2797 (2014).
314. White, J. P. *et al.* The AMPK/p27Kip1 Axis Regulates Autophagy/Apoptosis Decisions in Aged Skeletal Muscle Stem Cells. *Stem Cell Reports* **11**, 425–439 (2018).
315. Fiacco, E. *et al.* Autophagy regulates satellite cell ability to regenerate normal and dystrophic muscles. *Cell Death & Differentiation* **23**, 1839–1849 (2016).
316. Fortini, P., Iorio, E., Dogliotti, E. & Isidoro, C. Coordinated Metabolic Changes and Modulation of Autophagy during Myogenesis. *Frontiers in Physiology* **7**, (2016).
317. Wang, S. *et al.* Transient Activation of Autophagy via Sox2-Mediated Suppression of mTOR Is an Important Early Step in Reprogramming to Pluripotency. *Cell Stem Cell* **13**, 617–625 (2013).
318. Panopoulos, A. D. *et al.* The metabolome of induced pluripotent stem cells reveals metabolic changes occurring in somatic cell reprogramming. *Cell Research* **22**, 168–177 (2012).
319. Vazquez-Martin, A. *et al.* Mitophagy-driven mitochondrial rejuvenation regulates stem cell fate. *Aging* **8**, 1330–1352 (2016).
320. Zhang, H. *et al.* NAD $^{+}$ repletion improves mitochondrial and stem cell function and enhances life span in mice. *Science (1979)* **352**, 1436–1443 (2016).
321. López-Otín, C., Blasco, M. A., Partridge, L., Serrano, M. & Kroemer, G. The Hallmarks of Aging. *Cell* **153**, 1194–1217 (2013).
322. Santilli, V., Bernetti, A., Mangone, M. & Paoloni, M. Clinical definition of sarcopenia. *Clin Cases Miner Bone Metab* **11**, 177–80 (2014).
323. Cruz-Jentoft, A. J. *et al.* Sarcopenia: revised European consensus on definition and diagnosis. *Age and Ageing* **48**, 601–601 (2019).
324. Carlson, B. M. & Faulkner, J. A. Muscle transplantation between young and old rats: age of host determines recovery. *American Journal of Physiology-Cell Physiology* **256**, C1262–C1266 (1989).

325. Conboy, I. M. *et al.* Rejuvenation of aged progenitor cells by exposure to a young systemic environment. *Nature* **433**, 760–764 (2005).
326. Bernet, J. D. *et al.* p38 MAPK signaling underlies a cell-autonomous loss of stem cell self-renewal in skeletal muscle of aged mice. *Nature Medicine* **20**, 265–271 (2014).
327. García-Prat, L., Sousa-Victor, P. & Muñoz-Cánoves, P. Functional dysregulation of stem cells during aging: a focus on skeletal muscle stem cells. *FEBS Journal* **280**, 4051–4062 (2013).
328. Brack, A. S. *et al.* Increased Wnt Signaling During Aging Alters Muscle Stem Cell Fate and Increases Fibrosis. *Science (1979)* **317**, 807–810 (2007).
329. Hong, X. *et al.* Stem cell aging in the skeletal muscle: The importance of communication. *Ageing Research Reviews* **73**, 101528 (2022).
330. Price, F. D. *et al.* Inhibition of JAK-STAT signaling stimulates adult satellite cell function. *Nature Medicine* **20**, 1174–1181 (2014).
331. Cosgrove, B. D. *et al.* Rejuvenation of the muscle stem cell population restores strength to injured aged muscles. *Nature Medicine* **20**, 255–264 (2014).
332. Sinha, M. *et al.* Restoring Systemic GDF11 Levels Reverses Age-Related Dysfunction in Mouse Skeletal Muscle. *Science (1979)* **344**, 649–652 (2014).
333. Franco, I. *et al.* Somatic mutagenesis in satellite cells associates with human skeletal muscle aging. *Nature Communications* **9**, 800 (2018).
334. Shcherbina, A. *et al.* Dissecting Murine Muscle Stem Cell Aging through Regeneration Using Integrative Genomic Analysis. *Cell Reports* **32**, 107964 (2020).
335. Schwörer, S. *et al.* Epigenetic stress responses induce muscle stem-cell ageing by Hoxa9 developmental signals. *Nature* **540**, 428–432 (2016).
336. Zhu, P. *et al.* The transcription factor Slug represses p16Ink4a and regulates murine muscle stem cell aging. *Nature Communications* **10**, 2568 (2019).
337. Hwang, A. B. & Brack, A. S. Muscle Stem Cells and Aging. in 299–322 (2018). doi:10.1016/bs.ctdb.2017.08.008.
338. Gutmann, E. & Carlson, B. M. Regeneration and transplantation of muscles in old rats and between young and old rats. *Life Sciences* **18**, 109–114 (1976).
339. Rebo, J. *et al.* A single heterochronic blood exchange reveals rapid inhibition of multiple tissues by old blood. *Nature Communications* **7**, 13363 (2016).
340. Rai, R. *et al.* Downregulation of the Apelinergic Axis Accelerates Aging, whereas Its Systemic Restoration Improves the Mammalian Healthspan. *Cell Reports* **21**, 1471–1480 (2017).
341. Vinel, C. *et al.* The exerkine apelin reverses age-associated sarcopenia. *Nature Medicine* **24**, 1360–1371 (2018).
342. Elabd, C. *et al.* Oxytocin is an age-specific circulating hormone that is necessary for muscle maintenance and regeneration. *Nature Communications* **5**, 4082 (2014).
343. Schafer, M. J. *et al.* Quantification of GDF11 and Myostatin in Human Aging and Cardiovascular Disease. *Cell Metabolism* **23**, 1207–1215 (2016).

344. Harper, S. C. *et al.* Is Growth Differentiation Factor 11 a Realistic Therapeutic for Aging-Dependent Muscle Defects? *Circulation Research* **118**, 1143–1150 (2016).
345. Egerman, M. A. & Glass, D. J. The role of GDF11 in aging and skeletal muscle, cardiac and bone homeostasis. *Critical Reviews in Biochemistry and Molecular Biology* **54**, 174–183 (2019).
346. Egerman, M. A. *et al.* GDF11 Increases with Age and Inhibits Skeletal Muscle Regeneration. *Cell Metabolism* **22**, 164–174 (2015).
347. Lukjanenko, L. *et al.* Loss of fibronectin from the aged stem cell niche affects the regenerative capacity of skeletal muscle in mice. *Nature Medicine* **22**, 897–905 (2016).
348. Rozo, M., Li, L. & Fan, C.-M. Targeting β1-integrin signaling enhances regeneration in aged and dystrophic muscle in mice. *Nature Medicine* **22**, 889–896 (2016).
349. Tidball, J. G. Regulation of muscle growth and regeneration by the immune system. *Nature Reviews Immunology* **17**, 165–178 (2017).
350. Chazaud, B. Inflammation and Skeletal Muscle Regeneration: Leave It to the Macrophages! *Trends in Immunology* **41**, 481–492 (2020).
351. Oprescu, S. N., Yue, F., Qiu, J., Brito, L. F. & Kuang, S. Temporal Dynamics and Heterogeneity of Cell Populations during Skeletal Muscle Regeneration. *iScience* **23**, 100993 (2020).
352. Tidball, J. G., Flores, I., Welc, S. S., Wehling-Henricks, M. & Ochi, E. Aging of the immune system and impaired muscle regeneration: A failure of immunomodulation of adult myogenesis. *Experimental Gerontology* **145**, 111200 (2021).
353. Wang, Y. *et al.* Aging of the immune system causes reductions in muscle stem cell populations, promotes their shift to a fibrogenic phenotype, and modulates sarcopenia. *The FASEB Journal* **33**, 1415–1427 (2019).
354. Wang, Y., Welc, S. S., Wehling-Henricks, M. & Tidball, J. G. Myeloid cell-derived tumor necrosis factor-alpha promotes sarcopenia and regulates muscle cell fusion with aging muscle fibers. *Aging Cell* **17**, e12828 (2018).
355. Tobin, S. W. *et al.* Delineating the relationship between immune system aging and myogenesis in muscle repair. *Aging Cell* **20**, (2021).
356. Oh, J. *et al.* Age-associated NF-κB signaling in myofibers alters the satellite cell niche and re-strains muscle stem cell function. *Aging* **8**, 2871–2896 (2016).
357. Zhang, C. *et al.* Age-related decline of interferon-gamma responses in macrophage impairs satellite cell proliferation and regeneration. *Journal of Cachexia, Sarcopenia and Muscle* **11**, 1291–1305 (2020).
358. Patsalos, A. *et al.* In vivo GDF3 administration abrogates aging related muscle regeneration delay following acute sterile injury. *Aging Cell* **17**, e12815 (2018).
359. Blanc, R. S. *et al.* Inhibition of inflammatory CCR2 signaling promotes aged muscle regeneration and strength recovery after injury. *Nature Communications* **11**, 4167 (2020).
360. Ratnayake, D. *et al.* Macrophages provide a transient muscle stem cell niche via NAMPT secretion. *Nature* **591**, 281–287 (2021).

361. Taylor, R. C. & Dillin, A. Aging as an Event of Proteostasis Collapse. *Cold Spring Harbor Perspectives in Biology* **3**, a004440–a004440 (2011).
362. Sahu, A. *et al.* Age-related declines in α-Klotho drive progenitor cell mitochondrial dysfunction and impaired muscle regeneration. *Nature Communications* **9**, 4859 (2018).
363. Baraibar, M. A. *et al.* Impaired energy metabolism of senescent muscle satellite cells is associated with oxidative modifications of glycolytic enzymes. *Aging* **8**, 3375–3389 (2016).
364. Egan, D. F. *et al.* Phosphorylation of ULK1 (hATG1) by AMP-Activated Protein Kinase Connects Energy Sensing to Mitophagy. *Science (1979)* **331**, 456–461 (2011).
365. Liang, J. *et al.* The energy sensing LKB1–AMPK pathway regulates p27kip1 phosphorylation mediating the decision to enter autophagy or apoptosis. *Nature Cell Biology* **9**, 218–224 (2007).
366. Lee, I. H. *et al.* A role for the NAD-dependent deacetylase Sirt1 in the regulation of autophagy. *Proceedings of the National Academy of Sciences* **105**, 3374–3379 (2008).
367. Ou, X., Lee, M. R., Huang, X., Messina-Graham, S. & Broxmeyer, H. E. SIRT1 Positively Regulates Autophagy and Mitochondria Function in Embryonic Stem Cells Under Oxidative Stress. *STEM CELLS* **32**, 1183–1194 (2014).
368. Solanas, G. *et al.* Aged Stem Cells Reprogram Their Daily Rhythmic Functions to Adapt to Stress. *Cell* **170**, 678-692.e20 (2017).
369. Cerletti, M., Jang, Y. C., Finley, L. W. S., Haigis, M. C. & Wagers, A. J. Short-Term Calorie Restriction Enhances Skeletal Muscle Stem Cell Function. *Cell Stem Cell* **10**, 515–519 (2012).
370. Möpert, K. *et al.* Loss of Drp1 function alters OPA1 processing and changes mitochondrial membrane organization. *Experimental Cell Research* **315**, 2165–2180 (2009).
371. Ban-Ishihara, R., Ishihara, T., Sasaki, N., Mihara, K. & Ishihara, N. Dynamics of nucleoid structure regulated by mitochondrial fission contributes to cristae reformation and release of cytochrome *c*. *Proceedings of the National Academy of Sciences* **110**, 11863–11868 (2013).
372. Hulsen, T., de Vlieg, J. & Alkema, W. BioVenn – a web application for the comparison and visualization of biological lists using area-proportional Venn diagrams. *BMC Genomics* **9**, 488 (2008).
373. Parone, P. A. *et al.* Preventing Mitochondrial Fission Impairs Mitochondrial Function and Leads to Loss of Mitochondrial DNA. *PLoS ONE* **3**, e3257 (2008).
374. Corrado, M. *et al.* Deletion of the mitochondria-shaping protein Opa1 during early thymocyte maturation impacts mature memory T cell metabolism. *Cell Death & Differentiation* **28**, 2194–2206 (2021).
375. Ryu, D. *et al.* Urolithin A induces mitophagy and prolongs lifespan in C. elegans and increases muscle function in rodents. *Nature Medicine* **22**, 879–888 (2016).
376. Kuroda, Y. *et al.* Parkin interacts with Klokin1 for mitochondrial import and maintenance of membrane potential. *Human Molecular Genetics* **21**, 991–1003 (2012).

377. Okatsu, K. *et al.* PINK1 autophosphorylation upon membrane potential dissipation is essential for Parkin recruitment to damaged mitochondria. *Nature Communications* **3**, 1016 (2012).
378. Matsuda, N. *et al.* PINK1 stabilized by mitochondrial depolarization recruits Parkin to damaged mitochondria and activates latent Parkin for mitophagy. *Journal of Cell Biology* **189**, 211–221 (2010).
379. Stacpoole, P. W. The pharmacology of dichloroacetate. *Metabolism* **38**, 1124–1144 (1989).
380. Zhang, J. *et al.* Endothelial Lactate Controls Muscle Regeneration from Ischemia by Inducing M2-like Macrophage Polarization. *Cell Metabolism* **31**, 1136-1153.e7 (2020).
381. Mammucari, C. *et al.* FoxO3 Controls Autophagy in Skeletal Muscle In Vivo. *Cell Metabolism* **6**, 458–471 (2007).
382. Evano, B. & Tajbakhsh, S. Skeletal muscle stem cells in comfort and stress. *npj Regenerative Medicine* **3**, 24 (2018).
383. Sousa-Victor, P., Neves, J. & Muñoz-Cánoves, P. Muscle stem cell aging: identifying ways to induce tissue rejuvenation. *Mechanisms of Ageing and Development* **188**, 111246 (2020).
384. Galliot, B., Crescenzi, M., Jacinto, A. & Tajbakhsh, S. Trends in tissue repair and regeneration. *Development* **144**, 357–364 (2017).
385. Benayoun, B. A. *et al.* Remodeling of epigenome and transcriptome landscapes with aging in mice reveals widespread induction of inflammatory responses. *Genome Research* **29**, 697–709 (2019).
386. Shavlakadze, T. *et al.* Age-Related Gene Expression Signature in Rats Demonstrate Early, Late, and Linear Transcriptional Changes from Multiple Tissues. *Cell Reports* **28**, 3263-3273.e3 (2019).
387. Stegeman, R. & Weake, V. M. Transcriptional Signatures of Aging. *Journal of Molecular Biology* **429**, 2427–2437 (2017).
388. Franceschi, C. & Campisi, J. Chronic Inflammation (Inflammaging) and Its Potential Contribution to Age-Associated Diseases. *The Journals of Gerontology Series A: Biological Sciences and Medical Sciences* **69**, S4–S9 (2014).
389. Luan, P. *et al.* Urolithin A improves muscle function by inducing mitophagy in muscular dystrophy. *Science Translational Medicine* **13**, (2021).
390. Liu, S. *et al.* Effect of Urolithin A Supplementation on Muscle Endurance and Mitochondrial Health in Older Adults. *JAMA Network Open* **5**, e2144279 (2022).
391. WARBURG, O. On respiratory impairment in cancer cells. *Science* **124**, 269–70 (1956).
392. Yu, L., Chen, X., Wang, L. & Chen, S. The sweet trap in tumors: aerobic glycolysis and potential targets for therapy. *Oncotarget* **7**, 38908–38926 (2016).
393. Murley, A. & Nunnari, J. The Emerging Network of Mitochondria-Organelle Contacts. *Molecular Cell* **61**, 648–653 (2016).
394. Mishra, P. & Chan, D. C. Mitochondrial dynamics and inheritance during cell division, development and disease. *Nature Reviews Molecular Cell Biology* **15**, 634–646 (2014).
395. Hoque, A. *et al.* Mitochondrial fission protein Drp1 inhibition promotes cardiac mesodermal differentiation of human pluripotent stem cells. *Cell Death Discovery* **4**, 39 (2018).

396. Nagdas, S. *et al.* Drp1 Promotes KRas-Driven Metabolic Changes to Drive Pancreatic Tumor Growth. *Cell Reports* **28**, 1845-1859.e5 (2019).
397. Peiris-Pagès, M., Bonuccelli, G., Sotgia, F. & Lisanti, M. P. Mitochondrial fission as a driver of stemness in tumor cells: mDIVI1 inhibits mitochondrial function, cell migration and cancer stem cell (CSC) signalling. *Oncotarget* **9**, 13254–13275 (2018).
398. Vannini, N. *et al.* Specification of haematopoietic stem cell fate via modulation of mitochondrial activity. *Nature Communications* **7**, 13125 (2016).
399. Edwards, G. *et al.* Loss of AKAP1 triggers Drp1 dephosphorylation-mediated mitochondrial fission and loss in retinal ganglion cells. *Cell Death & Disease* **11**, 254 (2020).
400. Kim, K.-Y. *et al.* DRP1 inhibition rescues retinal ganglion cells and their axons by preserving mitochondrial integrity in a mouse model of glaucoma. *Cell Death & Disease* **6**, e1839–e1839 (2015).
401. Chan, D. C. Mitochondrial Dynamics and Its Involvement in Disease. *Annual Review of Pathology: Mechanisms of Disease* **15**, 235–259 (2020).
402. Chen, H. *et al.* Mitochondrial Fusion Is Required for mtDNA Stability in Skeletal Muscle and Tolerance of mtDNA Mutations. *Cell* **141**, 280–289 (2010).
403. Farge, G. *et al.* In Vitro-Reconstituted Nucleoids Can Block Mitochondrial DNA Replication and Transcription. *Cell Reports* **8**, 66–74 (2014).
404. Li, H. *et al.* Mic60/Mitofilin determines MICOS assembly essential for mitochondrial dynamics and mtDNA nucleoid organization. *Cell Death & Differentiation* **23**, 380–392 (2016).
405. Vincent, A. E. *et al.* The Spectrum of Mitochondrial Ultrastructural Defects in Mitochondrial Myopathy. *Scientific Reports* **6**, 30610 (2016).
406. John, G. B. *et al.* The Mitochondrial Inner Membrane Protein Mitofilin Controls Cristae Morphology. *Molecular Biology of the Cell* **16**, 1543–1554 (2005).
407. El Fissi, N. *et al.* Mitofusin gain and loss of function drive pathogenesis in Drosophila models of CMT 2A neuropathy. *EMBO Rep* **19**, (2018).
408. Liaghati, A. *et al.* Grx2 Regulates Skeletal Muscle Mitochondrial Structure and Autophagy. *Frontiers in Physiology* **12**, (2021).
409. Robertson, G. L. *et al.* DRP1-mediated mitochondrial fission is essential to maintain cristae morphology and bioenergetics. *bioRxiv* 2021.12.31.474637 (2022) doi:10.1101/2021.12.31.474637.
410. Peterson, C. M., Johannsen, D. L. & Ravussin, E. Skeletal Muscle Mitochondria and Aging: A Review. *Journal of Aging Research* **2012**, 1–20 (2012).
411. Tezze, C. *et al.* Age-Associated Loss of OPA1 in Muscle Impacts Muscle Mass, Metabolic Homeostasis, Systemic Inflammation, and Epithelial Senescence. *Cell Metabolism* **25**, 1374-1389.e6 (2017).
412. Busch, K. B., Kowald, A. & Spelbrink, J. N. Quality matters: how does mitochondrial network dynamics and quality control impact on mtDNA integrity? *Philosophical Transactions of the Royal Society B: Biological Sciences* **369**, 20130442 (2014).

413. Balsa, E. *et al.* ER and Nutrient Stress Promote Assembly of Respiratory Chain Supercomplexes through the PERK-eIF2α Axis. *Molecular Cell* **74**, 877-890.e6 (2019).
414. Nishijo, K. *et al.* Biomarker system for studying muscle, stem cells, and cancer *in vivo*. *The FASEB Journal* **23**, 2681–2690 (2009).
415. Suelves, M. *et al.* uPA deficiency exacerbates muscular dystrophy in MDX mice. *Journal of Cell Biology* **178**, 1039–1051 (2007).
416. Martin, M. Cutadapt removes adapter sequences from high-throughput sequencing reads. *EMBnet J* **17**, 10 (2011).
417. Li, B. & Dewey, C. N. RSEM: accurate transcript quantification from RNA-Seq data with or without a reference genome. *BMC Bioinformatics* **12**, 323 (2011).
418. Robinson, M. D., McCarthy, D. J. & Smyth, G. K. edgeR: a Bioconductor package for differential expression analysis of digital gene expression data. *Bioinformatics* **26**, 139–140 (2010).
419. Ritchie, M. E. *et al.* limma powers differential expression analyses for RNA-sequencing and microarray studies. *Nucleic Acids Research* **43**, e47–e47 (2015).
420. Reimand, J. *et al.* Pathway enrichment analysis and visualization of omics data using g:Profiler, GSEA, Cytoscape and EnrichmentMap. *Nature Protocols* **14**, 482–517 (2019).
421. Subramanian, A. *et al.* Gene set enrichment analysis: A knowledge-based approach for interpreting genome-wide expression profiles. *Proceedings of the National Academy of Sciences* **102**, 15545–15550 (2005).
422. Liberzon, A. *et al.* Molecular signatures database (MSigDB) 3.0. *Bioinformatics* **27**, 1739–1740 (2011).
423. Love, M. I., Huber, W. & Anders, S. Moderated estimation of fold change and dispersion for RNA-seq data with DESeq2. *Genome Biology* **15**, 550 (2014).
424. Sacco, A. *et al.* Short Telomeres and Stem Cell Exhaustion Model Duchenne Muscular Dystrophy in mdx/mTR Mice. *Cell* **143**, 1059–1071 (2010).
425. García-Prat, L. *et al.* FoxO maintains a genuine muscle stem-cell quiescent state until geriatric age. *Nature Cell Biology* **22**, 1307–1318 (2020).
426. Perdiguero, E. *et al.* p38/MKP-1–regulated AKT coordinates macrophage transitions and resolution of inflammation during tissue repair. *Journal of Cell Biology* **195**, 307–322 (2011).

ACKNOWLEDGMENTS

I would like to thank all the lab members from the PMC lab, especially to Dr. Joan Isern, Dr. Antonio Serrano, Dr. Eusebio Perdiguero, Dr. Jessica Segalés, Oleg Deryagin, Ángela Pollán, Dr. Laura Ortet, Ignacio Ramírez-Pardo, Silvia Campanario-Sanz, Marina Raya, José M. Ballestero, Vera Lukesova, Eva Andrés, Victoria Moiseeva for their invaluable technical supports and helpful discussions. I would also like to thank collaborators Drs José A. Enríquez, José M. Villalba, José A. González-Reyes, Marco Sandri, Ramon I Klein Geltink, Erika Pearce, Luca Scorrano for invaluable knowledge and/or reagents, as well as CNIC facility members Elena Prieto-García (CNIC FACS Facility), Veronica Labrador-Cantarero (CNIC Advanced Microscopy Facility); Alberto Benguría-Filippini (CNIC-Genomics Facility); Manuel J. Gómez-Rodríguez (CNIC-Bioinformatics Facility) for their technical supports.

SUPPLEMENTARY INFORMATION

SUPPLEMENTARY DATA on the informatic device

Supplementary Table 1. List of differentially expressed (DE) genes between *Drp1^{WT} vs Drp1$^{\Delta Pax7ER}$* in quiescence, 1-DPI and 3-DPI. DE genes were found using Bioconductor package limma with voom transformation and adjusted p value of 0.05 was set as the threshold for significance.

Supplementary Table 2. Gene expression matrices of G2_M, mitochondrial complex subunits (CI to CV subunits) as well as OXPHOS pahways of the following conditions: Quiescence *Drp1^{WT}* (QWT); Quiescence *Drp1$^{\Delta Pax7ER}$* (QKO); 1-DPI *Drp1^{WT}* (1DPI_WT); 1-DPI *Drp1$^{\Delta Pax7ER}$* (1DPI_KO), 3-DPI *Drp1^{WT}* (3DPI_WT); 3-DPI *Drp1$^{\Delta Pax7ER}$* (3DPI_KO). Data were represented in averaged value of transcript per million (TPM).

Supplementary Table 3. List of differentially expressed (DE) genes between young *vs* old in quiescence, 1-DPI and 3-DPI. DE genes were found using Bioconductor package limma with voom transformation and adjusted p value of 0.05 was set as the threshold for significance.

Supplementary Table 4. Gene expression matrices of G2_M, mitochondrial complex subunits (CI to CV subunits) as well as OXPHOS pahways of the following conditions: Quiescence young (QY); Quiescence old (QO); 1-DPI young (1DPI_Y); 1-DPI old (1DPI_O), 3-DPI young (3DPI_WT); 3-DPI old (3DPI_O). Data were represented in averaged value of transcript per million (TPM).

APPENDIX

In the course of my PhD Thesis, I have participated in two study of the laboratory and have collaborated in the publication of another article with collaborators (in which I am a first co-author) and in the writing of one review article (see below).

FoxO maintains a genuine muscle stem-cell quiescent state until geriatric age.

García-Prat L, Perdiguero E, Alonso-Martín S, Dell'Orso S, Ravichandran S, Brooks SR, Juan AH, Campanario S, Jiang K, **Hong X**, Ortet L, Ruiz-Bonilla V, Flández M, Moiseeva V, Rebollo E, Jardí M, Sun HW, Musarò A, Sandri M, Del Sol A, Sartorelli V, Muñoz-Cánoves P.

Nat Cell Biol. 2020 Nov;22(11):1307-1318.

In vivo transcriptomic profiling using cell encapsulation identifies effector pathways of systemic aging.

Mashinchian O*, **Hong X***, Michaud J, Migliavacca E, Lefebvre G, Boss C, De Franceschi F, Le Moal E, Collerette-Tremblay J, Isern J, Metairon S, Raymond F, Descombes P, Bouche N, Muñoz-Cánoves P, Feige JN, Bentzinger CF.

Elife. 2022 Mar 4;11:e57393.

Assessing Autophagy in Muscle Stem Cells.

Campanario S, Ramírez-Pardo I, **Hong X**, Isern J, Muñoz-Cánoves P. Assessing Autophagy in Muscle Stem Cells.

Front Cell Dev Biol. 2021 Jan 21;8:620409.

Stem cell aging in the skeletal muscle: The importance of communication.

Hong X, Campanario S, Ramírez-Pardo I, Grima-Terrén M, Isern J, Muñoz-Cánoves P.

Ageing Res Rev. 2022 Jan;73:101528.